PhD SCHOOL "VITO VOLTERRA" IN ASTRONOMICAL, CHEMICAL, EARTH, MATHEMATICAL AND PHYSICAL SCIENCES

EARTH SCIENCES PhD

XXIX CYCLE

"VIBRATIONAL INTERACTION BETWEEN URBAN AGGLOMERATES AND GEOLOGICAL SYSTEM WITH HETEROGENEOUS COMPOSITION"

Tutor:

Prof. Salvatore Martino

Co-Tutor:

Luca Lenti PhD

PhD Student:

Chiara Varone

ID Number: 1185664

A.A. 2016/2017

THESIS CONTENTS

INDEX

LIST OF FIGURES

Fig 3.6: Zonation of the Lazio region according to the maximum macroseismic intensity areas (from D.G.R. Lazio n. 545 of 26/11/2010).

Fig. 4.1: CTR (Regional technical Map) scale 10.000 – Black points indicate the location of the ambient noise recording stations (the fundamental resonance frequency is also reported); black triangles indicate the velocimetric array; the black square corresponds to the position of the calibration Soil Column A. The traces of the three geological cross-sections AA', BB' and CC' are also reported; the outcropping seismic bedrock corresponds to the screened areas (Bozzano et al. 2016).

Fig. 4.2: Examples of the HVSR results obtained from the noise measurements. See Fig. 4.1 for the noise measurements location.

Fig. 4.3: Geological cross sections along the AA', BB', CC' traces of Fig. 4.1. Legend: AL deposits: 1) Anthropic filling material (AL-AF); 2) Sandy-Clays characterized by a marked volcanic component (AL-VSC); 3) Peaty clays, plastic (AL-PC); 4) Clays and silts, plastic (AL-CS); 5) Peat (AL-PT); 6) Sands and silty sands (AL-SD); 7) Polygenic, loose and heterometric gravels, with volcanic and sedimentary components (AL-GR). VL deposits: 8) Undifferentiated pyroclastic material (VC). FP deposits: 9) Fluvio-palustrine deposits composed of loose gravels, sands and silts. PT deposits: 10) Sandy clays and silts, sometimes with freshwater gastropods (PT-SC) 11). Clays and silts with peaty layers (PT-CL); 12) Sands and silty sands. (PT-SD); 13) Loose gravels with heterometric sedimentary components (PT-GR). PP deposits: 14) Marine clays and silty clays; 15) Marine sands and silty sands. 16) Fault. 17) Borehole (Bozzano et al. 2016).

Fig. 4.4: 2D planar restitution of the high resolution 3D geological model of the Fosso di Vallerano valley referred to different depths a.s.l.. Key to legend: see Tab. 4.2 (Bozzano et al. 2016).

Fig. 4.5: a) Vs profiles corresponding to the best fit. Key to legend: see Tab. 4.2. b) Comparison between results of the numerical modelling and experimental data for the best fit Vs profile.

Fig. 4.6: Engineering geological model obtained for the subsoil of the Fosso di Vallerano valley. The velocity value corresponding to the volumetric threshold is also indicated (Bozzano et al. 2016).

Fig. 5.1: Synthetic input EQ – 1. a) Signal in time domain b) Fourier amplitude of the signal.

Fig. 6.9: Wave propagation maps of the vertical (top) and horizontal (middle) components of the displacement along the AA' coupled models. From left to right: AA'TS1, AA'-TS2, AA'-TS3. See description of building network page 61.

Fig. 6.10: Contour maps of the $A(f)_x$ functions distribution (top) along the AA' coupled models surface (bottom). From left to right: AA'-TS1, AA'-TS2, AA'-TS3. See description of building network page 61.

Fig. 6.11: Variation of the kinetic energy E(x) index (top) along the AA' coupled models surface (bottom).From left to right: AA'-TS1, AA'-TS2, AA'-TS3. See description of building network page 61.

Fig. 6.12: Examples of the Transfer Functions (TF) of the buildings composing the AA' coupled models. a) Building 4 in AA'-TS3 b) Building 10 in AA'-TS3.

Fig. 6.13: Wave propagation maps of the vertical (top) and horizontal (middle) components of the displacement along the BB' coupled models surface. From left to right: BB'-TS1, BB'-TS2, BB'-TS3. See description of building network page 61.

Fig. 6.14: Contour maps of the $A(f)_x$ functions distribution (top) along the BB' coupled models surface (bottom). From left to right: BB'-TS1, BB'-TS2. See description of building network page 61.

Fig. 6.15: Variation of the kinetic energy E(x) index (top) along the BB' coupled models surface (bottom). From left to right: BB'-TS1, BB'-TS2. See description of building network page 61.

Fig. 6.16: Examples of the Transfer Functions (TF) of the buildings composing the BB' coupled models. a) Building 1 in BB'-TS2 b) Building 10 in BB'-TS2

Fig. 6.17: Comparison between the variations of the kinetic energy E(x) of wave field Up perturbed by the progressive urbanization of the AA' coupled model.

Fig. 6.18: Wave propagation maps of the vertical (top) and horizontal (middle) components of the perturbed wave field (in terms of displacement) along the surface of AA' coupled models: From left to right: AA'TS1, AA'-TS2, AA'-TS3. See description of building network page 61.

LIST OF TABLES

Extended abstract

This PhD thesis evaluates Site-City Interaction (SCI - Guéguen et al. 2002, Bard et al. 2005, Guéguen and Bard 2005, Kham et al. 2006, Semblat et al. 2008), i.e., the influence of buildings on ground motion and local seismic responses. The free-field conditions of the ground surface, which consider the absence of structures that can generate vibrations, are widely used to analyse the local seismic response for both scientific and technical issues. Nevertheless, this assumption leads to a very strong approximation in urban areas, in which the dynamic interaction between the urban agglomerate and the soil cannot be neglected. Many bibliographic data showed the transmission of vibrations from buildings to the soil, i.e., the amplification of ground shaking during earthquakes and the generated wave field, which can propagate far from the city centre (Wirgin and Bard 1996, Guéguen et al. 2000, Kham et al. 2006, Semblat et al. 2008). Previously published studies mainly focused on engineering, while the geological component was strongly simplified. Thus, complex 1D amplification effects from the soil layering and 2D effects from the lateral heterogeneity, topography and shape of the seismic bedrock have been underestimated. The Fosso di Vallerano valley case study was chosen because this area is characterized by a highly heterogeneous geological setting and has recently experienced a massive expansion of urbanization during the last decade, which completely perturbed the free-field conditions of the original alluvial valley that was created by the tributaries of the Tiber River during the Holocene. In particular, the Fosso di Vallerano valley hosts the "Europarco Business Park", i.e., the highest buildings (120 m) in Rome. A preliminary phase of this research was dedicated to the reconstruction of the engineering-geological model of the valley, the 1D numerical modelling of the seismo-stratigraphic setting of the alluvial body (Bozzano et al. 2015, 2016) and the calibration of an absorbing layer system to remove spurious wave reflections at the model boundaries (Varone et al. 2014). Several geophysical investigations have also been conducted by considering both seismic events and noise measurements. In recent decades, great effort has been dedicated to numerical approaches to evaluate the local seismic response. Numerical modelling actually represents the main tool to estimate local seismic responses, particularly in urban areas, where geophysical measurements are often not suitable. A proper 2D numerical modelling of the seismic response in free-field conditions that considers the city agglomerate according to an SCI approach is conducted through the CESAR-LCPC FEM code, which considers two geological sections across the Fosso di Vallerano valley. The structural and dynamic features of different building typologies in the selected study area are also considered. The urban agglomerate in this valley mainly consists of residential reinforced

concrete (RC) buildings, which are characterized by rectangular or square geometry and heights from 6 m to 25 m. The valley also hosts particular type of buildings that are part of the "Europarco Business Park", including two skyscrapers (named "Europarco Tower" and "Eurosky Tower") that are 120 m and 155 m high, respectively. These towers are characterized by a rectangular plan geometry and consist of steel that is coupled with a reinforced concrete structure. The eigenmodes are computed through the CESAR-LCPC code to evaluate the dynamic characteristics of the buildings. All the buildings are modelled by considering their super-structure, i.e., columns and beams, and by assuming the concentrated masses and stiffness values in 2D. The main periods of the urban expansion are defined to evaluate the variations in the local response because of the increasing urbanization that was observed over the last decade. Overall, 5 models that assume SCI conditions are simulated. Ricker wavelets (Ricker 1943, 1953) of order 0 with PGD = 1 m (synthetic wavelet) and three real weak motions are applied as seismic input within the seismic bedrock of all the models by assuming visco-elastic conditions. The results are analysed in terms of wave propagation along the models' surfaces, the spatial variation in the amplification function and the distribution of the kinetic energy along the ground surface. The wave propagation maps show the effectiveness of the absorbing layer system on both sides and at the bottom of the models to dampen spurious waves. Indeed, no spurious contributions enter the valley through the boundaries or the bottom of the model. The presence of the buildings induces major changes in the propagated wave field, inducing a low ground motion at the building's foundation level and increasing the ground shaking in the area surrounding the structures. The influence of these buildings is also very important in the amplification function: all the modes under free-field surface conditions are nullified in the portions that are occupied by the buildings, and larger amplifications are calculated laterally and near the buildings' foundations. Additionally, a redistribution of the energy along the ground surface is shown by a strong reduction in the kinetic energy close to the building and an increase in the areas surrounding the buildings. These findings highlight that the presence of buildings significantly changes the seismic response of the alluvial valley at least at the local scale.

1. INTRODUCTION

In recent years, strong earthquakes have affected highly urbanized areas, leading to a high level of urban destruction: Italy 2009 ($M_L \approx 5.9$), Chile 2010 ($M_L \approx 8.8$), Japan 2011 ($M_L \approx 9.0$), Nepal 2015 ($M_L \approx 7.8$), Taiwan 2016 ($M_L \approx 6.6$) and Italy 2016 ($M_L \approx 6.0$). These events confirm the importance of a hazard analysis for urbanized areas that considers buildings as active components of the hazard and not only as victims, as already proposed by Guéguen et al. (2000; 2002).

The scientific community is aware of variations in free-field motion in basins because of physical phenomena such as resonance (Dobry and Vucetic 1987), basin-generated surface waves (Bard and Bouchon 1980, Kawase 1996, Graves et al. 1998, Narayan 2005, Chaljub et al. 2010; Semblat et al. 2010, Paolucci and Morstabilini 2006), basement focusing effects (Gao et al. 1996, Booth et al. 2004, Narayan and Kumar 2012, 2014a) and basin-transduced surface waves (Kawase 1993 Narayan 2010, 2012; Narayan and Kumar 2014b), while phenomena that are related to soil-structural interactions are usually not considered. In the case of multiple structures at the surface of alluvial deposits, the soil-structure-soil interaction is generalized to multiple interactions, which are defined as "Site-City Interactions" (Guéguen et al. 2002, Bard et al. 2005, Guéguen and Bard 2005). The term SCI (Site-City Interaction) was first proposed by Guéguen et al. (2002). Site–City Interactions (SCI) include the combined effects of basins, kinematic soil–structure interactions and inertial structure–soil interactions on a global scale (Bard et al. 2005). Several studies since the end of the 1990s addressed the topic of Site–City Interactions (SCI) according to the growing interest of the scientific community and administrative entities toward soil-structure-soil multiple interactions. Wirgin and Bard (1996) performed 2D numerical models to describe the diffraction patterns of surface waves because of the presence of buildings, while Tsogka and Wirgin (2003) assessed the effects of diffracted waves on buildings. Clouteau and Aubry (2001) and Clouteau et al. (2002) performed 3D numerical modelling through a boundary-element method (BEM) to evaluate the SCIs in Nice, France, and Mexico City, Mexico. Kham et al. (2006) and Semblat et al. (2008) conducted 2D numerical modelling to evaluate the influence of the geometry and typology of buildings in urban agglomerates, indicating that SCIs under double-resonance conditions can lead to significant variations in the seismic wave field compared to free-field motion. Other authors studied SCIs through an analytical approach: Guéguen et al. (2002) described the global city effects of urban agglomerates by adding the contribution from a series of single oscillators to represent the buildings, and Boutin and Roussillon (2004) focused on multiple interactions between buildings. Other studies have been conducted through an experimental approach. Guéguen et al. (2000) examined a reduced-scale structure in the Volvi EuroSeis Test site and recorded the wave field that was radiated by the structure, while Gallipoli et al. (2006) studied buildings as a seismic source in a test site in Italy. Chávez-García and Cárdenas-Soto (2002) and

Gallipoli et al. (2004) studied the influence of buildings through an H/V spectral ratios analysis. Ditomasso et al. (2010) evaluated the influence of a vibrating building on the free-field ground motion through a combined numerical and experimental approach. Chazelas et al. (2003) observed the interactions between structures through the soil with reduced-scale centrifuge experiments (Semblat and Luong 1998). These studies mainly focused on engineering aspects and highlighted that the effects of SCI on the ground motion strongly depend on the urban configuration, the city's heterogeneity and the building density, also proposing an empirical relationship to quantify the SCI effect (Guéguen et al., 2002), while the influence of geological components on SCI was simplified. The influence of 2D and 3D effects has not yet been considered: Sahar et al. (2015) evaluated the role of the basin shape, i.e., 2D effects according to Bard and Bouchon (1985), on SCI by considering different basin shapes, but only with a homogenous filling.

The goal of this PhD research is to evaluate the effects of SCI in heterogeneous geological systems by considering both geological and engineering features. The chosen case study is the Fosso di Vallerano valley in the southern region of Rome, Italy, a recently urbanized district of the city. The alluvial basin is characterized by a complex and heterogeneous geological setting and hosts the "Europarco Business Park", which contains the highest buildings in the city. Moderate to severe seismicity can affect the study area because of earthquakes that originate in the seismogenic zones that are close to the city (Molin et al. 1986). Several studies focused on the local seismic response in Rome's urban area (Rovelli et al. 1994, 1995; Bozzano et al. 2008, Bozzano et al. 2012, Caserta et al. 2012, Martino et al. 2015) and noted the amplification phenomena within this urban area.

To simulate the real setting of the study area, a high-resolution geological model is constructed to examine the 1D and 2D effects that are caused by the shape of the valley (Bard and Bouchon, 1985) and the presence of horizontal heterogeneities (Martino et al. 2015) and is coupled with high-resolution models of the hosted buildings.

This PhD research represents a contribution to the comprehension of the above phenomena, thus enabling researchers to determine the effect of urbanization on generated wave fields with respect to the theoretical "free-field" assumption.

1.1 Site-City Interaction (SCI) in the framework of the "Resilient City" concept

Resilience is derived from the Latin word *Resilio*, which means "to jump back" (Klein et al. 2003). Initially, the resilience concept was used in ecological, physical, psychological and psychiatric fields, but this term has been applied in many fields, including those that involve natural disasters. In the oldest definitions, authors like Wildawsky (1991), Holling (1995) and Horne (1998) presented resilience as a process reaction. Definitions focused on the keyword "have to face up; resist and absorb the negative impacts and get back to the normal as soon as possible", highlighting a reactive attitude. More recent resilience definitions, such as those by Pelling (2003), Comfort et al. (1999) and the United Nations Office for Disaster Risk Reduction - UNISDR (2005), widely use keywords such as "cope with" and "adaptation", highlighting resilience as an immediate response to natural disasters. The most popular approach that focuses on urban resilience is related to the capability to survive natural or man-made hazards, e.g., disasters, catastrophes, attacks, etc. (Ouyang et al. 2012; Campanella 2006). This definition of the resilience concept is different from the concept of resistance, which indicates the ability of a system to avoid variations with respect to the original state during a disturbance, thus absorbing the impact (Manyena, 2006). Individuals and communities are resilient when they can survive a disturbance thanks to essential goods, livelihood and culture; so the goal of a resilient community is to improve goods and resources to adapt to different circumstances (Manyena, 2006). Two typologies of urban resilience can be defined, namely, structural and social resilience, both of which refer to the capacity of interactions between human society and physical systems:

- Social resilience focuses on human societal frameworks, in which some levels can be defined: society, culture, religion and demography.
- Structural resilience deals with physical systems, which include infrastructures, buildings, territories and natural environments.

Cities are complex and dynamic systems in which technological and social components interact. A flexible link between physical and social components creates a "Resilient City". The planning of a city that can adapt to a natural disaster requires an urban and social setting that exhibits opposite characteristics, such as redundancy and efficiency, diversity and interdependence, strength and flexibility, autonomy and cooperation, and planning and adaptability. These characteristics define a "Resilient City", which can tolerate disruptions before reorganising around a new set of structures and anticipate, prepare for, respond to and recover from a disturbance (Drobniak, 2012), differing from the concept of a "Smart City".

According to Baron (2012), a “Smart City” mainly stands for a transition in municipal (metropolitan) services based upon the implementation of new technologies, which enables new pathways of delivery or brand new services that are related to communication, security and sustainability. A “Smart City” can be considered

- a specific strategic orientation toward the development of new (or revitalised) quarters in which technologies support interactions between service providers and consumers, force expected social behaviours or enhance civil security;
- a way of implementing technological solutions into existing urban structures, by which a real-time (or prompt) response is offered to citizens’ and businesses’ needs and to emerging risks and dangers.

New technologies that are related to “Smart Cities” support “Resilient Cities” via several long-term strategies or by mid-term or short-term programmes and task forces.

Contributions from engineering geology to the “Resilient City” concept can be invoked to improve both structural and social resilience. In particular, the technical component of engineering geology contributes to structural resilience through the scientific comprehension of natural phenomena and their interactions with the surrounding environment. For example, in this framework are the knowledge about the lithosphere structure, the identification of seismogenic structures and the comprehension of the waves from the seismigenic source. Engineering geology applications to urban planning can also contribute to structural and social resilience, facilitating the realization of hazard maps, vulnerability maps and the definition of response scenarios from possible natural disasters.

Studies of Site-City Interaction (SCI), evaluations of the role of SCIs on local seismic responses and the definition of an urban planning SCI based on seismic risk reduction can improve urban resilience, creating a “Resilient City”.

1.2 Thesis outline

Following this introductory chapter, this thesis comprises six other chapters dealing with topics and objective above mentioned. In particular:

- Chapter 2 ("Description of the case study") introduces the Fosso di Vallerano case study and reports the main features of the urban development that affected the area in the last decades.

- Chapter 3 ("Geological setting") introduces the geological and geomorphological setting of the Roman area providing a focus on the seismicity of the area.

- Chapter 4 ("Engineering-geological characterization of the study area") provides a detail analysis of the lithotechnical setting of the valley and of the geophysical data that allowed the construction of the engineering-geological model of the Fosso di Vallerano valley.

- Chapter 5 ("2D numerical modelling") presents the geological cross sections selected for the modelling and the main features of the CESAR-LCPC numerical code. It also provides a detail characterization of the 2D numerical models in terms of geometrical features, dynamic parameters characterizing soil and structures. The calibration of an absorbing layer system to reduce the presence of spurious waves generated at the models boundaries is also presented.

- Chapter 6 ("Main results from the simulation models") reports the main findings obtained from the 2D numerical modelling of the cross sections taken into account. More in particular it deal with ground motion, amplification levels and kinetic energy variation due to the presence of buildings.

- Chapter 7 ("Discussion") and 8 ("Conclusions") discuss the obtained results and draw some general conclusions pointing out some possible future research topics evolving from this study.

2. DESCRIPTION OF THE CASE STUDY

The Fosso di Vallerano valley is an alluvial valley in the southern region of Rome's urban area, approximately 10 km SE of the historical centre of the city. This valley, which is located on the left side of the Tiber River, is seated within the XII sub-municipality (*Municipio)* of Rome in the locations "Castellaccio" and "Torrino" (EUR District).

This area was selected because it is characterized by a very complex geological setting (highly heterogeneous soil deposits) and has recently experienced urban expansion, which completely perturbed the free-field conditions of the original alluvial valley from the tributaries of the Tiber River during the Holocene.

The study area is included in the I.G.M. topographic sheets n. 149 "Acilia" and n. 150 "Cecchignola" (scale 1:25.000) and in the Regional Technical Map (CTR) of Lazio Region n. 374140 and n. 387020 (scale 1:100.000).

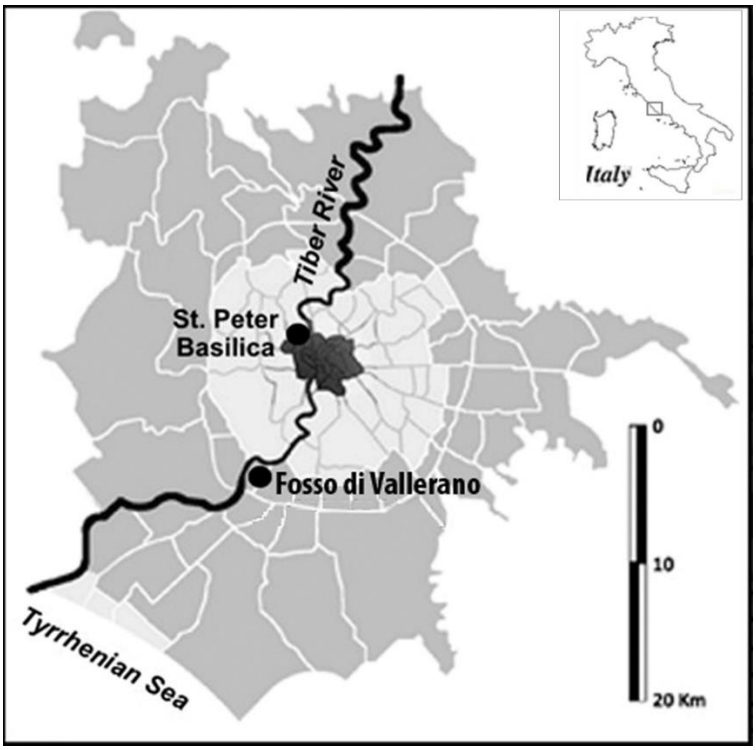

Fig. 2.1: Representation of the position of the Fosso di Vallerano valley within the municipality of Rome.

From a hydrological perspective, the Fosso di Vallerano valley is part of the drainage basin of the left tributary of the Tiber River, which extends from SE to NW and drains surface water from the Alban Hills and Castel Gandolfo area to the Tiber River (Ventriglia 2002). This basin consists of two sub-basins that join before the Tiber River confluence: the Vallerano creek in the SE portion and the Cecchignola creek in the NE portion. The Fosso di Vallerano basin is characterized by a flat portion

that corresponds to flood plains (10 m a.s.l.) that are bordered by hills (35-50 m a.s.l.). The area also exhibits a complex geomorphological setting because of a complex evolution that was linked to the Würmian glacio-eustatic cycle, which led to a series of successive deviations and rearrangements of the riverbed (Ascani et al. 2008).

This thesis focus on a flat portion (10 m a.s.l.) of the Fosso di Vallerano valley (Fig. 2.2), which is bordered to the north by the Montorio hill, to the east by the Monte delle Pozzonale hill, to the west by the Torrino hill, and partially by the Castellaccio hill to the south.

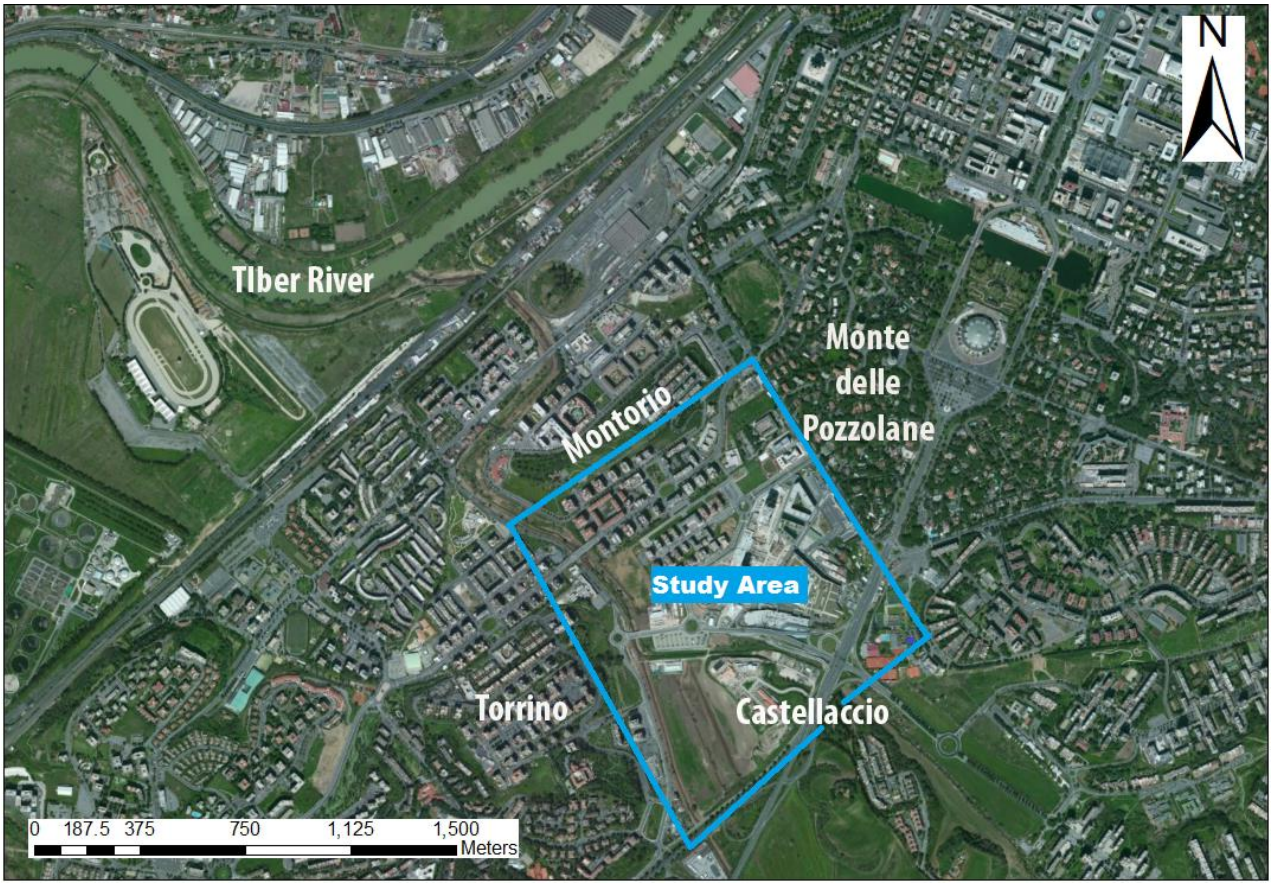

Fig. 2.2: Satellite view of the Fosso di Vallerano area. The blue line borders the portion of Fosso di Vallerano valley in which this study is focused on.

2.1 Urban development of the Fosso di Vallerano valley in the last decades

The Fosso di Vallerano valley and the surrounding areas represent a new expansion zone of the urban area of Rome. This portion of the city has seen the development of wide urban agglomerates over the last few decades, some of which are planned in the following years. In particular, the urbanization of the study area began in 2002 in the northern section of this region (Fig. 2.3a) with the realization of an urban complex that included residential buildings with concrete structures. These buildings are characterized by a square base and from 6 to 9 floors. This residential urban evolution progressively moved toward to the south in 2005, enveloping a large portion of the valley (Fig. 2.3b-c). From 2007 to the present, this urban development has continued throughout the southern portion of the study area (Fig. 2.3d-e-f), including residential, commercial and official buildings.

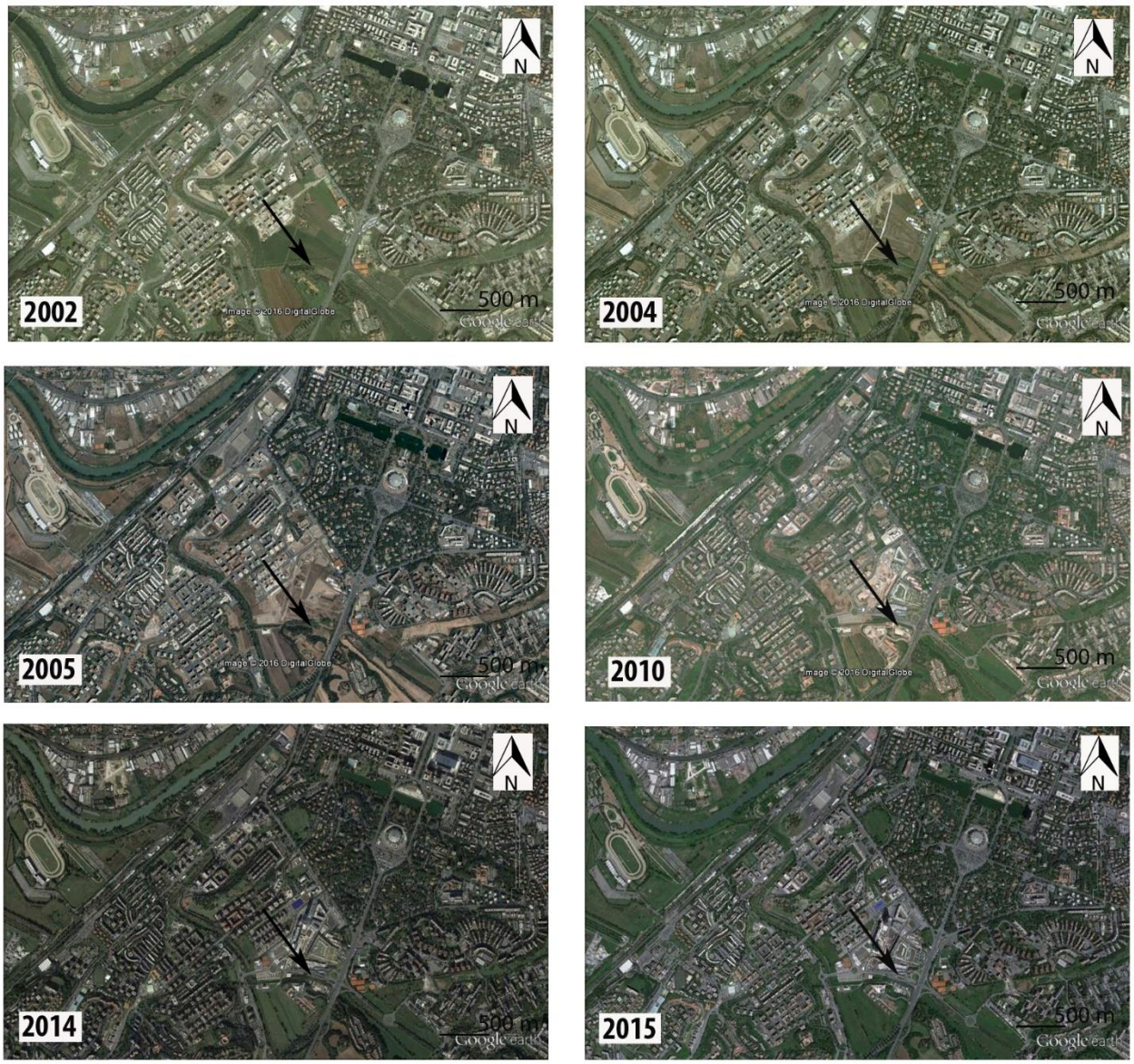

Fig. 2.3: Satellite views representing the urban development of the Fosso di Vallerano area from 2002 to 2015. The direction of the urban development is also indicated.

This last urban development phase is associated with buildings that belong to the "Europarco Business Park", which comprises a total of 10 buildings (Fig. 2.4):

- Seven office buildings, including the Italian Ministry of Health (*Ministero della Salute*). These reinforced concrete structures have 9 to 13 floors and are characterized by shallow foundations.
- One commercial centre, which is called Euroma 2 and represents one of the largest shopping centres in Rome. This building consists of 6 floors and a gross leasable area of 81.500 m^3. This building is characterized by a reinforced concrete structure and shallow foundations.
- Two skyscrapers, namely, the Eurosky and Europarco Towers, which host apartments and offices, respectively (Fig. 2.4a). These buildings have 33 floors and are characterized by a rectangular gross leasable area of around 30.000 m^3. These buildings are supported by a mixed structure with concrete columns and mixed steel-concrete beams. These buildings are founded on 201 piles (diameter of 1.2 m) with lengths of 57 m; all the piles are joined in the head by a shallow foundation with a thickness of 6.3 m. These structures are currently the tallest buildings in Rome.

Fig. 2.4: a) Photo view of the two "Europarco Business Park" towers during their construction in 2012 (left) and actual view of the towers from the terrace of Euroma2 shopping centre (right). b) Satellite views of the "Fosso di Vallerano" area from SE (left) and E (right).

In the following years, the study area is planned to host the new *Stadio della Roma*, an ultra-modern and innovative steel and glass structure that is wrapped in a stone scrim. The architecture of the *Stadio della Roma* (52.500 seats) resembles a modern colosseum and will be part of a complex that contains a series of shops, restaurants and bars, including a Roma Superstore and an interactive AS Roma Hall of Fame. This important and wide structure in the study area will necessitate changes to the transportation network, including strengthening existing transport networks (*Roma – Lido* and *Metro B* railways) and creating a new light railway system.

Fig. 2.5: Images of the new *Stadio della Roma* that is planned to be hosted in the area surrounding the Fosso di Vallerano valley (from http://www.asroma.com)

3. GEOLOGICAL SETTING

3.1 Geological setting of Rome

The geological evolution of Rome (Fig. 3.1-3.2) resulted from a combination of Miocene to Early Pleistocene extensional tectonic phases that were related to the Apennines' back-arc evolution (Patacca et al. 1990, Carminati et al. 2007), a Middle-Late Pleistocene phase in close connection with sea level oscillations (Karner and Marra 1998, Marra et al. 2008), and the activity of the volcanic district that surrounds the city (Karner and Marra 2001b, Giordano et al. 2006, Marra et al. 2009, 2014, Sottili et al. 2010).

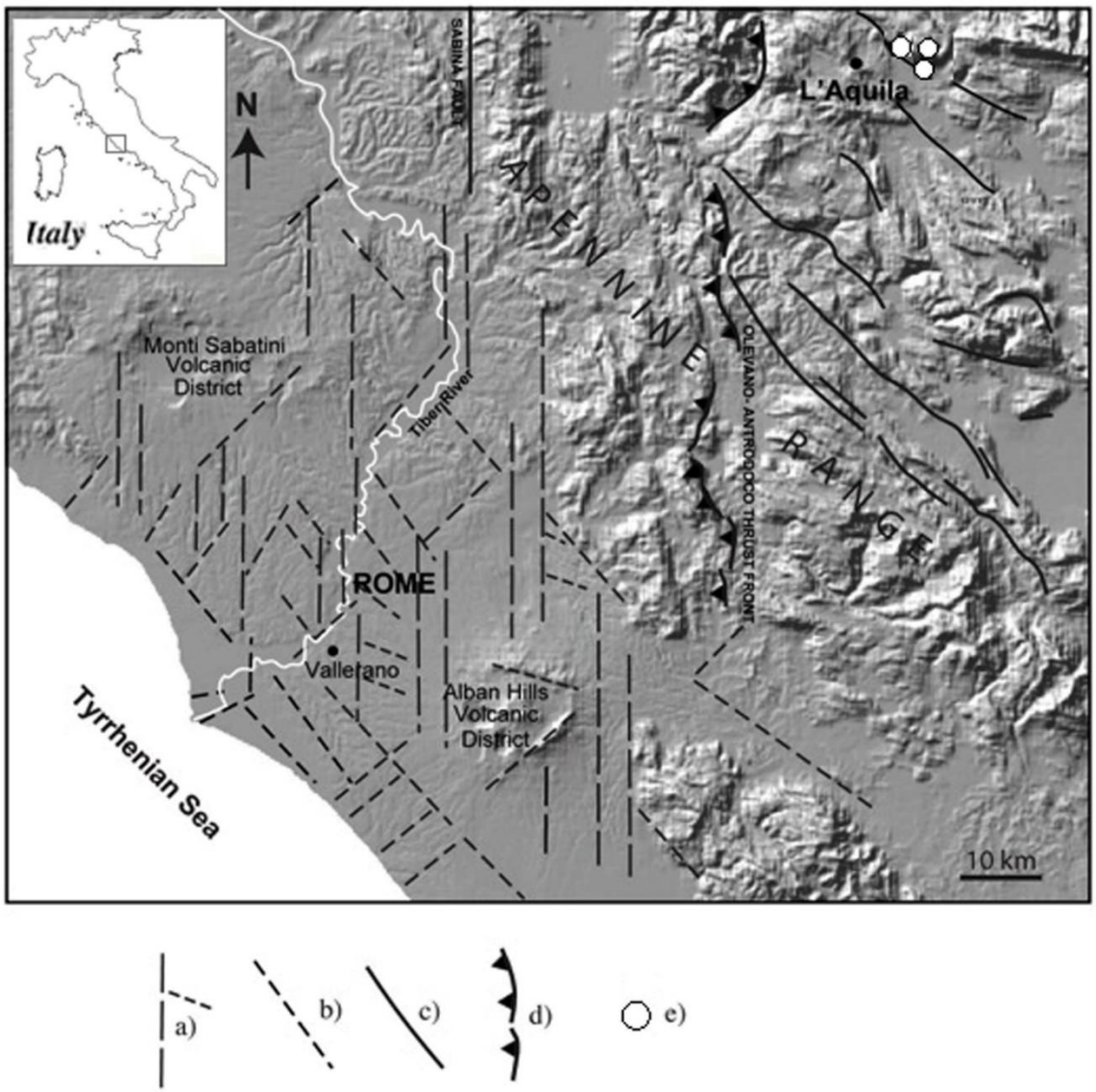

Fig. 3.1: Structural map of the Central Apennines including the area of Rome. a) Main N-S faults and conjugated fault systems; b) buried faults linked to the extensional tectonic regime; c) Seismogenetic faults; d) inactive thrust fronts; e) location of the 9th April 2009 L'Aquila earthquake (Mw 6.3) epicentre (Bozzano et al. 2016).

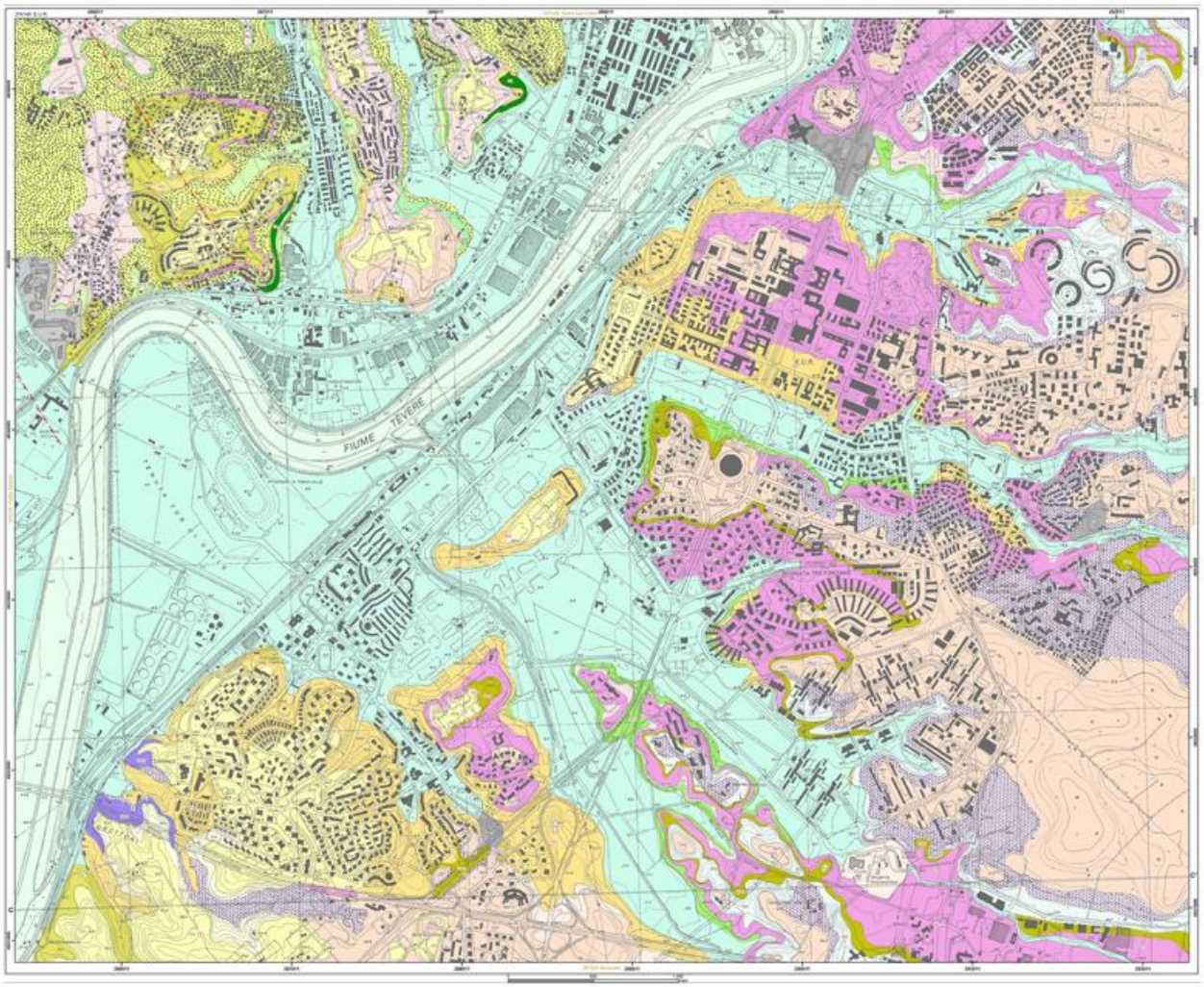

LEGEND

a2	Alluvial deposits	RED	Pozzolane rosse unit
l	Lacustrine deposits	SKF	Sacrofano succession
VSN2	Villa Senni units	KKA	Casale del Cavaliere unit
VSN1		PNO	Palatino unit
SVL	Setteville succession	TDC	Tor de Cenci unit
PNR	Pozzolane nere unit	CIL	S. Cecilia unit
LTT	La Storta succession	MTM2	Monte Mario formation
	Fault	MAV	Monte Vaticano formation

Fig. 3.2: Geological map of the study area.

3.1.1 Marine successions

A series of folds and thrusts affected the area during the Early Miocene, deforming Meso-Cenozoic shallow-marine carbonate deposits. The migration of these folds and thrusts created an extensional tectonics regime because of the opening of the Tyrrhenian back-arc basin (Carminati et al. 2007). This tectonic phase resulted in a *Horst* and *Graben* setting along the Tyrrenian margin and terrigenous marine sedimentation with the deposition of the Flysch Liguri Formation (Funiciello and Giordano 2008), which underlies the deep-sea marine deposits. These deposits were created by three main sedimentary cycles from many marine transgressions (Marra 1993, Marra and Rosa 1995). The first (Middle – Upper Pleistocene) led to the deposition of grey and blue-grey marly-clay and sand, which can be attributed to the Marne Vaticane Formation (Early Pleistocene) and represents the geological bedrock of Roman area (Marra et al. 1995). The second sedimentary cycle was associated with the deposition of the Limi di Farneto and Monte Mario Formations, which mainly consist of grey and yellow sand, highlighting a marine regressive process that led to typical coastal and lagoon sedimentation. The Monte delle Piche Formation is ascribable to a third marine cycle and consists of grey-green clay and sandy-clay with sand whose sedimentological characteristics are typical of shallow basins, indicating the reduction of the deeper areas of the sedimentary basin. This variation in the depositional conditions was caused by the regional uplift of the Tyrrenian margin, which led to the complete emersion of Rome, and is highlighted by the deposition of lagoon clay and sand from the Monte Ciocci - Monte delle Piche Formation, which represents a complete marine transgression (Karner et al. 2001a).

3.1.2 Upper-Middle Pleistocene continental successions

The deposition of the Monte Ciocci Unit and the following depositional units was strictly connected to glacio-eustatic oscillations because of glacial periods (Alvarez et al. 1995, Karner and Renne 1998, Karner and Marra 1998, Marra et al. 1998, Karner et al. 2001a, Florindo et al. 2007, Marra et al. 2008). Marra et al. (2008) distinguished 10 aggradational successions within the Paleo-Tiber depositional units, which corresponded to many glacial terminations between the Monte Ciocci – Monte delle Piche Formation (Marine isotope stages MIS 22) and the actual alluvial cycle of the Tiber River (MIS 1) (Fig. 3.3). These successions are generally fining-upward (Karner and Marra 1998), with coarse-grained gravel and sand that reaches 10 m in thickness at the base of each section. The basal coarse-grained deposits are followed by a relatively thin sand horizon, which grades upward into a several-meter-thick pack of silt and clay. The nature of these sediments is strictly connected with the volcanic activity of the volcanic district around Rome, which led to the continuous deposition

of pyroclastic deposits in the fluvial valley and from which the erosion of the aggradational successions originated.

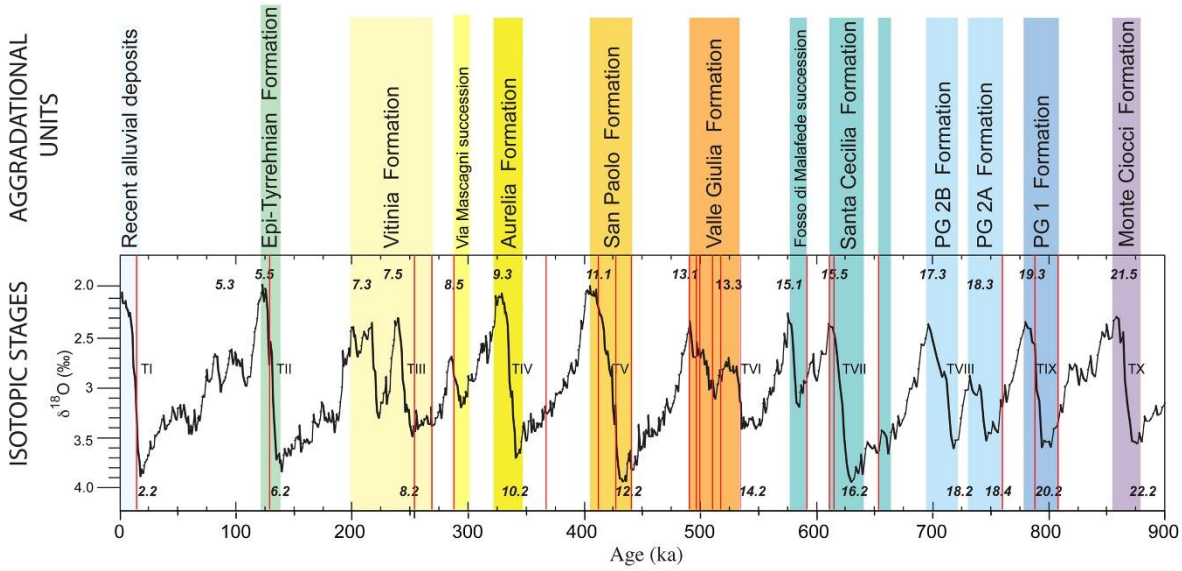

Fig. 3.3: $\delta^{18}O$‰ vs. time for the depositional units by the Paleo-Tiber River and its tributaries. The Marine Isotopic Stages (MIS) are also reported (Arabic numbers within the graph) (Bozzano et al. 2016).

The oldest continental deposits (Upper – Middle Pleistocene) of the Paleo-Tiber are associated with the eustatic uplift of three glacial cycles that were related to MIS 19, 17 and 15 (Marra et al. 1998) and led to the deposition of Ponte Galeria Formation (PG1 and PG2) and Santa Cecilia Formation (Ambrosetti and Bonadonna 1967, Ambrosetti et al. 1972, Conato et al. 1980, Bellotti et al. 1994, Marra et al. 1998, Milli et al. 2008). These deposits correspond to three aggradational cycles (PG 1, PG 2 and the Santa Cecilia Formation, Marra et al. 1998, Karner and Marra 1998), which are characterized by fluvial gravel and grey-blue clay with *Helicella ericetorum* (Conato et al. 1980) (PG 1, MIS 19), gravel and yellow coastal sand with *Arctica islandica* (Conato et al. 1980), lagoon clay ("Middle Clay", Marra et al. 1998), gravel and cross-laminated sand and clay with *Venerupis senescens* (Conato et al. 1980) (PG 2, MIS 17), and lagoon clay with *Cerastoderma* and aeolian sand (Conato et al. 1980) from bottom to top (Santa Cecilia Formation, MIS 15). The fluvial-marshy deposits of the Valle Giulia Formation (Karner and Marra 1998), which are characterized by cross-laminated polygenic gravel with calcareous pebbly and chert, followed by horizontal laminated silty sand that is partly cemented by calcium carbonate with volcanoclastic material, is associated with the following glacial cycle, MIS 13 (Marra and Rosa 1995). The sea-level high-stand that was correlated to the marine MIS 11 led to the deposition of the San Paolo Formation (Marra and Rosa 1995, Karner and Marra 1998), which exhibits different characteristics in different portions of Rome. These materials correspond to deposits from fluvial volcanoclastics ("Conglomerato Giallo", Fornaseri et

al. 1963) and yellow silty sand with pumices and a hazelnut silt and sand layer with scoria and pyroclastic material. The Aurelia Formation was deposited after the following erosional phase, which was associated with the isotopic stage MIS 10 during the eustatic sea-level rise of MIS 9 (Conato et al. 1980, Marra and Rosa 1995). The Aurelia Formation consists of white and hazelnut thickly layered silty sand; the top of the formation contains a para-sequence that is correlated with this sub-stage. The Vitinia Formation is associated with the marine high-stand of MIS 7 (Karner and Marra 1998); the succession consists of a basal conglomerate level with calcareous (80%) and chert pebbles within a yellow sandy-silt layer that is rich in quartz and pyroxene and gradually passes to coarse-grained calcareous and chert sand (Conato et al. 1980). The top of the formation is represented by a brown-red silty layer with analcime, calcareous concretions and fossils (vertebrates and molluscs). Deposits of marine terraces along the coast (Hearty and Dai Pra 1986, Basili and Bosi 1996, Bordoni and Valensise 1998) and fluvial terraces along the Aniene valley are associated with the following eustatic sea-level rise (MIS 5). The eustatic sea-level rise of the last inter-glacial period (MIS 1) led to the deposition of fluvial-lacustrine deposits within the Tiber and Aniene alluvial valleys. These river systems were eroded during the Würmian glacial period (18.000 yr) and progressively filled by fluvial and colluvial deposits between the Upper Pleistocene and Holocene.

3.1.3 Volcanic deposits

The activity of the Monti Sabatini and Alban Hills volcanic districts began around 0.8 Ma, during the Middle-Pleistocene (Karner et al. 2001b). These districts are part of the Roman Comagmatic Province (Washington 1906), which includes a volcanic chain that developed with an NW to SE orientation along the Tyrrenian margin of Italy, and are characterized by alkaline-potassium magma (Conticelli and Peccerillo 1992, Peccerillo 2005).

Volcanic products from the Alban Hills District exhibit compositions from K-foidite to tephrite and phonolitic tephrite (Trigila et al. 1995, Marra et al. 2003, Freda et al. 2006, Gaeta et al. 2006, Giordano et al. 2006, Marra et al. 2009). These materials are characterized by a low SiO_2 content ($\leq$ 45wt %) and a modal composition of clinopyroxene and leucite with accessory biotite, with the absence of sanidine and plagioclase. The activity of this volcanic district is represented by three main phases, each of which is characterized by different eruptive mechanisms and erupted volumes (De Rita et al. 1988, 1995, Giordano et al. 2006). The Tuscolano-Artemisio phase (561-351 ka; Karner et al. 2001a, Marra et al. 2009), which saw tens of cubic kilometres erupted, produced 5 depositional sequences. This volcanic phase is characterized by an initial sub-activity phase (Marra et al. 2009) with hydromagmatic characteristics (Palladino et al. 2001) that led to the deposition of the pyroclastic flows of the Tufo Pisolitico di Trigoria, Tufo del Palatino and Tufo delle Acque Albule, followed by

the “dry” depositions of the Pozzolane Rosse, Pozzolane Nere and Villa Senni Eruptive Sequence. An intermediate lower-energy phase (308 - 250 ka; Marra et al. 2003), which is characterized by strombolian activity from the central edifice of Monte delle Faete and effusive activity from the surrounding area, led to the deposition of leucitite lava flows (Trigila et al. 1995, Boari et al. 2009). A 50-ka quiescence preceded the recent hydromagmatic phase (200-36 ka; Marra et al. 2003, Freda et al. 2006, Giaccio et al. 2009), which led to the formation of maar and tuff ring structures.

The volcanic products of the Monti Sabatini District show higher SiO2 content (≥50 wt.% vs ≤45 wt.% of Alban Hill), with compositions from trachybasalt to trachytes and phonolites, and a modal composition of sanidine, leucite and clinopyroxene (Sottili et al. 2004, Masotta et al. 2010); this district is characterized by continuous activity in different areas (Karner et al. 2001a, Sottili et al. 2004). The first volcanic activity (582 – 410 ka; De Rita et al. 1993, Karner et al. 2001a) mainly affected the Morlupo area and the southern area of the Sabatini District (Sottili et al. 2004) and was characterized by pyroclastic flows and Plinian and sub-Plinian fall. The main eruptive activity began with the First Ashfall Deposits (582±2 ka; Karner et al. 2001a) and the Tufo Giallo di Castelnuovo di Porto (589±4 ka), followed by the Tufo Giallo di Via Tiberina (548±5 ka, Karner et al. 2001a), Tufo Giallo di Prima Porta (514±3 ka, Karner et al. 2001a) and Grottaperfetta pyroclastic sequence. These eruptions concluded the volcanic activity of the Morlupo crater. Afterward, an eruptive phase was concentrated in the southern portion of the Sabatini District (Sottili et al. 2004) and led to the deposition of a thick succession of fall deposits (Tufi Terrosi con Pomici Bianche; 499±6 ka), followed by the pyroclastic flow of the Tufo Rosso a Scorie Nere (449±2 ka; Karner et al. 2001a). The top of this succession is represented by scoria and pumice-fall deposits (Tufi Stratificati Varicolori di La Storta), which are mainly present in the western and southern areas of the Monti Sabatini District. Between 320 and 200 ka, the eruptive activity was concentrated in the Sacrofano and Lake Bracciano areas (Sottili et al. 2010, De Rita et al. 1996). Between 320 and 200 ka, the eruptive activity was concentrated in the Sacrofano and Lake Bracciano areas (Sottili et al. 2010, De Rita et al. 1996). Effusive activity was accompanied by major explosive events, including the Tufo di Bracciano (ca. 312 ka; Sottili et al. 2010) and Tufo Giallo di Sacrofano (285± 2 ka, Karner et al. 2001a) pyroclastic-flow eruptions. Finally, from 170 to 86 ka (Sottili et al. 2010), the late Monti Sabatini eruptive phase was characterized by dominant hydromagmatic and subordinate strombolian and effusive activity from several monogenetic tuff rings and scoria cones between the Bracciano and Sacrofano depressions (Marra et al. 2014).

According to the above-descripted geological setting, in synthesis it is possible to deduce that Tiber River and its tributaries valleys are composed by heterogeneous soft alluvial deposits while relieved areas are mainly composed by stiff volcanic deposits.

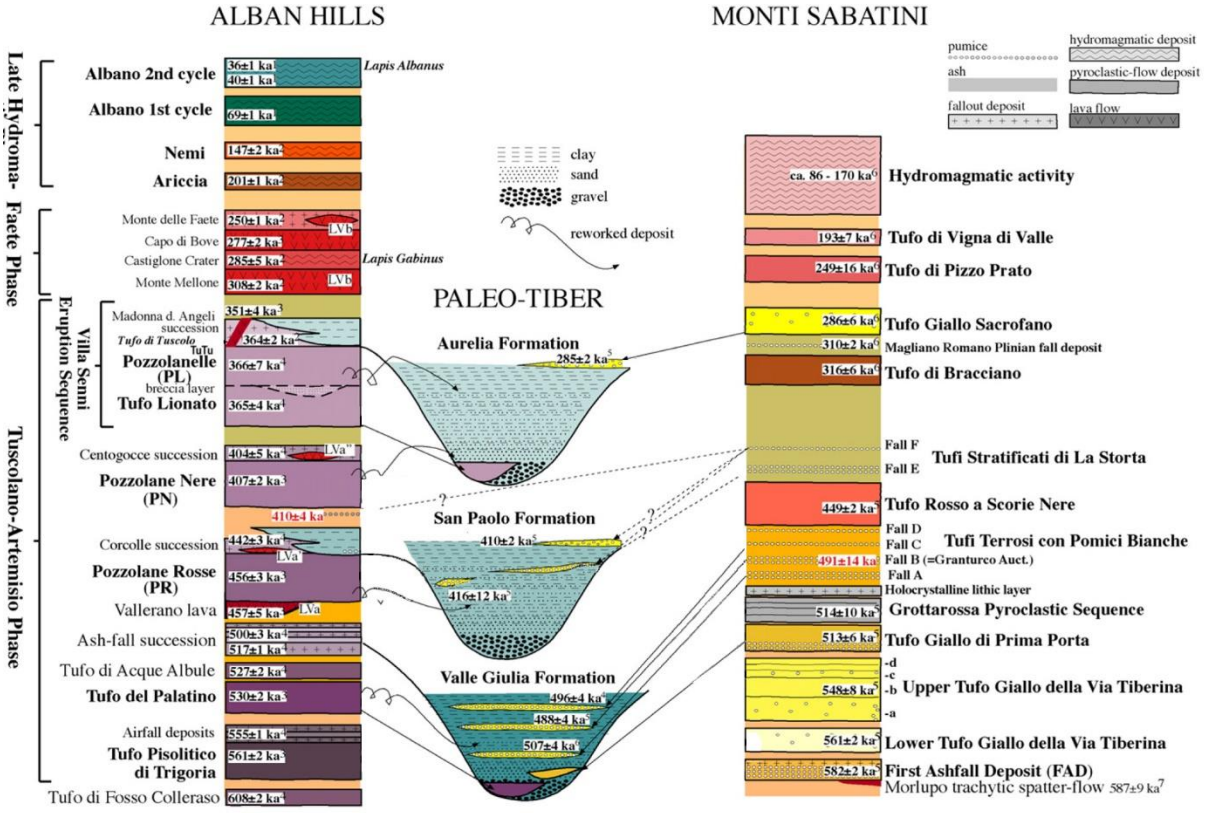

Fig. 3.4: Chronostratigraphic scheme of the Alban Hills and Monti Sabatini volcanic districts and relationships with the sedimentary deposits of the Paleo-Tiber in Rome. (Modified from Marra et al. 2014)

3.2 Seismicity of Rome

Rome is located in the Tyrrenian margin of Central Italy, which has been affected by an extensional tectonic phase behind the Apennines fold-and-thrust belt since the Messinian (Malinverno and Rayan 1986, Patacca et al. 1990, Carminati et al. 2007). This location is in a tectonically active zone with many seismogenic sources (DISS Working Group 2015) that can generate earthquakes of magnitudes up to M≈7.

Rome's seismic risk is related to 3 levels of seismicity (Molin et al. 1995, DBMI 2004, CPTI 2004), each of which is associated with a different seismogenic area and a maximum expected magnitude:

- far-field seismicity, which is connected to the seismogenic areas of the central-southern Apennines (maximum expected 6≤M≤7), with a macroseismic intensity in Rome up to VII or VIII MCS (Prestininzi et al. 2005);
- near-field seismicity, which is linked to the evolution of the Alban Hills volcanic district (maximum expected M≈5);

- urban seismicity, whose epicentres are located within the city area (maximum expected M≈4).

The ENEA Institute and the Lazio Region (*Regione Lazio*) territorial institution conducted a study that considered the seismicity of the urban area according to the national rule O.P.C.M. 3519/06 to define the seismic hazard of the Lazio Region and to update the regional seismic map. This study associated each municipally in Lazio to seismically homogeneous groups; the historical seismicity was analysed, and the spectra that represented each historical event and corresponded to the 90th percentile were defined. A spatial-statistical analysis of the parameters that characterized these spectra distinguished some main clusters with homogenous spectral characteristics, i.e., a main spectrum that represented the different spectra for each municipally in the cluster. A new seismic classification of the Lazio Region (Fig. 3.5) was proposed that expanded from this study according to the national rules DGR 387/09 and DGR 835/2009. Three zones (1 to 3) were defined to calibrate different levels of Seismic Microzonation (Scarascia Mugnozza 2011).

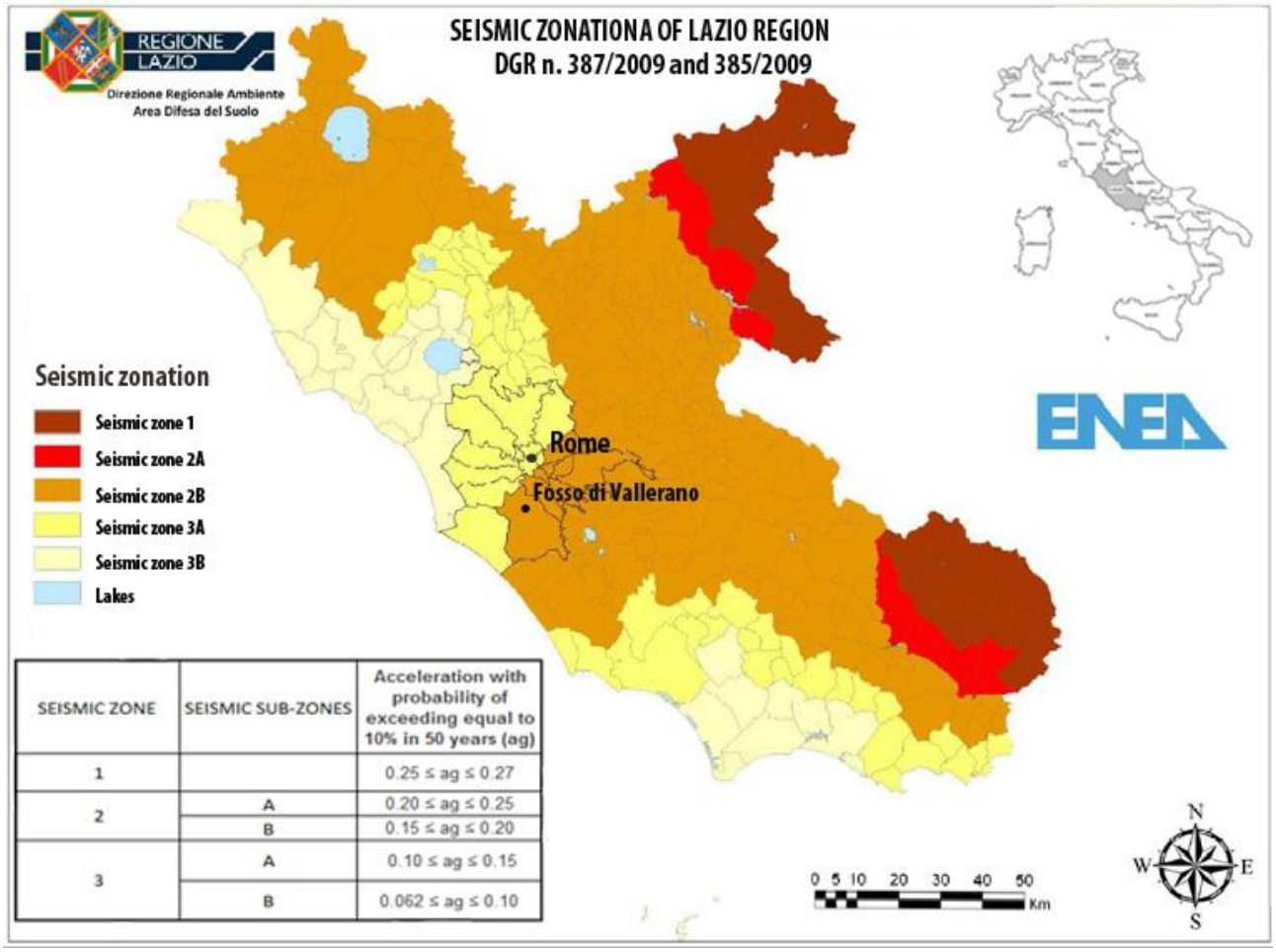

SEISMIC ZONE	SEISMIC SUB-ZONES	Acceleration with probability of exceeding equal to 10% in 50 years (ag)
1		0.25 ≤ ag ≤ 0.27
2	A	0.20 ≤ ag ≤ 0.25
	B	0.15 ≤ ag ≤ 0.20
3	A	0.10 ≤ ag ≤ 0.15
	B	0.062 ≤ ag ≤ 0.10

Fig 3.5: Seismic classification of Lazio Region and Peak of Ground Acceleration (PGA) with a return period of 475-year (associated with a 10% chance of exceedance in 50-years) associated to the different Seismic Hazard Zones. (Modified from DGR Lazio n.545 of 26/11/2010).

The city of Rome was divided into 19 UASs (Seismic Administrative Unit), one for each zone (or sub-zone) of the seismic classification of the Lazio Region (zones 2B and 3A). Starting from the seismic hazard, the maximum acceleration in the rock (PGA: Peak Ground Acceleration), with the probability exceeding 10% in 50 years (mean return time of 475 years), was calculated for each seismic zone (Fig. 3.6). The peak ground acceleration for the municipality of Rome varied from 0.075 to 0.200g (mean return time of 475 years). Additionally, 5 seismic inputs on rocks were defined for each seismic zone to be used as reference time-histories when evaluating the local seismic response, considering a strong-motion input (third level of Seismic Microzonation) according to the national rule D.G.R. Lazio n. 545 from 26 November 2010. These inputs were selected by consulting the European Strong Motion Database 5, with the seismological parameters (magnitude and epicentral distance) from the analysis of the regional seismic hazard used as keywords. Five natural accelerometric registrations with similar spectrum parameters were selected by considering the uniform hazard spectra (UHS) that represented each cluster. The same study by the ENEA Institute calculated the maximum macroseismic intensity of the territory (DBMI 2004, CPTI 2004) and Rome, with the intensity varying from VI to VII on the Mercalli–Cancani–Sieberg (MCS) scale.

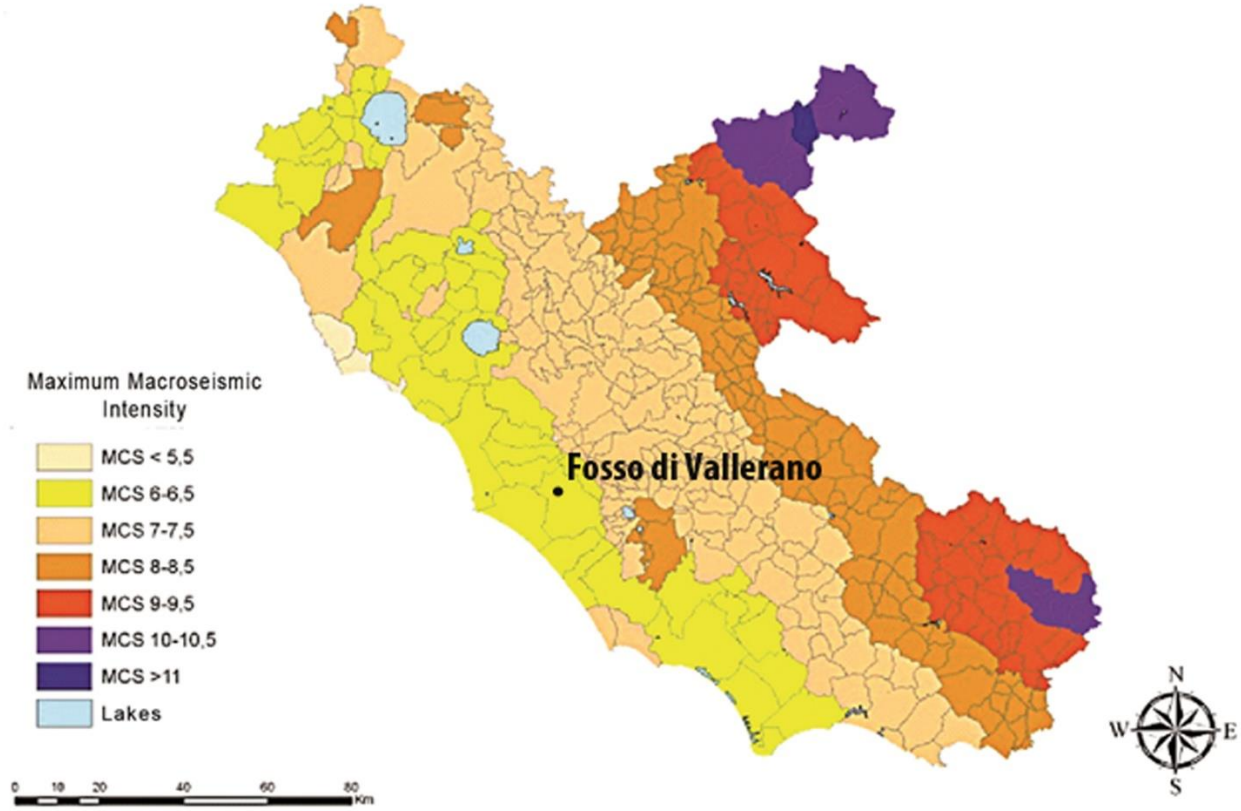

Fig 3.6: Zonation of the Lazio region according to the maximum macroseismic intensity areas (from D.G.R. Lazio n. 545 of 26/11/2010).

4. ENGINEERING-GEOLOGICAL CHARACTERIZATION OF THE STUDY AREA

A high-resolution engineering geological model is required to conduct a study of the alluvial setting in the case study area that is based on a numerical modelling approach. A series of boreholes, one cross-hole test, log stratigraphies and expeditious geomechanical on-site investigations (Pocket-Penetrometer and Pocket Vane-test) and geophysical investigations were analysed and organized in a Geographic Information System (GIS). The geognostic and geophysical data from the first phase of this thesis, the obtained geological model and the high-resolution engineering-geological model are described in the following sections.

4.1 Geophysical investigations

The available geophysical data mainly consisted of seismometric records with seismic noise measurements and velocimetric temporary arrays that were installed to record weak-motion events during the tail end of the L'Aquila seismic sequence. Additional seismic noise measurements were collected in the framework of this PhD thesis. In particular, five ambient noise surveys were conducted in the Fosso di Vallerano valley from 2009 to 2014 by using three different triaxial velocimetric stations for a total of 56 measurements (some examples are reported in Fig. 4.2). The first survey was performed with a 4-Hz digital tromometer TROMINO (Micromed) that was set to a 128-Hz sampling frequency and acquired 20-min-long noise samples at different hours of the day. Since 2012, four additional surveys have been performed with a 1.4-Hz SL06 acquisition system (SARA Instruments) that was set to a 200-Hz sampling frequency and a LENNARTZ LE3D/5-s sensor that was coupled with a REFTEK 130 digitizer at a 250-Hz sampling frequency. Noise samples that ranged from 45 min to 2 h long were acquired at different hours of the day. The ambient noise analysis (Fig. 4.1) showed the homogeneous response of the valley with a fundamental resonance frequency of 0.8±0.1 Hz; however, the surrounding reliefs showed no significant resonance peaks in the HVSR functions. A free-field seismometric array was operated in STA/LTA (Short Time Average to Long Time Average) acquisition mode in the Fosso di Vallerano valley from June to July 2009 to record weak-motion events during the tail end of the L'Aquila seismic sequence and to compare the results to those that were obtained from the noise analysis. The array (Fig. 4.1) consisted of two stations, whose locations were selected according to both the noise survey results and the requirement of identifying low noise, free-field spots in an urbanized area.

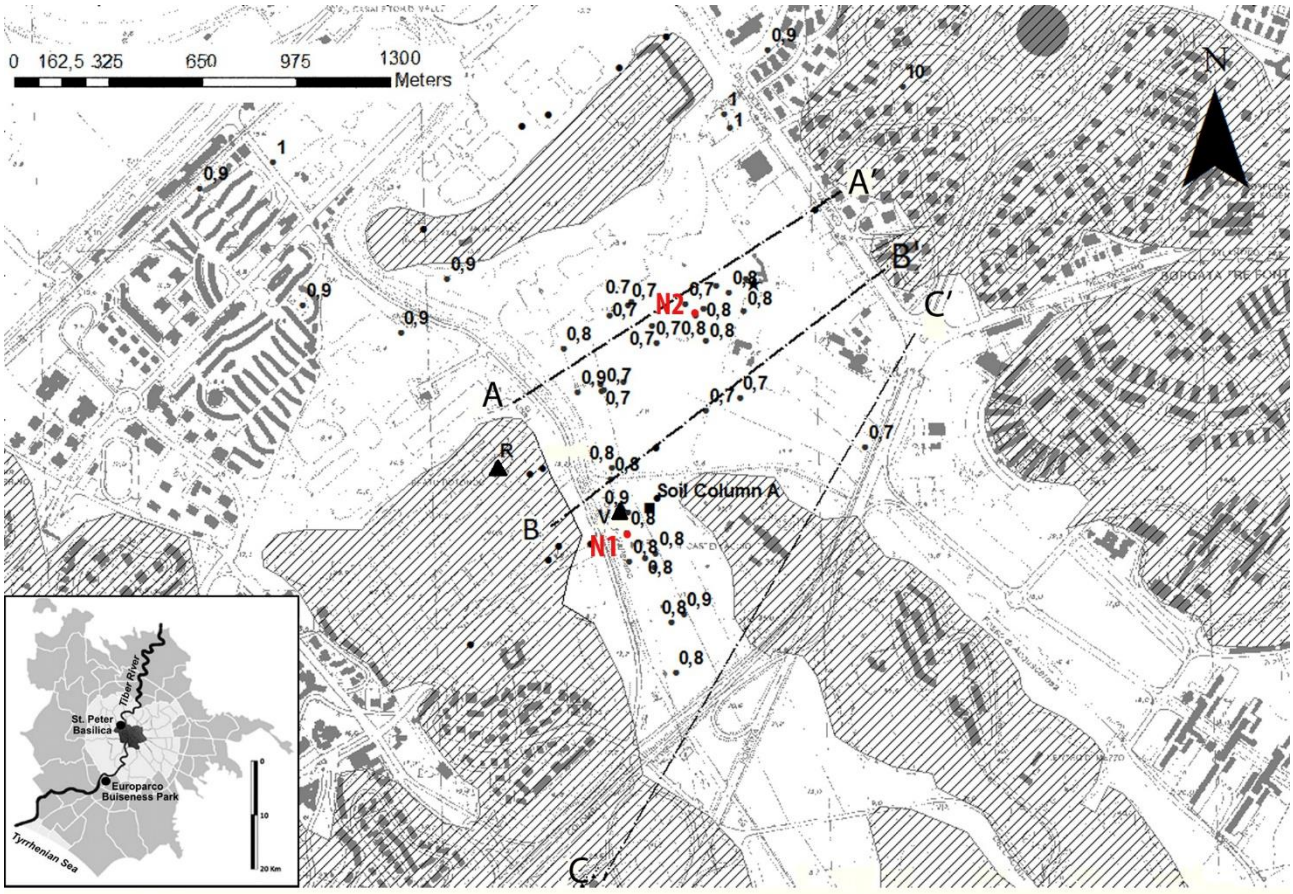

Fig. 4.1: CTR (Regional technical Map) scale 10.000 – Black points indicate the location of the ambient noise recording stations (the fundamental resonance frequency is also reported); black triangles indicate the velocimetric array; the black square corresponds to the position of the calibration Soil Column A. The traces of the three geological cross-sections AA', BB' and CC' are also reported; the outcropping seismic bedrock corresponds to the screened areas (Bozzano et al. 2016).

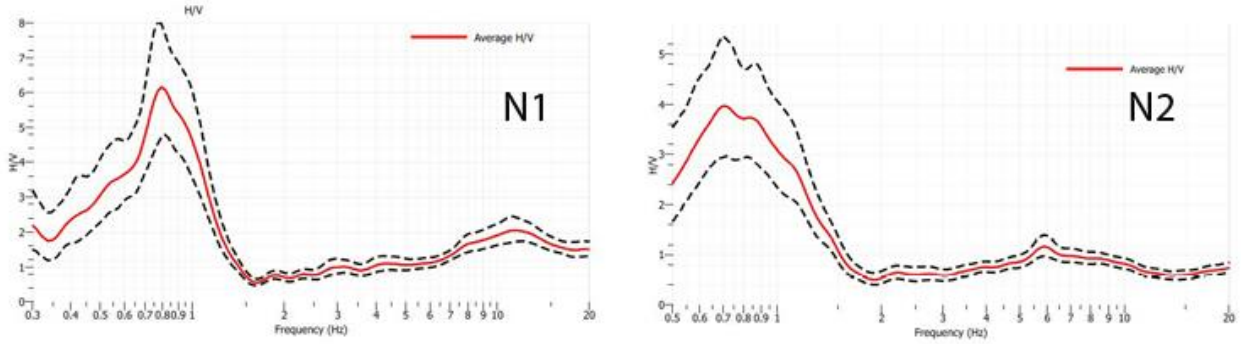

Fig. 4.2: Examples of the HVSR results obtained from the noise measurements. See Fig. 4.1 for the noise measurements location.

Each station contained three single components: a triaxially arranged 1-Hz velocimeter (SS1 Kinemetrics), a 24-bit data logger (K2 Kinemetrics) and a GPS device for absolute timing. One station (V) was located on alluvial deposits in the NE sector of the valley, while a reference (R) station (*sensu* Borcherdt 1994) was placed on locally outcropping seismic bedrock, which corresponded to the volcanic hills that bordered the valley, i.e., where no evidence of amplification was suggested by noise analysis. The seismometric array recorded approximately 30 earthquakes within a magnitude range of 2.6-4.6. In this study, only 10 records (Tab. 4.1) were considered because they did not show disturbances from human activities. These earthquakes were used to determine the average Receiver Functions (RF) (Lermo et al. 1993) and the average Standard Spectral Ratio (SSR) on site, which were computed from the spectral ratios of the horizontal components that were recorded for each event in the alluvial valley to the equivalent components that were recorded at the reference site (Borcherdt 1994).

Date	Magnitude	Seismic district	DISS source	Epicentral distance	Valle	Ref. Site	Event code
	Ml			km			
22-Jun-09	4.6	Gran Sasso	ITCS013	100	x	x	EQ-6
23-Jun-09	4.0	Gran Sasso	ITCS073	110	x	x	EQ-7
30-Jun-09	3.5	Monti Reatini	ITCS013	99	x	x	EQ-12
03-Jul-09	3.6	Aquilano	ITCS013	95	x	x	EQ-13
03-Jul-09	3.3	Aquilano	ITCS072	91	x	x	EQ-15
12-Jul-09	4.2	Aquilano	ITCS013	96	x	x	EQ-18
12-Jul-09	3.8	Aquilano	ITCS013	97	x		EQ-19
13-Jul-09	2.7	Monti Reatini	ITCS028	104		x	EQ-20
14-Jul-09	2.8	Aquilano	ITCS013	96		x	EQ-21
15-Jul-09	2.9	Aquilano	ITCS013	98		x	EQ-22

Tab. 4.1: List of the 10 earthquakes recorded by the free-field seismometric array installed from June until July 2009 and taken into account in this thesis.

The obtained results proved the high quality of the reference site because no significant amplification effects were suggested by the RFs; on the contrary, both the RFs and the SSR functions for the V station showed a well-defined peak at 0.8 Hz, which matched the noise analysis results.

4.2 High-resolution geological model

Available geognostic data from 250 boreholes were obtained from bibliographic data (Ventriglia 2002) and technical reports. These data were distributed over an area of 25 km^2 and a length from 10 to 70 m. One cross-hole test, log stratigraphies and expeditious geomechanical on-site investigations (Pocket-Penetrometer and Pocket Vane-test) from technical reports and official archives of the study area (Bozzano et al. 2000, Ventriglia 2002) were considered. Five main litho-stratigraphic groups were distinguished based on these borehole data:

- Plio-Pleistocene marine sediments (Marne Vaticane, Monte Mario e Monte Ciocci/delle Piche Formations), which represent the geological bedrock of the area (PP);
- Pleistocene alluvial sediments that were deposited by the Paleo-Tiber 4 River (Santa Cecilia Formation; MIS 15; 650-600 ka; Marra and Florindo 2014) (PT);
- Volcanic deposits that erupted from the Alban Hills and the Monti Sabatini volcanic district (561-365 ka; Karner et al. 2001b) (VL);
- Pre – Würmian fluvio-palustrine deposits (Valle Giulia - San Paolo – Aurelia and Vitinia Formation; 500 – 200 ka; Karner and Marra 1998) (FP);
- Recent alluvial deposits that filled the valley incisions since the end of the Würmian regression to the present (MIS 1; 18 ka-present; Marra et al. 2013) (AL);

Seven geological sections (three of them reported in Fig. 4.3) were realized by cross-correlating the boreholes' log stratigraphies, and the analysis sections in Fig. 4.3 highlighted an interesting and complex setting of the valley from geological and geomorphological perspectives. In particular, when moving from NW to SE (cross sections from AA' to CC'),

- The cross section AA' is characterized by the presence of a unique alluvial valley from geological and geomorphological perspectives;
- The cross section BB' is characterized by the presence of a unique alluvial valley from a geomorphological perspective but 2 different geological alluvial valleys;
- The cross section CC' is characterized by the presence of a unique alluvial valley from geological and geomorphological perspectives.

This geological setting can be related to syn-sedimentary tectonic activity that dislocated the geological bedrock (PP units) and the overlying PT deposits, leading to a horst and graben structure. The horst structure, which comprises the Castellaccio hill (cross section CC' in Fig. 4.3) is present in

the middle portion of the valley (cross section BB’ in Fig. 4.3) as a buried structure and is absent in the northern area (cross section AA’ in Fig. 4.3).

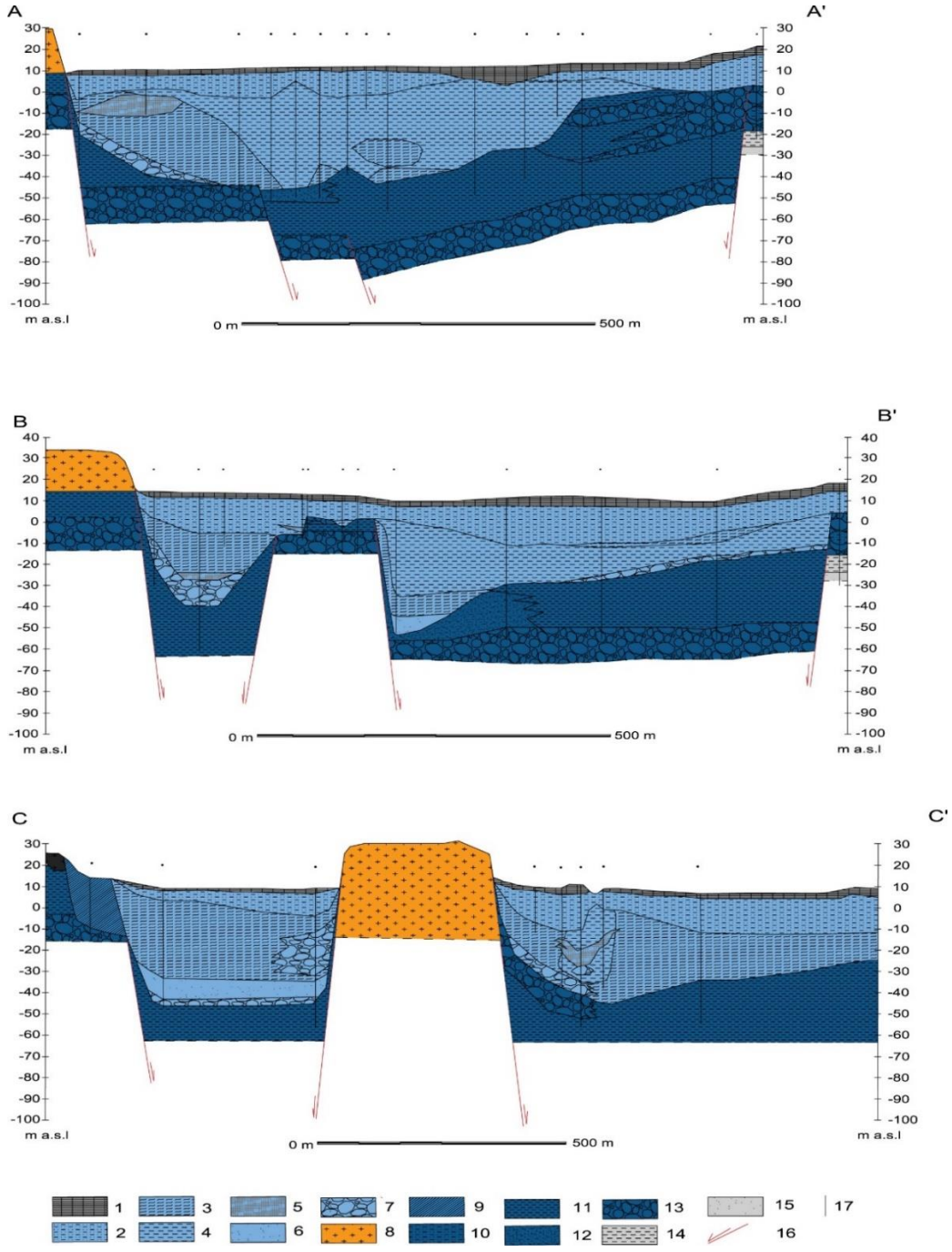

Fig. 4.3: Geological cross sections along the AA’, BB’, CC’ traces of Fig. 4.1. Legend: AL deposits: 1) Anthropic filling material (AL-AF); 2) Sandy-Clays characterized by a marked volcanic component (AL-VSC); 3) Peaty clays, plastic (AL-PC); 4) Clays and silts, plastic (AL-CS); 5) Peat (AL-PT); 6) Sands and silty sands (AL-SD); 7) Polygenic, loose and heterometric gravels, with volcanic and sedimentary components (AL-GR). VL deposits: 8) Undifferentiated pyroclastic material (VC). FP deposits: 9) Fluvio-palustrine deposits composed of loose gravels, sands and silts. PT deposits: 10) Sandy clays and silts, sometimes with freshwater gastropods (PT-SC) 11). Clays and silts with peaty layers (PT-CL); 12) Sands and silty sands. (PT-SD); 13) Loose gravels with heterometric sedimentary components (PT-GR). PP deposits: 14) Marine clays and silty clays; 15) Marine sands and silty sands. 16) Fault. 17) Borehole (Bozzano et al. 2016).

This evidence highlighted the spatial analysis of the geological sections and distinguished the 3D distribution of the units that comprised the alluvial body to better understand the complex geological setting of the valley.

The main outcome from this 3D model was evidence of a highly heterogeneous alluvial filling that is characterized by both vertical and lateral litho-technical contacts (Fig. 4.3 – 4.4). In particular, intense erosive processes occurred during the last Würmian glacial period because of similar effects from both the regional uplift (Hearty and Dai Pra 1986, Karner et al. 2001a) and the eustatic low-stand. These erosive processes created deep fluvial incisions that were filled during the post-Würmian eustatic rise by the recent alluvial deposits. The recent sediments (AL) are characterized by remarkable vertical and lateral heterogeneities and originated from the coupled processes of alluvation and colluvation and from possible secondary syn-sedimentary tectonic activity (Fig. 4.3 – 4.4). A more detailed stratigraphic analysis highlighted the presence of peaty clay and peat deposits that fill most of the valley and reach a thickness of 45 m. These peaty and peaty-clay deposits indicated that the alluvial valley was mostly characterised by a low-energy hydrographic regime and the presence of stagnant water during the Holocene, causing the emplacement of abundant organic matter. At the same time, the north-western area of the valley was characterized by a low-energy environment, which was responsible for the deposition of clays without organic matter, suggesting more straightforward lacustrine conditions that hindered the formation of peat. Active subsidence in this sector, which was linked to weak tectonics that reactivated the faults that dislocated the Paleo-Tiber 4 deposits, may explain the deposition of the lacustrine clay and the capture of the river bed north of the Montorio Hill, as highlighted by Ascani et al. (2008). The more recent clayey-sandy deposits are characterized by a marked volcanic component from erosive processes that involved outcropping volcanic deposits. Fans of Paleo-Tiber 4 basal deposits are interlayered by lateral unconformities with the clays and peaty clays because of slope denudation processes that involved the flanks of the valley. The resulting alluvial fill is characterised by significant lithological heterogeneity because of the presence of lens- to disc-like depositional bodies.

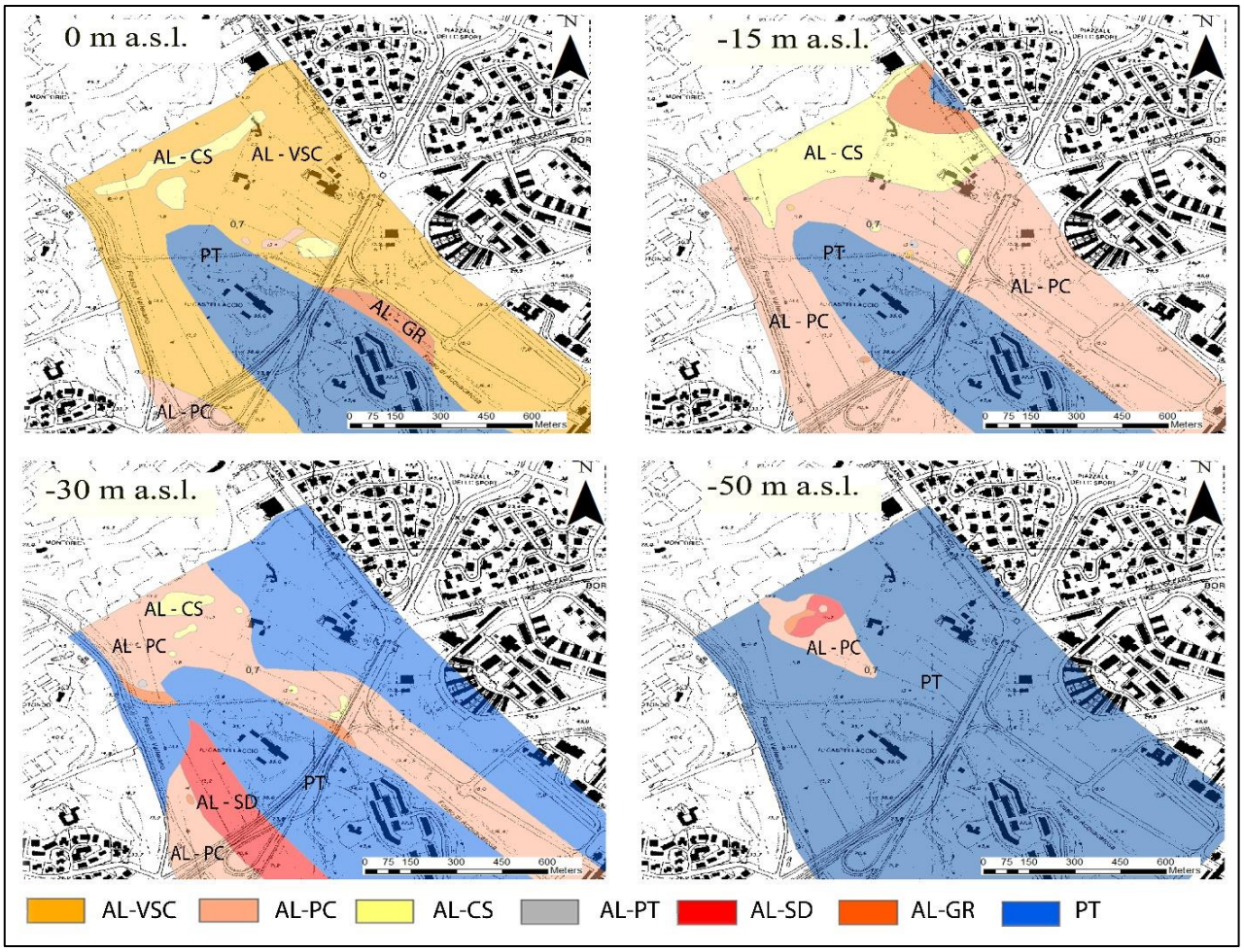

Fig. 4.4: 2D planar restitution of the high resolution 3D geological model of the Fosso di Vallerano valley referred to different depths a.s.l..Key to legend: see Tab. 4.2 (Bozzano et al. 2016).

4.3 Engineering-geological model

The attribution of dynamic properties to the subsoils of the Fosso di Vallerano valley was derived at a single location and the obtained seismo-stratigraphy was extrapolated to the area by considering the stratigraphic setting from the reconstructed geological model to obtain an engineering-geological model for the following numerical analysis. The seismometric records were used to calibrate the local seismo-stratigraphy based on the reconstructed high-resolution geological model. This calibration was conducted by a comparison between the instrumental records and the outputs from the 1D numerical modelling through the EERA (Equivalent – linear Earthquake Response Analysis, Bardet et al. 2000) code. This study focused on the analysis of a soil column from the velocimetric station V (Fig. 4.4 – 4.5a), which is located in the Fosso di Vallerano valley. Three earthquakes, each representing one of three seismogenic areas (including several seismogenic sources according to DISS 3.2.0. see #EQ-6, EQ-12, and EQ-13 in Tab. 4.1), were applied as seismic inputs for the

numerical modelling. The obtained acceleration time histories were used to calibrate the numerical model; each recorded event at the R station was deconvoluted at the column base and applied as input (*incrop*) to obtain the signal that was modified by the soil column at the surface (*outcrop*).

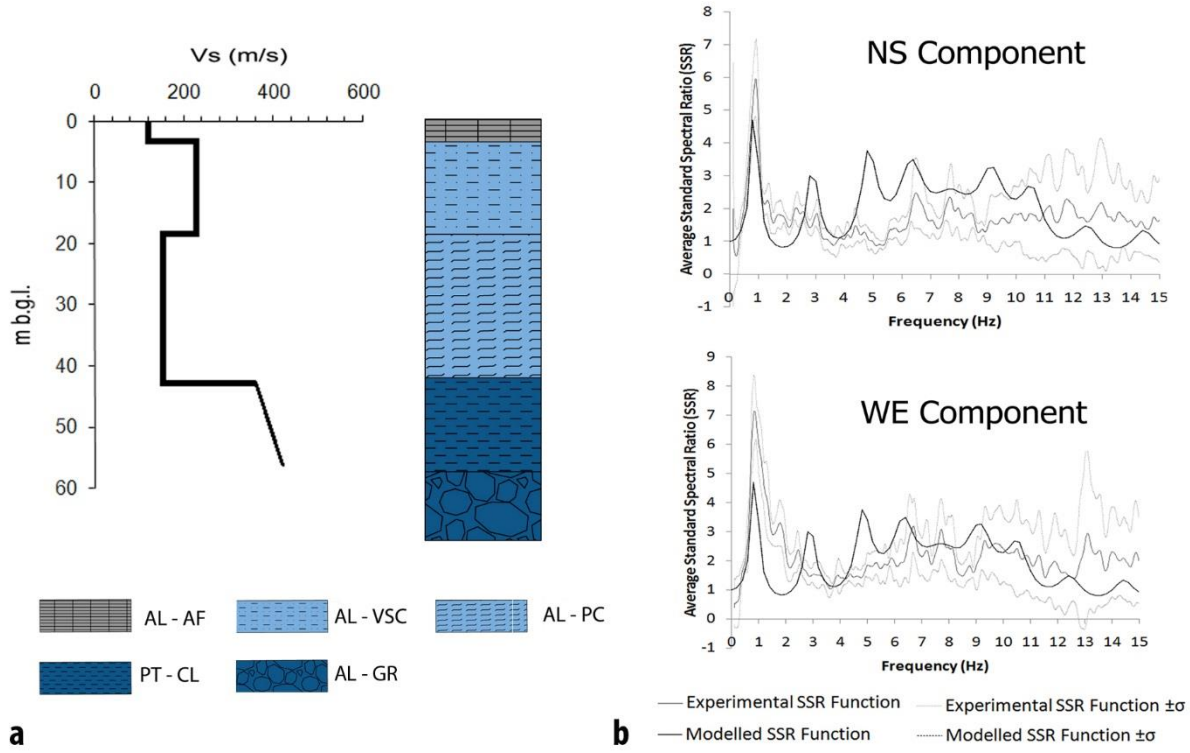

Fig. 4.5: a) Vs profiles corresponding to the best fit. Key to legend: see Tab. 4.2. b) Comparison between results of the numerical modelling and experimental data for the best fit Vs profile.

The spectral ratio between the outcrop signal at the column surface and the input signal, which was also deconvoluted at the outcrop, represents the seismic local amplification function, A(f), of the ground column (Borcherdt 1994).

This function is comparable with the SSR function for the same earthquake by considering the records at the R and V stations. The adopted calibration procedure in this study was performed through a sensitivity analysis by assuming the stratigraphy from the high-resolution 3D geological reconstruction and by varying the shear wave velocity (Vs) values along the calibration soil column A. Mechanical and dynamic properties were attributed to each litho-technical unit according to literature data (Bozzano et al. 2008, Caserta et al. 2012) (Tab. 4.2). Each numerical modelling was performed by separately applying the horizontal components (NS and WE) of each recorded earthquake. An average function with its standard deviation was then computed to be compared to the average SSR, which represents our experimental A(f). A "trial and error" convergence was performed to best fit the experimental A(f) with the numerical function; the best results (Fig. 4.5b) were obtained for the V(s) values in Fig. 4.5a. The performed sensitivity analysis enabled us to best

fit the Vs profile along the soil column (Tab 4.2 – Fig. 4.5a); the final seismo-stratigraphy matched other literature data (Bozzano et al. 2008; Caserta et al. 2012).

	Lithology	Initial values			Best fit values
		γ (kN/m^3)	Vs (m/s)	G_0 (MPa)	Vs (m/s)
Alluvial Body - AL	AF (Anthropic fill material)	17	118	82	118
	VSC (volcano- clastic sandy clays)	16.5	180	53	**225**
	PC (Peaty clays)	17.2	190	64	**150**
	CL (Silty clays)	18.3	235	66	235
	PT (Peat)	12.7	140	25	140
	SD (Sands)	19.2	417	334	417
	GR (Gravel)	21.0	713	1068	713
Paleo-Tiber Deposits - PT	CL (Silty clays)	18.3	1100	101	**357**
	SD (Sands)	19.2	1100	334	417
	GR (Gravel)	21.0	1100	1068	1100

Tab 4.2: Initial values of the dynamic properties attributed to the litotechnical units and best fit values obtained by the sensitivity analysis performed.

Additionally, this procedure produced some relevant evidence: i) different Vs values were observed in the AL-VSC deposits of the Fosso di Vallerano valley compared to similar alluvial deposits from the Tiber River and its tributaries, and ii) the seismic bedrock in the Fosso di Vallerano valley is located at the top of the Paleo-Tiber 4 gravel (Pleistocene) and does not correspond to the local geological bedrock (i.e., the Holocene/Pleistocene discontinuity contact) or the outcropping seismic bedrock, which consists of volcanic deposits. These observations represent relevant differences compared to the main Tiber River valley, where the seismic bedrock coincides with the top of the gravel level at the base of the most recent alluvial deposits (Bozzano et al. 2008). The calibrated seismo-stratigraphy was extrapolated to the Fosso di Vallerano valley by i) considering the geometry and juxtaposition of the stratigraphic levels from the high-resolution geological model, ii) verifying the correspondence between geological units and the seismic strata, and iii) attributing the dynamic properties that were used for the calibration model to the seismic strata. A connection was found between the Holocene alluvial units and the seismic strata, which represent visco-elastic deposits that are up to 75 m thick and have Vs values from 118 to 713 m/s. Pleistocene deposits that were 5 to 50 m thick were distinguished in an upper seismic stratum, including the geological units PT-CL and PT-SD, which exhibited visco-elastic behaviour and had Vs values from 357 m/s to 607 m/s, and in

a lower seismic stratum that corresponded to the PT-GR, which represents the local seismic bedrock and has a Vs value of 1100 m/s. The resulting engineering-geological model is summarised in the synoptic diagram of Fig. 4.6.

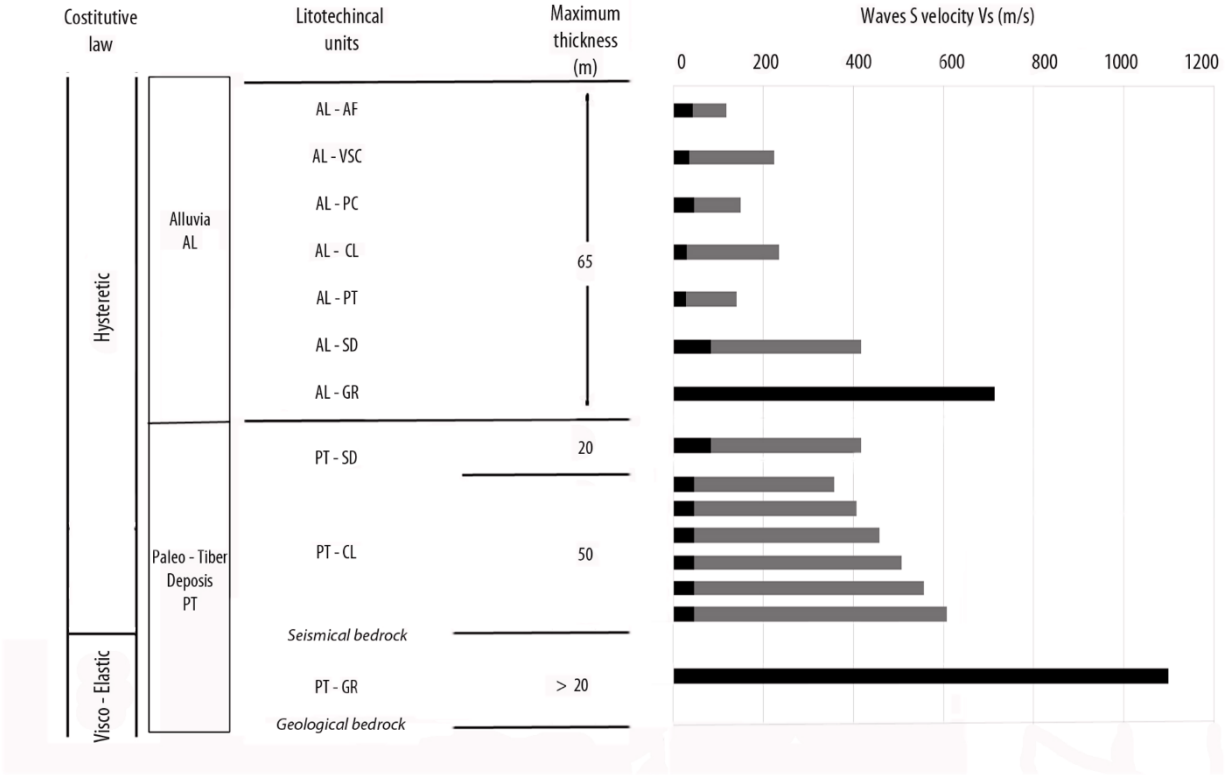

Fig. 4.6: Engineering geological model obtained for the subsoil of the Fosso di Vallerano valley. The velocity value corresponding to the volumetric threshold is also reported (Bozzano et al. 2016).

A 1D-plus-lateral-wave local seismic response should be expected according to Bard and Bouchon (1985) because of the shape ratio (*sensu* Bard and Bouchon 1985) of the Fosso di Vallerano valley along the three sections AA' (0.18), BB' (eastern valley: 0.87, western valley: 0.20), and CC' (eastern valley: 0.44, western valley: 0.19) and the impedance contrast between the Pleistocene silty-clayey deposits (PT-AR) and the local seismic bedrock, i.e., the top of the basal Paleo-Tiber 4 Pleistocene gravels (PT-GR) (AA'= 2.8; BB'= eastern valley: 2.7, western valley: 2.8; CC'= eastern valley: 2.8, western valley: 2.6). Nonetheless, the local seismic response is likely significantly conditioned by lateral contacts that are related to lithological hetereogeneities (Martino et al. 2015). Thus, a 2D numerical modelling of this study's geological cross sections is required to evaluate the seismic response under free-field conditions and the effects of SCI.

5. 2D NUMERICAL MODELLING

5.1 Design of the 2D numerical modelling

5.1.1 Selected geological cross sections and seismic excitations

The numerical modelling in § 5.2 – 5.3 focused on the geological cross sections AA' and BB', which are shown in Fig. 4.2 (portion of the alluvial valley with urban development). The geological cross section CC' was not considered because this profile corresponds to a free-field condition, i.e., the absence of buildings to modify the seismic response. The simulations were performed by assuming visco-elastic behaviour for the materials that comprised the alluvial filling. The models were excited by synthetic and natural seismic inputs. The synthetic input was a 0^{th}-order Ricker wavelet (Ricker 1943, 1953), which was applied as a horizontal displacement with a PGD (Peak Ground Displacement) of 1 m and a frequency from 0.1 to 15 Hz (EQ – 1, Fig. 5.1).

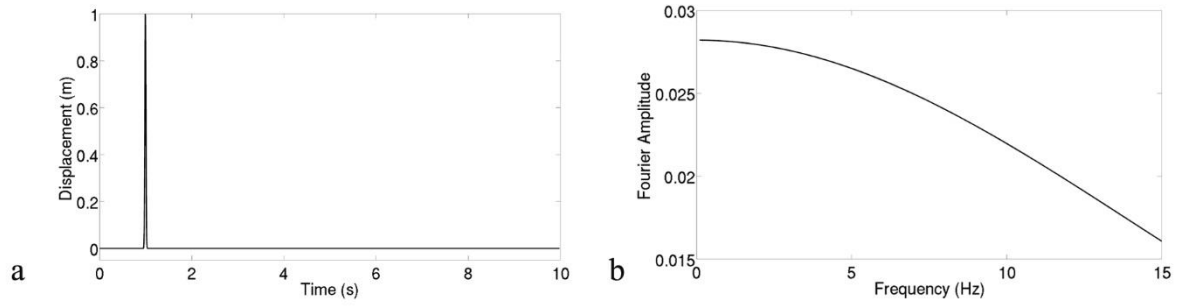

Fig. 5.1: Synthetic input EQ – 1. a) Signal in time domain b) Fourier amplitude of the signal.

The natural input was chosen among the weak motions that were recorded by the velocimetric array that operated in the Fosso di Vallerano valley during the summer of 2009 (§ 4.1). Three earthquakes, each of which representing three seismogenic areas (EQ-7, EQ-12, and EQ-13 in Tab. 4.1), were selected as input in the numerical modelling. The horizontal component of each earthquake, which was characterized by a high PGA (Peak Ground Acceleration), was applied as a shear wave (SH) in terms of displacement at the seismic bedrock level of the models.

The PGAs that characterized the three chosen weak motions (Tab 5.1) were used to identify the horizontal components that were characterized by higher PGAs: i) EQ – 7: Component NS, ii) EQ – 12: Component WE, and iii) EQ – 13: Component NS.

	PGA (g)	
Weak motion	NS Component	WE Component
EQ - 7	1.459E-03	9.832E-04
EQ - 12	4.888E-04	6.347E-04
EQ - 13	4.361E-04	3.089E-04

Tab. 5.1: Synthesis of the PGA values of the horizontal components of the selected low-magnitude earthquakes.

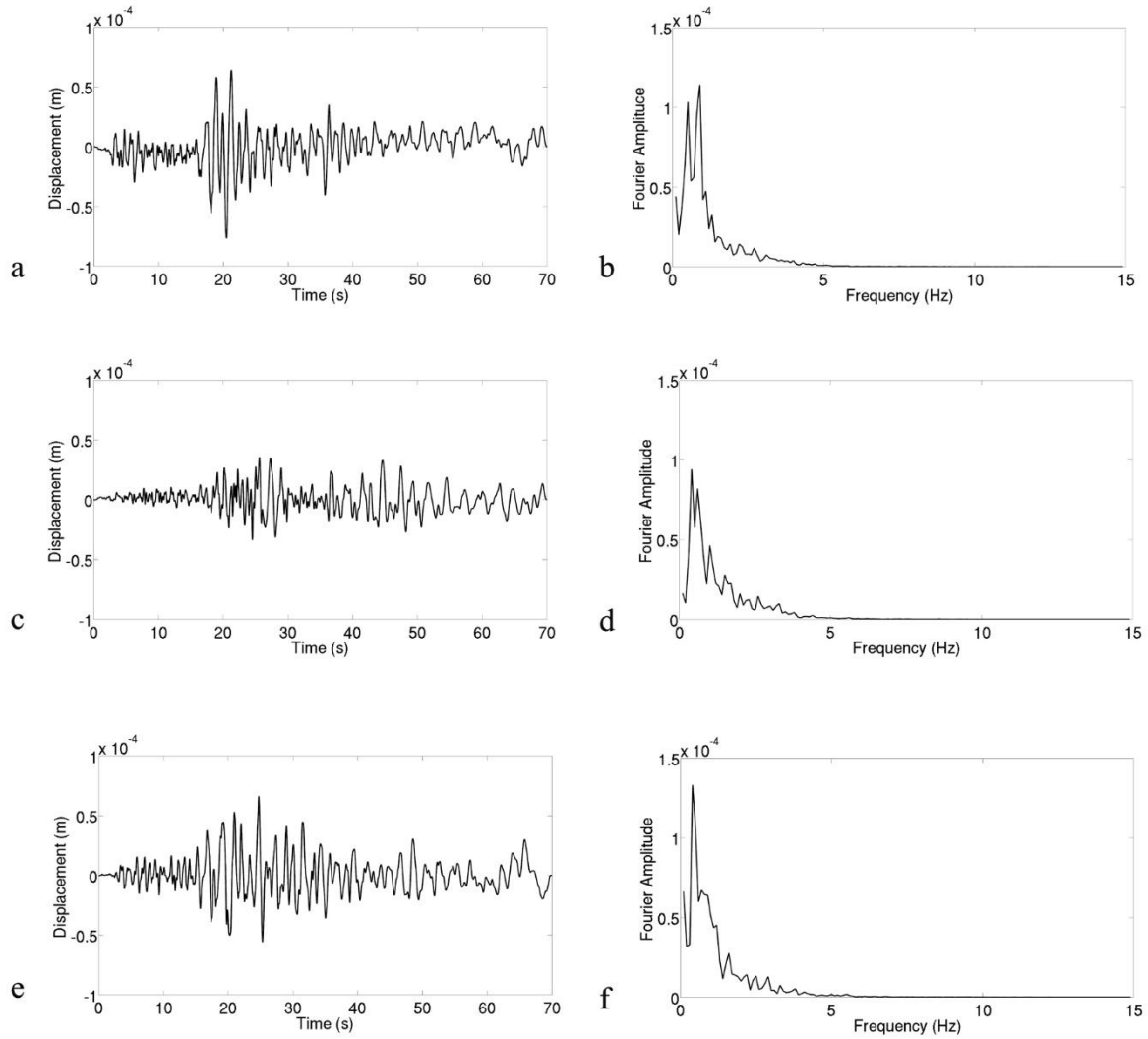

Fig. 5.2: Recorded earthquakes. a) EQ – 7: Signal in time domain b) EQ – 7: Fourier amplitude of the signal. c) EQ – 12: Signal in time domain d) EQ – 12: Fourier amplitude of the signal. e) EQ – 13: Signal in time domain f) EQ – 13: Fourier amplitude of the signal.

The three chosen components of the earthquakes (EQ-7_NS, EQ-12_WE, and EQ-13_NS in Tab. 4.1) were characterized by a PGD of $6.41*10^{-5}$, $3.54*10^{-5}$ and $6.62*10^{-5}$ m, respectively and a frequency from 0 to 5 Hz according to the far-field nature of the earthquakes.

5.1.2 Description FEM in dynamics

This code is a FEM (Finite Elements Method) software composed of 23 modules calculation allowing to investigate the main engineering and geological engineering topics. In this thesis, 2 of the 23 modules have been used: elasto-dynamics (DYNI module) for the evaluation of the response of a system under a dynamic stress and modal analysis ("MODE module") for the calculation of the eigenmodes of the structures.

The DYNI module computes dynamics by direct integration, the response of a system submitted to a dynamic load; it enables proceeding with a step-by-step resolution of the dynamic equilibrium equation [1]:

$$[M]\{\ddot{X}(t)\}+[C]\{\dot{X}(t)\}+[K]\{X(t)\}=\{F(t)\} \qquad [1]$$

where:

- $X(t)$: Vector of nodal displacements for the given structure,
- $\dot{X}(t), \ddot{X}(t)$: Speed and acceleration vectors,
- $F(t)$: Vector of imposed loads as a function of time,
- $[M], [C], [K]$: Mass, damping and stiffness matrices of the structure, respectively.

Time domain approach is able to solve linear problems for which matrices K, C and M are constant with time; the integration over time is based on Newmark's algorithm, which is implicit and unconditionally stable.
It is possible to define a Rayleigh-type damping matrix that assumes the following form [2]:

$$[C]=a.[K]+b.[M] \qquad [2]$$

where *a* and *b* are constants controlling the frequency dependence.
The modal approach has been designed to seek the p eigenvalues λ_i closest to a given value λ_0, along with the p associated eigenvectors $\{\Phi_i\}$ satisfying the following relation [3]:

$$[K]\{\Phi_i\} = \lambda_i [M]\{\Phi_i\} \quad (i = 1, p) \qquad [3]$$

where:

- $[M], [K]$: Mass and stiffness matrices of the structure, respectively.

The subspace method is employed herein to identify these eigenmodes.

The numerical modelling phase of this work was carried out through CESAR-LCPC code (Humbert et al. 2005) dedicated to civil, tunnel and geotechnical engineering.

5.1.3 Calibration of the absorbing layers system

One of the main drawbacks of the FEM 2D numerical modelling approach in elasto-dynamics is the presence of spurious waves that are reflected at the model's artificial boundaries. This point is particularly critical for the analysis of wave propagation in heterogeneous or layered systems, as in this thesis.

In this regard, Semblat et al. (2011) proposed an absorbing layer solution (CALM), based on Rayleigh/Caughey damping formulation [2].

The loss factor η associated to Rayleigh damping can be written as [4]:

$$\eta = 2\xi = \frac{b}{\omega} + a\ \omega \qquad [4]$$

where is ω the circular frequency and ξ is the damping ratio.

Considering the relationship between internal friction and frequency for Rayleigh damping, for weak to moderate damping values, there is a simple relation between the inverse of the quality factor Q^{-1} and the damping ratio ξ [5]:

$$Q^{-1} = 2\xi \qquad [5]$$

For Rayleigh damping, the loss factor is infinite for zero and infinite frequencies; the rheological model perfectly meeting the requirements of attenuation-frequency dependence and instantaneous and long-term effects is a particular type of generalized Maxwell model. The Rayleigh coefficients can be related to the rheological parameters of the Generalized Maxwell model [6]:

$$\begin{cases} b = \dfrac{E(\xi_1 + \xi_2)}{\xi_1^2} \\ a = \dfrac{\xi_2}{E} \end{cases} \qquad [6]$$

Thus it is possible to model the absorbing layer system with appropriate damping properties (i.e.

Rayleigh/Caughey damping coefficients) in order to attenuate the spurious reflections at the model boundaries. The General Maxwell model (Fig. 5.3 left) is characterized by a band-pass behaviour and in order to define a reference attenuation value (inverse of the quality factor Q^{-1}) characterizing the absorbing layer, the minimum attenuation value will be chosen at the predominant frequency of the input (Fig. 5.4 right).

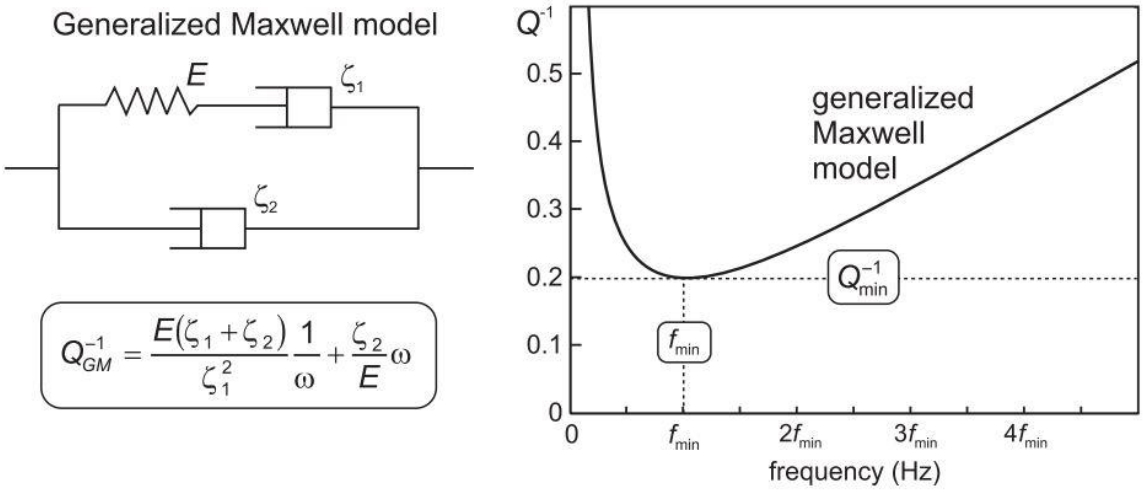

Fig. 5.3: General Maxwell model and associated attenuation curve (from Semblat et al. 2011)

From the equation of the damping ratio [2] it is possible to define the frequency of minimum damping ω_{min} from the Rayleigh coefficients according to the relation [7]:

$$\omega_{\min} = \sqrt{\frac{b}{a}} \qquad [7]$$

Choosing the minimum of attenuation $Q^{-1}{}_{min}$ (or damping value ξ) at the predominant frequency of the input f_R, it is then possible to obtain the following relation [8]:

$$\omega_R = 2\pi f_R = \sqrt{\frac{b}{a}} \qquad [8]$$

According to the Rayleigh damping relation, the obtained system [9] can be used to define the Rayleigh damping coefficients in the absorbing layer system, choosing the predominant frequency of the input f_R and the minimum of attenuation $Q^{-1}{}_{min.}$

$$\begin{cases} Q_{\min}^{-1} = 2\,\xi_{\min} = \dfrac{b}{\omega_R} + a\,\omega_R \\ \omega_R = 2\pi\, f_R = \sqrt{\dfrac{b}{a}} \end{cases} \qquad [9]$$

In the study by Semblat et al. (2011), the efficiency of the method was assessed through 1D and 2D FEM simulations, and the best results were obtained when considering a damping variation up to $Q_{min}^{-1} \approx 2$ (ξ =1.0), as defined by a linear function in the heterogeneous case (five layers with piecewise constant damping) and by linear and square root functions in a continuous layer case. This theoretical study was performed by considering a simple model with a homogeneous elastic medium and an absorbing lateral layered boundary. This approach has not yet been tested for heterogeneous deposits, which are characterized by vertical and lateral contacts among layers with different mechanical and dynamic properties. Thus, the efficiency of absorbing layers for highly heterogeneous deposits must be examined by additional numerical tests. A new numerical model was designed according to the geometry that was proposed by Semblat et al. (2011) while introducing two horizontal and homogeneous sub-layers (Fig. 5.4 a-b).

The modelling was performed through the FEM code by applying a 2nd-order Ricker wavelet (Ricker 1943, 1953), which is characterized by a predominant frequency of 10 Hz according to Semblat et al. (2011), as a synthetic input and by applying this input as a vertical displacement onto a portion of the surface (Fig. 5.4 a-b).

The results of the model were analysed to choose the most efficient features (i.e., thickness and damping) of the absorbing layer system. This procedure considered 10 impedance contrasts from 1.4 to 13.8 between the 2 horizontal sub-layers to represent the physical domain of interest.

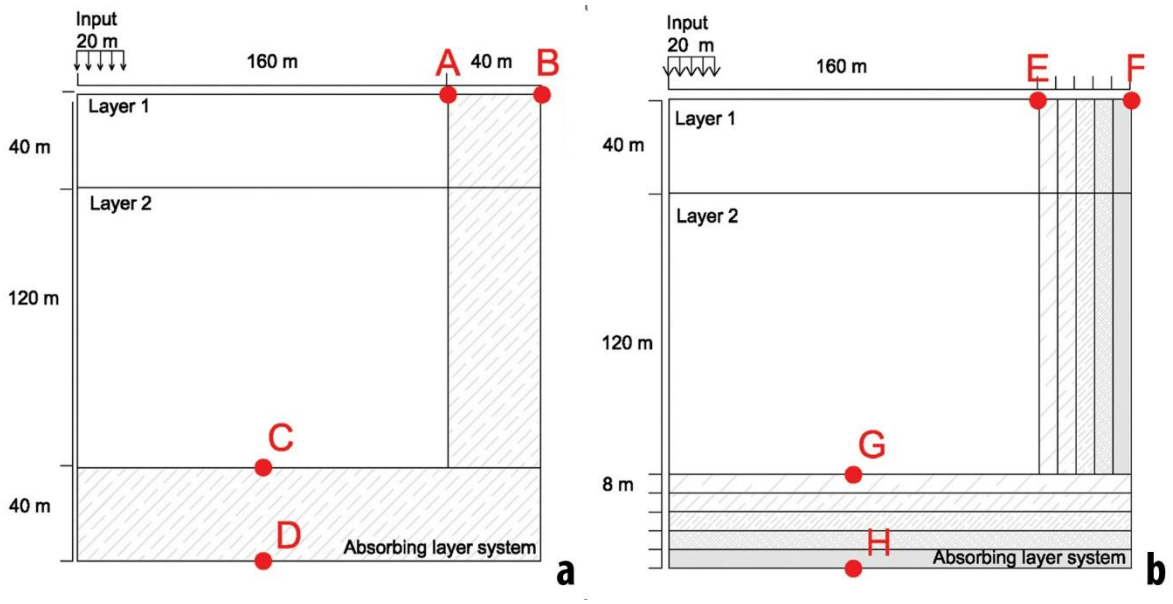

Fig 5.4: Geometry of the models constructed to carry out the absorbing layer parametric analysis and position of the control points. a) Model considering HOL b) Model considering HEL.

This parametric analysis was performed to evaluate the reduction in the efficiency of the absorbing layer in relation to the longest wave lengths that propagated in the model, which were a function of the maximum wave velocity of the 2 considered sub-layers.

Two different typologies of the absorbing layer system were considered: the first corresponded to a homogenous absorbing layer (HOL), which was characterized by a homogenous damping value $Q_{min}^{-1} \approx 1.0$, or $\xi = 0.5$, and the second corresponded to a heterogeneous layer (HEL) with 5 sub-layers that was characterized by a damping value that linearly varied from $Q_{min}^{-1} \approx 0.2$, or $\xi = 0.1$ (in the inner portion of the absorbing layer system), to $Q_{min}^{-1} \approx 2$, or $\xi = 1.0$, at the boundary of the numerical model.

The displacement (both the vertical and horizontal components) was analysed at 4 control points within each model to evaluate the efficiency of the absorbing layer system. The results when considering impedance contrasts of 1.4, 6.9 and 13.8 between the 2 sub-layers are presented here (Fig. 5.5-5.6-5.7-5.8).

Analysing the results from the surface (Fig. 5.5-5.6) indicated that both the HOL (Fig. 5.4a) and HEL (Fig. 5.4b) damped all the waves (both the vertical and horizontal in Figs. 5.5 and 5.6, respectively) from the model with all the impedance contrasts. The displacement at point E was always larger than that at point A and increased with the impedance contrast (I.C.). This effect is caused by the different damping values that characterised the interior of the absorbing layer system (i.e., $\xi = 0.5$ for the HOL and $\xi = 0.1$ for the HEL).

An analysis of the displacement variation at the bottom of the model (points C and D in the HOL model and points G and H in the HEL model) produced more complex results (Fig. 5.7-5.8). The

displacement values at point G were higher than those at point C according to the different damping values that characterized the interior of the absorbing layer systems.

Additionally, the efficiency of the absorbing layer system was strongly influenced by the velocities that characterized the 2 sub-layers in the model. All the waves were damped for a low impedance contrast (IC=1.4; Fig. top 5.7 – top 5.8), while only some of the waves were damped for a higher impedance (IC=6.9; Fig. middle 5.7 – middle 5.8) up to the highest impedance contrast (IC=13.8, bottom 5.7 – bottom 5.8), for which all the waves reached the boundary of the model. These considerations were valid for both the HOL and HEL systems and for all the components (horizontal and vertical) of the displacement.

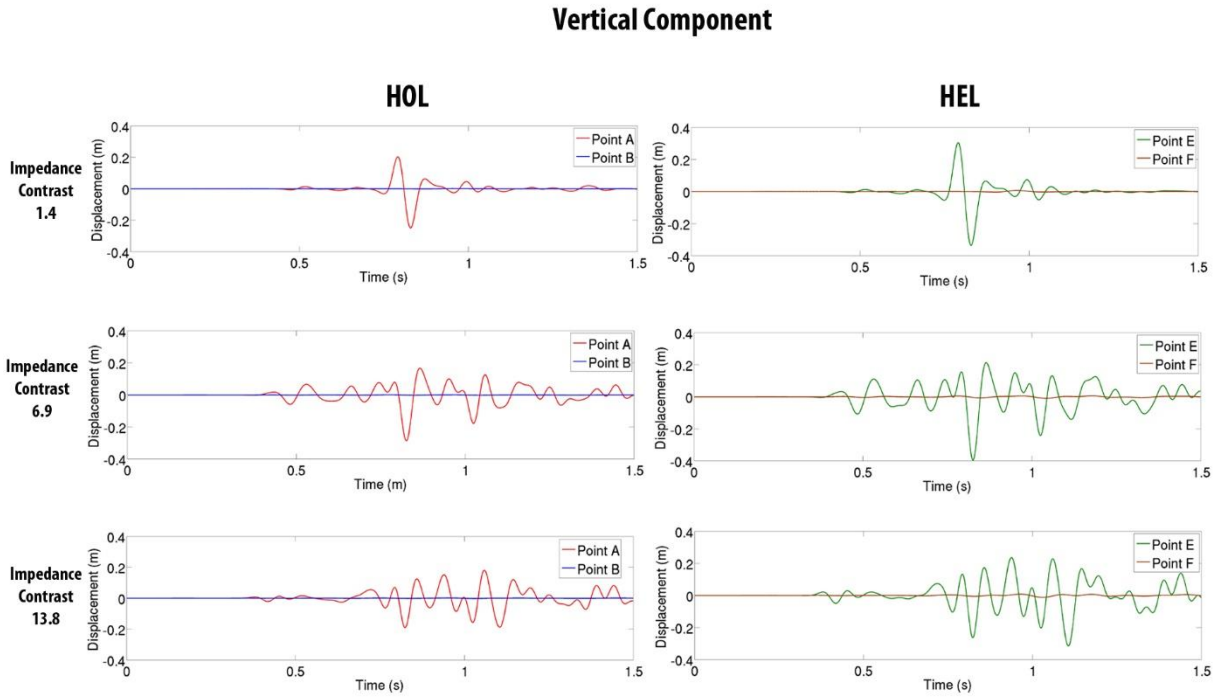

Fig. 5.5: Variation of the vertical component of the displacement at the model surface for the three different impedance contrasts: IC= 1.4 (top), IC=6.9 (middle) and IC= 13.8 (bottom). Results considering the HOL (left) and the HEL systems are shown.

The reduction in the PGD (Peak Ground Displacement) and the Arias Intensity IA by the HOL and HEL at the bottom of the models was evaluated to quantify the efficiency of the system and choose the typology of the absorbing layers for the following modelling step.

As proposed by Arias (1970) IA is defined as [10]

$$IA = \frac{\pi}{2g}\int_0^{\infty} a(t)^2\,dt \qquad [10]$$

In particular, the percentage of the PGD and AI that was damped by the absorbing layer system was calculated and reported in Tab. 5.2.

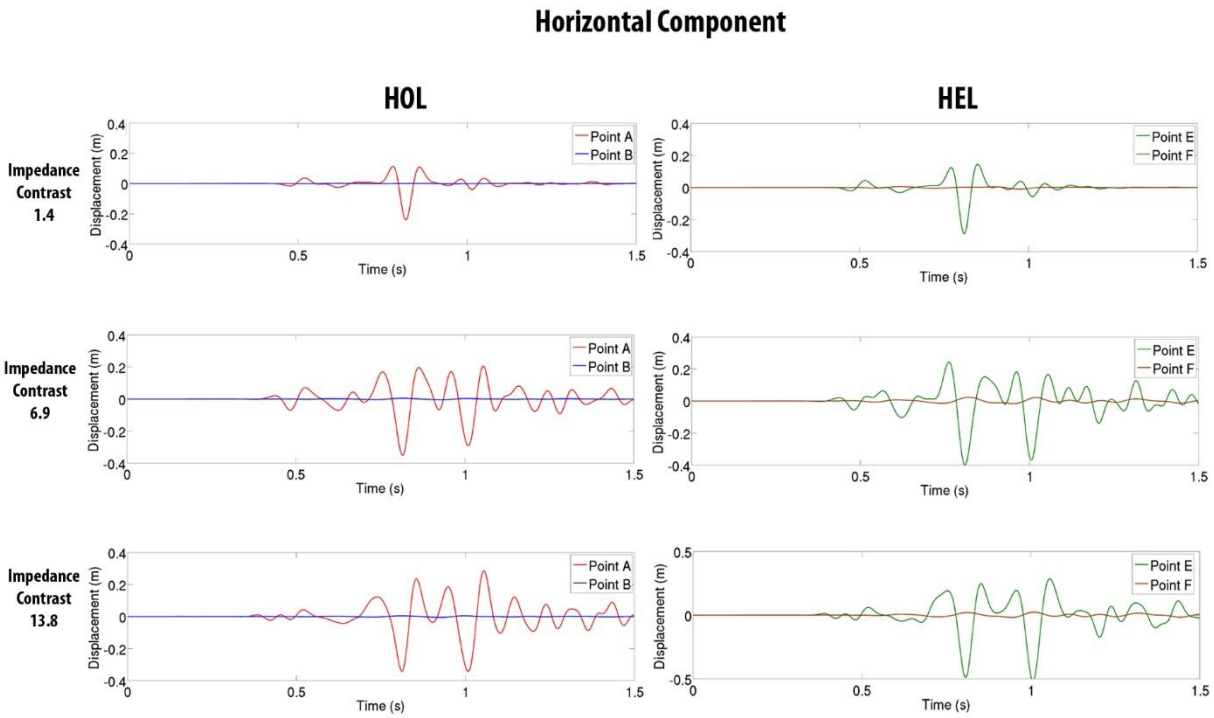

Fig. 5.6: Variation of the horizontal component of the displacement at the model surface for the three different impedance contrasts: IC= 1.4 (top), IC=6.9 (middle) and IC= 13.8 (bottom). Results considering the HOL (left) and the HEL systems are shown.

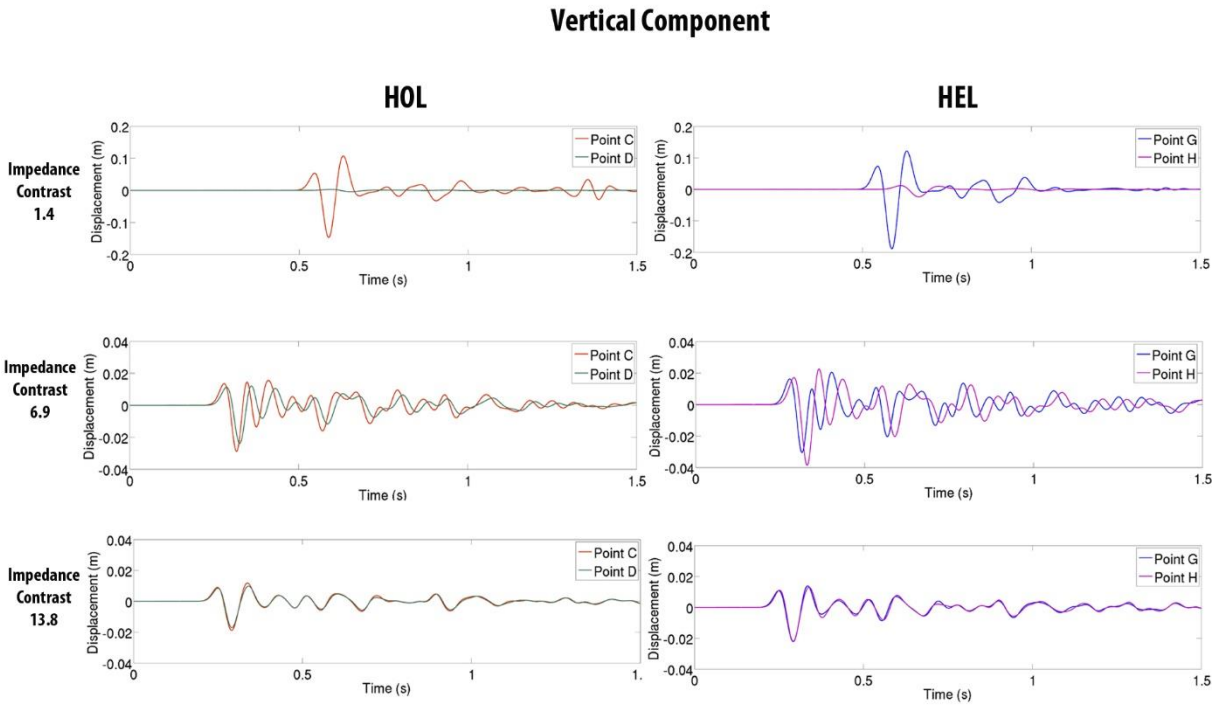

Fig. 5.7: Variation of the vertical component of the displacement at the model bottom for the three different impedance contrasts: IC= 1.4 (top), IC=6.9 (middle) and IC= 13.8 (bottom). Results considering the HOL (left) and the HEL systems are shown.

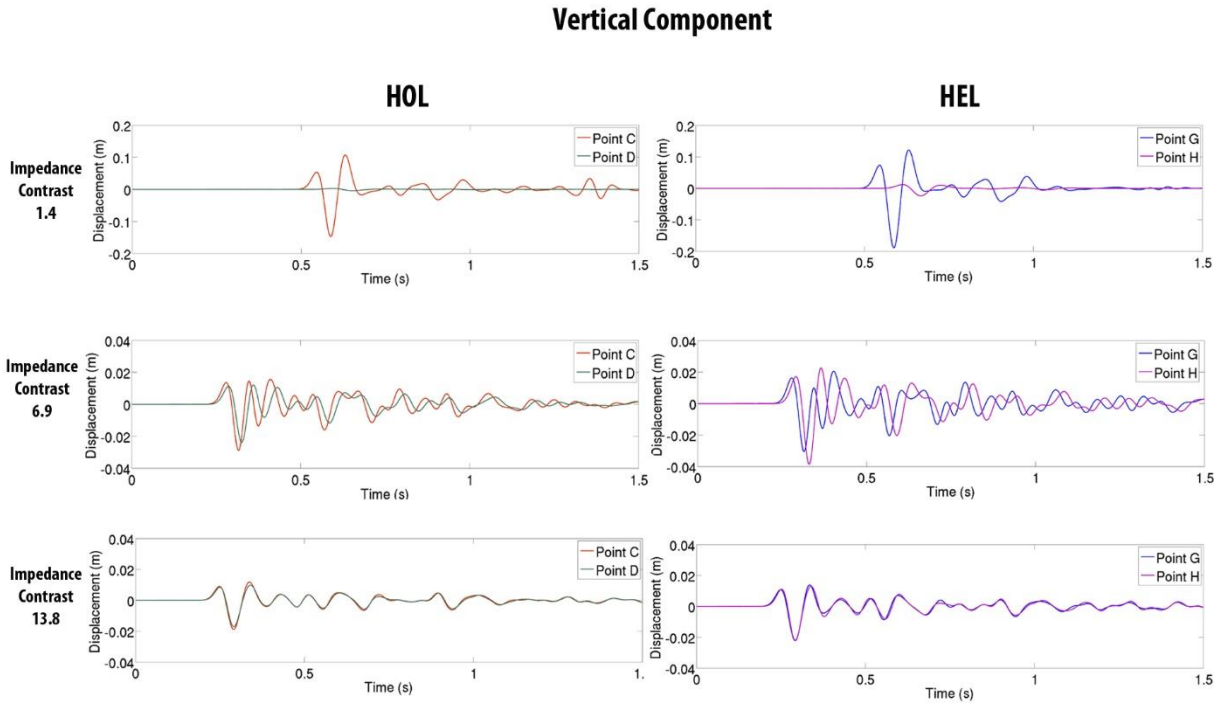

Fig. 5.8: Variation of the horizontal component of the displacement at the model bottom for the three different impedance contrasts: IC= 1.4 (top), IC=6.9 (middle) and IC= 13.8 (bottom). Results considering the HOL (left) and the HEL systems are shown.

	HOL					
	PGDh			AIh		
	IC= 1.4	IC= 6.8	IC= 13.8	IC= 1.4	IC= 6.8	IC= 13.8
Surface	99%	99%	98%	100%	100%	100%
Bottom	98%	69%	**-23%**	100%	88%	44%
	HEL					
	PGDh			AIh		
	IC= 1.4	IC= 6.8	IC= 13.8	IC= 1.4	IC= 6.8	IC= 13.8
Surface	96%	94%	95%	100%	100%	100%
Bottom	87%	**-26%**	1%	99%	15%	**-4%**
	HOL					
	PGDv			AIv		
	IC= 1.4	IC= 6.8	IC= 13.8	IC= 1.4	IC= 6.8	IC= 13.8
Surface	100%	100%	99%	100%	100%	100%
Bottom	97%	17%	9%	100%	58%	17%
	HEL					
	PGDv			AIv		
	IC= 1.4	IC= 6.8	IC= 13.8	IC= 1.4	IC= 6.8	IC= 13.8
Surface	98%	98%	96%	100%	100%	100%
Bottom	87%	**-26%**	1%	99%	15%	**-4%**

Tab. 5.2: Percentage of damped waves by the absorbing layer system

The reduction in the PGD and AI (Tab. 5.2), which were the output of the analysis of the displacement variation in the time domain, confirmed the efficiency of the absorbing layer system along the surface. Both absorbing layer systems (HOL and HEL) damped almost all the waves from the model boundaries, including for a high impedance contrast. The results at the bottom of the model were more complex: both HOL and HEL strongly reduced the PGD and AI for low IC values, while higher IC values (6.9 – 13.8) decreased the efficiency of the absorbing layer system, sometimes increasing the PGD and AI values (Tab. 5.2) at the model boundaries. The high IC values were associated with the reflection and refraction of waves with different incidences in the absorbing layer system. The wave field in this model must be carefully studied for high IC values to better understand the causes of the strong efficiency reduction at the bottom of the model.

Recently, Zafati et al. (2016) proposed a modified CALM, an implicit time integration method that can be employed in absorbing layers independently from the elastic domain with the explicit time integration method. This approach was defined to improve the efficiency of the CALM method (Semblat et al. 2011), and its application could probably increase the attenuation of spurious waves at the bottom of the model.

In full 2D numerical modelling, the seismic input would be placed at the seismic bedrock level (not at the top of the model). Thus, the absorbing layer system at the bottom would not include reflected and refracted waves from the model (only the input motion that is applied within the seismic bedrock), and the efficiency is not compromised. The efficiency of both absorbing layer systems was the highest at the model surface, as highlighted during the calibration process. The HEL system was used for the following 2D numerical modelling to determine the gradual damping of the waves.

5.2 2D numerical modelling when assuming free field conditions

The geometry of the geological cross sections AA’ and BB’ was implemented in the FEM (CESAR-LCPC software), and the geometrical shape of all the geological units in the alluvial filling was defined (Fig. 5.9). A numerical seismic bedrock (NM in Tab. 5.3) with a thickness of 150 m was positioned at the bottom of the alluvial deposits (Fig. 5.9) according to the deepest point of each section. The seismic inputs were applied as an S-wave motion within the seismic bedrock, i.e., at the middle of the numerical seismic bedrock (around 75 m below the deepest point of each section) (Fig. 5.9). The outcropping seismic bedrock corresponded to the outcropping volcanic deposit (VC in Fig. 4.8 and Tab. 5.3). According to Semblat et al. (2011), the thickness of the absorbing layer system equals the largest wavelength λ [11] that characterizes the model:

$$\lambda = \frac{V}{f} \qquad [11]$$

where V is the wave velocity and f is the frequency.

The thickness of the absorbing layer system was set to 2000 m according to the largest velocity value that corresponded to Vp in the seismic bedrock (1905 m/s) and the lowest frequency value of the inputs (0.95 Hz). This system consisted of 5 sub-layers with a damping value from $Q_{min}^{-1} \approx 20$, or $\xi = 10$ (in the inner portion of the model), to $Q_{min}^{-1} \approx 200$, or $\xi = 100$ (at the extreme lateral boundary of the model).

The chosen configuration of the absorbing layer system was characterized by the presence of 5 sub-layers (HEL) along the lateral and bottom boundaries of the model (Fig. 5.9).

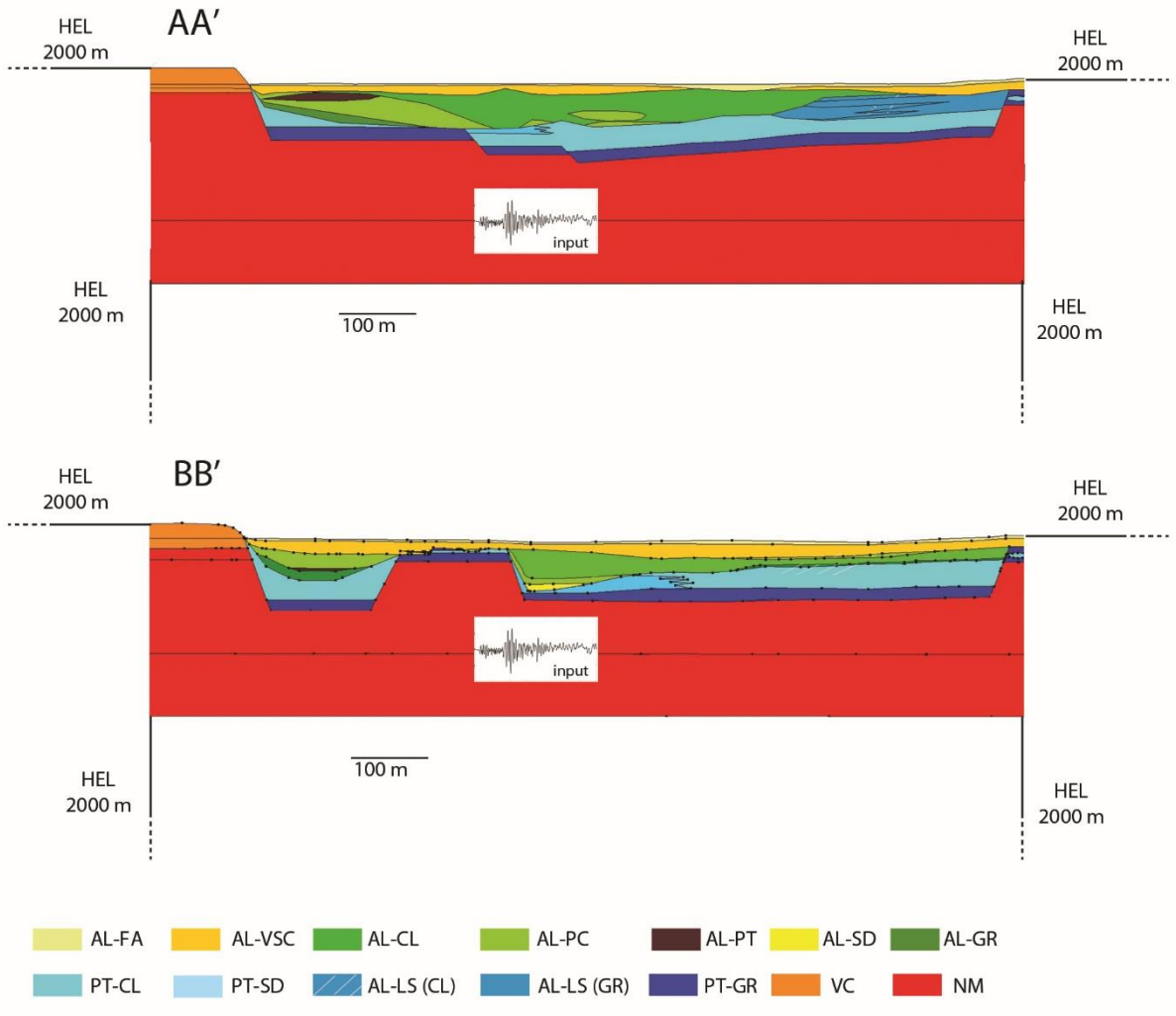

Fig. 5.9: Representation of the numerical models geometrical setting. The position of the seismic inputs is also indicated.

The mesh that was used to discretise the model was characterized by three-noded linear elements. As reported by Semblat and Pecker (2009), the element size strongly influences the numerical error.

Numerical dispersion from coarse mesh can under-estimate the amplitude and over-estimate the velocities (both group and phase). This factor can be reduced by choosing a suitable element size for the wavelength of the problem. The element size Δh was defined to avoid numerical dispersion according to the following relationship [12]:

$$\Delta h = \frac{\lambda}{12} \qquad [12]$$

where λ = wavelength and Δh = element size.

Element sizes of 1 m in the first case and 10 m in the second case were chosen to solve the problem up to a frequency of 10 Hz according to the lowest S-wave velocity of the alluvial deposits (118 m/s) and the largest velocity (1100 m/s) for the seismic bedrock and the absorbing layer system. Consequently, the models of the cross sections AA' and BB' consisted of 282795 and 269917 nodes, respectively.

The properties of the materials were assigned according to the results of the seismo-stratigraphy calibration in § 4.3. The parameters that characterized the materials are listed in Tab. 5.3. The best fit of the calibration process for the PT-CL unit (see § 4.3) was obtained by considering a linear increase in the S-wave velocity within the layer. Implementing this linear increase in the 2D model was not possible, and a unique Vs value was assigned to the PT-CL unit. The conditions that were applied to the model boundaries were fixed boundary conditions.

Lithological units	**ρ (kg/m^3)**	**V_s (m/s)**	**V_p (m/s)**	**ν**	**G (Mpa)**	**E (Mpa)**	**ξ (%) Strain=0.001%**	**a_0**	**a_1**
AL-AF	1732.9	118.3	221.3	0.30	24.3	60.6	1	0.5027	1.99E-04
AL-VSC	1682.0	225	420.9	0.30	85.1	212.9	1	0.5027	1.99E-04
AL-CL	1865.4	235	439.6	0.30	103.0	257.5	2	1.0053	3.98E-04
AL-CP	1753.3	150	280.6	0.30	39.4	98.6	3	1.2252	7.35E-04
AL-PT	1294.6	140	261.9	0.30	25.4	63.4	1	0.5027	1.99E-04
AL-GR	2140.7	713	1333.9	0.30	1088.3	2720.6	1	0.5027	1.99E-04
AL/PT-SD	1957.2	417	780.1	0.30	340.3	850.8	1	0.5027	1.99E-04
PT-CL	1865.4	357	667.9	0.30	237.7	594.4	3	1.2252	7.35E-04
AL-LS (AR)	1865.4	250	467.7	0.30	116.6	291.48	3	1.2252	7.35E-04
AL-LS (GH)	2140.7	550	1028.9	0.30	647.6	1618.9	1	0.5027	1.99E-04
PT-GR	2140.7	1100	2057.9	0.30	2590.2	6475.5	1	0.5027	1.99E-04
VC	1834.9	1100	1905.3	0.25	2220.2	5550.5	1	0.5027	1.99E-04
NM	2140.7	1100	1905.3	0.25	2590.2	6475.5	0.5	0.2042	1.22E-04

Tab. 5.3: Properties attributed to the materials in the numerical models.

5.3 2D numerical modelling of SCI

The progressive development of the urban agglomerate in each geological cross section (AA' and BB' in Fig. 4.2) was modelled to evaluate the progressive influence of the buildings on the local seismic response of the valley, assuming free-field conditions. Each building was previously characterized from a structural perspective, and the dynamic behaviour was modelled to evaluate the fundamental period of each structure. The geological cross sections (before modelled under free-field conditions) were progressively populated with buildings according to the temporal development of the Fosso di Vallerano valley (§ 2.1).

5.3.1 Main steps of urban expansion

The analysis of the urban development in the Fosso di Vallerano valley in § 2.1 defined the main urbanization steps of the two analysed cross sections. Geological representative cells with sizes of 125 m for the AA' section and 180 m for the BB' section were defined. The buildings in the cells in each section were considered to define the various urbanization steps.
Three main urbanization steps could be defined in the geological cross section AA' (Fig. 4.2):

- 2005: Eight buildings were present in the central portion of the AA' cross section (TS1 in Fig. 5.10);
- 2009: One building was built in the eastern portion of the section (TS2 in Fig. 5.10);
- 2011: The construction of the "Europarco Business Park" began, and Eurosky Tower was included in the cells of AA' (TS3 in Fig. 5.11).

In summary, three time steps were defined for a total of 10 buildings in the geological representative cells of the AA' cross section.

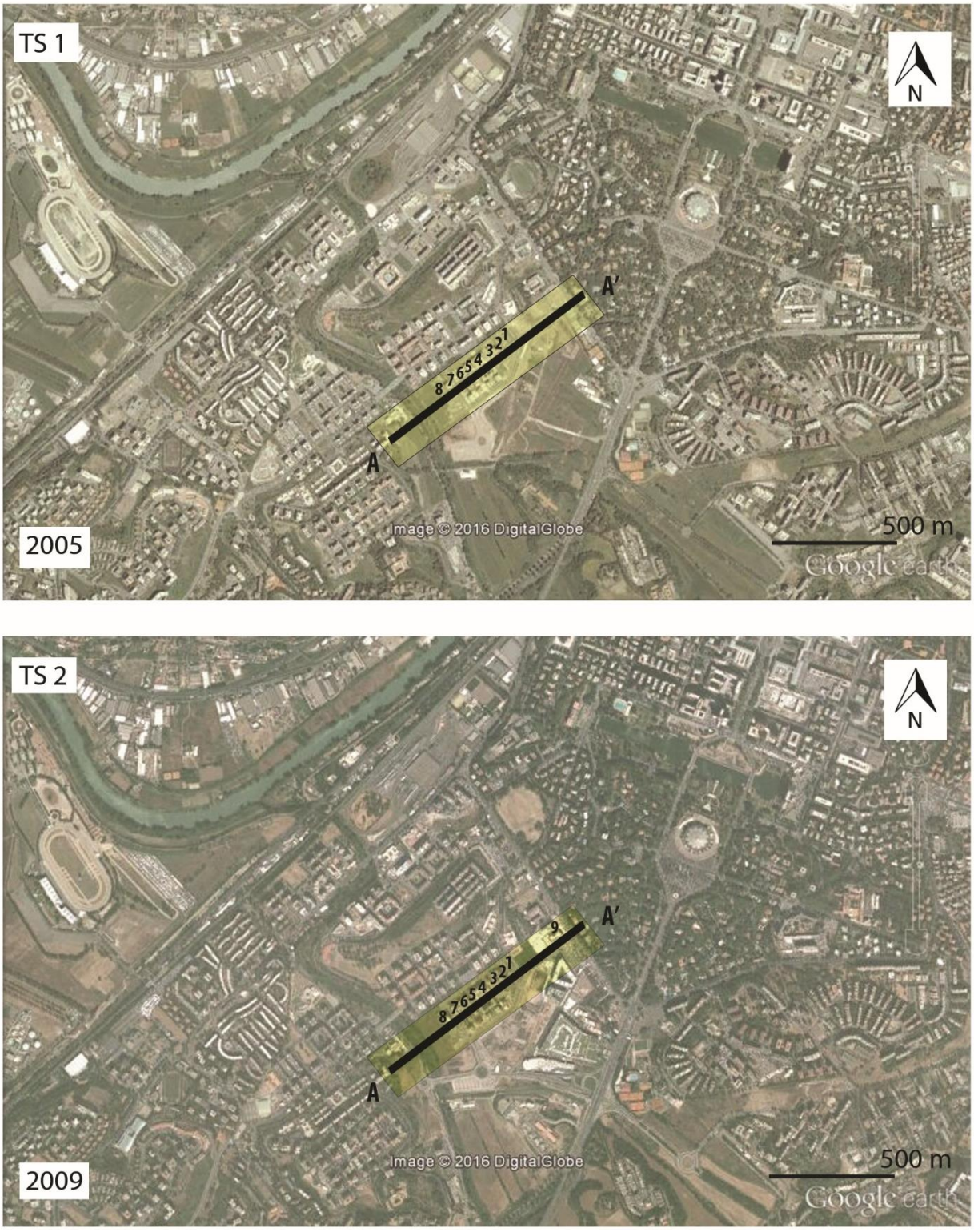

Fig. 5.10: Satellite view of the Fosso di Vallerano valley in 2005 (TS1) and 2009 (TS2). The track of the AA' geological cross section and the corresponding geological representative cell are shown. The ID numbers of the modelled buildings are also reported.

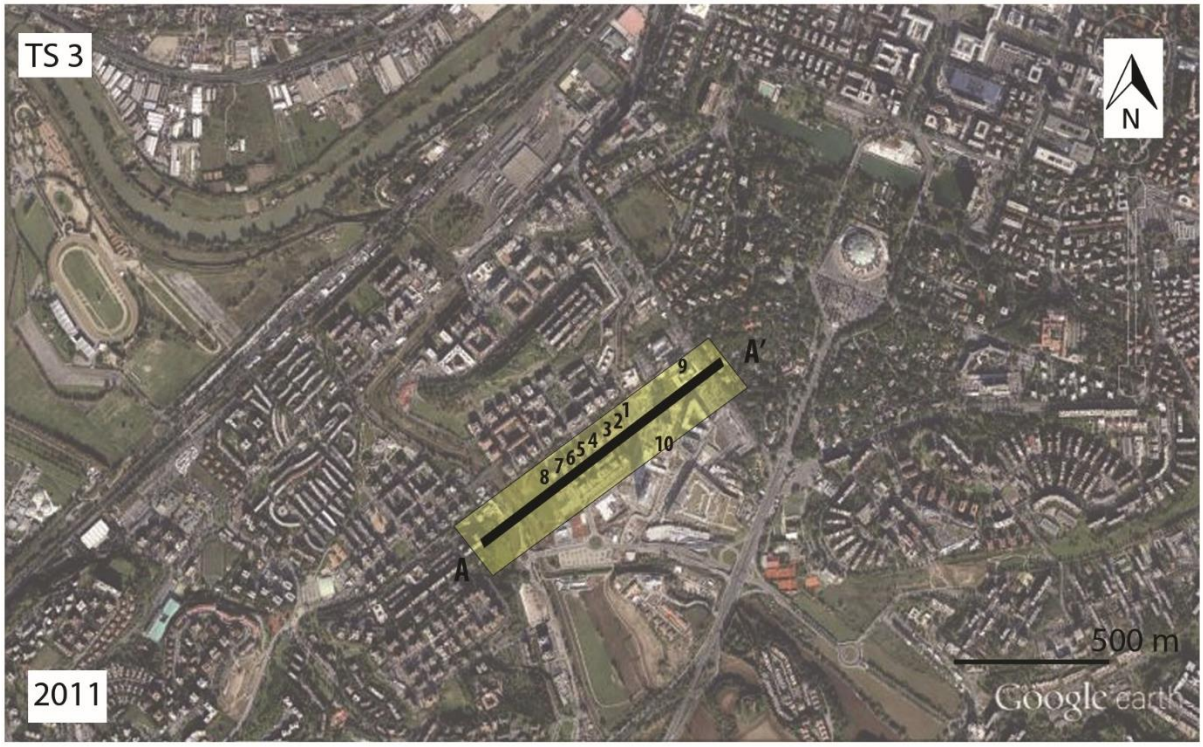

Fig. 5.11: Satellite view of the Fosso di Vallerano valley in 2011 (TS3). The track of the AA' geological cross section track and the corresponding geological representative cell are shown. The ID numbers of the modelled buildings are also reported.

Two urbanization steps could be defined in the cross section BB' (Fig. 4.2):

- 2006: One building was built in the eastern portion of the section (TS1 in Fig. 5.12);
- 2011: Three buildings in the "Europarco Business Park" (including Europarco and Eurosky Towers) and two minor buildings were contained in the geological representative cells of BB' (TS2 in Fig. 5.12)

In summary, two time steps were defined for a total of 6 buildings in the geological representative cells of the BB' cross section.

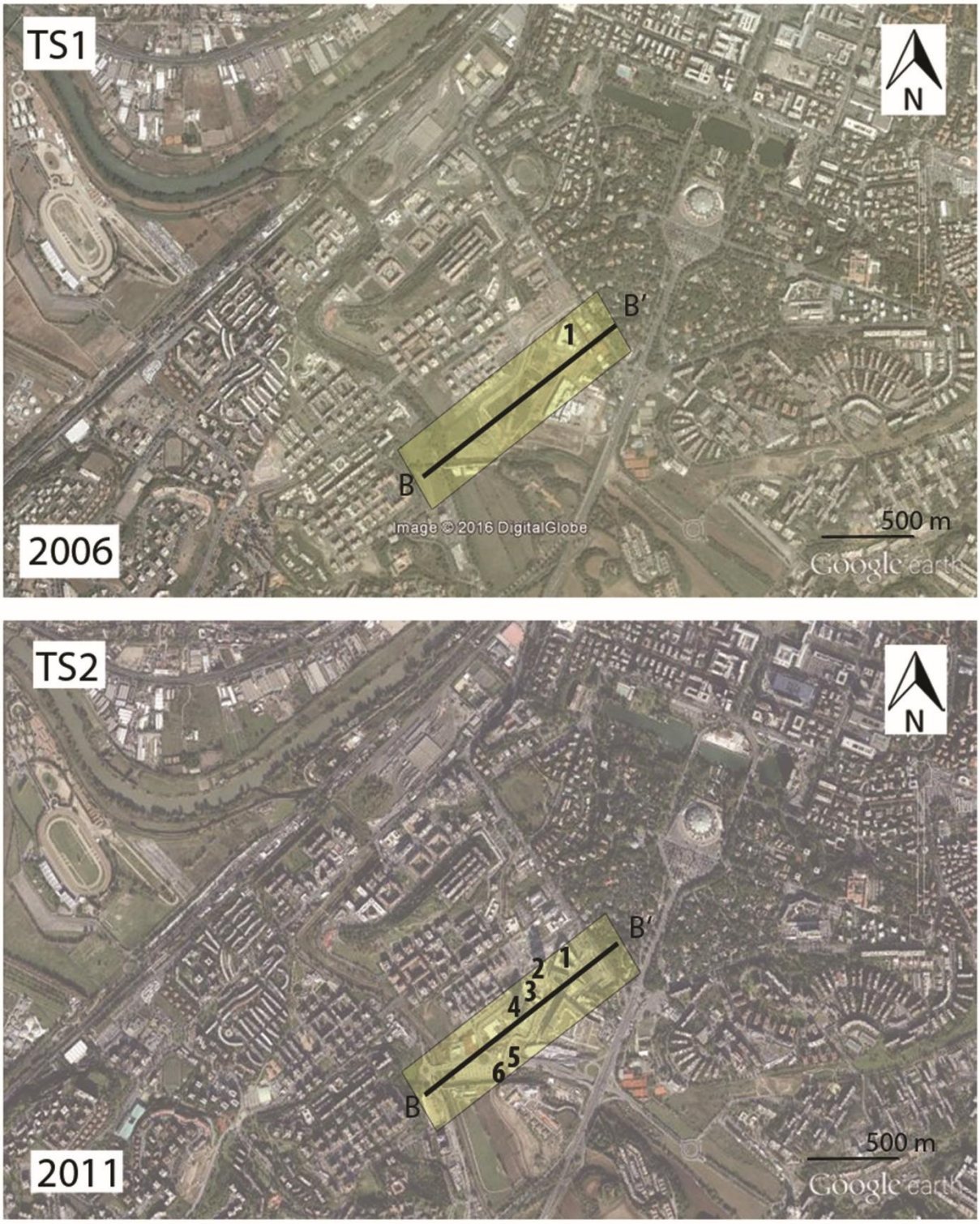

Fig. 5.12: Satellite view of the Fosso di Vallerano valley in 2005 (TS1) and 2009 (TS2). The track of the BB' geological cross section track and the corresponding geological representative cell are shown. The ID numbers of the modelled buildings are also reported.

5.3.2 Structural and dynamic characterization of the buildings

A preliminary characterization of the buildings from geometrical and structural perspectives was conducted to evaluate the dynamic behaviour of each building in the following numerical SCI simulations. The geometry of the buildings was recorded through a field survey to define the shape, the base area and the number of floors of each building. Then, a historical characterization of these buildings was conducted to define the construction materials and typology of the bearing structure and foundation.

Most of these buildings were built in recent decades and are residential buildings, so I can deduce whether they are characterized by a reinforced concrete structure and a shallow foundation. In particular, the two towers that were built in 2011 were researched in detail. Information from the team builders of the "Europarco Business Park" (Colombo 2012) revealed that the skyscrapers are characterized by a mixed bearing structure of steel and reinforced concrete. In particular, the beams and shallow foundation are characterized by a steel structure, while the columns are reinforced concrete structures. Additionally, the team builders indicated that both structures have deep foundations (60 m) that are linked to shallow foundations with a thickness of 6 m; the piles are reinforced concrete structures. The characteristics of these buildings, which are summarized in Tab. 5.5, were used to simulate the dynamic behaviour of the buildings.

Numerical modelling was conducted through a modal analysis with the FEM (CESAR – LCPC software). Each structure was simulated according to its super-structures; in particular, all the beams, columns and shallow foundations were modelled as volume elements (some examples are reported in Fig. 5.13). The volume elements were discretized by three-noded linear elements, and the bases of the buildings were blocked by assuming a fixed boundary condition (no horizontal or vertical motions).

The thickness of the shallow foundation was 1 m for all the buildings except the skyscrapers, for which the shallow foundation's thickness was 6 m. The deep foundations were modelled by assuming that each pile could be represented by a Timoshenko beam (Timoshenko 1921, 1922) with a diameter of 1.2 m and a length of 60 m. The beam-to-column junctions were considered stiff junctions (only horizontal movements were allowed, and rotation and flexion were prevented).

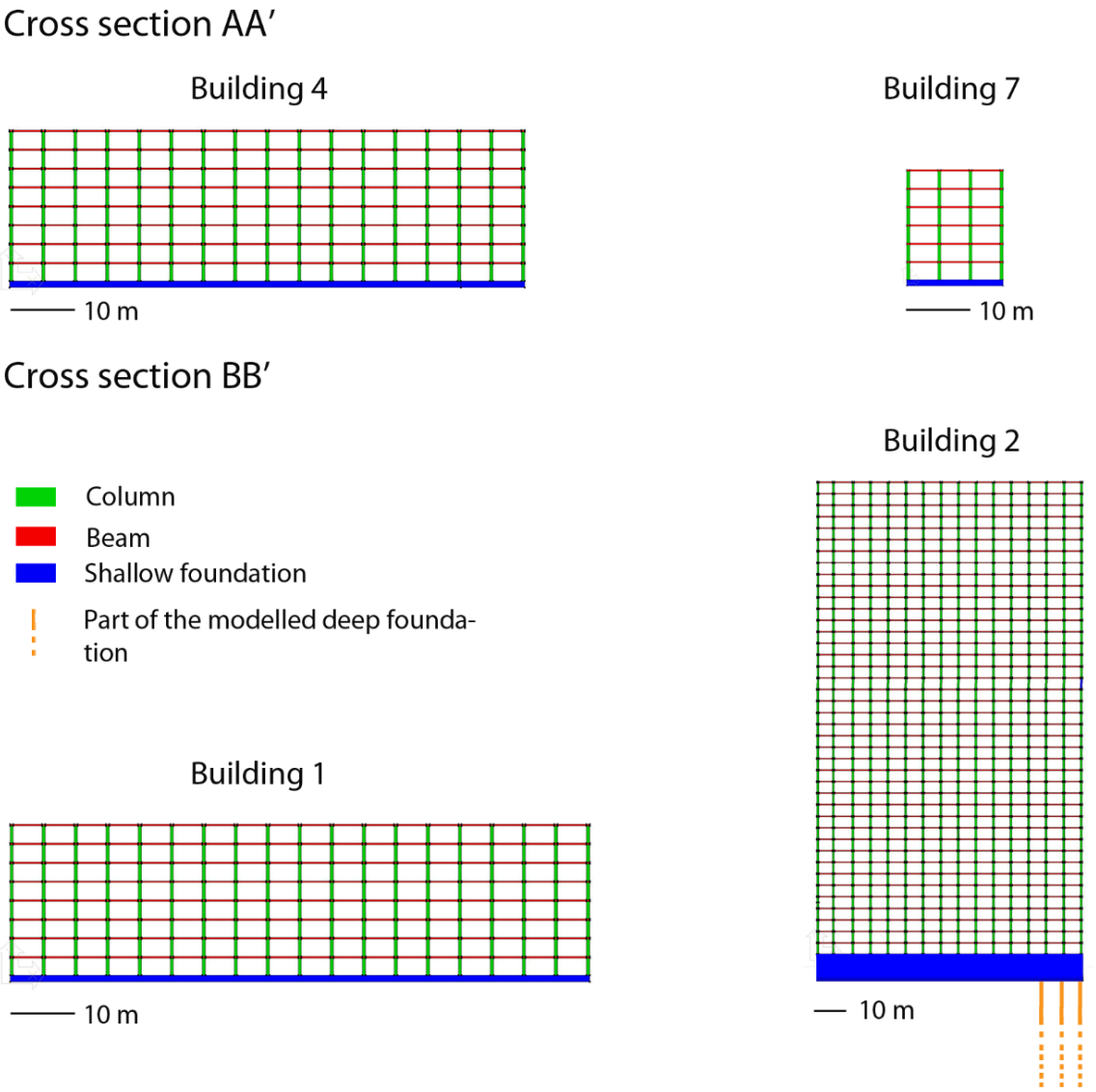

Fig. 5.13: Examples of numerical models of the simulated buildings. Part of the deep foundation is reported (out of scale). See § 5.3.2 for piles details.

The beam stiffness was considered to be much higher than the stiffness of the columns (up to two orders of magnitude) to achieve an infinitely rigid beam with infinitely rigid beam-to-column joints. A 2D projection of the 3D mass and stiffness of the buildings was created to conduct a 2D simulation of 3D structures. The stiffness and masses of the 2D bearing structures considered the stiffness and masses of the 3D bearing structures.

The stiffness values for the different materials are reported in Tab. 5.2.

	Young Modulus (Mpa)			
	Column	Beam	Shallow foundation	Deep Foundation
Reinforced concrete	3.00E+04	3.00E+06	3.00E+06	3.00E+04
Steel + Reinforced concrete		2.10E+07	2.10E+07	

Tab. 5.4: Stiffness values attributed to the materials which compose the 3D bearing structure.

The resonance period of each building (Tab. 5.5) was evaluated through numerical modelling. The results matched the geometrical and structural parameters of the buildings.

Cross section AA'				
ID Building	**Height (m)**	**Type of foundation**	**Tipe of bearig structure**	**Foundamental frequency (Hz)**
1	20	Shallow Foundation	Reinforced concrete	6.3
2	20	Shallow Foundation	Reinforced concrete	6.4
3	20	Shallow Foundation	Reinforced concrete	6.3
4	20	Shallow Foundation	Reinforced concrete	5.3
5	18	Shallow Foundation	Reinforced concrete	6.7
6	18	Shallow Foundation	Reinforced concrete	6.7
7	18	Shallow Foundation	Reinforced concrete	6.7
8	24	Shallow Foundation	Reinforced concrete	5.5
9	15	Shallow Foundation	Reinforced concrete	6.3
10	120	Deep Foundation	Steel + Reinforced concrete	0.5
Cross section BB'				
ID Building	**Height (m)**	**Type of foundation**	**Tipe of bearig structure**	**Foundamental frequency (Hz)**
1	24	Shallow Foundation	Reinforced concrete	4.1
2	120	Deep Foundation	Steel + Reinforced concrete	0.5
3	33	Shallow Foundation	Reinforced concrete	3.8
4	120	Deep Foundation	Steel + Reinforced concrete	0.5
5	6	Shallow Foundation	Reinforced concrete	20
6	7	Shallow Foundation	Reinforced concrete	36

Tab. 5.5: Geometrical and structural features of the modelled buildings. The fundamental resonance frequency of each building is also reported.

5.3.3 Description of the coupled models

A series of coupled models that contained the geological and engineering components were simulated to model the presence of urban complex on heterogeneous soil and evaluate the progressive influence of the buildings on the local seismic response. The simulated buildings (§ 5.3.2) were added to the numerical models, assuming free-field conditions. All the buildings were inserted into the coupled numerical models according to their super-structures, i.e., all the bearing structures that were simulated during the previous phase of the dynamic characterization of the buildings. The parameters for the geological filling, the mesh sizes and the assumed boundary conditions were presented in § 5.2, while the parameters and the mesh sizes that characterized the engineering components are shown in § 5.3.3.

The models that represented the urban development steps in § 5.3.1 consisted of the following:

- Cross section AA': TS1= 293038 nodes; TS2= 295918 nodes; TS3= 313847 nodes (Fig. 5.14);
- Cross section BB': TS1= 274810 nodes; TS2= 323702 nodes (Fig. 5.15).

All the coupled models were loaded by the seismic inputs in § 5.1.1.

A preliminary expeditious evaluation of the SCI effect taking into account the urban density, the geometrical and dynamic characteristics of the buildings and the "free field" response of the soil have been evaluated. This have been carried out applying the empirical relationship proposed by Guéguen et al., 2002 [13]:

$$\frac{E_{kb}}{E_{ks}} \approx \sum_{i=1}^{n} \frac{S_{bi}}{S_s} \cdot \frac{h_{li}}{H_s} \cdot \frac{f_s^2}{\tilde{f}^2} \qquad [13]$$

Where $\frac{S_{bi}}{S_s}$ is the urban density, $\frac{h_{li}}{H_s}$ is the building height to thickness of soil ratio and $\frac{f_s^2}{\tilde{f}^2}$ is the resonance criterion. This relationship represents the ratio between the total kinematic energy of an ensemble of buildings (E_{kb}) and the total kinematic energy of the sedimentary deposit (E_{ks}); ratio values higher than 0.1 indicate strong SCI effects. The obtained $\frac{E_{kb}}{E_{ks}}$ values for the here presented Site-City settings are: AA'-TS1= 4.2, AA'-TS2= 5.1, AA'-TS3=5.2 and BB'-TS1= 1.2 and BB'-TS2= 74.8 indicating strong SCI effects. This latter value is very high according to the presence of two small and wide buildings, characterized by resonance frequency equal to 20Hz and 36Hz.

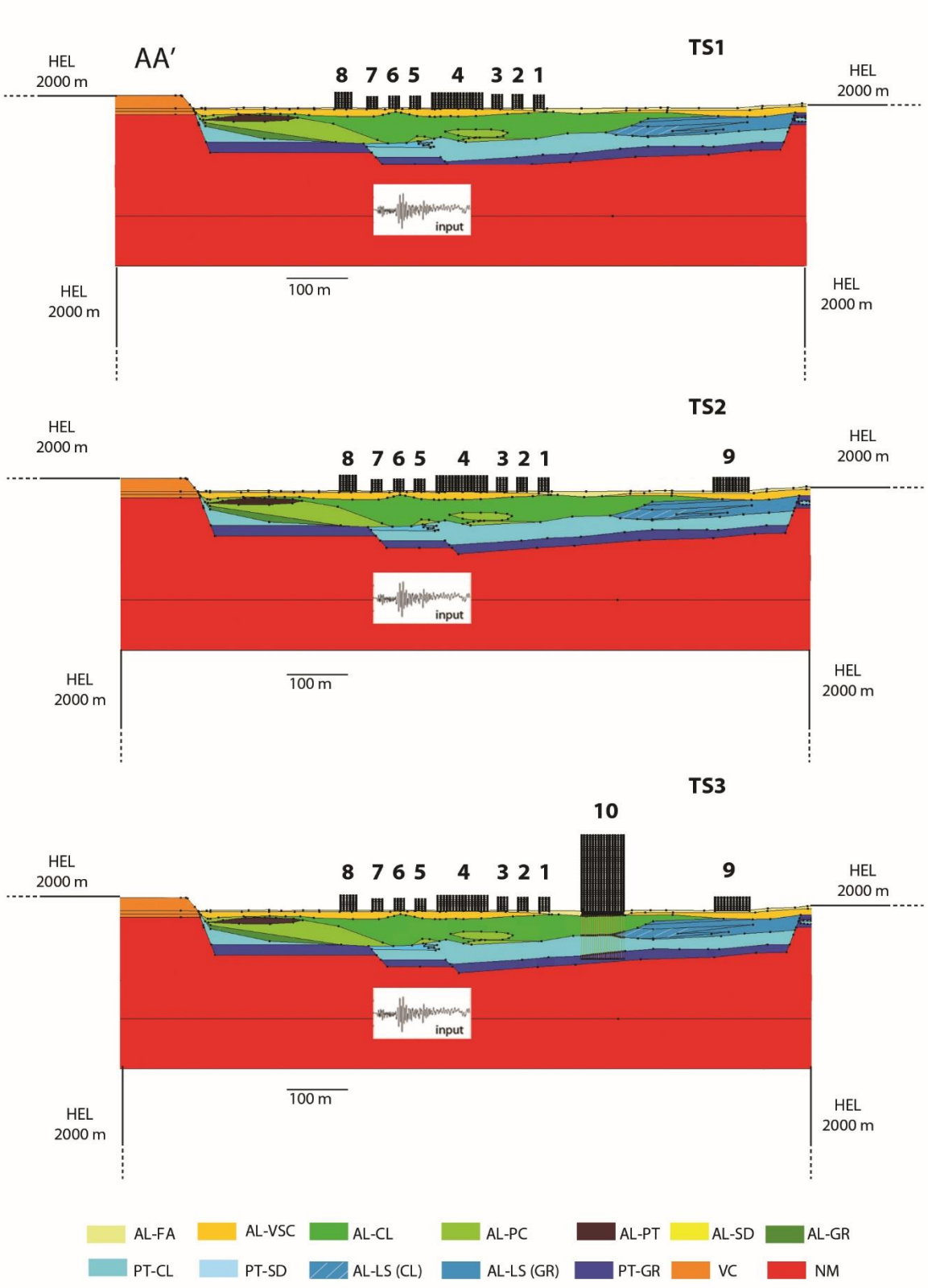

Fig. 5.14: Numerical models designed along the cross section AA', composed of geological subsoil and urban complex (SCI condition).

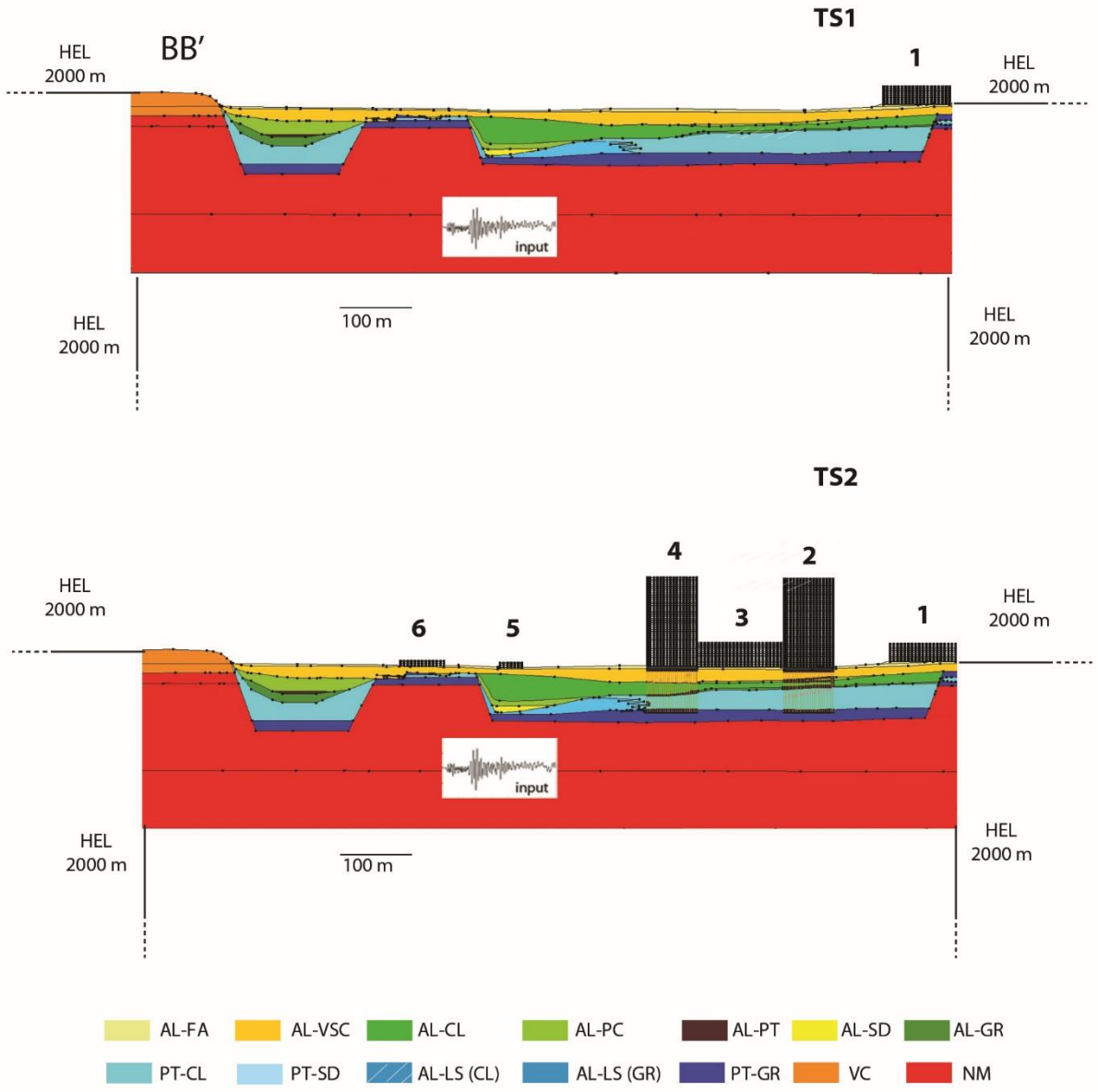

Fig. 5.15: Numerical models designed along the cross section BB', composed of geological subsoil and urban complex (SCI condition).

6. MAIN RESULTS FROM THE SIMULATION MODELS

6.1 Definition of the criteria

The results from the numerical simulations are presented below. The numerical outputs consisted of displacement values for different conditions (i.e., free-field and SCI conditions) along the free surface of the numerical domain and at the top and bottom of the buildings for the SCI condition. The main physical parameters of the ground motion were then compared by assuming different conditions (i.e., free-field and SCI conditions).

The wave propagation maps (WPM) along the models' surfaces enabled us to analyse the reflection and refraction of the waves because of the shape of the valleys (Fig. 6.1 – 6.5) and verify the efficiency of the absorbing layer system (Fig. 6.2 – 6.6). All the wave propagation maps showed the displacement distribution along the models' surfaces in the time range from 0 to 5 s, in which the ground motion was meaningful.

The numerical results were also analysed in terms of amplification functions along the valley; the amplification functions A(f) (*sensu* Borcherdt 1970, 1994) were obtained according to the spectral ratio between the horizontal component of the signals at all the points along the models' surfaces and the average of five modelled horizontal components of signals on the outcropping seismic bedrock (point R in Fig. 4.1). The $A(f)_x$ functions were interpolated through a Kriging regression and summarized in contour maps under different conditions. The variation in the ground energy along the models' surfaces was evaluated through the definition [14] by Kham et al. (2006) to provide a global assessment of the Site–City Interactions:

$$E(x) = \frac{\rho(x)}{T} \int_0^T \left[\frac{\mathrm{du}}{\mathrm{dt}}(x,t)\right]^2 \mathrm{dt} \qquad [14]$$

where ρ is the density, T is the signal duration, u is the displacement, and t is the time.

The dynamic behaviour of the buildings under SCI conditions (AA'-TS1, AA'-TS2, and AA'-TS3 in Fig. 5.14; BB'-TS1 and BB'-TS2 in Fig. 5.15) was analysed to verify the correspondence between the modelled dynamic behaviour and resonance periods of individual buildings in the coupled models (AA'-TS1, AA'-TS2, and AA'-TS3 in Fig. 5.14; BB'-TS1 and BB'-TS2 in Fig. 5.15). In particular, the transfer functions (TF) of the buildings were calculated.

This analysis also focused on the perturbed wave field (U_P) from the urban complex to better understand the role of SCI on free-field conditions, which was performed by computing the difference [15] between the displacement value at each point on the surface when assuming free-field (U_f)

conditions and the displacement at the same points by assuming SCI conditions (U_{SCI}) in the coupled modelling (AA'-TS1, AA'-TS2, and AA'-TS3 in Fig. 5.14; BB'-TS1 and BB'-TS2 in Fig. 4.15).

$$U_P = U_f - U_{\mathrm{SCI}} \qquad [15]$$

The obtained diffracted and reflected wave field were analysed in terms of wave propagation maps of the total wave field along the free surface and by considering a series of frequency bands that were centred on the resonance frequencies of the buildings. In this case, the displacement was exaggerated by a factor of 10 to highlight the ground motion.

In the following, the results that were obtained when forcing the models with the synthetic input (EQ – 1 in Fig. 5.1) are presented because they represent key results to understand the aforementioned phenomena. The results that were obtained when stressing the model with real earthquakes (EQ-7, EQ-12, and EQ-13 in Fig. 5.2) are reported in the Appendix.

6.2 Results of 2D numerical modelling when assuming free field conditions

The results of the numerical simulation of the AA' model are presented first. The wave propagation maps of the horizontal and vertical displacement along the AA' model surface (Fig. 6.1) showed how the valley (central portion of the model) was characterized by different wave arrival times because of the different thicknesses of the alluvial filling. Moreover, the model showed 1D and 2D amplification phenomena because of the thickness of the alluvial filling and the shape of the valley, respectively. The outcropping bedrock (left side of the AA' model) showed no significant wave refraction or reflection. An analysis of the displacement highlighted the efficiency of the absorbing layer system in damping the waves from all sides of the model's numerical domain. Within the first 200 m of the HEL, all the waves were damped and no displacement was observed (example on the right side of the model in Fig. 6.2).

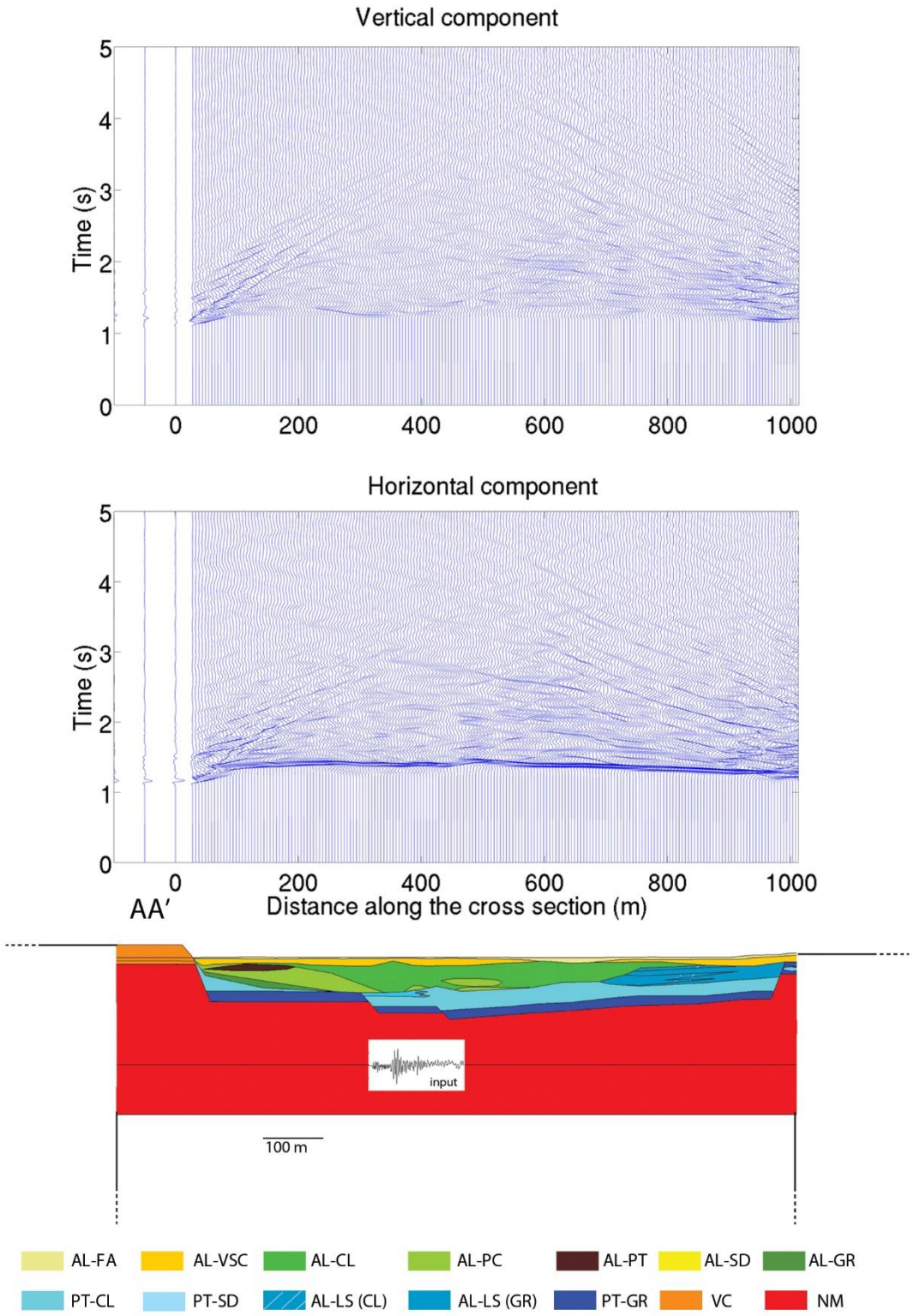

Fig. 6.1: Wave propagation maps of the vertical (top) and horizontal (middle) components of the displacement along the AA' model surface (bottom).

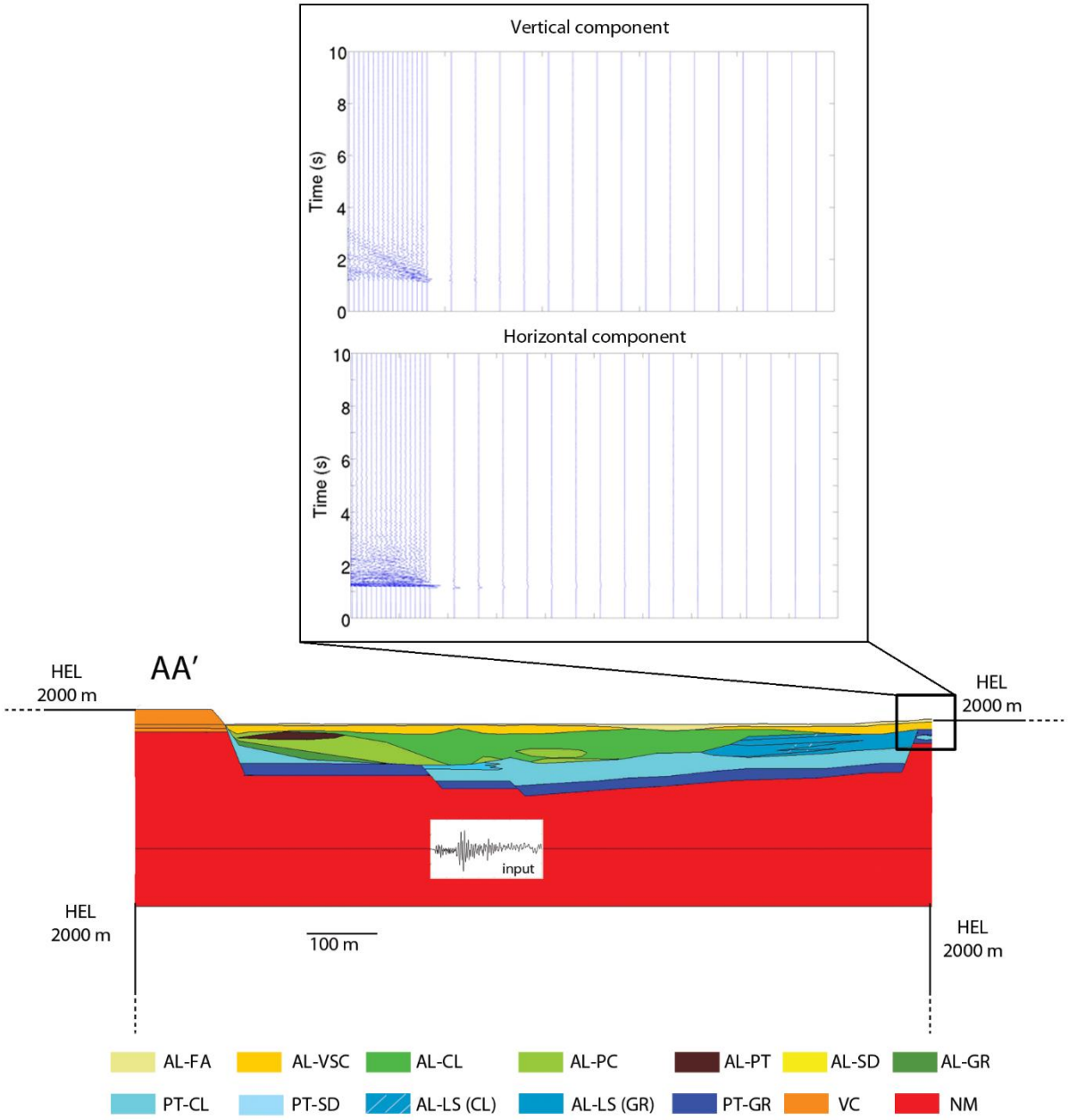

Fig. 6.2: Zoom of the wave propagation maps of the vertical (top) and horizontal (bottom) components of the displacement at the transition between the model and the absorbing layer system (HEL) of AA' model surface.

An analysis of the $A(f)_x$ (Fig. 6.3) highlighted the non-homogeneous distribution of the resonance peaks along the valley, while no amplification peaks were present along the outcropping bedrock (left side of the AA' model). The first resonance peak ranged from 0.8 Hz to 1.2 Hz along the valley in relation to the thickness of the alluvial resonant filling. These results agree with experimental results obtained from ambient noise measurement shown in § 4.1-4.2.

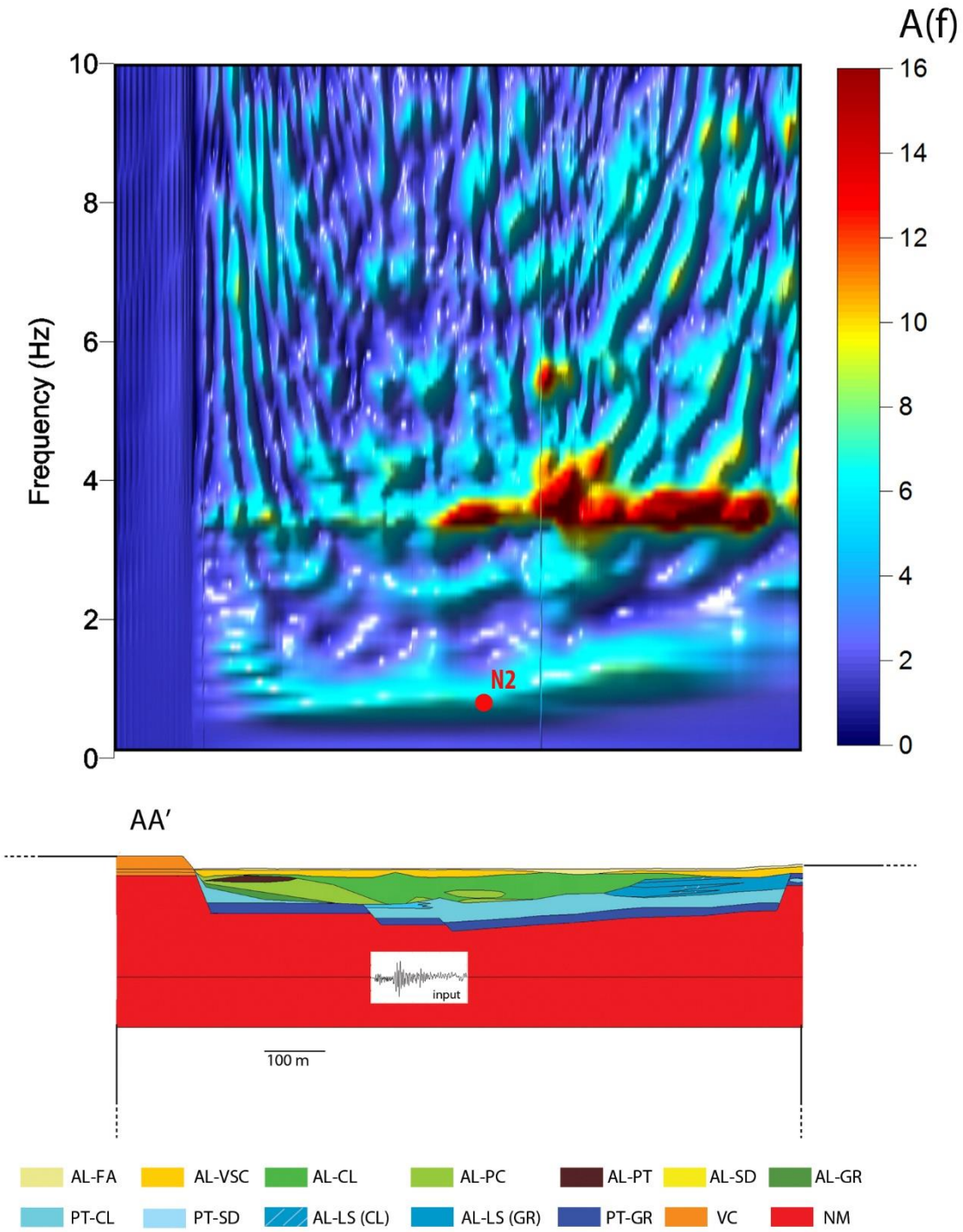

Fig. 6.3: Contour map of the $A(f)_x$ functions distribution (top) along the AA' model surface (bottom). The location of noise measurement are also reported (see Fig. 4.2 for legend).

Upper modes occur because of peculiar stratigraphic settings along a section; the impedance contrast from the presence of the litho-technical unit AL-VSC created an upper mode in the frequency range of 3.5 – 4 Hz. The amplification value of this mode was much higher on the left side of the model, which exhibited a combined effect from the AL-VSC unit and the landslide (AL-LS).

The variation in *E(x)* along the AA' model's surface (Fig. 6.4) highlighted higher ground energy values (up to 10 times higher) along the valley with respect to the outcropping bedrock. The main portion of the valley was characterized by *E(x)* values from 500 to 1500 J/m^3, while the energy in the western portion of the model, in which the thickness of the alluvial resonant filling decreased, was higher (above 2000 J/m^3).

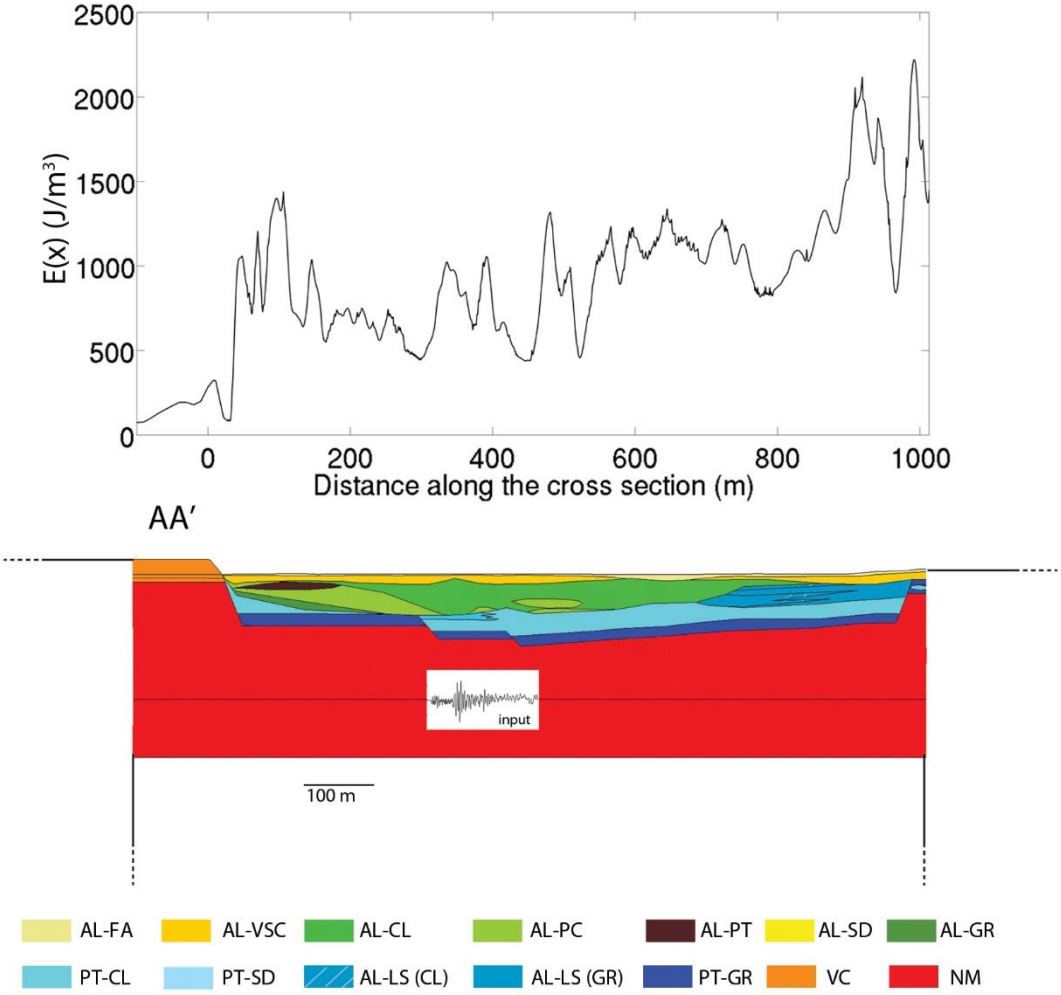

Fig. 6.4: Variation of the kinetic energy E(x) index (top) along the AA' model surface (bottom).

The results of the numerical simulation of the BB' model showed similar features to the AA' model, except for the portion of the model that was characterized by a peculiar setting. The wave propagation maps of the horizontal and vertical displacement along the BB' model's surface (Fig. 6.5) showed different arrival times of the seismic waves, particularly in the western and eastern portions of the valley because of the thickness and shape of the valley.

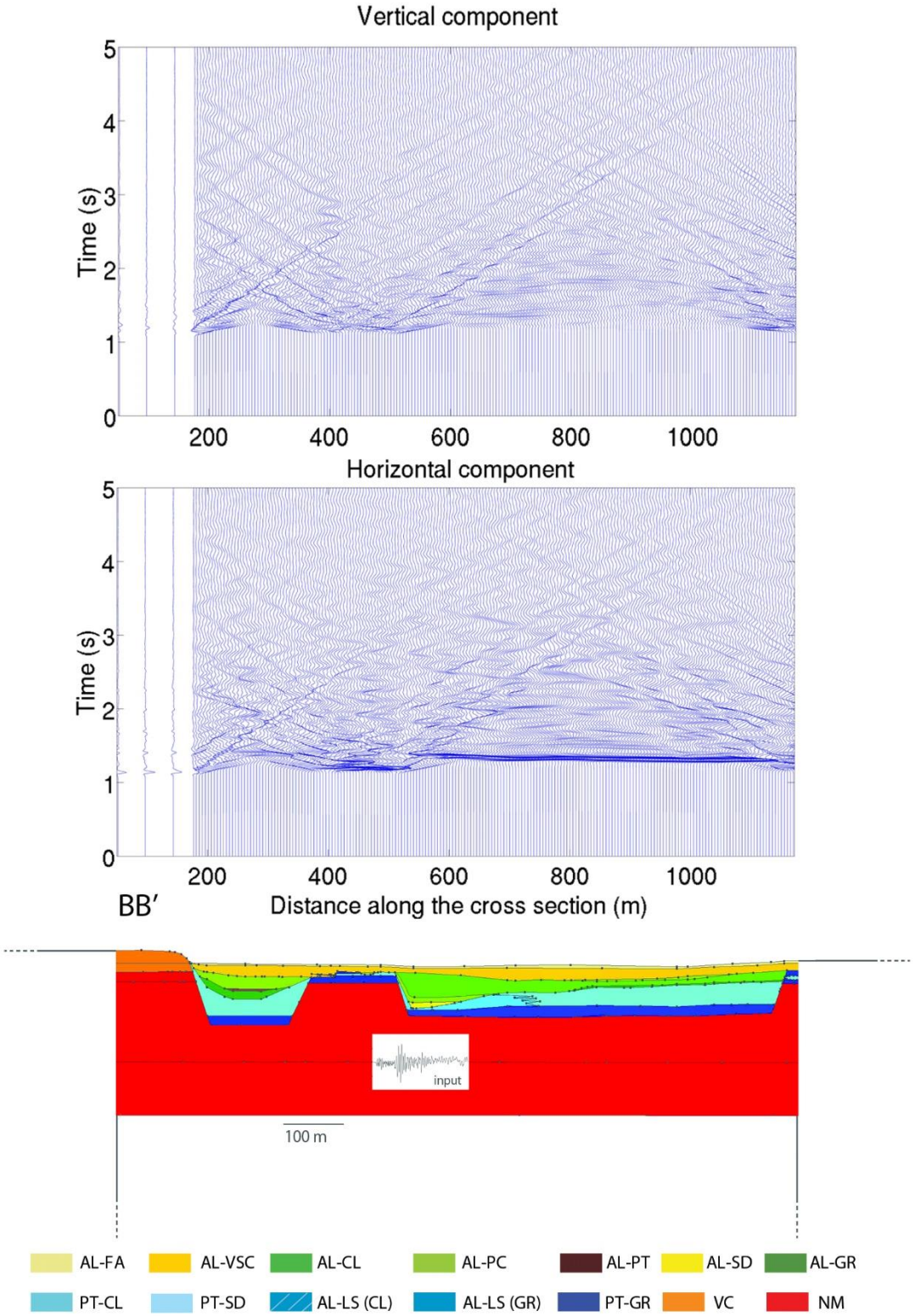

Fig. 6.5: Wave propagation maps of the vertical (top) and horizontal (middle) components of the displacement along the BB' model surface (bottom).

The wave propagation maps showed 1D and 2D amplification phenomena because of the stratigraphic setting of the alluvial filling and the shape of the valley, respectively. The outcropping bedrock (left side of the BB' model) showed no significant wave refraction or reflection. An analysis of the

displacement at the transition between the model and the absorbing layer system confirmed the efficiency of the HEL from the AA' numerical simulation. Additionally, all the waves in the first 200 m of the HEL in the BB' model were damped and no displacement was present (example on the right side of the model in Fig. 6.6).

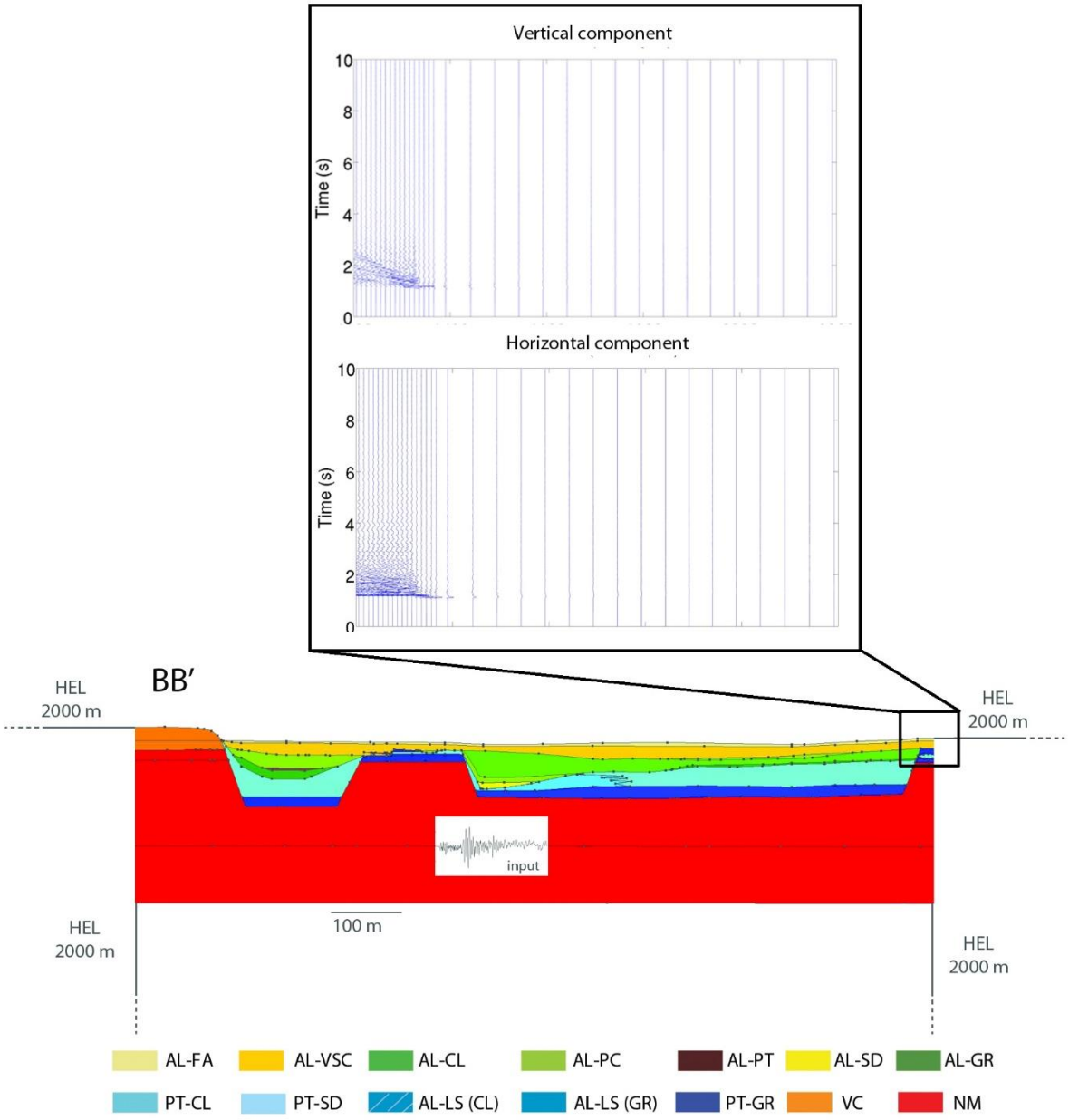

Fig. 6.6: Zoom of the wave propagation maps of the vertical (top) and horizontal (bottom) components of the displacement at the transition between the model and the absorbing layer system (HEL) of BB' model surface.

An analysis of the $A(f)_x$ (Fig. 6.7) highlighted the non-homogenous distribution of the resonance peaks along the valley; in particular, a wide portion of the section was characterized by a first resonance peak around 1 Hz, while the upper resonance modes occurred because of the peculiar heterogeneity in each portion of the valley. The position and the amplitude of the first resonance peak

agrees with the results obtained from HVSR and SSR analysis (Fig. 4.1 - 4.2 in § 4.1 and Fig. 4.5 in §4.3).

Indeed, the central and eastern portions of the valley showed a first resonance peak at a higher frequency value (around 3 Hz), while upper modes from the peculiar heterogeneity in each portion of the valley were also present.

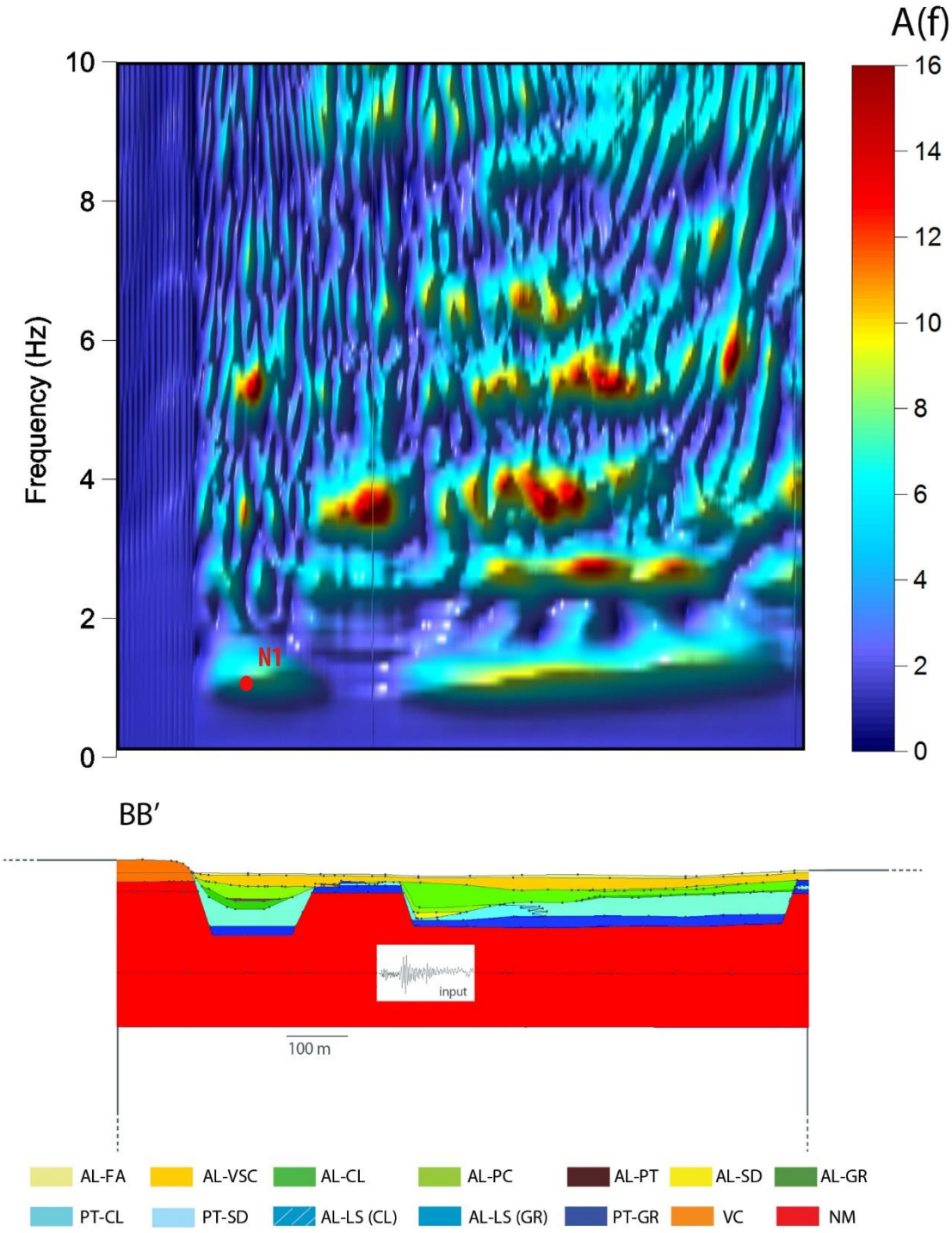

Fig. 6.7: Contour map of the $A(f)_x$ distribution (top) along the BB' model surface (bottom). The location of noise measurement are also reported (see Fig. 4.2 for legend).

The energy distribution along the BB' model's surface (Fig. 6.8) was non-homogeneous. The *E(x)* values did not vary within a narrow range, as with the AA' model, but instead ranged from 500 to 4000 J/m^3. The central area of the valley was characterized by thinner alluvial deposits, which corresponded to higher *E(x)* values (about 4000 J/m^3). In particular, the maximum energy value was 3737 J/m^3, almost two times higher than the maximum value of the AA' model (2221 J/m^3).

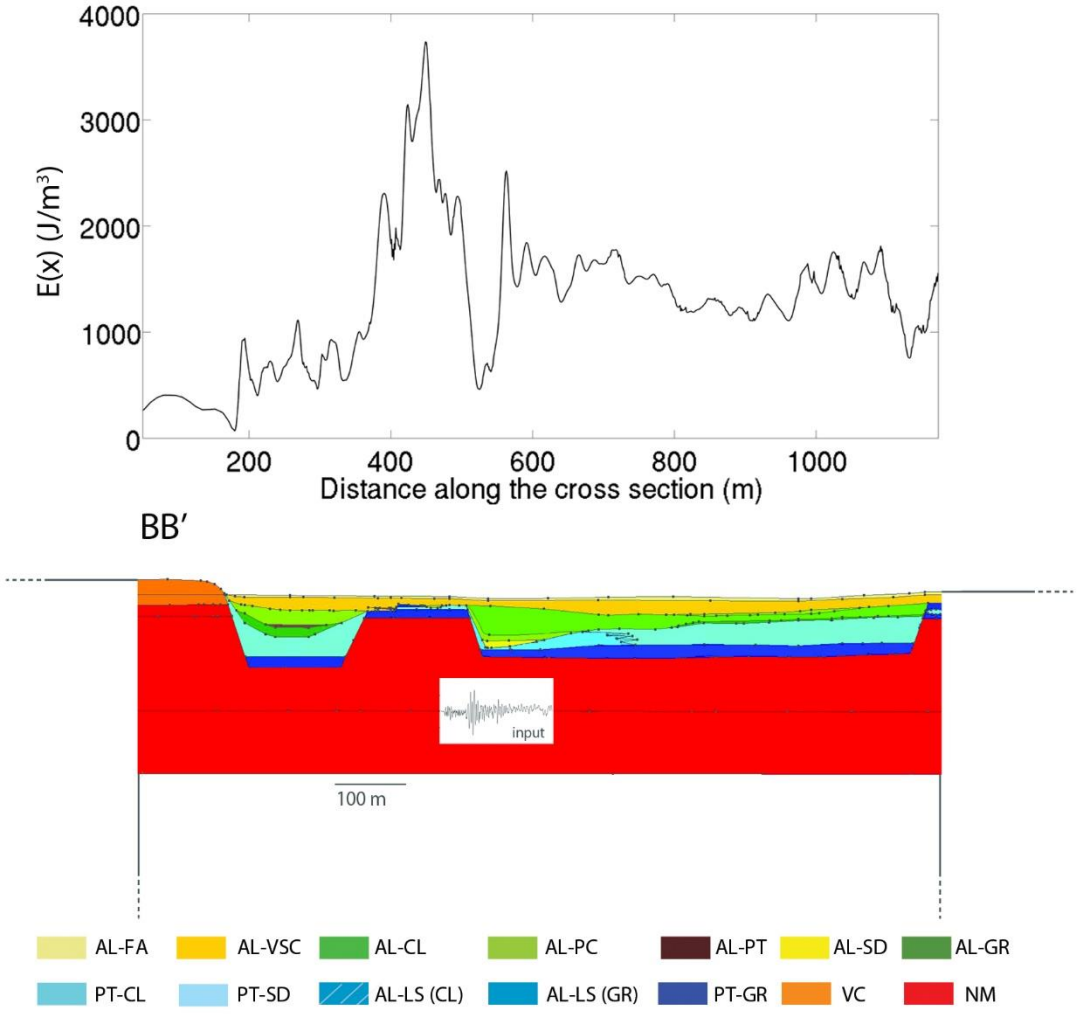

Fig. 6.8: E(x) distribution index (top) along the BB' model surface (bottom).

6.3 Results of the 2D numerical modelling when assuming SCI conditions

The wave propagation maps of the horizontal and vertical displacement along the surfaces of the AA' coupled models (AA'-TS1, AA'-T2, and AA'-TS3 in Fig. 6.9) showed the influence of urbanization on the ground motion with respect to free-field conditions. The effect of buildings was combined with the influence of the geological setting of the valley. In particular, the seismic waves had different arrival times because of the different thicknesses of the alluvial deposits and 2D effects because of the shape of the valley (Fig. 6.9). Two additional phenomena from the presence of these buildings may be identified. The first was related to the presence of buildings with small volumes and masses (e.g., buildings 1-2-3-5-6-7-8 in the AA'-TS1, AA'-TS2, and AA'-TS3 models), which strongly reduced the ground motions close to the buildings' foundations. The second effect was ascribable to the presence of buildings with larger volumes and masses (e.g., building 8 in the AA'TS1 model, buildings 8-9 in the AA'-TS2 model and buildings 8-9-10 in the AA'-TS3 model), which induced negligible ground motion at the foundation level.

Both the 1D and 2D amplification effects close to the buildings from the shape of the valley and the heterogeneities of the deposits were reduced by the effect of SCI. These effects persisted in the portions of the models without structures. The presence of buildings also increased the duration of the ground motion with respect to free-field conditions. The influence of these urban networks was equally visible in the horizontal and vertical components of the ground motion. An analysis of the $A(f)_x$ distribution along the AA' coupled models (AA'-TS1, AA'-TS2, and AA'-TS3 in Fig. 6.10) highlighted the complex distribution of the amplification functions. The non-homogenous distribution of the resonance peaks under free-field conditions along the valley was strongly modified and complicated by the presence of these buildings. The distribution of the amplification peaks close to the buildings was modified according to the two typologies of the aforementioned phenomena. In particular, the presence of buildings with small volumes and masses (e.g., buildings 1-2-3-5-6-7 in the AA'-TS1, AA'-TS2, and AA'-TS3 models) led to an additional amplification peak in the frequency range of 0.8-1.2 Hz that was not observed in the free-field case.

This phenomenon was also noticed close to buildings 8-9 in the AA'-TS2 and AA'-TS3 models, which showed comparable results to the buildings with larger volumes and masses from the wave propagation analysis. Moreover, another peak (approximately 1.5 Hz) was observed near building 9 for the AA'-TS2 and AA'-TS3 models under SCI conditions, while this peak was not obvious in the free-field case.

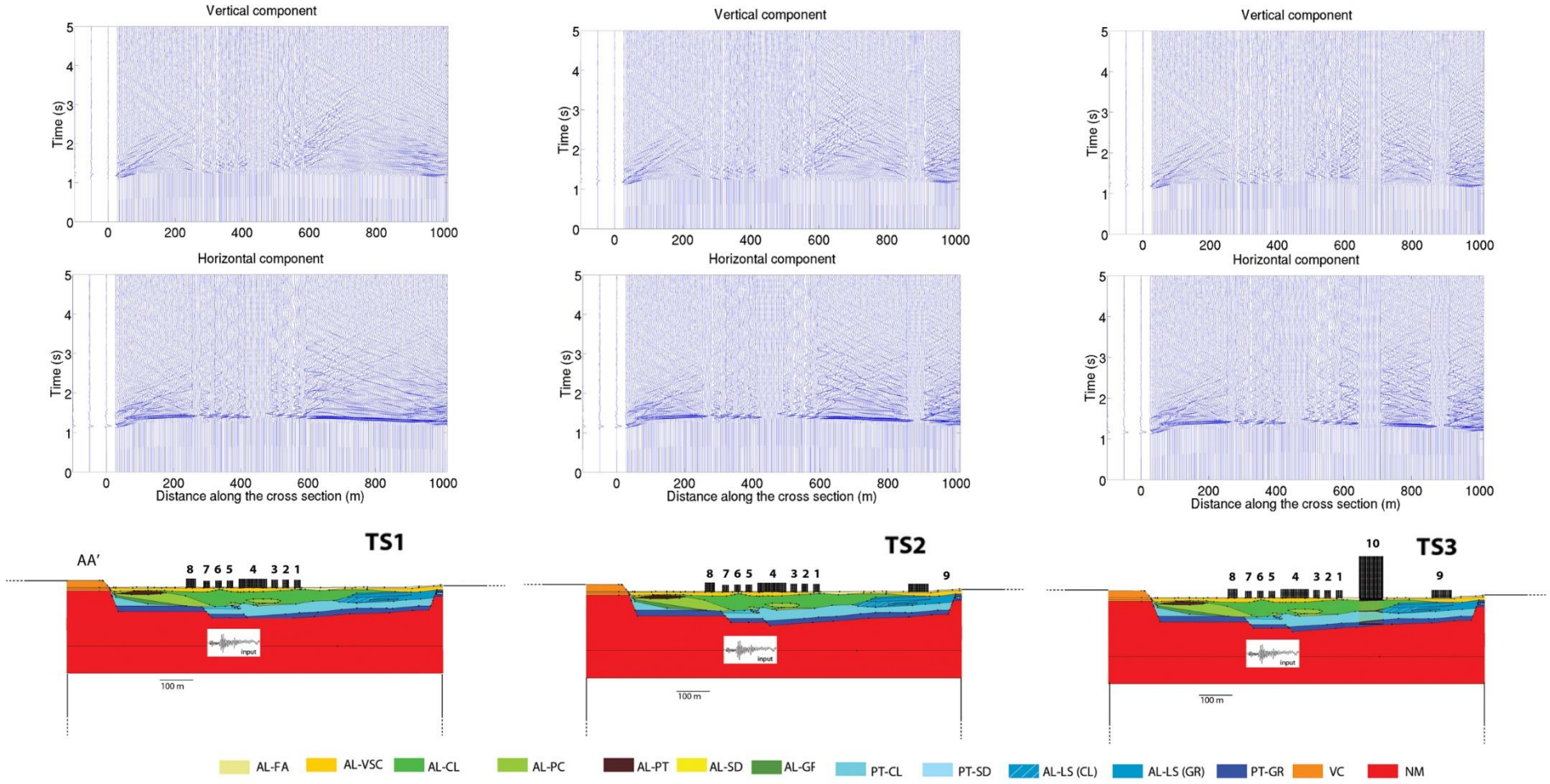

Fig. 6.9: Wave propagation maps of the vertical (top) and horizontal (middle) components of the displacement along the AA' coupled models. From left to right: AA'TS1, AA'-TS2, AA'-TS3. See description of building network page 61.

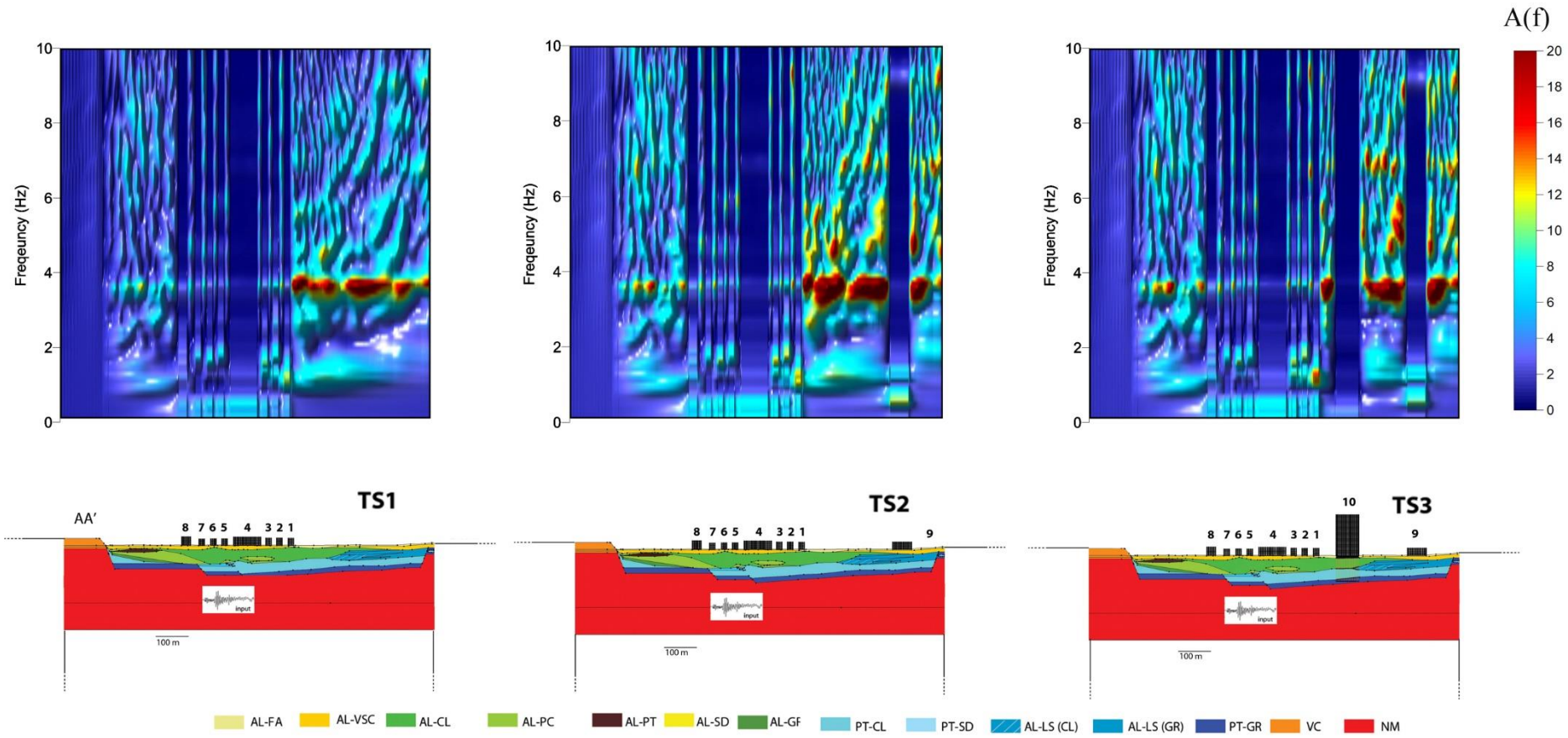

Fig. 6.10: Contour maps of the $A(f)_x$ functions distribution (top) along the AA' coupled models surface (bottom). From left to right: AA'-TS1, AA'-TS2, AA'-TS3. See description of building network page 61.

All the amplification peaks near the buildings with larger volumes and masses (e.g., building 10 in the AA'-TS3 model) disappeared and no amplification effects were observed. The portions of the valley that surrounded the buildings were characterized by higher numbers of amplification peaks and a greater amplification level for each peak.

The *E(x)* index distribution along the AA' coupled models' surfaces (AA'-TS1, AA'-TS2, and AA'-TS3 in Fig. 6.11) showed strong reduction close to the buildings and an increase in the surrounding areas. The coupled model that represented the first urbanization step (AA'-TS1 in Fig. 6.11) showed a strong reduction in *E(x)* close to the buildings with smaller volumes and masses (i.e., buildings 1-2-3-5-6-7 in the AA'-TS1 model), while a strong energy drop was observed in the portion of the valley with building 8, which was characterized by a larger volume and mass. This energy abatement was also observed for buildings 4 and 9 in the AA'-TS2 model and buildings 4, 9 and 10 in the AA'-TS3 model. The increasing *E(x)* values in the area surrounding the buildings was more obvious for the AA'-TS2 and AA'-TS3 models than for the AA'-TS1 model because of the larger building density and the related influence of the SCI conditions. The kinetic energy on the free surface reached approximately 3200 J/m^3 in the AA'-TS3 coupled model, while the maximum E(x) value was approximately 2000 J/m^3 when assuming free-field conditions.

The transfer functions (TF) of the buildings were derived to verify that the buildings that were modelled in the coupled models (AA'-TS1, AA'-TS2, and AA'-TS3) were vibrating and were characterized by the same resonance frequency in the previous phase of this research (§ 5.3.2). An analysis of the TFs indicated that the buildings 1 to 8 in the AA'-TS1 model and buildings 1 to 9 in the AA'-TS2 and AA'-TS3 models showed vibrational behaviour that was characterized by a first resonance peak at the frequency that was modelled in § 5.3.2. (e.g., in Fig. 6.12a). The TF of building 10 in the AA'-TS3 model (Fig. 6.12b) showed the vibrational modes of the structure, but the principal resonance peak was not the mode that was modelled in § 5.3.2. The minimum attenuation value of the Generalized Maxwell model from the numerical modelling was selected to be the predominant frequency of the input (10 Hz), but the fundamental frequency of building 10 (0.5 Hz) fell within the portion of the Rayleigh curve in which the damping tended to infinity. The main resonance of the structure (0.5 Hz) was completely damped and only the upper modes were visible.

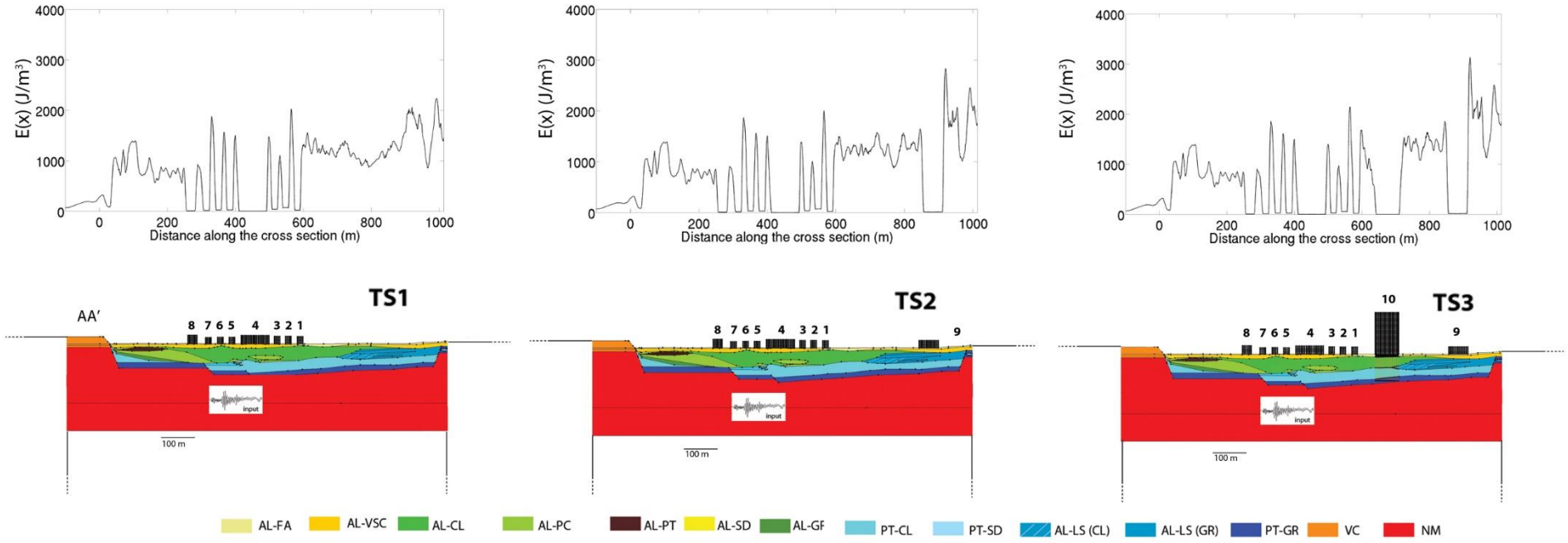

Fig. 6.11: Variation of the kinetic energy E(x) index (top) along the AA' coupled models surface (bottom).From left to right: AA'-TS1, AA'-TS2, AA'-TS3.

See description of building network page 61.

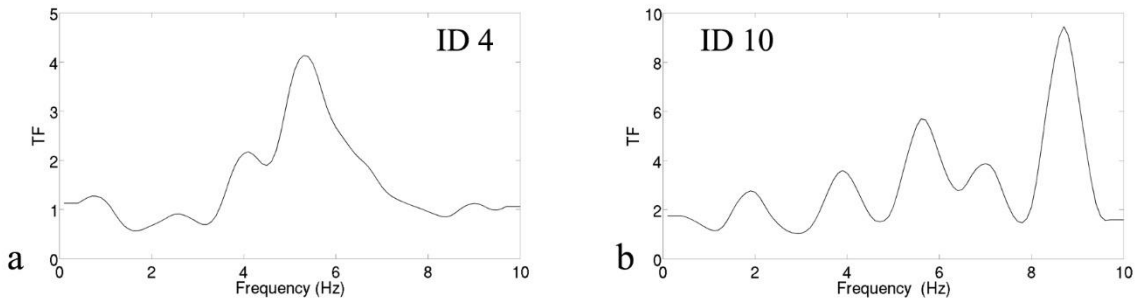

Fig. 6.12: Examples of the Transfer Functions (TF) of the buildings composing the AA' coupled models. a) Building 4 in AA'-TS3 b) Building 10 in AA'-TS3.

The influence of the buildings on both the ground motion and the seismic response for the BB' coupled models (BB'-TS1 and BB'-TS2 in Fig. 5.15) matched the results for the AA' coupled models (AA'-TS1, AA'-TS2, and AA'-TS3 in Fig. 6.9-6.10-6.11). In particular, the wave propagation of the horizontal and vertical displacement along the surfaces of the BB' coupled models (BB'-TS1 and BB'-T2 in Fig. 6.13) showed how the presence of buildings increased the effects because of the geological setting of the valley. The different arrival times of the waves from the different thicknesses of the resonant alluvial filling and the 2D effects from the shape of the valley (Fig. 6.13) were constant in the portion of the valley that was characterized by free-field conditions, i.e., no structures present to vibrate. The two aforementioned phenomena from the AA' coupled models were observed near the buildings. The presence of buildings with smaller volumes and masses (i.e., buildings 5-6 in the BB'-TS2 model) in the BB' coupled models strongly reduced the ground motion. Meanwhile, the presence of buildings with larger volumes and masses (e.g., building 1 in the BB'-TS1 model and buildings 1-2-3-4 in the BB'-TS2 model) completely abated the ground movement. The presence of buildings nullified the 1D and 2D effects in the portion of the valley that hosted the structures. Additionally, the presence of buildings increased the duration of the ground shaking, and the influence of the urban complex was equally visible in the horizontal and vertical components of the displacement. The $A(f)_x$ distribution along the BB' coupled models (BB'-TS1 and BB'-TS2 in Fig. 6.14) was strongly influenced by the presence of buildings, which complicated the non-homogeneous response of the alluvial valley.

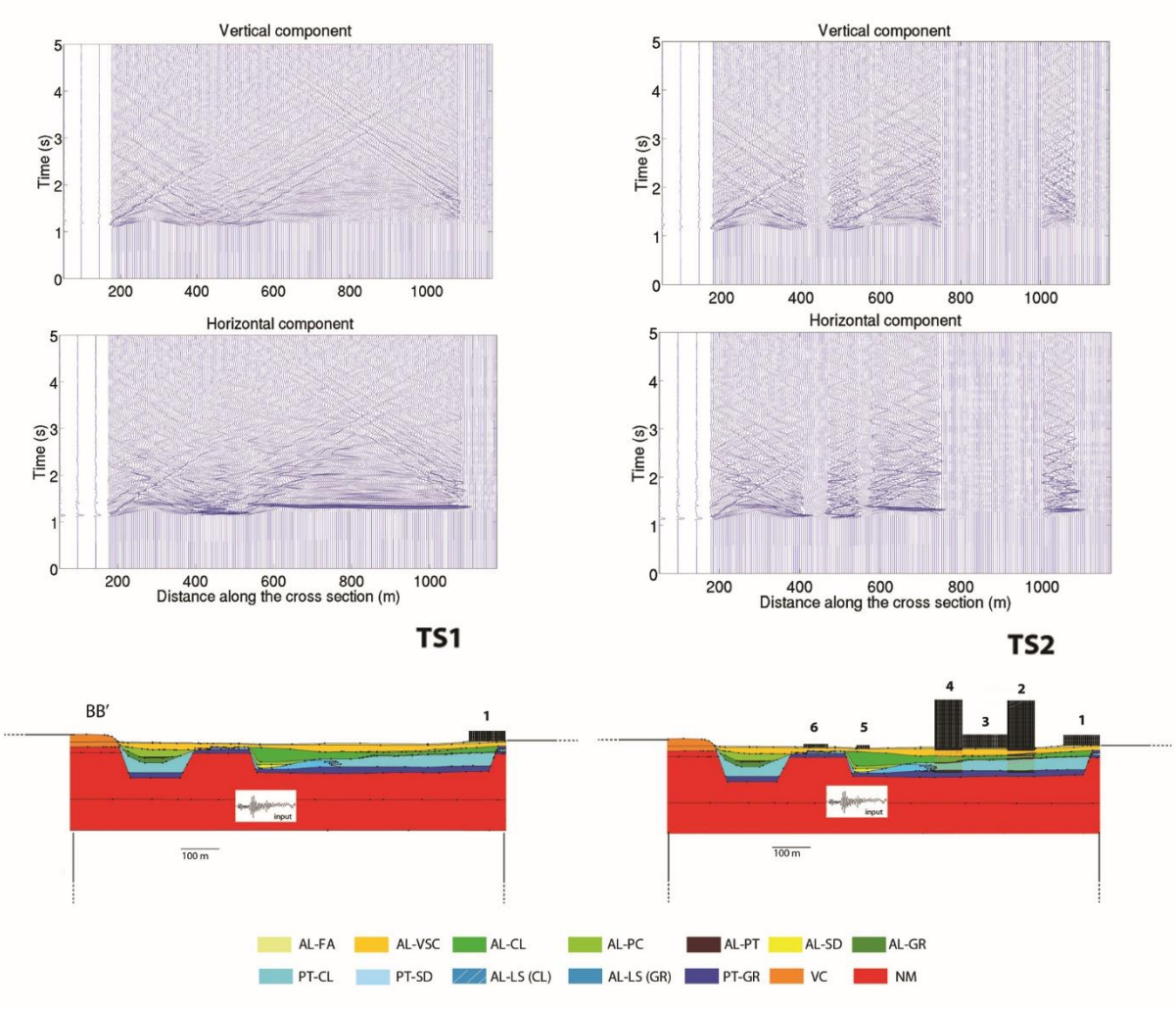

Fig. 6.13: Wave propagation maps of the vertical (top) and horizontal (middle) component of the displacement along the BB' coupled models surface. From left to right: BB'TS1, BB'-TS2, BB'-TS3. See description of building network page 61.

In particular, buildings with smaller volumes and masses (e.g., buildings 5-6 in the BB'-TS2 models) induced an additional amplification peak in the frequency range of 1.0-1.5 Hz. Buildings with larger volumes and masses (i.e., building 1 in the BB'-TS1 model and buildings 1-2-3-4 in the BB'-TS2 model) nullified the entire amplification functions. The presence of this additional peak was not directly caused by surface wave propagation; a time band analysis of the amplification function's distribution indicated that this peak was instantaneous and constant throughout the signal's duration. Conversely to the $A(f)_x$ distribution along the surface of the AA' coupled models (AA'-TS1, AA'-TS2, and AA'TS3 in Fig. 6.10), the buildings with small volumes and masses (e.g., buildings 5-6 in the BB'-TS2 model) and those with larger volumes and masses (e.g., building 1 in the BB'-TS1 model and buildings 1-2-3-4 in the BB'-TS2 model) exhibited the same phenomena in the BB' coupled models (BB'-TS1 and BB'-TS3) in terms of both the wave propagation and $A(f)_x$ distribution. The

portions of the valley that lacked buildings exhibited an increasing number of amplification peaks and a greater related amplification level.

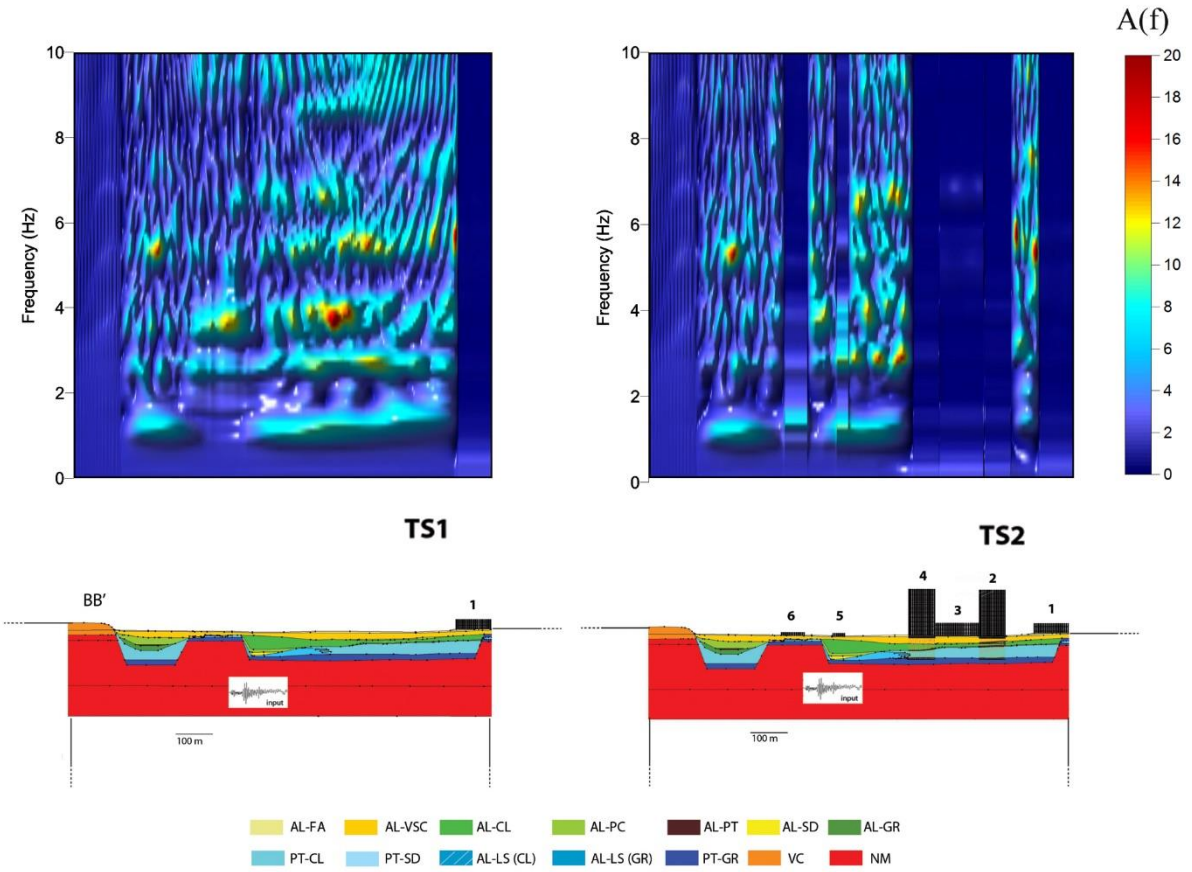

Fig. 6.14: Contour maps of the $A(f)_x$ functions distribution (top) along the BB' coupled models surface (bottom). From left to right: BB'-TS1, BB'-TS2. See description of building network page 61.

The variation in the *E(x)* values along the BB' coupled models' surfaces (BB'-TS1 and B'-TS2 in Fig. 6.14) showed a strong reduction in the energy close to the buildings and an increase in the *E(x)* index in the surrounding areas, which matched the results for the AA' coupled models (AA'-TS1, AA'-TS2, and AA'-TS3 in Fig. 6.11). A strong reduction in the kinetic energy was observed in the vicinity of buildings with small volumes and masses (e.g., buildings 5-6 in the BB'-TS2 model). The energy was completely nullified in the portion of the valley with building 1 in the BB'-TS1 model and buildings 1-2-4 in the BB'-TS2 model; these structures had large volumes and masses. The *E(x)* index increased in the surrounding areas and was larger in the BB'-TS1 model than in the BB'-TS2 model. Conversely to the AA' coupled models (AA'-TS1, AA'-TS2, and AA'-TS3 in Fig. 6.11), the progressive increase in urbanization redistributed the energy around the buildings, without any kinetic energy peaks. The maximum value of *E(x)* was 4400 J/m^3 in the central region of the BB'-TS1

coupled model, while the corresponding area under free-field conditions had a maximum value of 3737 J/m^3.

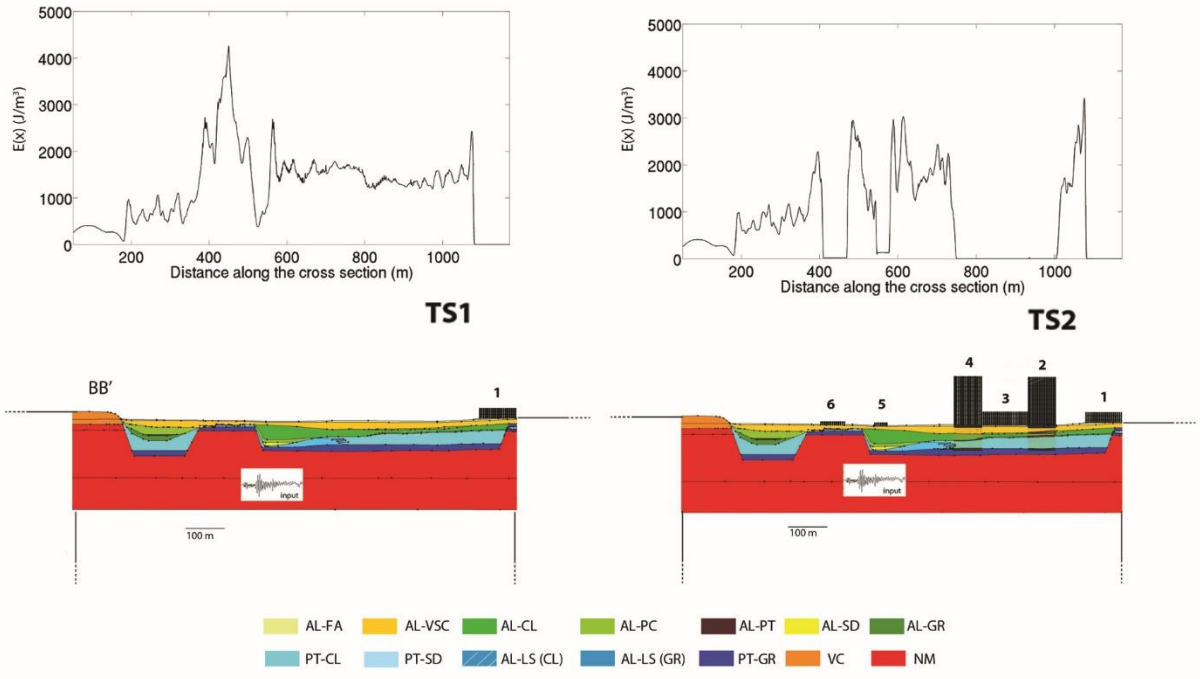

Fig. 6.15: Variation of the kinetic energy E(x) index (top) along the BB' coupled models surface (bottom). From left to right: BB'-TS1, BB'-TS2. See description of building network page 61.

The transfer functions (TF) of the buildings in the BB' coupled models (BB'-TS1 and BB'-TS2 in Fig. 5.15) were derived to verify the correspondence between the fundamental frequency from modal analysis (§ 5.3.2) and the fundamental frequency of the structures in the coupled models. The TF analysis indicated that building 1 in the BB'-TS1 model and buildings 1-3-5-6 in the BB'-TS2 model were characterized by comparable vibrational behaviour to that in § 5.3.2. (e.g., in Fig. 6.16a). The TFs of buildings 2 and 4 in the BB'-TS2 model (e.g., in Fig. 6.16b) showed similar characteristic features as building 10 in the AA'-TS3 model (Fig. 6.12b).

In summary, the analysis of the total wave field highlighted two main phenomena in terms of the effects of SCI: i) the complete nullification of the ground motion, amplification values and kinetic energy close to buildings with large volumes and masses, and ii) the partial reduction of the aforementioned parameters close to buildings with smaller volumes and masses. The ground motion, amplification values and kinetic energy increased the areas surrounding the structures.

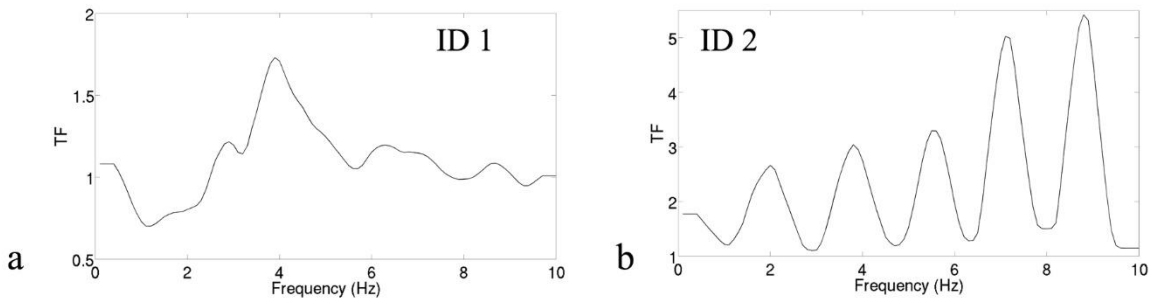

Fig. 6.16: Examples of the Transfer Functions (TF) of the buildings composing the BB' coupled models. a) Building 1 in BB'-TS2 b) Building 10 in BB'-TS2.

6.4 Analysis of the wave field when perturbed by the presence of buildings

The results in § 6.2 showed that the buildings strongly modified the physical parameters of the local seismic response (LSR) of the alluvial valley. The wave field when perturbed by the urban complex (U_P) was obtained according to relationship [15] to highlight the variation in the LSR from SCI.
The variation in the *E(x)* values of the perturbed wave field (U_P) along the AA' coupled models' surfaces (Fig. 6.17) highlights that the presence of buildings induces a strong redistribution on the kinetic energy along the basin. This phenomenon determines a focusing of the kinetic energy of the perturbed wave field in some portion of the valley characterized by complex geological setting (complex 2D seismic response) or by high number of buildings.

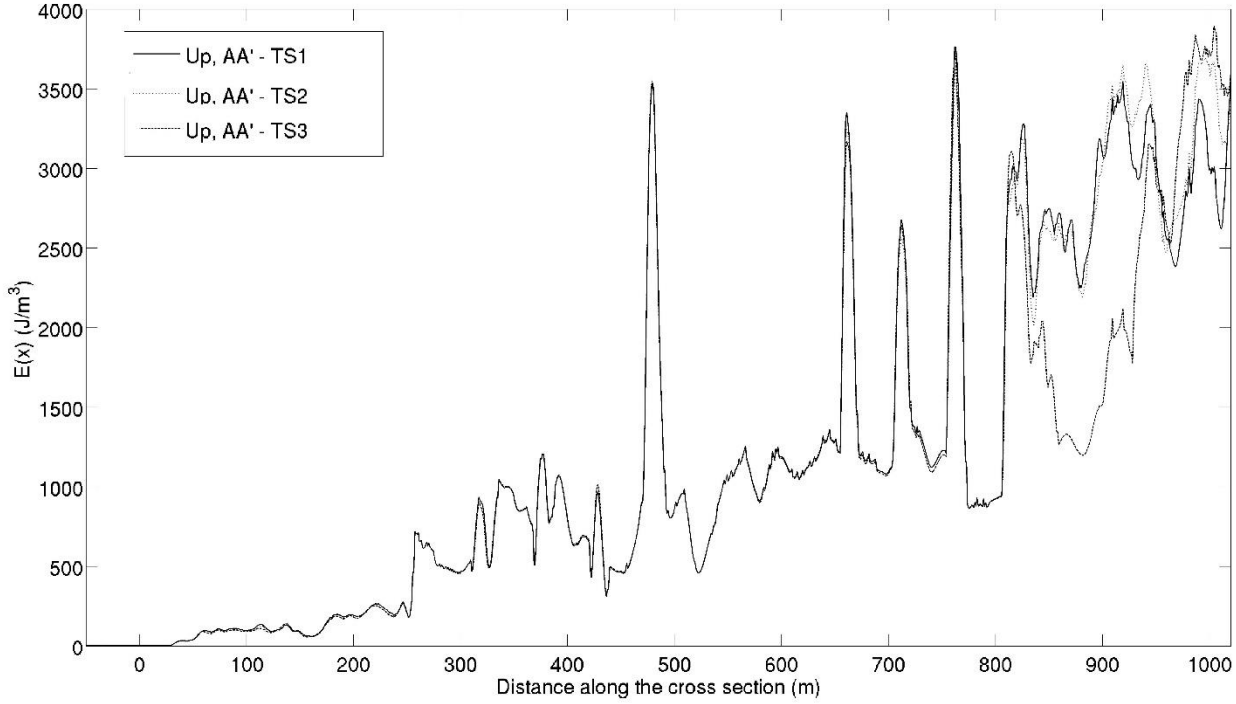

Fig. 6.17: Comparison between the variations of the kinetic energy E(x) of wave field *Up* perturbed by the progressive urbanization of the AA' coupled model.

An analysis of the U_P's propagation along the AA' coupled models (AA'-TS1, AA'-T2, and AA'-TS3 in Fig. 6.18) confirmed that the buildings changed the ground motion throughout the valley and not only close to the buildings, as apparently shown by the analysis of the wave propagation maps of the total field (AA'-TS1, AA'-T2, and AA'-TS3 in Fig. 6.9). Fig. 6.18 shows that the progressive increase in urbanization reduced the 2D effects because of the shape of the valley. This reduction was more visible along the horizontal component than along the vertical component according to the typologies of the applied input (see § 5.1).

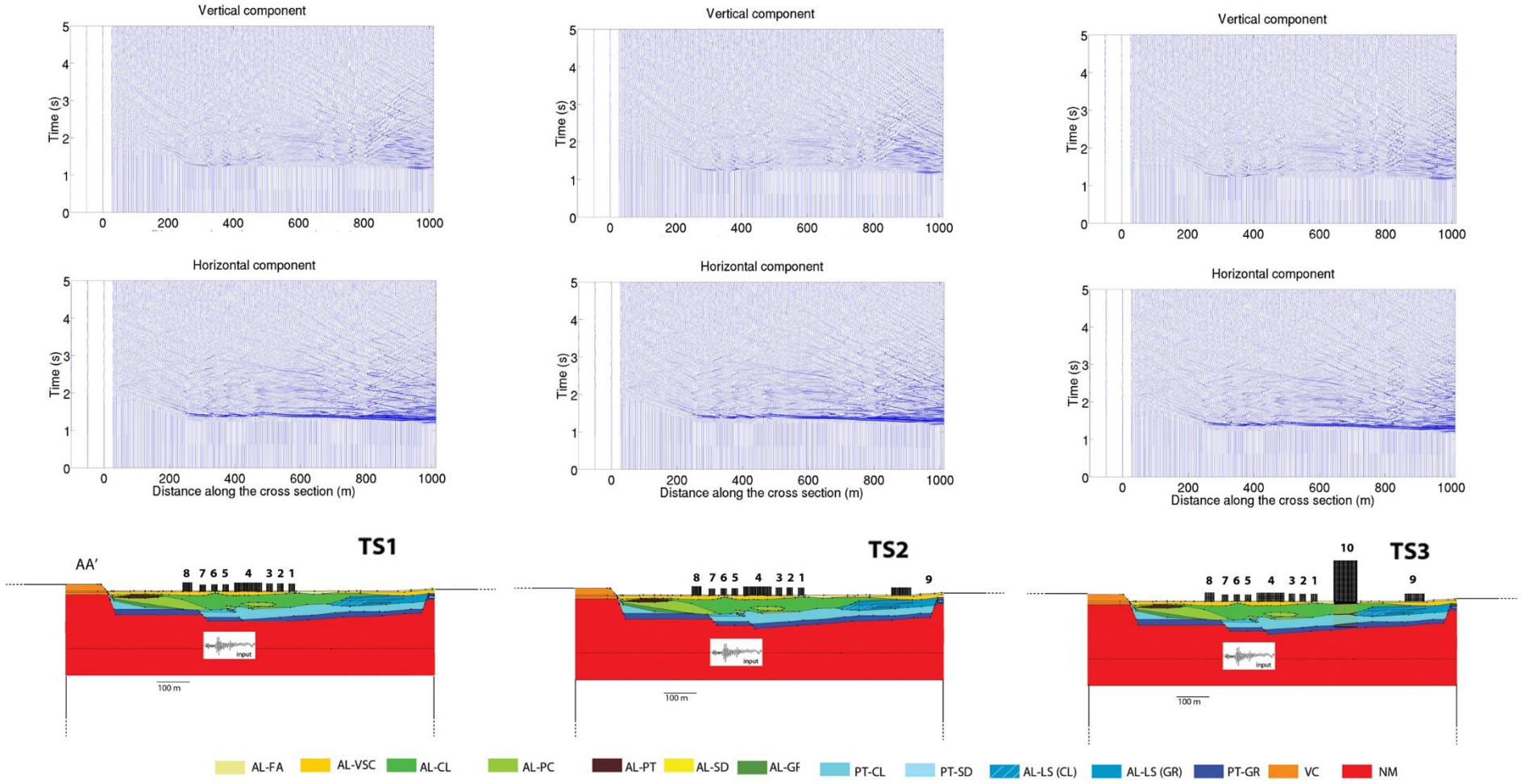

Fig. 6.18: Wave propagation maps of the vertical (top) and horizontal (middle) components of the perturbed wave field (in terms of displacement) along the surface of AA' coupled models: From left to right: AA'TS1, AA'-TS2, AA'-TS3. See description of building network page 61.

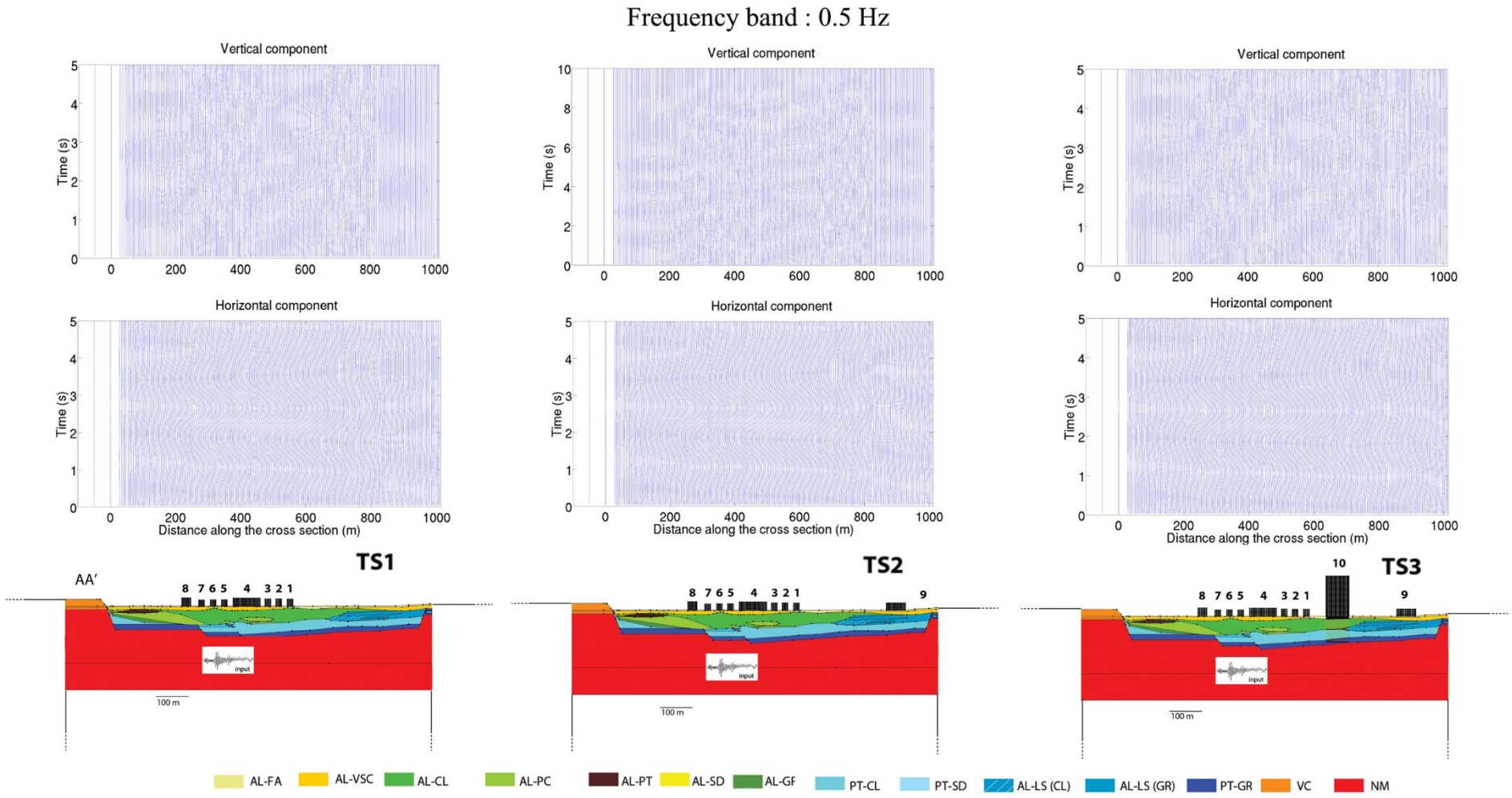

Fig. 6.19: Wave propagation maps of the vertical (top) and horizontal (middle) components of the perturbed wave field (in terms of displacement within the frequency band 0.25-0.75 Hz) along the surface of AA' coupled models: From left to right: AA'TS1, AA'-TS2, AA'-TS3. See description of building network page 61.

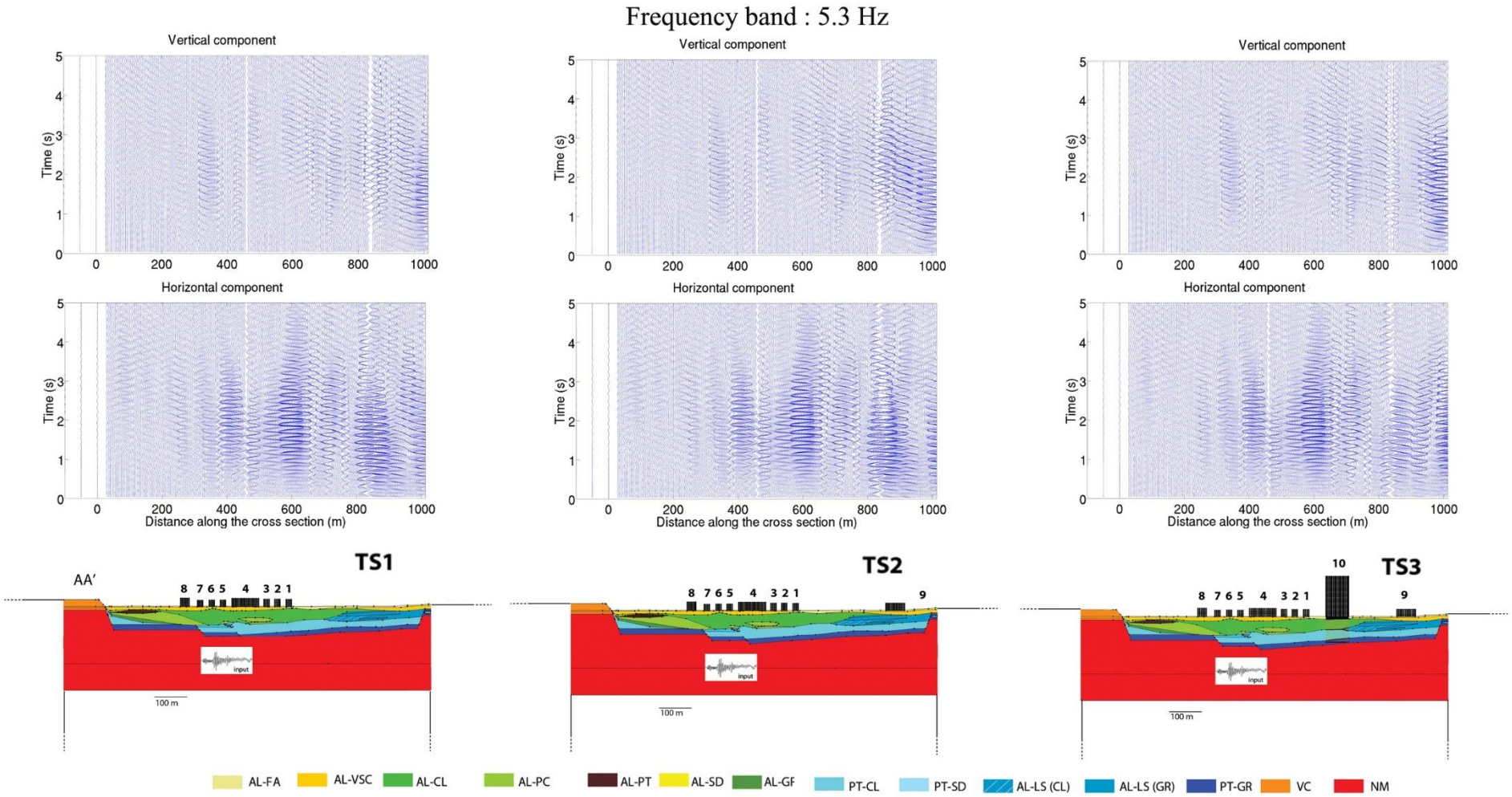

Fig. 6.20: Wave propagation maps of the vertical (top) and horizontal (middle) components of the perturbed wave field (in terms of displacement within the frequency band 5.05-5.55 Hz) along the surface of AA' coupled models: From left to right: AA'TS1, AA'-TS2, AA'-TS3. See description of building network page 61.

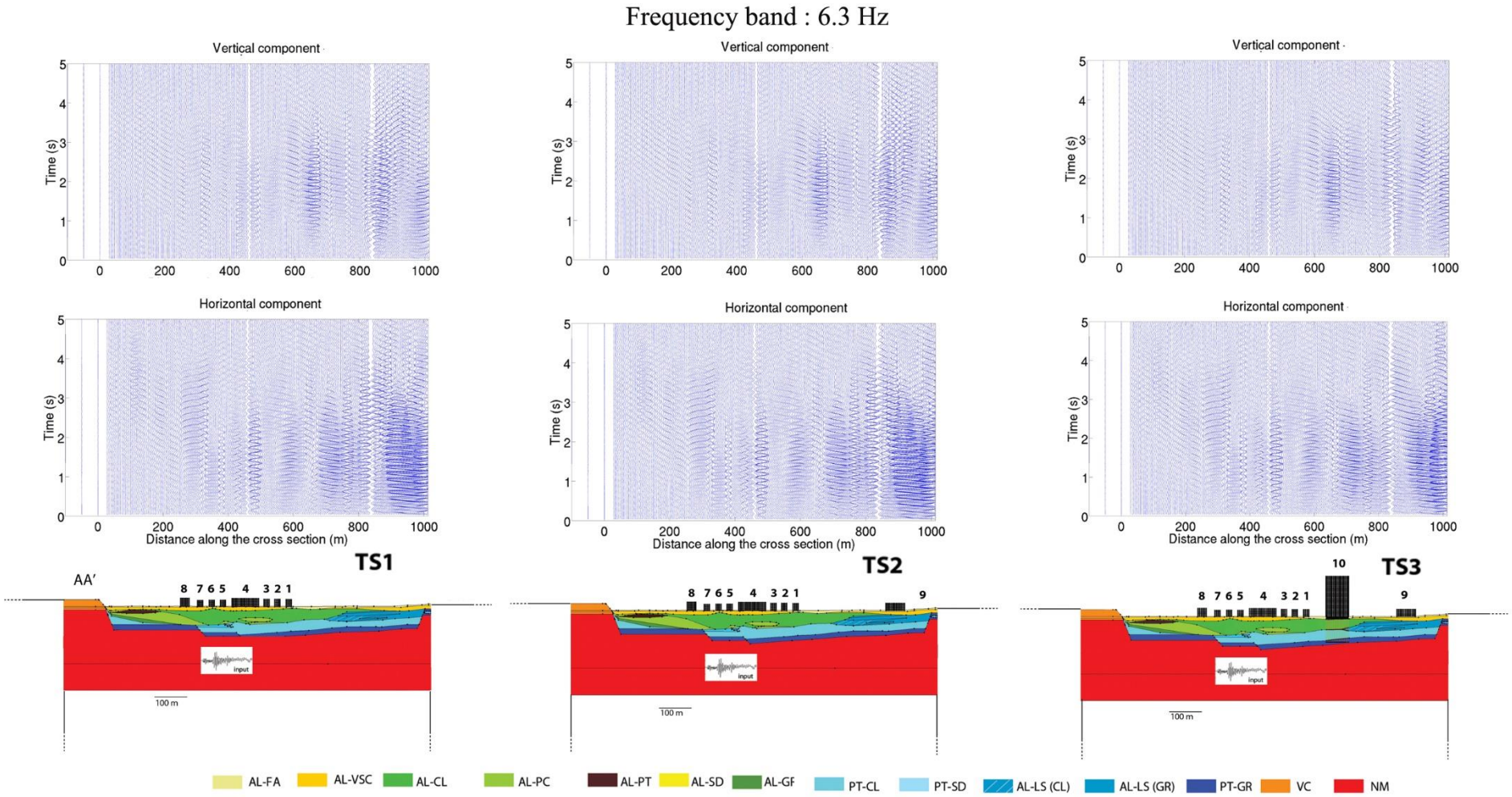

Fig. 6.21: Wave propagation maps of the vertical (top) and horizontal (middle) components of the perturbed wave field (in terms of displacement within the frequency band 6.05-6.55 Hz) along the surface of AA' coupled models: From left to right: AA'TS1, AA'-TS2, AA'-TS3. See description of building network page 61.

The frequency band of the perturbed wave field (U_P) was analysed to better understand the role of each building on the variation in the LSR from SCIs. A series of frequency bands that were centred on the fundamental frequencies of each building and characterized by a width of 0.5 Hz were defined and the corresponding U_P was obtained. The results that corresponded to the most significant frequency bands (0.5±0.25 Hz, 5.3±0.25 Hz, and 6.3±0.25 Hz) are reported in Fig. 6.19-6.20-6.21. According to Fig. 6.19, the influence of the buildings appeared to be very low, probably because the damping effect was larger, as mentioned in the analysis of the vibrational behaviour of building 10 (§ 6.2), which corresponded to the central frequency of the band.

An analysis of the U_p in the frequency bands of 5.3±0.25 Hz (Fig. 6.20) and 6.3±0.25 Hz (Fig. 6.21) confirmed that the buildings modified the ground motion throughout the valley and not only in their surroundings. The initial urbanization step (AA'-TS1 in Fig. 6.19) and the progressive increase in the number of buildings (AA'-TS2 and AA'-TS3 in Fig. 6.20 and Fig. 6.21) influenced the ground motion of the entire valley. In particular, some portions of the valley that did not host buildings were still influenced by the presence of the urban agglomerate in the surrounding areas for a given frequency band. At the same time, other free-field portions of the valley were less affected by the presence of buildings given a high number of buildings.

This consideration was also valid for the frequency band of 6.3±0.25 Hz (Fig. 6.21) on the fundamental frequency of building 9, which was included in the AA'-TS2 and AA'-TS3 models but not in the AA'-TS1 model. A frequency band analysis confirmed that the influence of the buildings was more visible along the horizontal component than along the vertical component of the ground motion according to the typologies of the applied input (see § 5.1).

The U_p that was perturbed by the presence of buildings in the BB' coupled models confirmed the results from the AA' coupled models and showed some peculiarities because of the peculiar geological setting of the model, which enables us to better understand this phenomenon.

The variation in the E(x) values of the perturbed wave field (UP) along the BB' coupled models' surfaces (Fig. 6.22) shows that the progressive urbanization induces a strong redistribution on the kinetic energy along the basin. More in particular it is clearly in Fig. 6.22 a focusing of the kinetic energy in portion of the valley characterize by complex seismic response.

Additionally, the presence of the urban complex determined the variation in the ground motion throughout the valley and not only near the buildings (BB'-TS1 and BB'-TS2 in Fig. 6.23). The progressive development of the urbanization reduced the 2D effects because of the shape of the valley. The presence of only one building on the right side of the model (building 1 in the BB'-TS1 model; Fig. 6.23) modified the ground motion throughout the valley, with a particular focus on the variation in the area with a complex geological setting, i.e., higher 2D effects. In particular, the presence of

building 1 in the BB'-TS1 model strongly reduced the 2D effects because of the presence of the buried tectonic structure in the central portion of the model. The reduction in the 2D effects from the shape of the valley and the heterogeneities of the alluvial deposits became more relevant with a higher number of buildings. Additionally, the variation in the ground motion in the BB' coupled models was more evident along the horizontal component than along the vertical component, as discussed above. Anyway, in the case of BB'-TS2 the vertical component of the displacement (Fig. 6.23 top) seem to be more sensitive in comparison with the results obtained for the same component in case of AA' models (Fig. 6.18 top). As proposed by Colombi et al. 2016, this phenomenon can be related to the partial conversion of the Rayleigh waves into S-waves directed into the interior of the soil by buildings 2 and 4 that are associable to a series of graded vertical array of resonators.

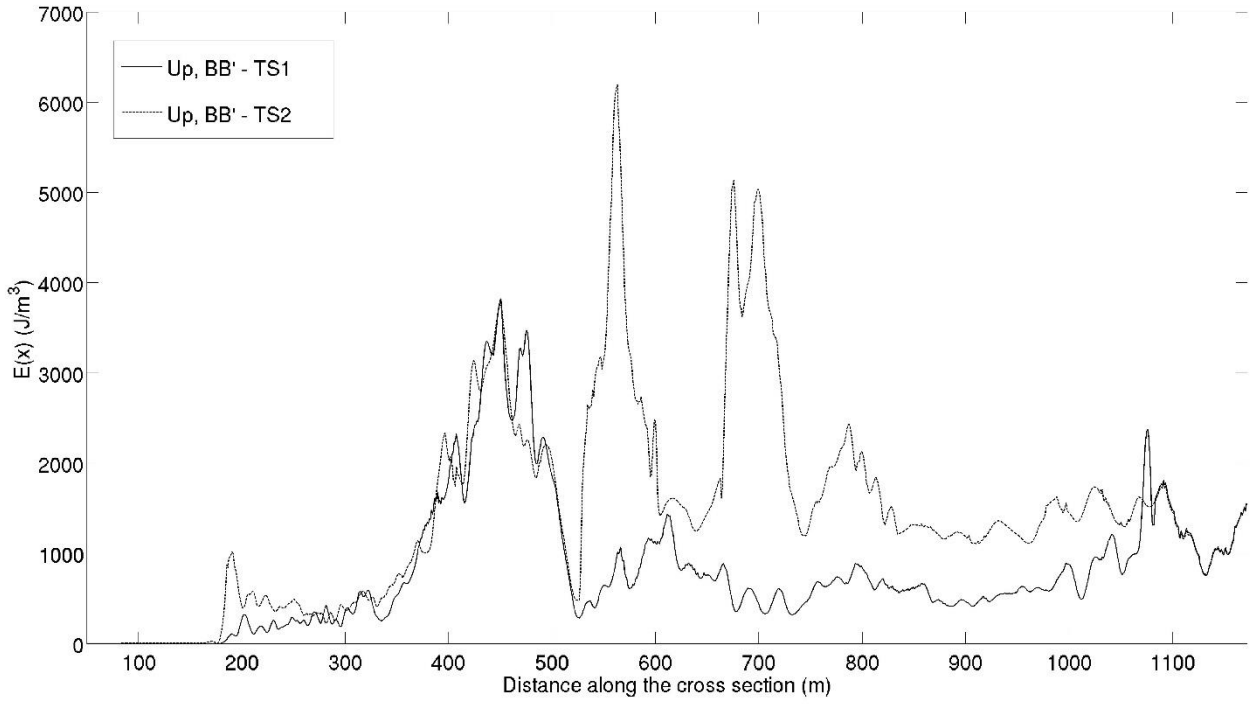

Fig. 6.22: Comparison between the variations of the kinetic energy E(x) of wave field *Up* perturbed by the progressive urbanization of the BB' coupled model.

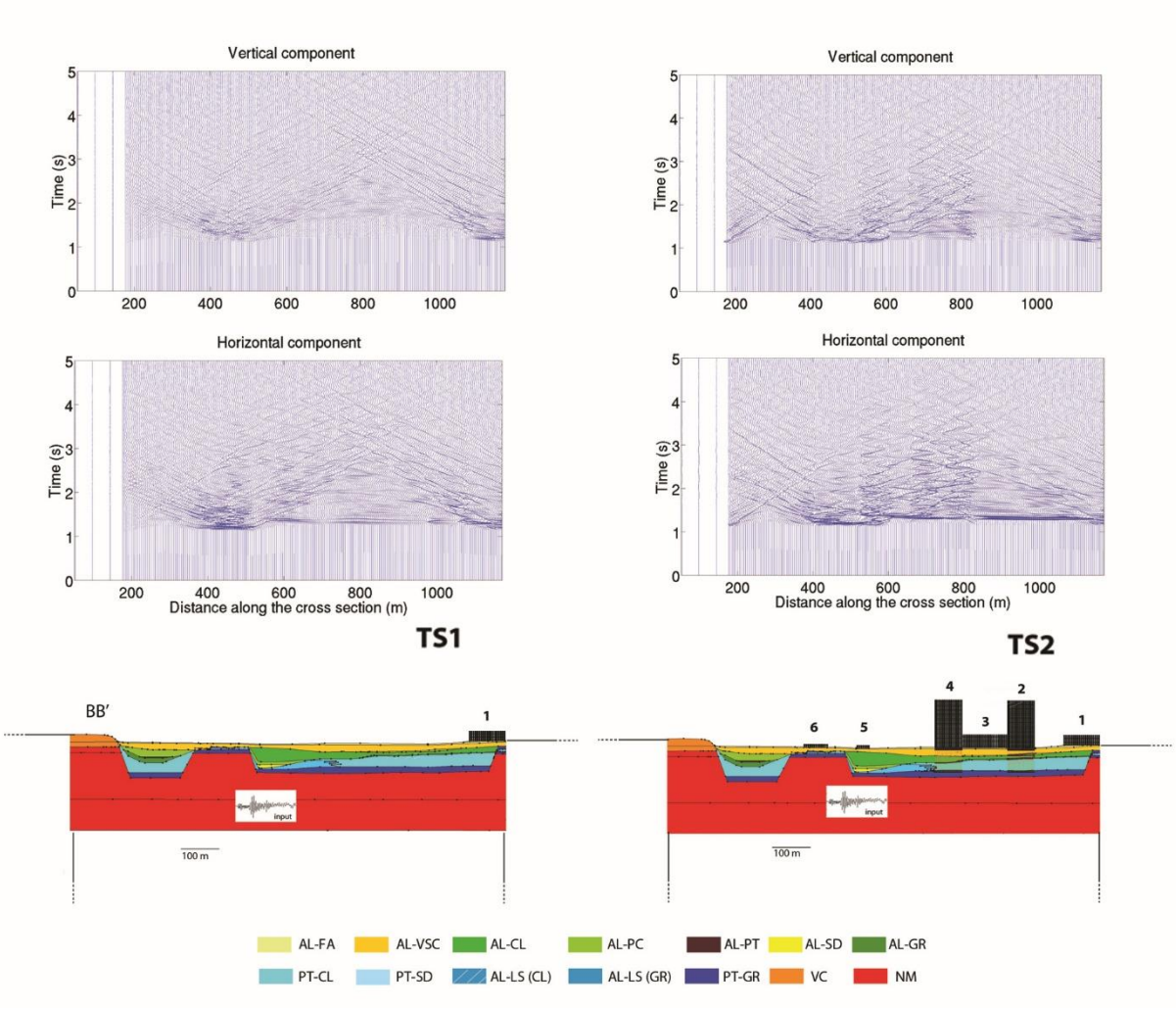

Fig. 6.23: Wave propagation maps of the vertical (top) and horizontal (middle) components of the perturbed wave field (in terms of displacement) along the surface of BB' coupled models: From left to right: BB'TS1, BB'-TS2. See description of building network page 61.

The frequency band of the perturbed wave field was analysed, and a series of frequency bands that were centred on the fundamental frequencies of each building and characterized by a width of 0.5 Hz were defined. Frequency bands of 0.5±0.25 and 3.8±0.25 Hz were considered to be the most significant in the BB' coupled models, and the corresponding wave propagation maps are reported in Fig. 6.24 and Fig. 6.25, respectively. Similarly to the AA' coupled models, the influence of the buildings for the frequency band of 0.5±0.25 Hz was very low in the BB' coupled models (Fig. 6.24) according to the damping effects. This result was confirmed by an analysis of the vibrational behaviour of buildings 2 and 4 (§ 6.2).

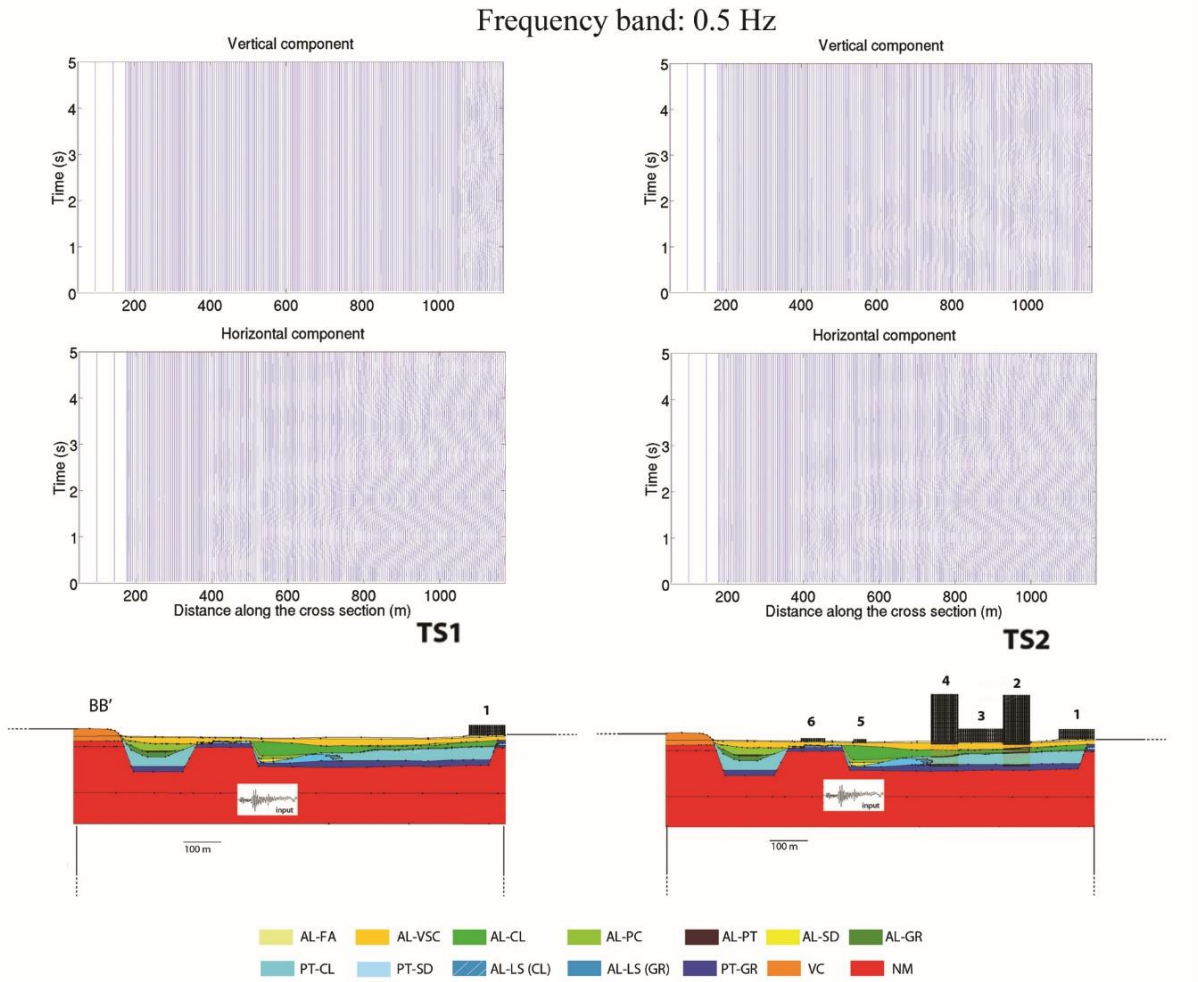

Fig. 6.24: Wave propagation maps of the vertical (top) and horizontal (middle) components of the perturbed wave field (in terms of displacement within the frequency band 0.25-0.75 Hz) along the surface of BB' coupled models: From left to right: BB'TS1, BB'-TS2. See description of building network page 61.

An analysis of the U_p in the frequency band of 3.8±0.25 Hz (Fig. 6.25) highlighted the influence of the buildings on the ground shaking, which differed from that in the AA' coupled models (Fig. 6.20-6.21). The effect of urbanization for the frequency band of 3.8±0.25 Hz (Fig. 6.25), which was centred on the fundamental frequency of building 4 in the BB'-TS2 model, was not characterized by the same spatial distribution in the BB'-TS1 and BB'-TS2 models. Conversely to the AA' case, the influence of the buildings in the BB'-TS2 model affected portions of the valley that were not affected in the BB'-TS1 model. This phenomenon may have been caused by the peculiar geological setting of the BB' model, in contrast to the simplest setting of the AA' model. The progressive increase in urban development increased the influence of SCI on the ground motions.

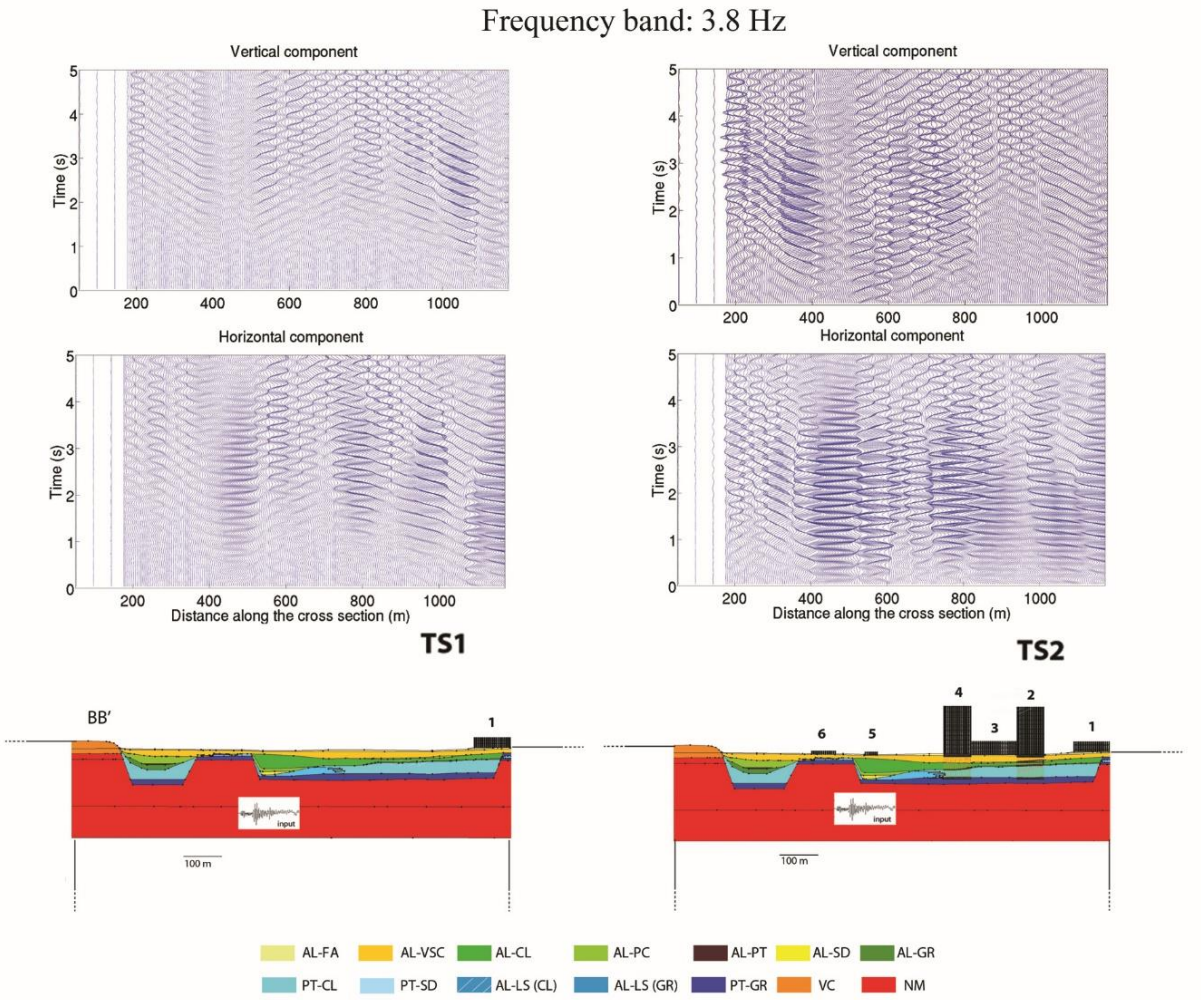

Fig. 6.25: Wave propagation maps of the vertical (top) and horizontal (middle) components of the perturbed wave field (in terms of displacement within the frequency band 3.55-4.05 Hz) along the surface of BB' coupled models: From left to right: BB'TS1, BB'-TS2. See description of building network page 61.

In summary, our analysis of the perturbed wave field indicated that the presence of buildings could influence the RSL of the entire valley and not only the areas close to the buildings. The effects of SCI reduced the 2D effects because of the shape of the valley and the heterogeneity of the alluvial deposits; this influence was more visible under a complex geological setting, i.e., complex RSL.

7. DISCUSSION

The results that were obtained when assuming free-field conditions (§ 6.1) highlighted the complex amplification phenomena that affected the case study area. These findings matched those of several studies that focused on the seismic response of Rome (Rovelli et al. 1994, 1995; Bozzano et al. 2008; Bozzano et al. 2012; Caserta et al. 2012; Martino et al. 2015).

This complexity of the amplification functions was determined by the presence of a large number of higher order modes and the non-homogeneous distribution of very high amplification levels. This feature could be related to the highly heterogeneous nature of the alluvial body, leading to strong 2D effects that were controlled by lateral heterogeneities (Martino et al., 2015) and the shape of the valley (basin effect, *sensu* Bard and Bouchon 1985). The area of the valley that was characterized by strong variations in the layer thickness played a fundamental role in the distribution of the amplification functions. This result matches that of Semblat et al. (2005), who noted that a high number of upper modes would characterize the amplification functions with the presence of strong lateral heterogeneities. These authors also highlighted that the presence of a highly heterogeneous geological setting, in terms of both vertical and horizontal heterogeneities, would increase the amplification levels compared to the ordinary amplification values that would be obtained for simplified geological models. Additionally, the analysis of the first amplification peak in the AA' and BB' models showed a non-homogeneously distributed frequency position of this peak along the portions of the valley with a similar stratigraphic setting. This phenomenon may have been related to the presence of vertical and horizontal heterogeneities within the alluvial body, creating a different initial amplification peak. However, as presented by Chávez-Garcia et al. (2002), this phenomenon may have also been related to the interactions of surface waves if any obvious amplification change could not be identified in the wave trains. In this case, we could not separate the contribution from each phenomenon to the non-homogeneous distribution of the frequency position of the first amplification peak. However, the analysis of the WPM (§ 6.1) suggested the predominant influence of the heterogeneities with respect to the surface waves at the frequency at which the first amplification peak was observed.

The here presented results suggest the strong role of 2D effects from both lateral heterogeneities (Martino et al. 2015) and the basin shape (Bard and Bouchon 1985) on the free-field local seismic response. The ratio between the 2D and 1D amplification functions was determined for both models to quantify the role of the aforementioned 2D effects, and the results are reported in Figs. 7.1 and 7.2. The two components of the ratio were the amplification functions from the numerical modelling of a series of 1D soil columns along the cross section and the 2D fully numerical modelling of the same cross section; both the 1D and 2D models were forced by EQ-12. This analysis of the 2D/1D ratio

revealed higher 2D amplification levels that the corresponding 1D levels along all the models' surfaces. The 2D amplification levels were up to 7 times higher than the corresponding 1D values, showing the strong role of 2D effects on the amplification phenomena within the Fosso di Vallerano valley.

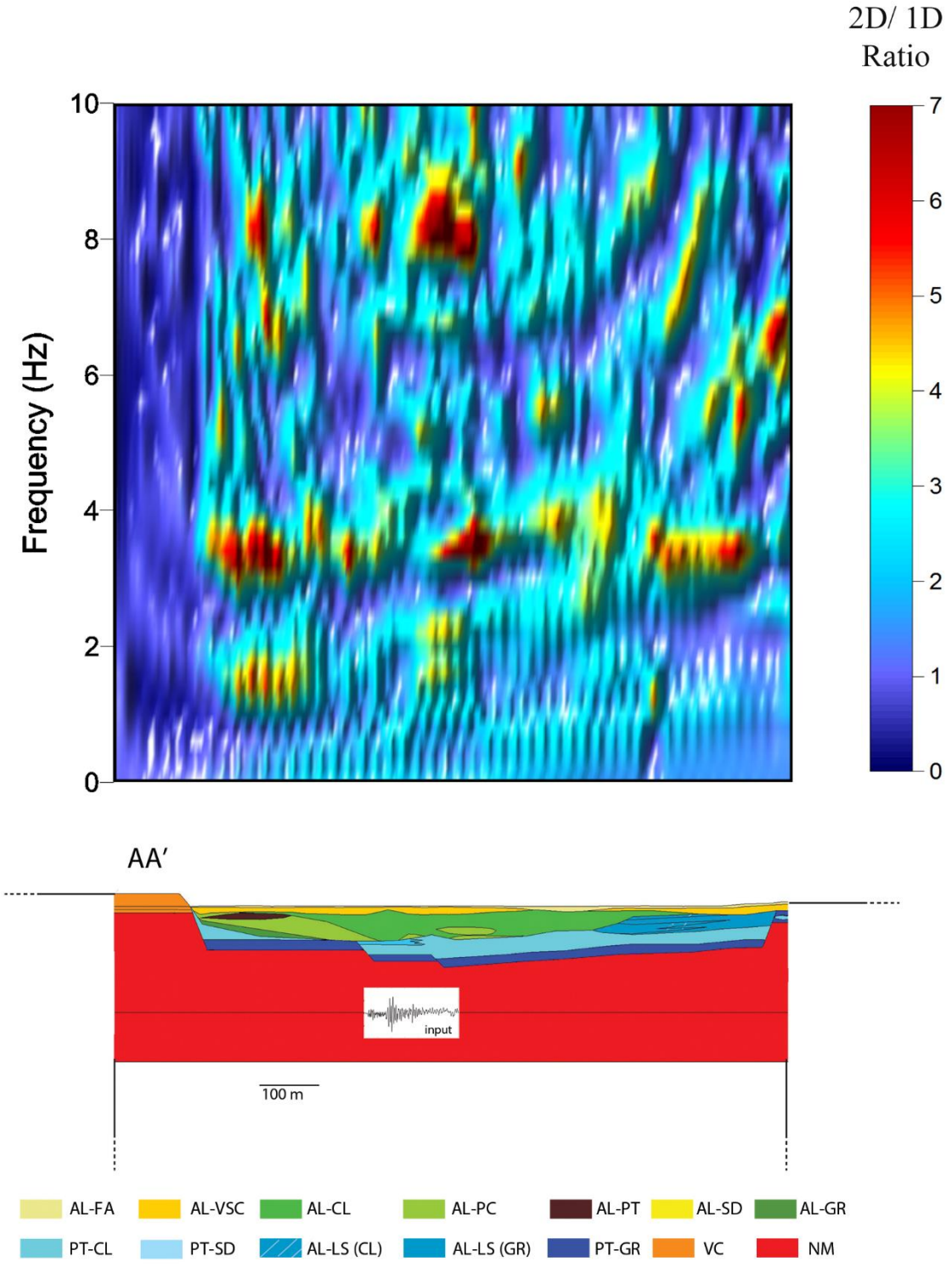

Fig. 7.1: Ratio between 2D amplification function and 1D amplification function along the surface of AA' model.

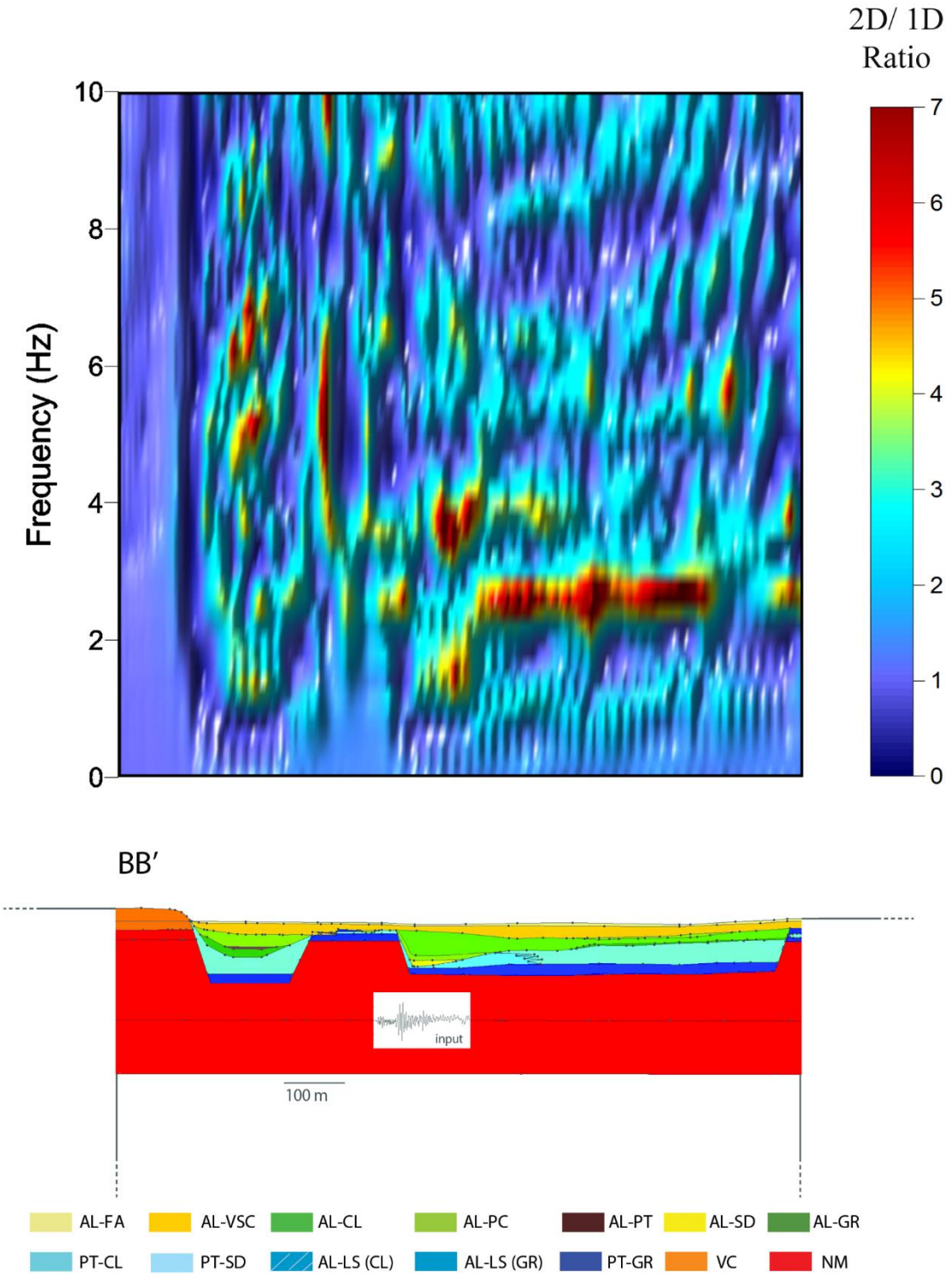

Fig. 7.2: Ratio between 2D amplification function and 1D amplification function along the surface of BB' model.

The results in § 6.2-6.3 showed that the buildings induced significant variations in the physical parameters of the ground motion because of strong site effects. A comparative analysis of the results was conducted to quantify the influence of the buildings on the free-field seismic response. The differences between the amplification functions when assuming SCI ($A(f)_{x\_SCI}$) and free-field conditions ($A(f)_{x\_f}$) were obtained to evaluate the influence of the city within the frequency domain, and an aggravation factor ($A_{ag}(f)_x$) was derived according to relationship [16]:

$$A_{ag}(f)_x = \frac{A(f)_{x\_SCI}}{A(f)_{x\_f}} \qquad [16]$$

The computed distribution $A_{ag}(f)_x$ of the aggravation factor was interpolated through a Kriging regression and synthetized in a contour map for each condition. The $A_{ag}(f)_x$ value varied from 0 to 5, assuming values lower than 1 when the free-field amplification was higher than that when assuming SCI conditions and values higher that 1 when the presence of buildings induced higher amplification levels than those when assuming free-field conditions.

The spatial distribution $A_{ag}(f)_x$ of the aggravation factor indicated that the presence of buildings, as already discussed in § 6, reduced most of the amplification peaks in the portions of the section that were occupied by structures, while the first amplification peak was incremented with respect to the free-field conditions (Figs. 7.3 and 7.4). This increase was not as relevant for buildings with larger volumes and masses as for buildings with smaller volumes and masses (2 times vs. 5 times) and was not visible from the analysis of the $A(f)_x$ distribution. The $A_{ag}(f)_x$ factor distribution indicated an increase in the amplification peaks close to the buildings (up to 5 times with respect to those under free-field conditions) (Figs. 7.3 and 7.4). The presence of buildings in the AA'-TS2 and AA'-TS1 models in Fig. 7.1 increased the amplification level (up to 1.5 times) in the vicinity of the seismic bedrock, while no increases were observed in the AA'-TS1 (Fig. 7.3), BB'-TS1 and BB'-TS2 models (Fig. 7.4).

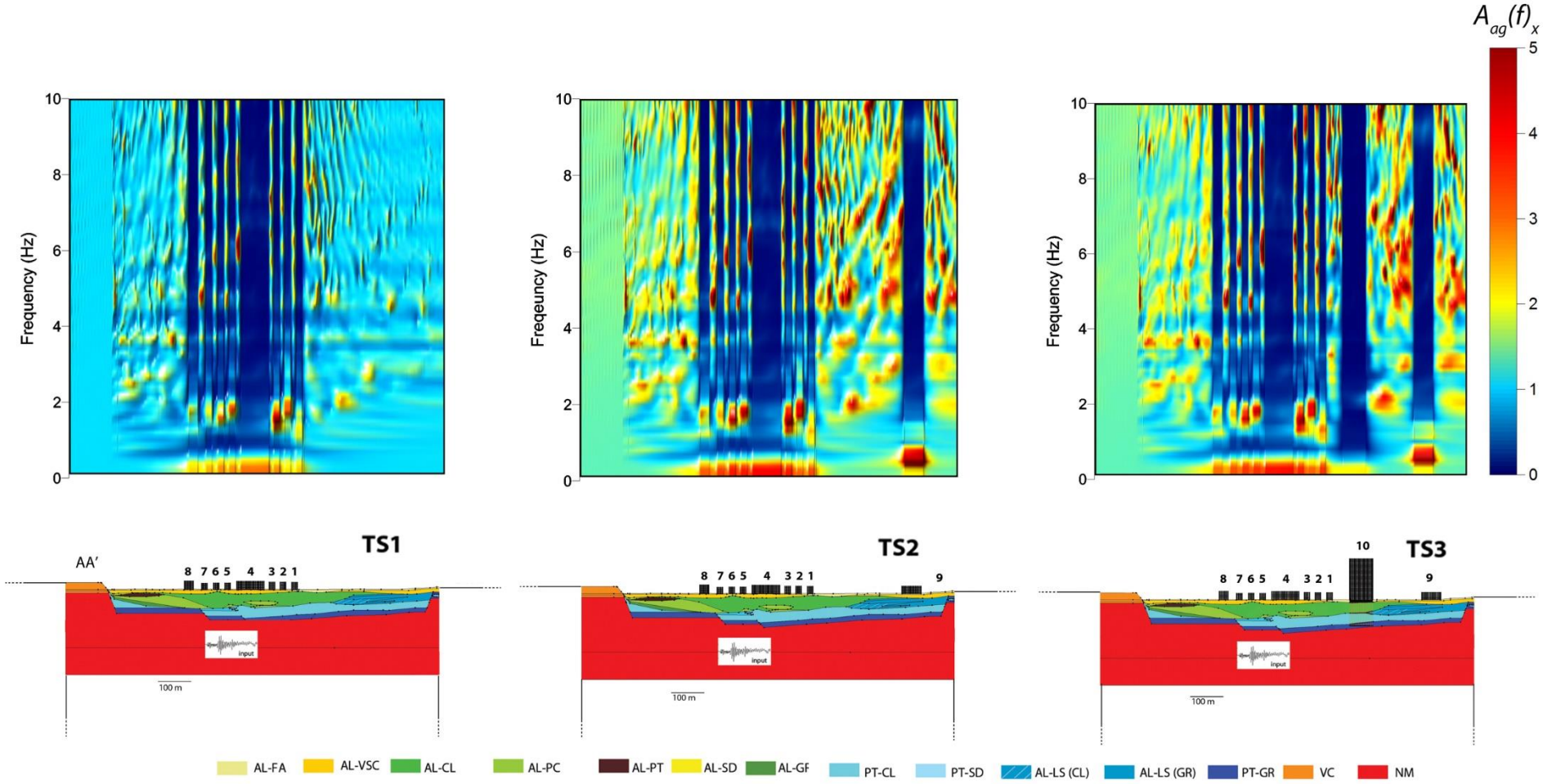

Fig. 7.3: $A_{ag}(f)_x$ distribution (top) along the surface of AA' coupled models. From left to right: AA'-TS1/AA', AA'-TS2/AA', AA'-TS3/AA'. See description of building network page 61.

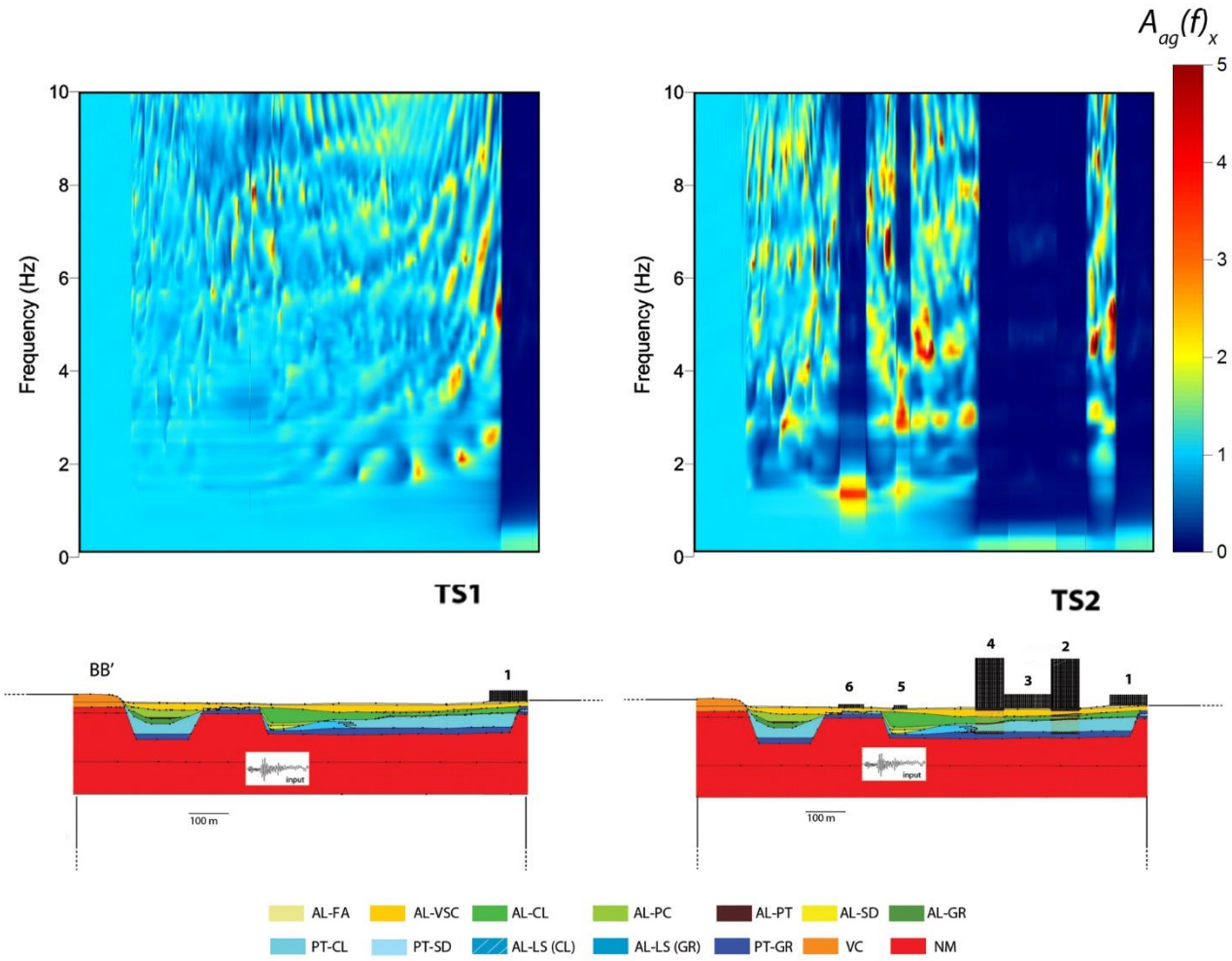

Fig. 7.4: $A_{ag}(f)_x$ distribution (top) along the surface of BB' coupled models. From left to right: BB'-TS1/BB', BB'-TS2/BB'. See description of building network page 61.

The non-homogenous variation in the amplification peaks (decrease or increase) showed no obvious dependence on the building typology, the city setting or the geological setting, which suggests combined effects from several phenomena.

This complexity in the amplification and de-amplification from SCIs was previously discussed by Guéguen et al. (2000). These authors highlighted that the ground motion amplification significantly increases or decreases according to the exact location of the buildings, their features and the site location because of the complexity of the wave field, which may generate constructive and destructive interferences. Additionally, many authors (Bard and Bouchon 1985; Bielak et al. 1999; Chammas et al. 2003, Sánchez-Sesma and Luzon 1995; Semblat et al. 2000, 2003, 2005) highlighted that surface waves may propagate across an entire city, suggesting a possible strong contribution from this type of wave to local site amplification. This contribution could be significant for highly heterogeneous alluvial sites, as in this case study.

An analysis of the obtained results suggested the possible generation of surface waves (Rayleigh waves because of the identical velocities of the horizontal and vertical components) that affected the models when assuming free-field conditions. The ratios between the *E(x)* distributions for the coupled models (AA'-TS1, AA'-TS2, and AA'-TS3 in Fig. 5.14 and BB'-TS1 and BB'-TS2 in Fig. 5.15) and the corresponding free-field models (AA' and BB' in Fig. 5.9) were computed to determine the influence of buildings on the kinetic energy along the ground surface.

The variation in the ratios along the surfaces of the models (Figs. 7.5 and 7.6) confirmed that the buildings strongly reduced the *E(x)* value, as already discussed in § 6.1. This reduction was large in the vicinity of buildings 4 and 9 in the AA'-TS2 model, buildings 4-9-10 in the AA'-TS3 model (Fig. 7.5), building 1 in the BB'-TS1 model and buildings 1-2-3-4 in the BB'-TS2 model (Fig. 7.6), confirming the results in § 6. This reduction in the kinetic energy matched the results by Kham et al. (2005). As highlighted by these authors, this reduction is controlled by two factors: the ratio between the soil and building frequencies (the closer these frequencies, the larger the reduction), and the building density (the greater the building density, the larger the decrease).

In our case study, the *E(x)* reduction was mostly controlled by the building density rather than by the frequency ratio because we could not define a clear relationship between the building frequencies and the *E(x)* reduction. The building type and the high urbanization of the area caused the SCIs to be controlled by an "inertial effect" rather than a soil-structure dynamic interaction, which was still present. This observation matches the results by Guéguen et al. (2002). These authors highlighted that the site-city effects are strengthened for cities with a large number of high-rise buildings, a high density of built surfaces and for which many buildings meet the frequency coincidence criterion. These conditions were confirmed by Semblat et al. (2009), who showed that the distribution of the ground energy can be very irregular in an irregular city and strongly depends on the city configuration and building type, suggesting a fundamental role of the "inertial effect" on SCI.

The areas that surrounded the buildings were characterized by an increase in the kinetic energy, which was larger in the BB' coupled models that in the AA' models. In particular, the *E(x)* index ratio reached 2.8 in the former, indicating a kinetic energy level that was 2.8 times higher than the corresponding energy under free-field conditions, while the ratio in the latter reached 2.2, indicating an energy level that was almost twice as high with respect to free-field conditions.

This kinetic energy increase was not homogenously distributed along the non-urbanized portions of the area and strongly increased in the eastern portion of the AA' coupled model and in the central portion of the BB' coupled model, i.e., the areas that were characterized by the most complex geological settings. This result suggests the control of vertical and horizontal heterogeneities on the seismic ground energy.

However, as presented by Semblat et al. (2006), a surface discontinuity in a city setting can determine an energy singularity. In this case, both phenomena may have contributed to the strong kinetic energy increase in the models, but we could not distinguish the role of each phenomenon. At the same time, the presence of deep foundations under some buildings, some of which reached the seismic bedrock, did not seem to influence the non-homogenous distribution of the kinetic energy. In particular, a numerical test without deep foundations was conducted to verify that the seismic ground energy was not influenced by deep foundations, which could theoretically transmit energy to the seismic bedrock and influence the energetic setting of the models.

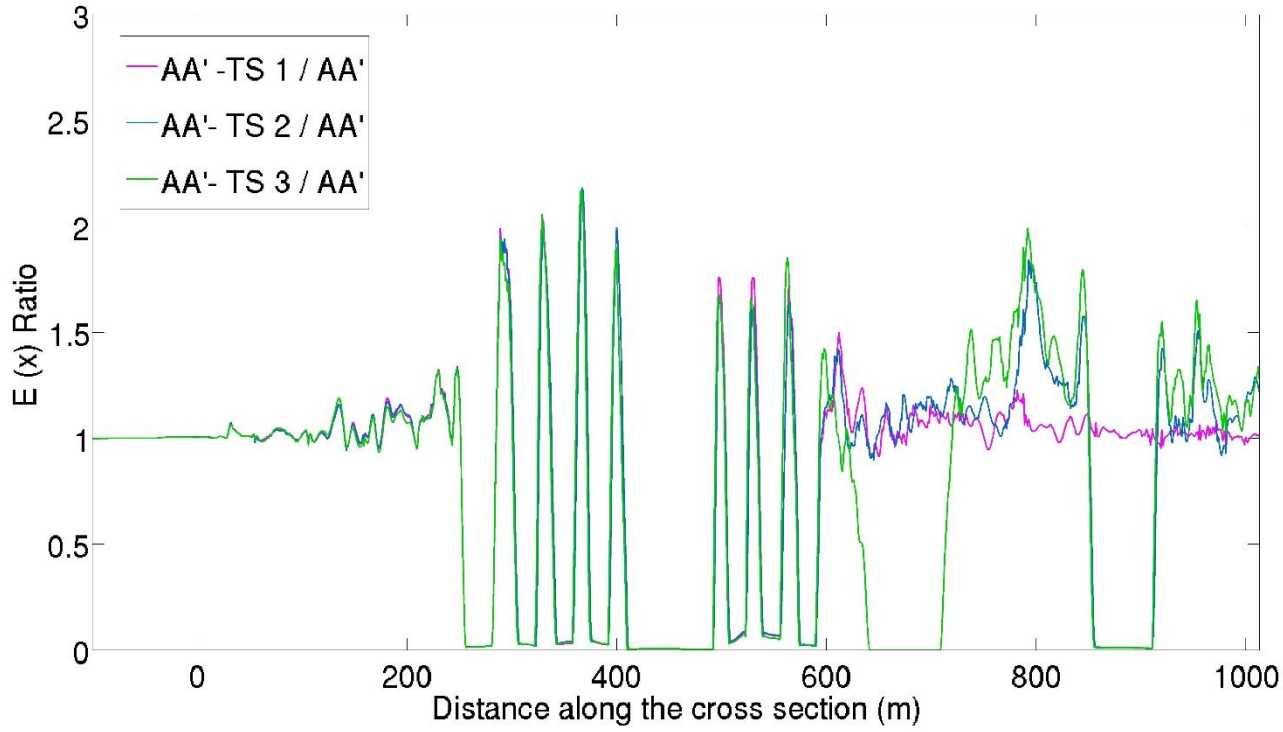

Fig. 7.5: Variation of the ratio between the kinetic energy E(x) index assuming SCI and free field condition along the AA' model surface.

This discussion of this study's results for a highly heterogeneous geological site further confirmed the findings by Guéguen et al. (2002, 2005), Kham et al. (2005) and Semblat et al. (2006). The influence of buildings on the seismic ground motion may not be a local phenomenon that is linked to a single building but instead should be considered at a global scale in densely urbanized areas.

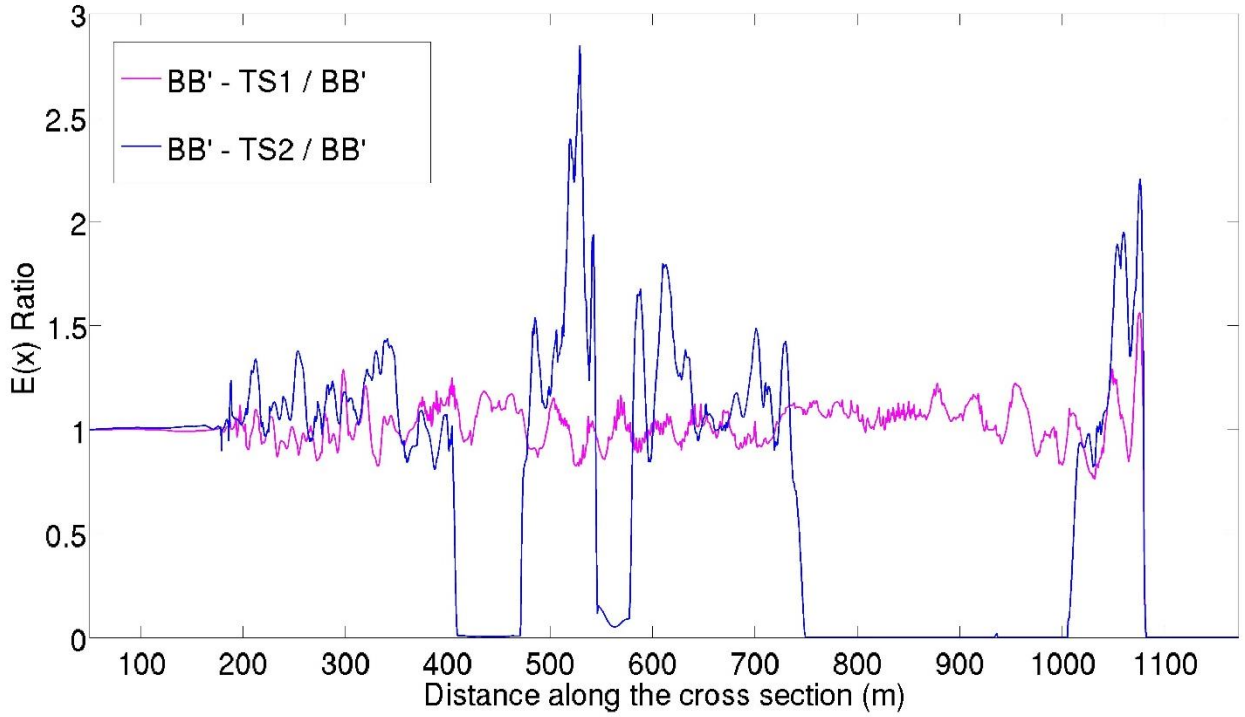

Fig. 7.6: Variation of the ratio between the kinetic energy E(x) index assuming SCI and free field condition along the BB' model surface.

8. CONCLUSIONS

This PhD research evaluated the effects of SCI by considering the geological and engineering components of highly heterogeneous geological systems. The Fosso di Vallerano valley (Rome, Italy) was selected as a case study because of its complex and heterogeneous geological setting. Moreover, this region is a recently urbanized district of Rome and hosts the "Europarco Business Park", which has the highest buildings in the city.

A high-resolution engineering-geological model of the study area that considered 1D and 2D effects was created to perform reliable simulations. The latter effects refer to both the shape of the valley (Bard and Bouchon 1985) and the presence of horizontal heterogeneities (Martino et al. 2015). A coupled analysis was performed by simulating buildings through high-resolution dynamic modelling. The main steps of the urban evolution were examined, and the results were analysed in terms of the main physical parameters of the ground motion according to the frequency bands (i.e., ground shaking, spatial distribution of the amplification functions and kinetic energy along the surface).

The main findings indicated a strong effect from the buildings on the theoretical free-field conditions, which significantly modified the wave field's characteristics.

In particular, the presence of buildings significantly reduced the kinetic energy of the ground motion and the seismic amplification close to the buildings, while these parameters increased in the surrounding areas.

Two different effects from SCI could be deduced: the first was caused by the presence of buildings with small volumes and masses, and the second was caused by the presence of buildings with large volumes and masses. Both kinematic and inertial interactions affected the SSI (Soil-Structure Interactions) and SCI, but we could not adequately distinguish these specific effects. The effect from the presence of buildings with large volumes and masses was probably caused by the predominance of inertial interactions with respect to kinematic interactions. This effect completely nullified the ground motion, amplification values and kinetic energy close to the buildings because of the inertial forces that were generated at the soil-foundation contact.

The presence of buildings with small volumes and masses, i.e., structures with lower inertia, increased the relevance of kinematic interactions with respect to the previous case. This effect did not completely reduce the aforementioned seismic parameters, probably because of soil deformation according to the RSL and the dynamic parameters of the deposits. In both types of interactions, the generated wave field may have affected the ground motion's characteristics along the free surface, increasing the amplification values and kinetic energy in the areas that surrounded the structures.

This study's numerical modelling was also performed to determine the possible role of SCI in heterogeneous alluvial deposits because this feature has rarely been discussed in previous studies. Although differences in the seismic response are evident in homogeneous and heterogeneous alluvial deposits, the performed numerical modelling could not distinguish the contributions from the buildings with respect to the single heterogeneity in the SCI. A parametric analysis that focuses on the positions of the buildings with respect to the valley (i.e., local heterogeneities) and the typology of the structures is recommended for future research. A non-linear numerical modelling of this system is also required to understand the behaviour of the system during strong earthquakes according to the typology of the alluvial soil in the Fosso di Vallerano valley.

Future projects may include 3D numerical simulations, which can consider the spatial variations in the valley and the building properties to evaluate the effects of SCI on the three components of ground motion. In this case, additional conditions that consider the azimuth of the incident motion and the directivity of the seismic waves within the valley could provide a more complete outcome of the expected effects.

The possible implications of this research include implementing an SCI approach into the new Technical standards for construction (NTC 2016) and seismic microzonation studies, in which free-field conditions are widely applied. This assumption produces non-negligible approximations, mainly for highly urbanized areas.

Moreover, an SCI-based approach to seismic risk reduction should improve urban resilience through reasonable city management, thus creating a "Resilient City" that can defend areas of social and cultural interest through aware urban planning of the surroundings.

ACKNOWLEDGEMENTS

I wish to thank everyone who has contributed to this PhD Research with significant support, proposals, critics and observations. I would firstly like to thank Prof. Salvatore Martino and Luca Lenti PhD for their support and guidance. This thesis would not have been happened without them. I would also like to acknowledge Prof. José Delgado Marchal and Prof. Philippe Guéguen for their review and useful suggestions to improve this manuscript.

I would like to thank Prof. Jean-François Semblat for all the valuable discussions, his helpful advisors and his review to this thesis and Benoit Peboscq for his help in the informatics framework. I would like to thank IFSTTAR (The French institute of science and technology for transport, development and networks) and LCPC (*Laboratoire Central des Ponts et Chaussées*) University Paris-Est for allowing the use of the CESAR – LCPC software for the PhD research and hosting me for my visiting research periods.

I wish to thank Prof. Francesca Bozzano and Prof. Gabriele Scarascia Mugnozza for their contribution to the development of the PhD research project.

I wish to thank Antonella Paciello, Guido Martini and Salomon Hailemikael (ENEA) for their support to the geophysical field surveys and Fabrizio Marra (INGV) for his contribution to the geological model construction. I would like to thank all “The Guys of the Cage”, Roberto Moriconi, Lorenzo Masci, Elisa Brizi, Luca Schilirò, Stefano Rivellino, Sebastian Martinez Araçena, Anna Claudia Vecchioni, Fabrizio Pelosi, Michele Carpinone, Youssef Abboud, and Abdul Karim Jamal Eddine for sharing the PhD research period with me.

Last, but not least, I would like to thank those around me for their time, patience, and encouragement. First and foremost, my parents and my brother, but also all my friends from all around the world.

Finally, I want to thank myself for never giving up.

REFERENCES

Alvarez W., Ammerman A.J., Renne P.R., Karner D.B., Terrenato N., Montanari A. (1996) - *Quaternary fluvial-volcanic stratigraphy and geochronology of the Capitoline hill in Rome.* Geology. 24: 751-754.

Ambrosetti P., Bonadonna F.P. (1967) - *Revisione dei dati sul Plio-Pleistocene di Roma*. Atti Accademia Gioenia di Scienze Naturali in Catania 18: 33-72.

Ambrosetti P., Azzaroli A., Bonadonna F.P., Follieri M. (1972) - *A scheme of Pleistocene chronology for the Tyrrhenian side of Central Italy*. Boll. Soc. Geol. It. 91: 169-184.

Arias A. (1970) - *A Measure of Earthquake Intensity*. R.J. Hansen, ed. Seismic Design for Nuclear Power Plants, MIT Press, Cambridge, Massachusetts, 438-483.

Ascani F., Bozzano F., Buccellato A., Del Monte M., Matteucci R., Vergari F. (2008) - *Evoluzione del paesaggio e antiche vie di drenaggio nell'area de "Il Castellaccio" (Roma) da indagini geologiche, geomorfologiche e archeologiche*. In Geologica Romana 41:55-77.

Bard P.Y., Bouchon M. (1980) - *The seismic response of sediment filled valley, part-I: the case of incident of SH waves*. Bull Seismol Soc Am 70:1263–1286

Bard P.-Y., Bouchon M. (1985) - *The two dimensional resonance of sediment filled valleys*. Bull. Seism. Soc. Am. 75: 519–541.

Bard P.Y., Chazelas J.L., Gue´guen P., Kham M., Semblat J.F. (2005) - *Site–city interaction. Chapter 5 of the book ''assessing and managing earthquake risk (geo-scientific and engineering knowledge for earthquake risk mitigation: developments, tools and techniques)'',* Oliveira CS, Roca A, Goula X Editors, Springer (new book series on geotechnical, geological and earthquake engineering). Hardcover. ISBN: 1-4020-3524-1:91-114.

Bardet J.P., Ichii K., Lin C.H. (2000) - *EERA. A computer program for Equivalent-linear Earthquake site Response Analyses of layered soil deposits.* University of Southern California, Department of Civil Engineering, user's manual

Baron M. (2002) - *Do we need smart cities for resilience.* Journal of Economics & Management. 10: 31- 46.

Basili R., Bosi C. (1996) - *Morfo-litostratigrafia dell'area romana in sinistra Tevere.* Il Quaternario 9: 273-280

Bellotti P., Chiocchini U., Castorina F., Tolomeo L. (1994) - *Le unità clastiche Plio-pleistoceniche tra Monte Mario e la costa tirrenica.* In Bollettino della Società Geologica Italiana, 113: 3-24.

Bielak, J., Xu J., Ghattas O. (1999) - *Earthquake ground motion and structural response in alluvial valleys.* J. Geotech. Geoenviron. Eng. 125: 413–423.

Boari E., Avanzinelli R., Melluso L., Giordano G., Mattei M., De Benedetti A., Morra V., Conticelli S. (2009) - *Isotope geochemistry (Sr-Nd-Pb) and petrogenesis of leucite-bearing volcanic rocks frm "Colli Albani" volcano, Roman Magmatic Province, Central Italy: inferences on volcano evolution and magma genesid.* Bulletin of Volcanology 71: 977-1005.

Booth D.B., Wells R.E., Givler R.W. (2004) - *Chimney damage in the greater Seattle area from the Nisqually earthquake of 28 February 2001.* Bull Seismol Soc Am 94:1143–1158.

Borchedt R. D., (1970) - *Effects of local geology on ground motion near San Francisco Bay.* Bull. Seism. Soc. Am. 60, 29–61.

Borcherdt R.D., (1994) - *Estimantes of site-dependent response spectra for design (methodology and* justification) Earthq. Spectra 10: 617-653.

Bordoni P. Valensise G. (1998) - *Deformation of the 125 ka marine terrace in Italy: Tectonic implications, in: I. S. Stewart, (Ed.) Coastal Tectonics.* Geol. Soc. Spec. Pub., 146: 71-110.

Boutin C., Roussillon P. (2004) - *Assessment of the urbanization effect on seismic response.* Bull. Seism. Soc. Am., 94(1): 251-268.

Bozzano F., Andreucci A., Gaeta M., Salucci R. (2000) - *A geological model of the buried Tiber River valley beneath the historical centre of Rome.* Bull. Eng. Geol. Env. 59:1 - 21.

Bozzano F., Caserta A., Govoni A., Marra F., Martino S. (2008) - *Static and dynamic characterization of alluvial deposits in the Tiber River Valley: New data for assessing potential ground motion in the City of Rome.* Journal of Geophysical Research, 113, B01303.

Bozzano F., Martino S., Giacomi A.C., Lenti L., Martini G., Santisi D'Avila M.P. (2012) - *Numerical modeling of nonlinear dynamic shear strains in heterogeneous soils by 1D-3C finite difference SWAP*. Proc. 15 World Conference on Earthquake Engineering, 24-28 September 2012, Lisboa, paper 0427.

Bozzano F., Marra F., Martino S., Paciello A., Scarascia Mugnozza G., Varone C. (2015) - *The local seismic response of the Fosso di Vallerano valley (Rome, Italy) based on a high resolution geological model*. Rend. Online Soc. Geol. It. 35, 29-32.

Bozzano F., Lenti L., Marra F., Martino S., Paciello A., Scarascia Mugnozza G., Varone C. (2016) - *Seismic response of the geologically complex alluvial valley at the "Europarco Business Park" (Rome – Italy) through instrumental records and numerical modelling.* Italian Journal of Engineering Geology and Environment. 16(1), 37-55.

Campanella T.J. (2006) - *Urban Resilience and the Recovery of New Orleans.* Journal of the American Planning Association. 72(2)141-146.

Caserta A., Martino S., Bozzano F., Govoni A., Marra F. (2012) - *Dynamic properties of low velocity alluvial deposits influencing seismically-induced shear strains: the Grottaperfetta valley test-site (Rome,* Italy).Bull Earthquake Eng, 10:1133-1162.

Carminati E., Corda L., Mariotti G., Brandano M. (2007) - *Tectonic control on the architecture of a Miocene carbonate ramp in the Central Apennines (Italy): Insights from facies and backstripping* analyses. Sedimentary Geology 198: 233–253.

Chammas, R., Abraham O., Cote P., Pedersen H., Semblat J.F. (2003) - *Characterization of heterogeneous soils using surface waves: homogenization and numerical modelling.* Int. J. Geomech. (ASCE) 3(1): 55–63.

Chávez-García F., Raptakis D., Makra K., Pitilakis K. (2002) - *Site effects at Euroseistest—II. Results from 2D numerical modeling and comparison with observations.* Soil Dyn. Earthquake Eng.19:23-39.

Chávez-García F. J., Cárdenas-Soto M. (2002) - *The contribution of the built environment to the freefield ground motion in Mexico city*. Soil Dyn. Earthquake Eng. 22: 773–780.

Chazelas J.L., Guéguen P.H., Bard P.Y., Semblat J.F. (2003) - *Modeling of the site-city effect with centrifuge small scale model (instrumental techniques validation)* (in French), 6th National Conference on Earthquake Eng. (AFPS 2003), I, 245-252, Palaiseau, France.

Chaljub E., Moczo P., Tsuno S., Bard P.Y., Kristek J., Kaser M., Stupazzini M., Kristekova M. (2010) - *Quantitative comparison of four numerical predictions of 3D ground motion in the Grenoble Valley, France*. Bull Seismol Soc Am 100:1427–1455

Clouteau D., Aubry D. (2001) - *Modification of ground motion in dense urban areas*. J. Comput. Acoust., 6: 1659-1675.

Clouteau D., Ishizawa O., Mezher N. (2002) - *Seismic wave propagation in a random city*. 7th National Conf. on Earthquake Eng., Boston.

Colombi A., Colquitt D., Roux P., Guenneau S., Craster R.V. (2016). *A seismic metamaterial: The resonant metawedge.* Nature Scientific Report, 6: Article number: 27717. doi:10.1038/srep27717

Colombo C. (2012) – *Prefabbricato e in opera. 120 m in 24 mesi.* Il Nuovo Cantiere 6: 16-23 ISSN: 0029-6325.

Comfort L., Wisner B, Cutter R., Pulwarty K., Oliver-Smoth A., Wiener J., Fordham M., Peacock W., Krimgold F. (1999) - *Reframing disaster policy: the global evolution of vulnerable communities* Environmental Hazards. 1: 39–44.

Conato V., Esu D., Malatesta A., Zarlenga F. (1980) - *New data on the Pleistocene of Rome.* Quaternaria, 22: 131-176.

Conticelli S., Peccerillo A. (1992) - *Petrology and geochemistry of potassic and ultrapotassic volcanism in central Italy: petrogenesis and inferences on the evolution of the mantle sources.* Lithos 28: 221-240.

CPTI04 (2004) - *Catalogo parametrico dei Terremoti Italiani dal 217 a.C. al 2002*. INGV. Website http://emidius.mi.ingv.it/cPti04/

DBMI04 (2004) - *Database macrosismico Italiano*. INGV. Website http://emidius.mi.ingv.it/Dbmi04

De Rita D., Funiciello R., Parotto M. (1988) - *Geological Map of the Colli Albani Volcanic Complex.* Progetto Finalizzato Geodinamica C.N.R., Rome, Italy.

De Rita D., Di Filippo M., Rosa C. (1996) - *Structural evolution of the Bracciano volcano-tectonic depression, Sabatini Volcanic District, Italy. In: McGuire, W.J., Jones, A.P., Neuberg, J. (Eds): Volcano Instability on the Earth and Other Planets.* Geological Society of London Special Publication 110: 225-236.

DISS Working Group (2015) - *Database of Individual Seismogenic Sources (DISS), Version 3.2.0: A compilation of potential sources for earthquakes larger than M 5.5 in Italy and surrounding areas*. http://diss.rm.ingv.it/diss/, © INGV 2015 - Istituto Nazionale di Geofisica e Vulcanologia - All rights reserved; DOI:10.6092/INGV.IT-DISS3.2.0.

Ditommaso R., Mucciarelli M., Gallipoli M.R, Ponzo F.C. (2010) - *Effect of a single vibrating building on free-field ground motion: numerical and experimental evidences.* Bull Earthquake Eng 8(3): 693-703

Dobry R, Vucetic M (1987) - *Dynamic property and seismic response of soft clay deposits*. In: Proceedings of international symposium on geotechnical engineering of soft soil. Mexico City, 51–87

Drobniak A. (2012) - *Exploring the Urban Resilience Concept.* Presentation Delivered at Regional Studies Association Research Network on Transition and Resilience for Post- Industrial Agglomerations in Central Europe Seminar, Katowice, 30th January 2012.

Florindo F., Karner D.B., Marra F., Renne P.R., Roberts A.P., Weaver R. (2007).- *Radioisotopic age constraints for Glacial Terminations IX and VII from aggradational sections of the Tiber River delta in Rome, Italy*. Earth and Planetary Science Letters 256: 61–80.

Fornaseri M., Scherillo A., Ventriglia U. (1963) - *La regione vulcanica dei Colli Albani: il Vulcano Laziale. Consiglio Nazionale delle Ricerche (C.N.R.)*. Rome, Italy, 561.

Freda C., Gaeta M., Karner D.B., Marra F., Renne P.R., Taddeucci J., Scarlato P., Christensen J.N., Dallai L. (2006) - *Eruptive history and petrologic evolution of the Albano multiple maar (Alban Hills, Central Italy)*. Bull. Volc, 68: 567-591, DOI 10.1007/s00445-005-0033-6.

Funiciello R., Giordano G. (2008) - *Note illustrative della Carta Geologica d'Italia*. Scala 1:50.000. Foglio n° 374 Roma

Gaeta M., Freda C., Christensen J.N., Dallai L., Marra F., Karner D.B., Scarlato P. (2006) - *Time-dependent geochemistry of clinopyroxene from the Alban Hills (Central Italy): Clues to the source and evolution of ultrapotassic magmas.* Lithos 86: 330-346.

Gallipoli M.R., Mucciarelli M., Castro R.R., Monachesi G., Contri P. (2004). - *Structure, soil-structure response and effects of damage based on observations of horizontal-to-vertical spectral ratios of microtremor*s, Soil Dyn. Earthq. Eng., 24: 487–495.

Gallipoli M.R., Mucciarelli M., Ponzo, F., Dolce M., D'Alema E., Maistrello M. (2006) - *Buildings as a seismic source: analysis of a release test at Bagnoli, Italy*. Bull. Seismol. Soc. Am., 96: 2457–2464.

Gao S., Liu H., Davis P.M., Knopoff G.L. (1996) - *Localized amplification of seismic waves and correlation with damage due to the Northridge earthquake.* Bull Seismol Soc Am 86:S209–S230.

Giaccio B., Marra F., Hajdas I., Karner D.B., Renne P.R., Sposato A. (2009) - *$^{40}Ar/^{39}Ar$ and ^{14}C geochronology of the Albano maar deposits: implications for defining the age and eruptive style of the most recent explosive activity at the Alban Hills Volcanic District, Italy.* Journ. of Volc. and Geoth. Res., 185(3):203-213. doi:10.1016/j.jvolgeores.2009.05.011

Giordano G., De Benedetti A.A., Diana A., Diano G., Gaudioso F., Marasco F., Micelli M., Mollo S., Cas R.A.F., Funiciello R. (2006) - *The Colli Albani caldera (Roma, Italy): Stratigraphy, structure and petrology.* Journal of Volcanology and Geothermal Research. 155 (1-2): 49-80.

Graves R.W., Pitarka A., Somerville P.G. (1998) - *Ground-motion amplification in the Santa Monica area: effect of shallow basin edge structure.* Bull Seismol Soc Am 88:1224–1242.

Guéguen P., Bard P.Y., Oliveira C.S. (2000) - *Experimental and numerical analysis of soil motions caused by free vibrations of a building model*. Bull. Seism. Soc. Am., 90(6): 2037-2043.

Guéguen P., Bard P.Y., Chávez-García F.J. (2002) - *Site-City Interaction in Mexico City-Like environments: An Analytical Study*. Bull. Seism. Soc. Am., 92(2): 794-811.

Gueguen P., Bard P.Y. (2005) - *Soil–structure and soil–structure–soil interaction: experimental evidence at the Volvi test site.* J Earthq Eng 9(5):657–693.

Hearty P.J., Dai-Pra G. (1986) - *Aminostratigraphy of Quaternary marine deposits in the Lazio region of central Italy, in: A. Ozer, C. Vita-Finzi (Eds.) Dating Mediterranean shorelines.* Zeitschrift fuer Geomorphologie, Supplementband, 62: 131-140.

Holling C.S., Schindler D.W., Walker B.W., Roughgarden J. (1995) - *Biodiversity in the functioning of ecosystems: an ecological synthesis.* In C. Perrings, K.G. Maler, C. Folke, C.S. Holling and B.O. Jansson (eds.) Biodiveristy loss: economic and ecological issues. Cambridge University Press, Cambridge. 44–83.

Horne J.F., Orr J.E. (1998) - *Assessing Behaviours that Create Resilient Organisations*. Employment Relations Today. 24(4): 29–39.

Humbert P., Fezans G., Dubouchet A., Remaund D. (2005) – *CESAR-LCPC: A computing software package dedicated to civil engineering uses.* Bullettin del Laboratoires des Ponts et Chaussée, 256/257: 7-37.

Kham M., Semblat J.F., Bard P., Dangla P. (2006) - *Seismic site-city interaction: main governing phenomena through simplified numerical models*. Bull. Seismol.Soc. America, 96(5): 1934-1951.

Kawase H. (1996) - *The cause of damage belt in Kobe: ''the basin-edge effect'', constructive interference of the direct S waves with the basin-induced diffracted/Rayleigh waves.* Seismol Res Lett 67:25–34.

Karner D.B., Marra F. (1998) - *Correlation of fluvio deltaic aggradational sections with glacial climate history: a revision of the classical Pleistocene stratigraphy of Rome.* Geol. Soc. Am. Bull., 110:748-758.

Karner D.B., Renne, P.R. (1998) - *$^{40}Ar/^{39}Ar$ geochronology of Roman province tephra in the Tiber River Valley: age calibration of Middle Pleistocene sea-level changes*. Geol. Soc. Amer. Bull. 110: 740–747.

Karner D. B., Marra F., Florindo F., Boschi E. (2001a) - *Pulsed uplift estimated from terrace elevations in the coast of Rome: evidence for a new phase of volcanic activity?* Earth Planet. Sci. Lett., 188: 135-148.

Karner D.B., Marra F., Renne P.R. (2001b) - *The history of the Monti Sabatini and Alban Hills volcanoes: groundwork for assessing volcanic-tectonic hazards for Rome.* J. Volc. And Geoth. Res., 107: 185-215.

Kawase H. (1993) - *Effects of surface and subsurface irregularities in earthquakes and ground motions.* Architectural Institute of Japan. Part I, Ch. 3, section 3.3: 118–155

Klein R.J.T, Nicholls R.J., Thomalla F. (2003) - *Resilience to natural hazards: How useful is this concept?* Environmental Hazards. 5: 35–45.

Lermo J.F., Francisco S., Chavez-Garcia J. (1993) - *Site effect avaluation using spectral rations with only one station.* Bull. Seismol. Soc. Am. 83:1574-1594.

Malinverno A., Ryan W.B.F. (1986) - *Extension in the Tyrrhenian sea and shortening in the Apennines as results of arc migration driven by sinking of the lithosphere*. Tectonics, 5: 227-245.

Marra F. (1993) - *Stratigrafia ed assetto geologico-strutturale dell'area romana tra il Tevere e il Rio Galeria.* In Geologica Romana, 29: 515-535.

Marra F., Rosa C. (1995) - *Stratigrafia ed assetto geologico dell'area romana. In: "La geologia di Roma. Il Centro Storico"*. A cura di R. Funiciello. Memorie Descrittive Della Carta Geologica d'Italia 50: 48 - 118.

Marra F., Carboni M.G., Di Bella L., Faccenna C., Funiciello R., Rosa C. (1995) - *Il substrato plio-pleistocenico nell'area romana*. Bollettino della Società Geologica Italiana, 114:195-214.

Marra F., Florindo F., Karner D.B. (1998) – *Paleomagnetism and geochronology of early Middle Pleistocene depositional sequence near Rome: comparison with the deep-sea* $\delta^{18}O$ *record* . Earth and Planetary Sc. Lett. 159: 147-164

Marra F., Freda C., Scarlato P., Taddeucci J., Karner D.B., Renne P.R., Gaeta M., Palladino D.M., Trigila R. Cavarretta G. (2003) - *Post-caldera activity in the Alban Hills Volcanic District (Italy):* $^{40}Ar/^{39}Ar$ *geochronology and insights into magma evolution*. Bull. Volc., 65:227-247.

Marra F., Florindo F., Boschi E. (2008) - *History of glacial terminations from the Tiber River, Rome: Insights into glacial forcing mechanisms.* Paleoceanography 23.

Marra F., Karner D.B., Freda C., Gaeta M., Renne P. (2009) - *Large mafic eruptions at Alban Hills Volcanic District (Central Italy): Chronostratigraphy, petrography and eruptive behavior*. Journal of Volcanology and Geothermal Research. 179(3-4): 217-232.

Marra F., Bozzano F., Cinti F.R. (2013) - *Chronostratigraphic and lithologic features of the Tiber River sediments (Rome, Italy): implications on the Post-glacial sea-level rise and Holocene climate.* Global and Planetary Change, doi.org/10.1016/j.gloplacha.2013.05.002.

Marra F., Deocampo D., Jackson M.D., Ventura G. (2014) - *The Alban Hills and Monti Sabatini volcanic products used in ancient Roman masonry (Italy): An integrated stratigraphic, archaeological, environmental and geochemical approach.* Earth Science Reviews, 108(3-4):115-136.

Marra F., Florindo F. (2014) - *The subsurface geology of Rome (Italy): sedimentary processes, sea-level changes and astronomical forcing*. Earth-Science Reviews, DOI:10.1016/j.earscirev.2014.05.001.

Martino S., Lenti L., Gelis C., Giacomi A.C., Santisi D'Avila P., Bonilla F., Bozzano F., Semblat J.F. (2015) - *Influence of lateral heterogeneities on strong motion shear strains: simulations in the historical center of Rome (Italy).* BSSA, 105(5):2604-2624.

Masotta M., Gaeta M., Gozzi F., Marra F., Palladino D.M., Sottili G. (2010) - *H_2O- and temperature-zoning in magma chambers: the example of the Tufo Giallo della Via Tiberina eruptions (Sabatini Volcanic District, central Italy).* Lithos 118: 119-130.

Mayena S.B. (2006) – *The concept of resilience revised.* Disasters, 30 (4): 433-450. ISSN 0361-3666

Milli S., Moscatelli M., Palombo M.R., Parlagreco L., Paciucci M. (2008) - *Incised valleys, their filling and mammal fossil record – A case study from Middle-Upper Pleistocene deposits of the Roman Basin (Latium, Italy)* (in Amorosi A., Haq B.U. & Sabato L., eds: Advances in Application of Sequence Stratigraphy in Italy). GeoActa (Special Publication), 1: 667-87.

Molin D., Ambrosini S., Castenetto S., Di Loreto E., Liperi L., Paciello A. (1986.) - *Aspetti della sismicita` storica di Roma.* Mem. Soc. Geol. It., 35: 439–448.

Narayan J.P. (2005) - *Study of basin-edge effects on the ground motion characteristics using 2.5-D modeling.* Pure Appl Geophys 162:273–289.

Narayan J.P. (2010) - *Effects of impedance contrast and soil thickness on the basin transduced Rayleigh waves and associated differential ground motion.* Pure Appl Geophys 167:1485–1510.

Narayan J.P. (2012) - *Effects of P-wave and S-wave impedance contrast on the characteristics of basin transduced Rayleigh waves.* Pure Appl Geophys 169:693–709.

Narayan J.P., Kumar V. (2012) - *Numerical study of effects of synclinal basement topography on ground motion characteristics* (Paper No. 3144). In: Proceedings of the 15th world conference on earthquake engineering (15WCEE) Lisbon, Portugal.

Narayan J.P., Kumar V. (2014a) - *P-SV wave time-domain finite-difference algorithm with realistic damping and a combined study of effects of sediment rheology and basement focusing.* Acta Geophys 62(3). doi:10.2478/s11600-013-0199-9

Narayan J.P., Kumar R. (2014b) - *Spatial spectral amplification of basin-transduced rayleigh waves.* Nat Hazards 71:751–765.

Ouyang M., Dueñas-Osorio L., Min X. (2012) - *A Three-Stage Resilience Analysis Framework for Urban Infrastructure Systems*. Structural Safety 36-37: 23-31.

Palladino D.M., Gaeta M., Marra F. (2001) - *A large k-foiditic hydromagmatic eruption from the early activity of the Alban Hills Volcanic District (Italy).* Bulletin of Volcanology 63: 345-359.

Paolucci R., Morstabilini L. (2006) - *Non-dimensional site amplification functions for basin edge effects on seismic ground motion.* In: 3rd International symposium on the effects of surface geology on seismic motion Grenoble, France, 30 August–1 September 2006.

Patacca E., Sartori R., Scandone P. (1990) - *Tyrrhenian basin and apenninic arcs: kinematic relations since late Tortonian times*. Mem. Soc. Geol. It., 45: 425-451.

Peccerillo A. (2005) - *Plio-Quaternary volcanism in Italy: Petrology, geochemistry, geodynamics.* Springer-Verlag, Berlin.

Pelling M. (2003) - *The Vulnerability of Cities: Natural Disasters and Social Resilience*. Earthscan, London.

Prestininzi A., Pugliese A., Romeo R.W. (2005) - *Proposed seismic classification of Italy and related actions*. Italian Journal of Engineering Geology and Environment, 05/1. DOI:10.4408/IJEGE.2005-01.O-04.

Ricker N. (1943) - *Further developments in the wavelet theory of seismogram structure.* Bull. Seismol. Soc. Am., 33 (3):197-228.

Ricker N. (1953) - *The form and law of propagation of seismic wavelet.* Geophysics, 18: 10-40.

Rovelli A, Caserta A, Malagnini L, Marra F. (1994) - *Assessment of potential strong motions in the city of Rome.* Ann. Geofisc. 37: 1745–1769.

Rovelli A, Malagnini L, Caserta A, Marra F. (1995) - *Using 1-D and 2- D modelling of ground* motion for seismic zonation criteria: Results for the city of Rome. Ann. Geofisc. 38: 591– 605.

Sánchez-Sesma, F. J., Luzon F. (1995) - *Seismic response of threedimensional alluvial valleys for incident P, S and Rayleigh waves.* Bull. Seism. Soc. Am. 85: 269–284.

Scarascia Mugnozza G. (2011) - *La pericolosità sismica nel Lazio: pericolosità sismica di base, analisi di risposta sismica locale e studi per la microzonazione sismica.* Università La Sapienza, 2011.

Semblat J.-F., Luong M.P. (1998) - *Wave propagation through soils in centrifuge experiments*. J. Earthquake Eng. 2(1): 147–171.

Semblat, J.-F., Duval A.M., Dangla P. (2000) - *Numerical analysis of seismic wave amplification in Nice (France) and comparisons with experiments.* Soil Dyn. Earthquake Eng. 19 (5):347–362.

Semblat, J. F., Paolucci R., Duval A.M. (2003) - *Simplified vibratory characterization of alluvial basins.* C. R. Geosci. 335(4): 365–370.

Semblat, J. F., Kham M., Parara E., Bard P.Y., Pitilakis K., Makra K., Raptakis D. (2005) - *Site effects: basin geometry vs soil layering.* Soil Dyn. Earthquake Eng. 25(7-10): 529–538.

Semblat J.F, Kham M., Bard P.Y, (2008) - *Seismic-Wave Propagation in Alluvial Basins and Influence of Site-City Interaction*. Bull. Seismol. Soc. Am. 98(6): 2665-2678.

Semblat J.F. and Pecker A. (2009) – *Waves and Vibrations in Soils: Earthquakes, Traffic, Shocks, Contruction works.* IUSS Press Istituto Universitario di Studi Superiori di Pavia.

Semblat J.F., Lokmane N., Driad-Lebeau L., Bonnet G. (2010) - *Local amplification of deep mining induced vibrations part 2: simulation of ground motion in a coal basin.* Soil Dyn Earthq Eng 30(10):947–95..

Semblat J.F., Lenti L., Gandomzadeh A. (2011) - *A simple multi-directional absorbing layer method to simulate elastic wave propagation in unbounded domains.* Int. J. Numer. Meth. Eng., 85: 1543-1563.

Sahar D., Narayan J.P, Kumar N. (2015) - *Study of role of basin shape in the site–city interaction effects on the ground motion characteristics.* Nat Hazards (2015) 75:1167–1186

Sottili G., Palladino D.M., Zanon V. (2004) - *Plinian activity during the early eruptive history of the Sabatini Volcanic District, Central Italy.* Journal of Volcanology and Geothermal Research 135: 361-379.

Sottili G., Palladino D.M., Marra F., Jicha B., Karner D.B., Renne P. (2010) - *Geochronology of the most recent activity in the Sabatini volcanic district, Roman Province, central Italy*. Journal of Volcanology and Geothermal Research 196(1-2):20-30.

Timoshenko S.P. (1921) - *On the correction factor for shear of the differential equation for transverse vibrations of bars of uniform cross-section*. Philosophical Magazine: 744.

Timoshenko S.P. (1922) - *On the transverse vibrations of bars of uniform cross-section*. Philosophical Magazin: 125.

Trigila R., Agosta E., Currado C., De Benedetti A.A., Freda C., Gaeta M., Palladino D.M., Rosa C. (1995) Petrology. In: Trigila, R. (Ed) - *The Volcano of the Alban Hills*. Università degli Studi di Roma "La Sapienza", Rome, Italy, 95-165.

Tsogka C., Wirgin A. (2003) - *Simulation of seismic response in an idealized city.* Soil Dyn. Earthquake Eng. 23: 391–402.

UNISDR (United Nations International Strategy for Disaster Risk Reduction) (2005) - *Hyogo Framework for 2005–2015: Building the Resilience of Nations and Communities to Disasters.*

Varone C., Lenti L., Martino S. (2014) - Engineering-geological and numerical modeling for the evaluation of the vibrational interaction between the city agglomerate and heterogeneous geological system: preliminary results. *Atti del 33° Convegno GNGTS, Bologna (Italy), v. 2 Caratterizzazione sismica del territorio.*

Ventriglia U. (2002) - *Geologia del territorio del Comune di Roma* a cura dell'amministazione Provinciale di Roma

Washington H.S. (1906) - *The Roman Comagmatic Region, Carnegie Institute*, Publ. no. 57 Washington.

Wildavsky A. (1991) - *Searching for Safety*. Transaction, New Brunswick, NJ.

Wirgin A., Bard P.Y. (1996) - *Effects of buildings on the duration and amplitude of ground motion in Mexico city*. Bull. Seism. Soc. Am., 86(3): 914-920.

Zafati E., Brun M., Djeran-Maigre I., Prunier F. (2016) - *Design of an efficient multi-directional explicit/implicit Rayleigh absorbing layer for seismic wave propagation in unbounded domain using a strong form formulation.* Int. J. Numer. Meth. Engng., 106:83–112.

Official web site of A.S Roma football team: **http://www.asroma.com**

Appendix

Results obtained assuming free field condition

Contour map of the $A(f)_x$ functions distribution (top) along the AA' model surface (bottom) forced by EQ-7 earthquake.

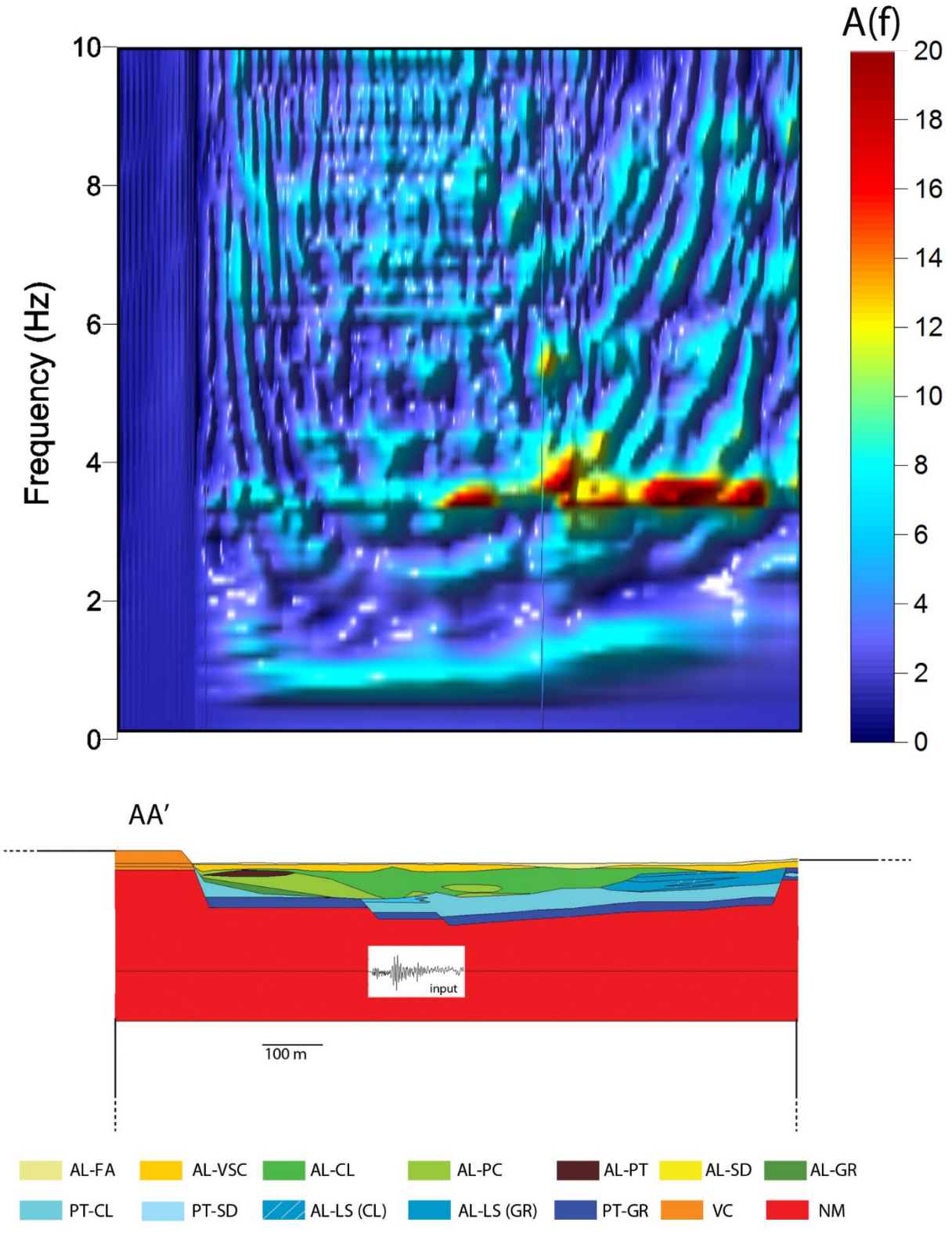

Variation of the kinetic energy E(x) index (top) along the AA’ model surface (bottom) forced by EQ-7 earthquake.

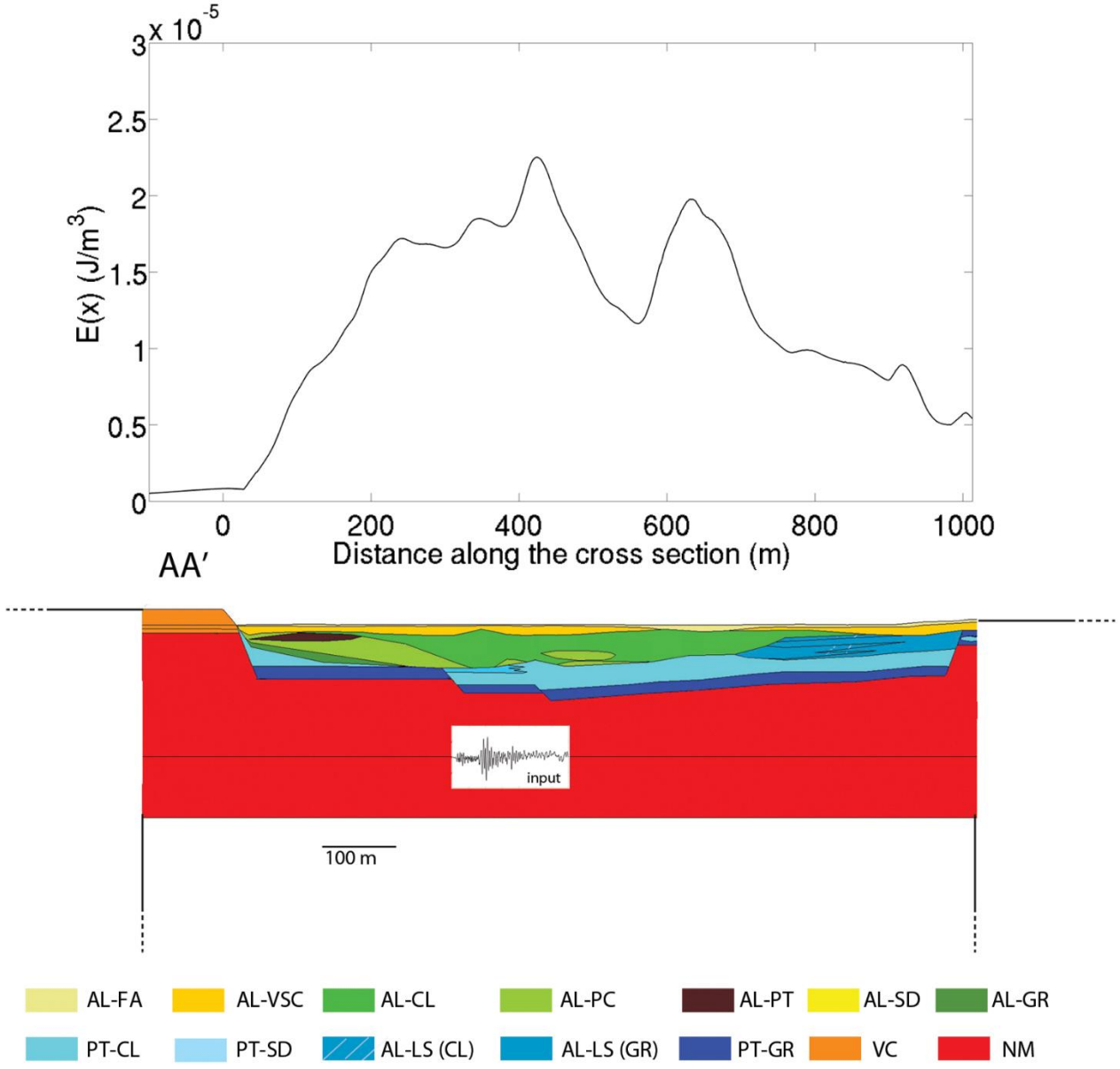

Contour map of the $A(f)_x$ functions distribution (top) along the AA' model surface (bottom) forced by EQ-12 earthquake.

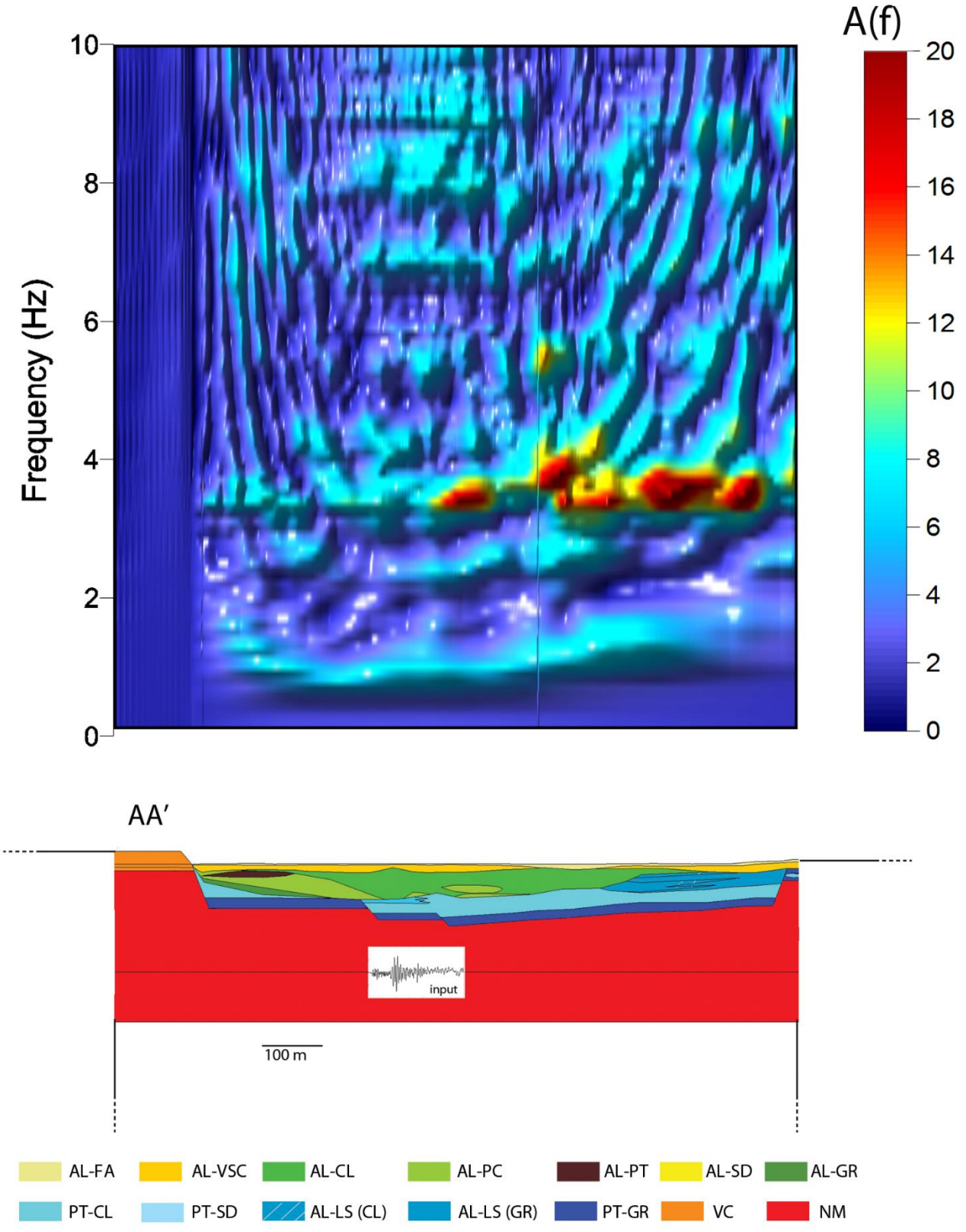

Variation of the kinetic energy E(x) index (top) along the AA’ model surface (bottom) forced by EQ-12 earthquake.

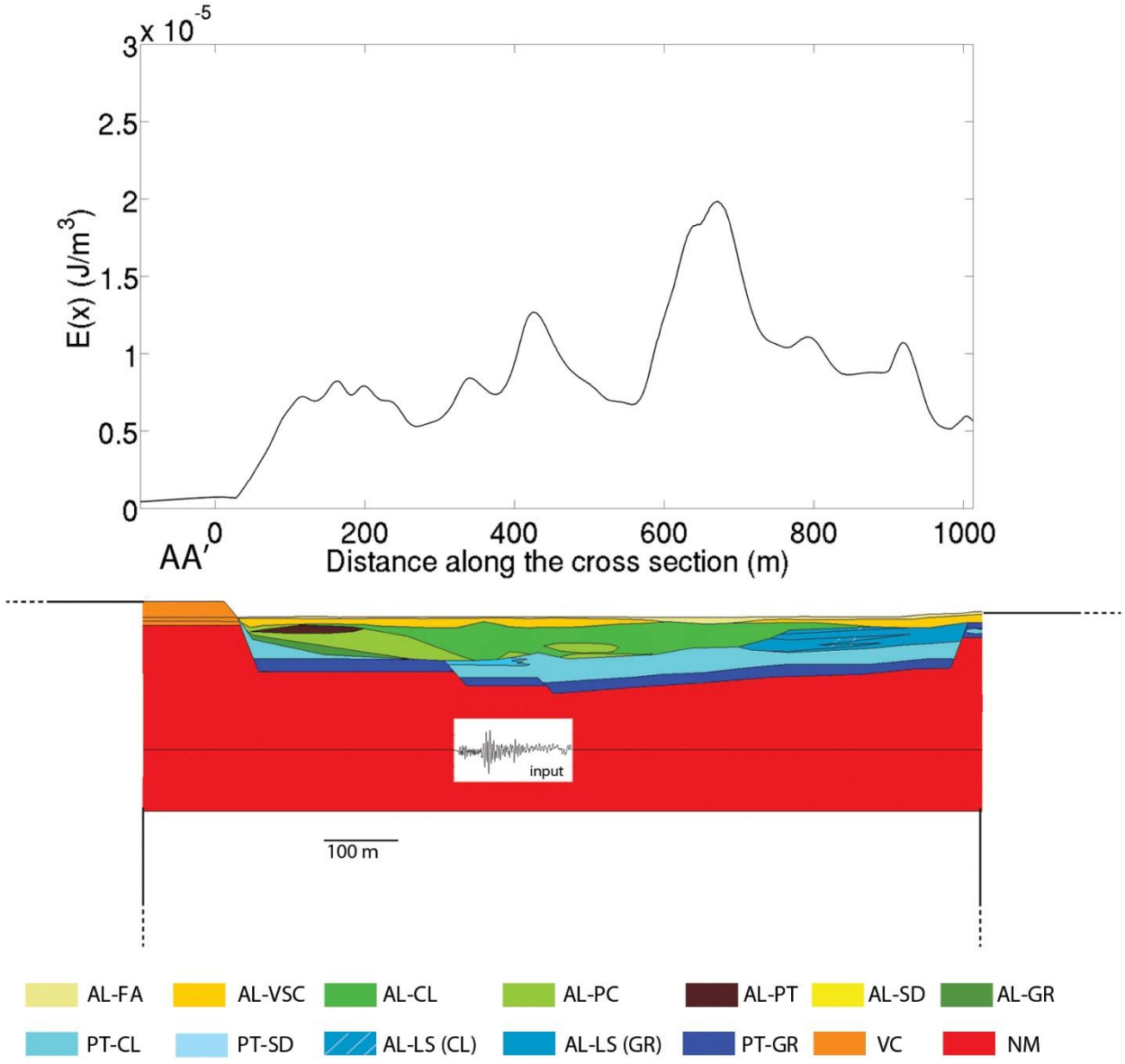

Contour map of the $A(f)_x$ functions distribution (top) along the AA' model surface (bottom) forced by EQ-13 earthquake.

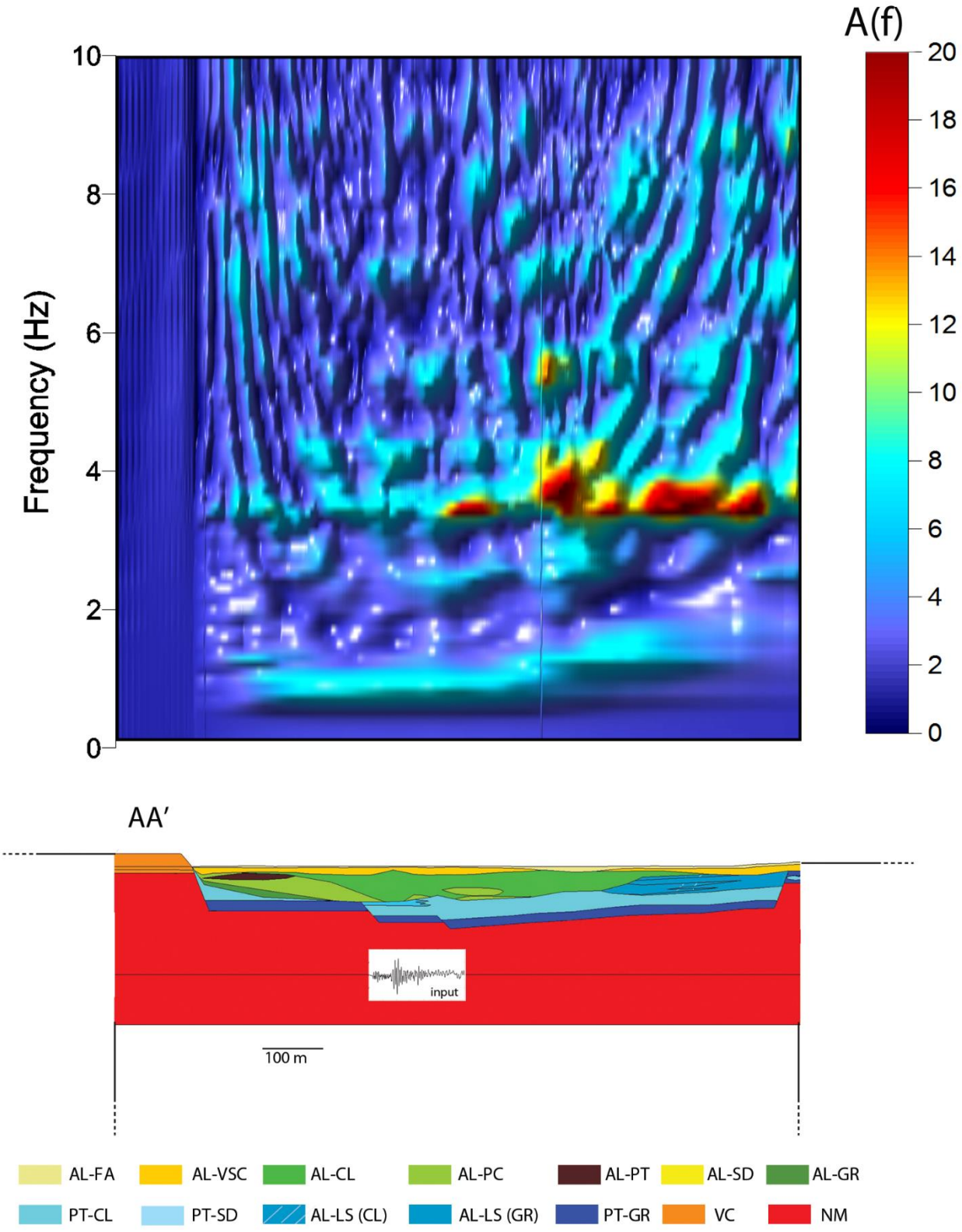

Variation of the kinetic energy E(x) index (top) along the AA’ model surface (bottom) forced by EQ-13 earthquake.

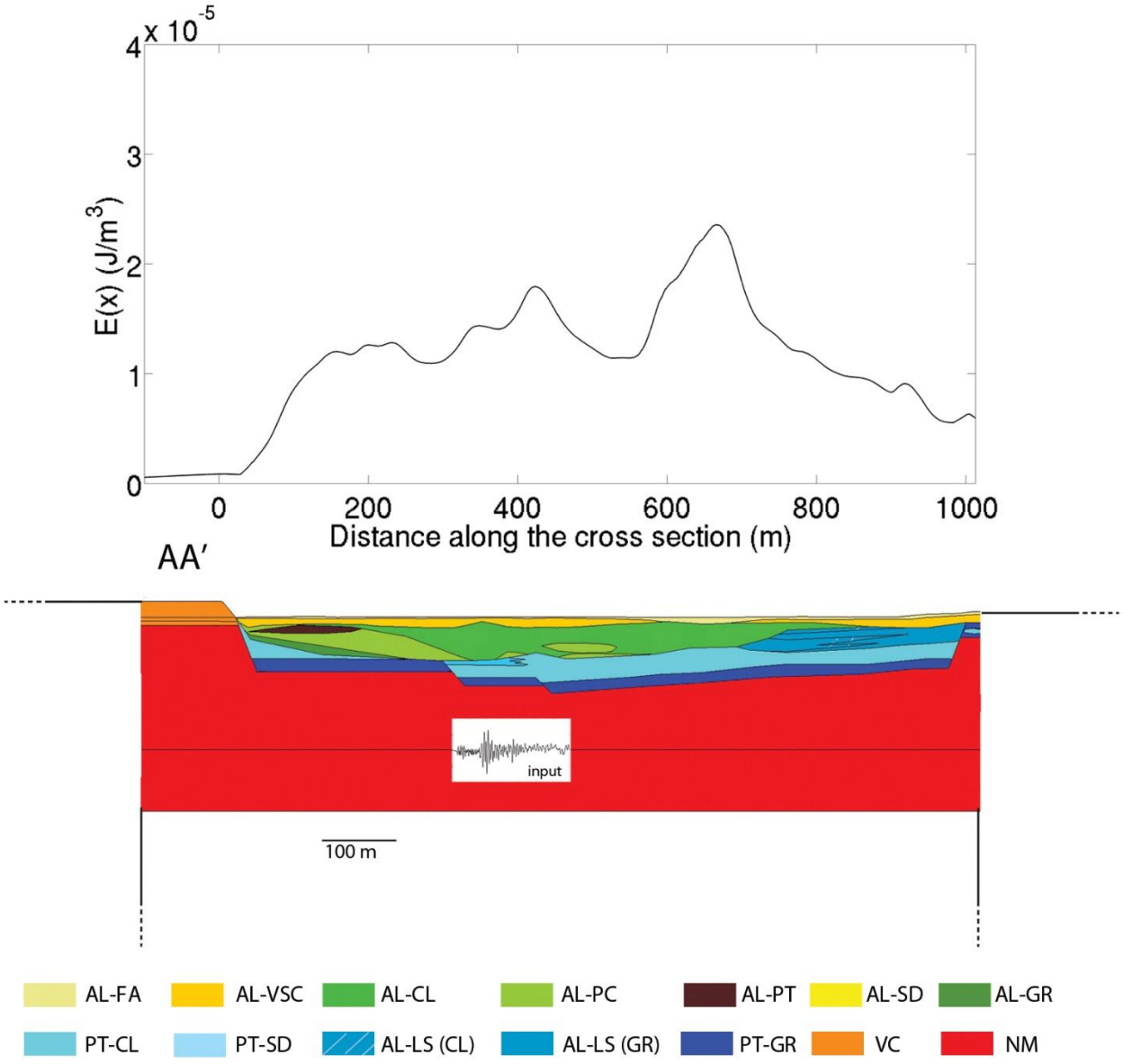

Contour map of the $A(f)_x$ functions distribution (top) along the BB' model surface (bottom) forced by EQ-7 earthquake.

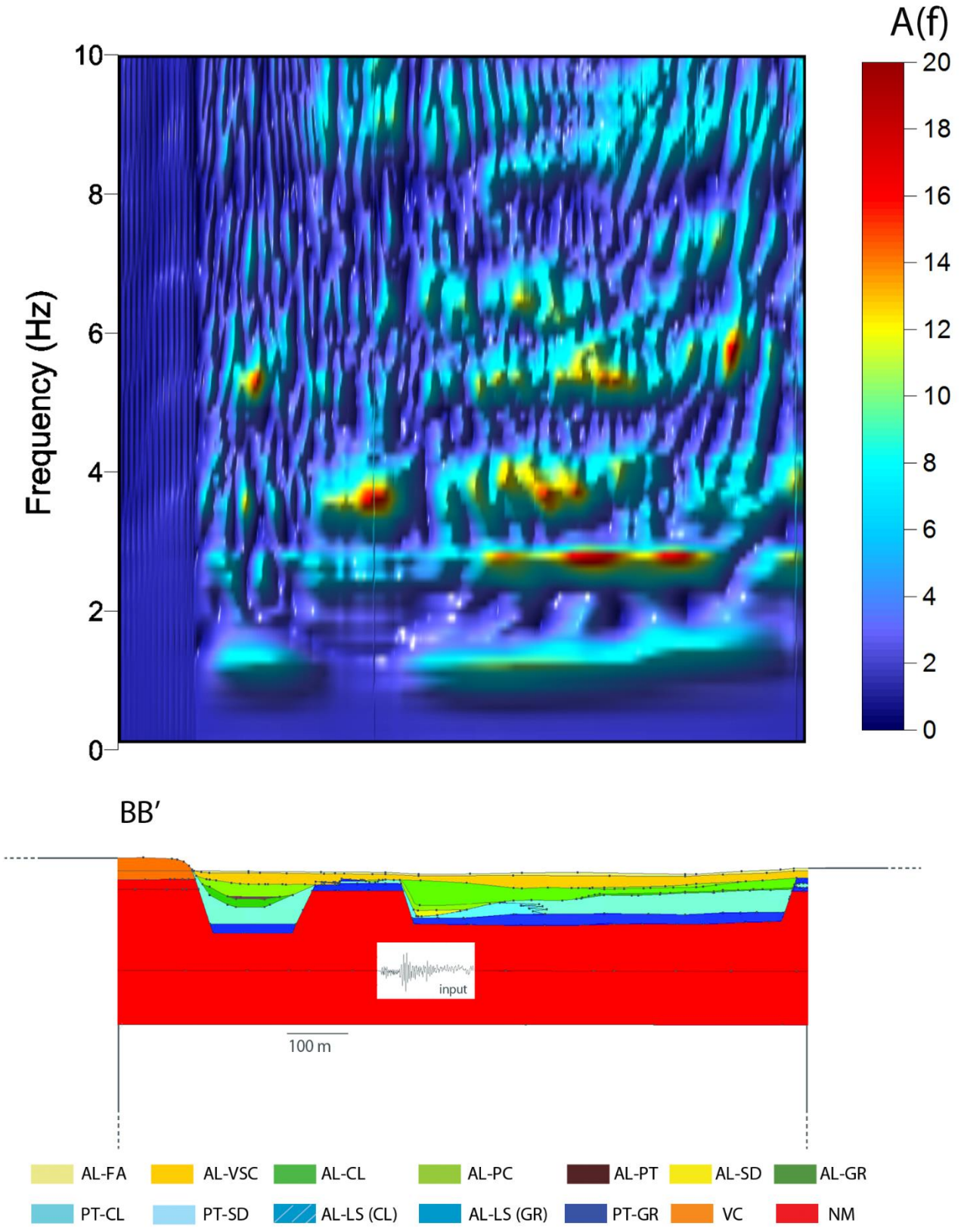

Variation of the kinetic energy E(x) index (top) along the BB’ model surface (bottom) forced by EQ-7 earthquake.

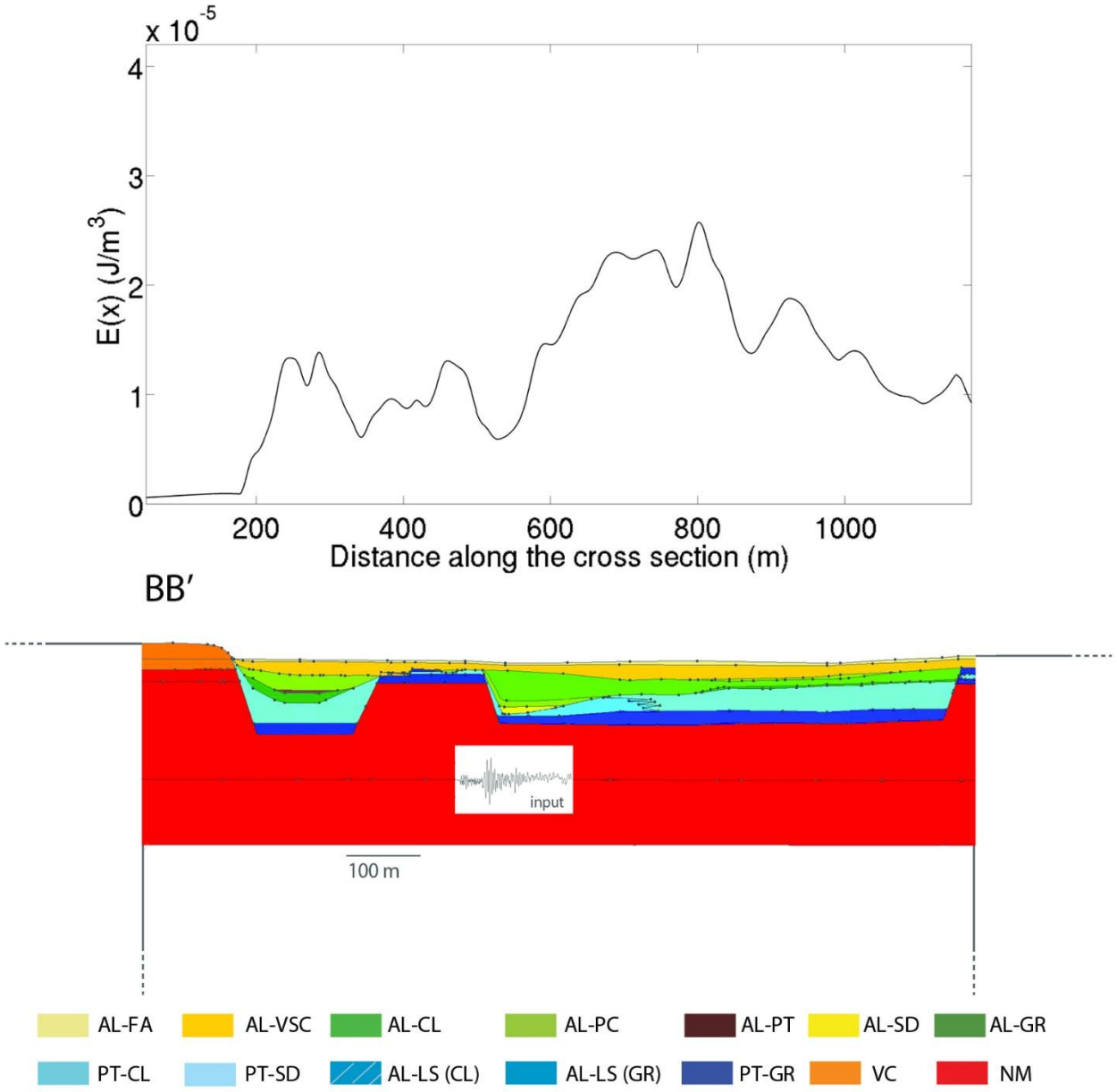

Contour map of the $A(f)_x$ functions distribution (top) along the BB' model surface (bottom) forced by EQ-12 earthquake.

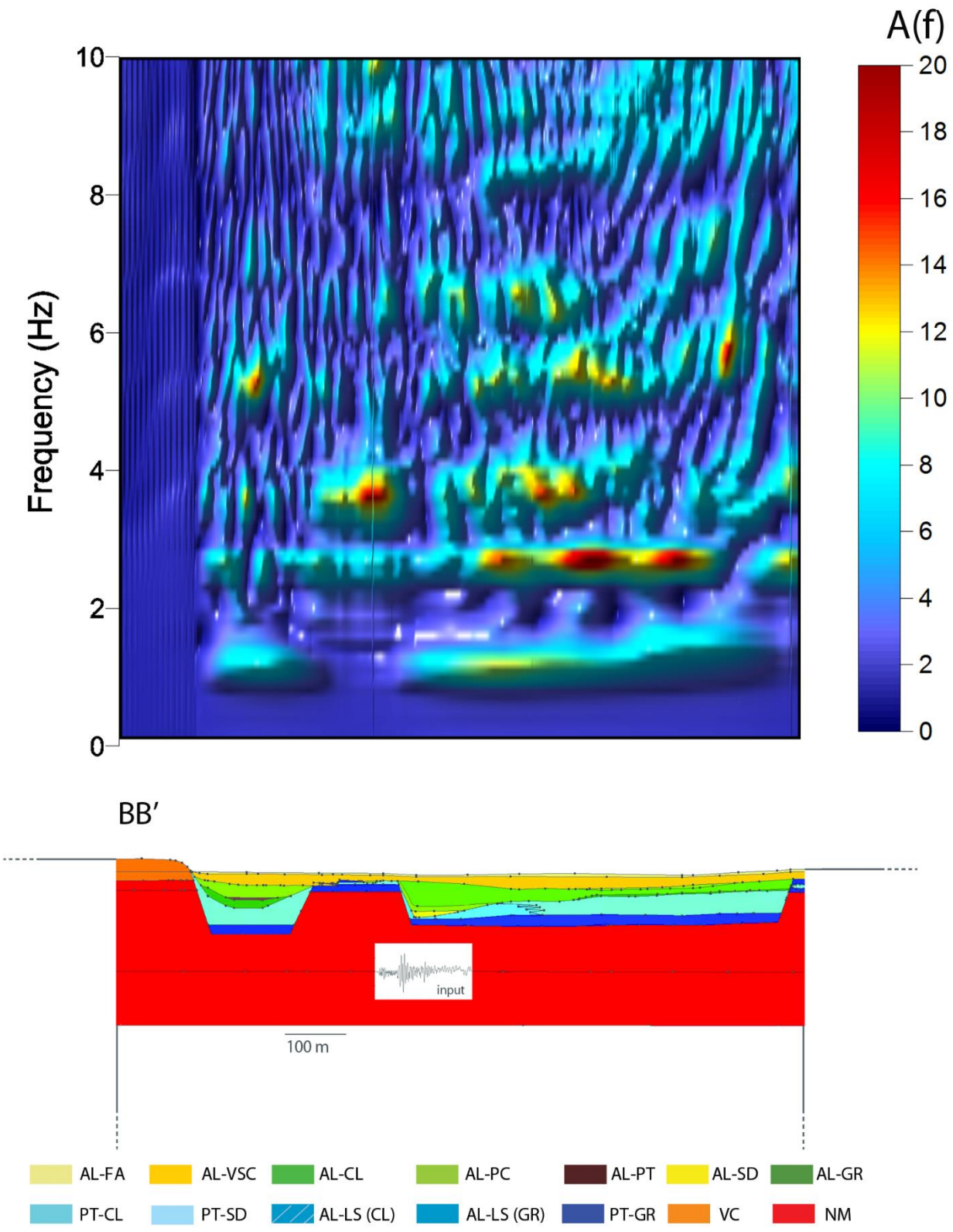

Variation of the kinetic energy E(x) index (top) along the BB’ model surface (bottom) forced by EQ-12 earthquake.

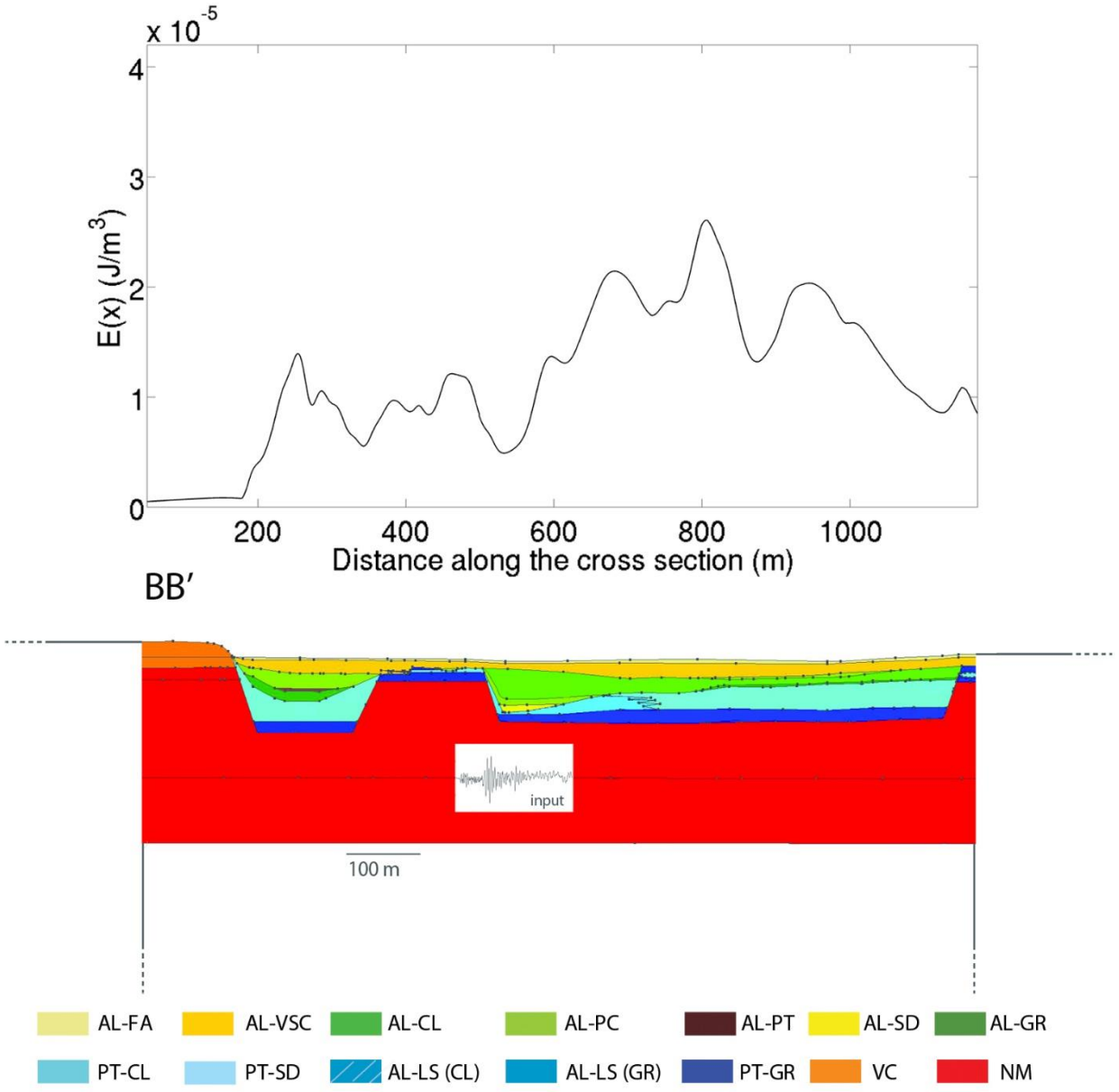

Contour map of the $A(f)_x$ functions distribution (top) along the BB' model surface (bottom) forced by EQ-13 earthquake.

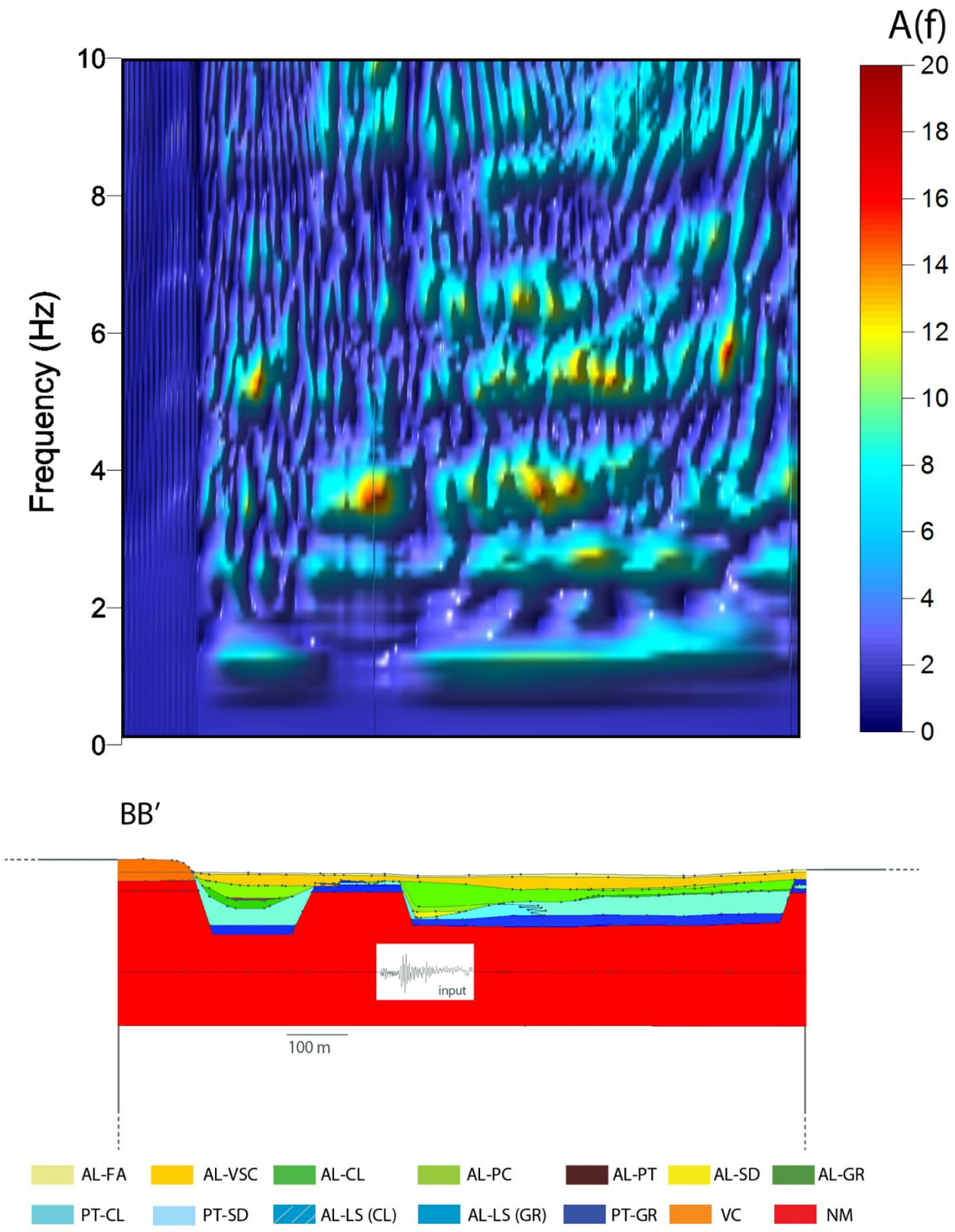

Variation of the kinetic energy E(x) index (top) along the BB’ model surface (bottom) forced by EQ-13 earthquake.

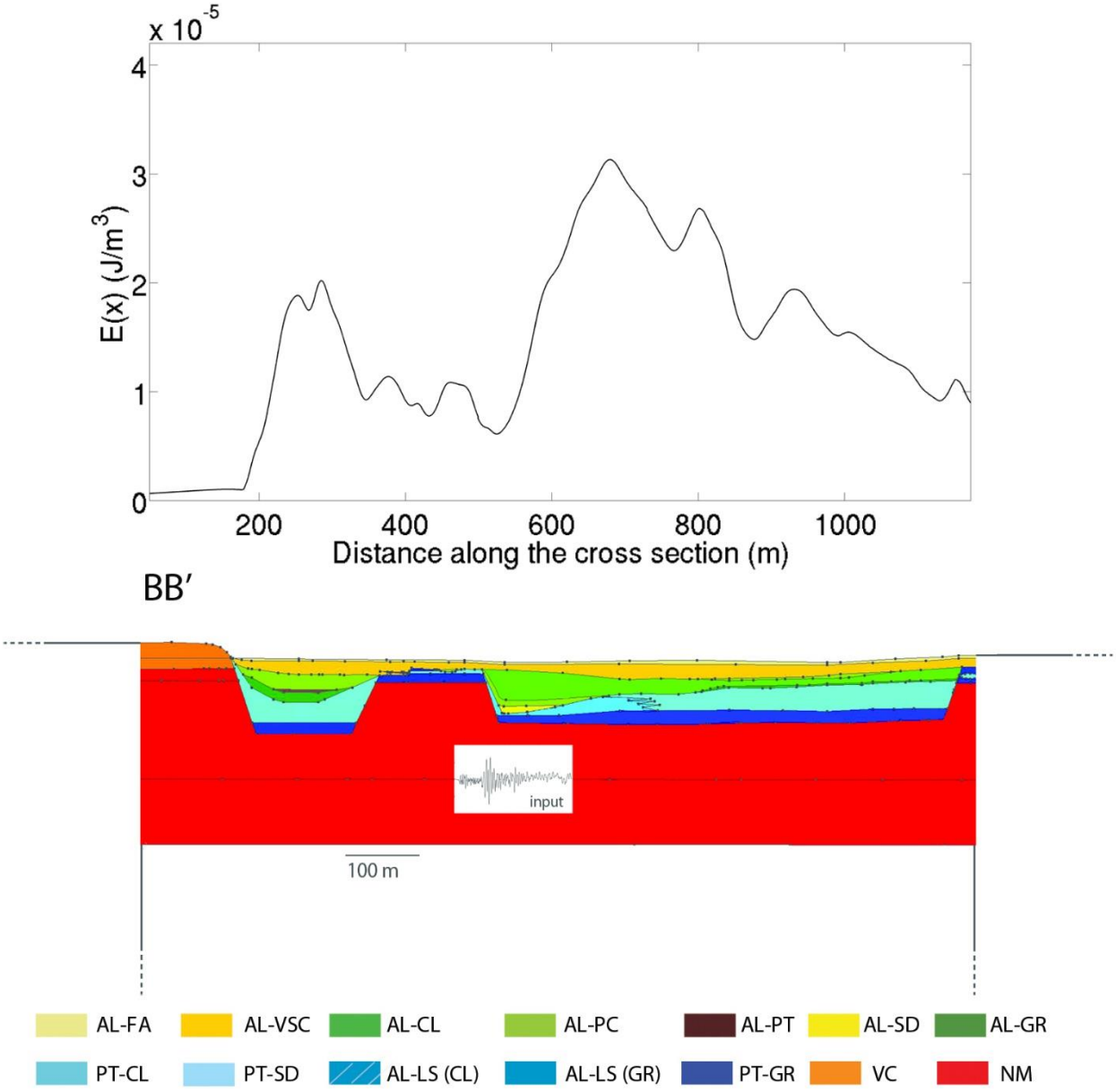

Results obtained assuming SCI condition

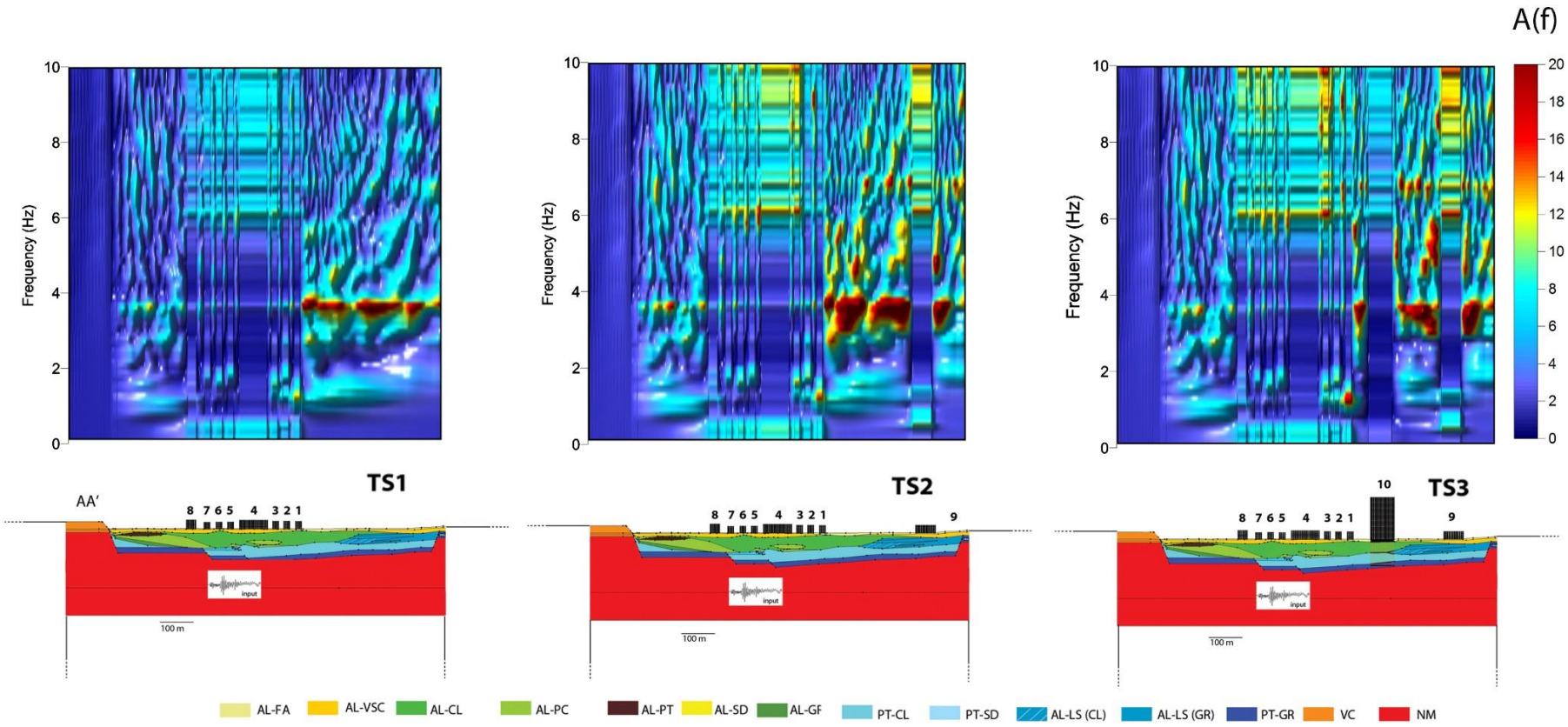

Contour map of the $A(f)_x$ functions distribution (top) along the **AA'** coupled model surface (bottom) forced by EQ-7 earthquake.

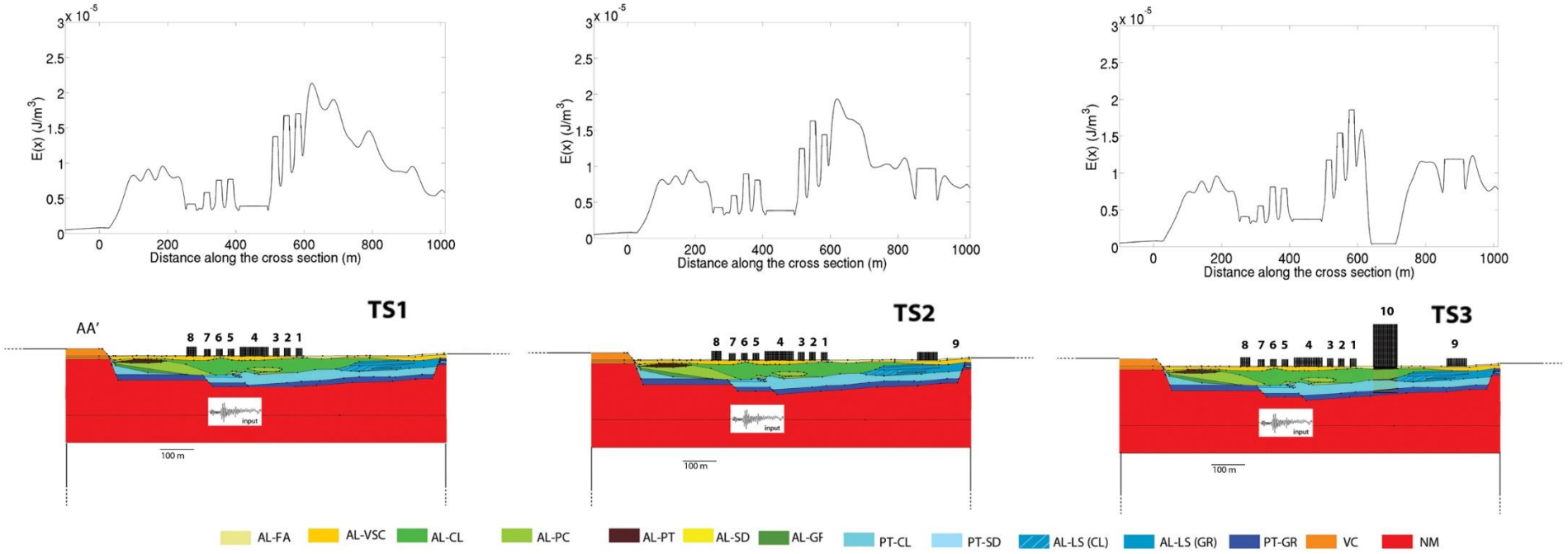

Variation of the kinetic energy E(x) index (top) along the AA' coupled model surface (bottom) forced by EQ-7 earthquake.

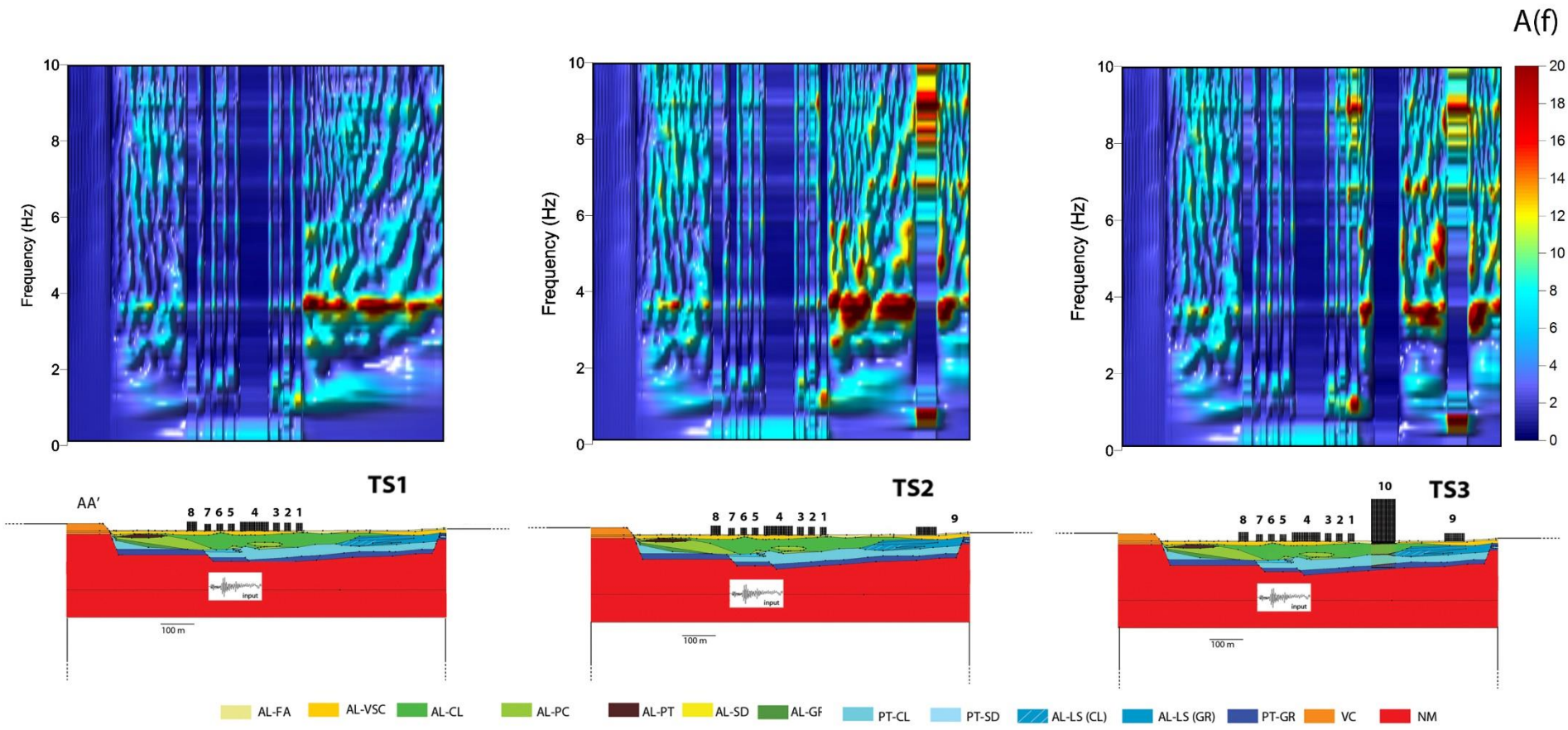

Contour map of the $A(f)_x$ functions distribution (top) along the AA' coupled model surface (bottom) forced by EQ-12 earthquake.

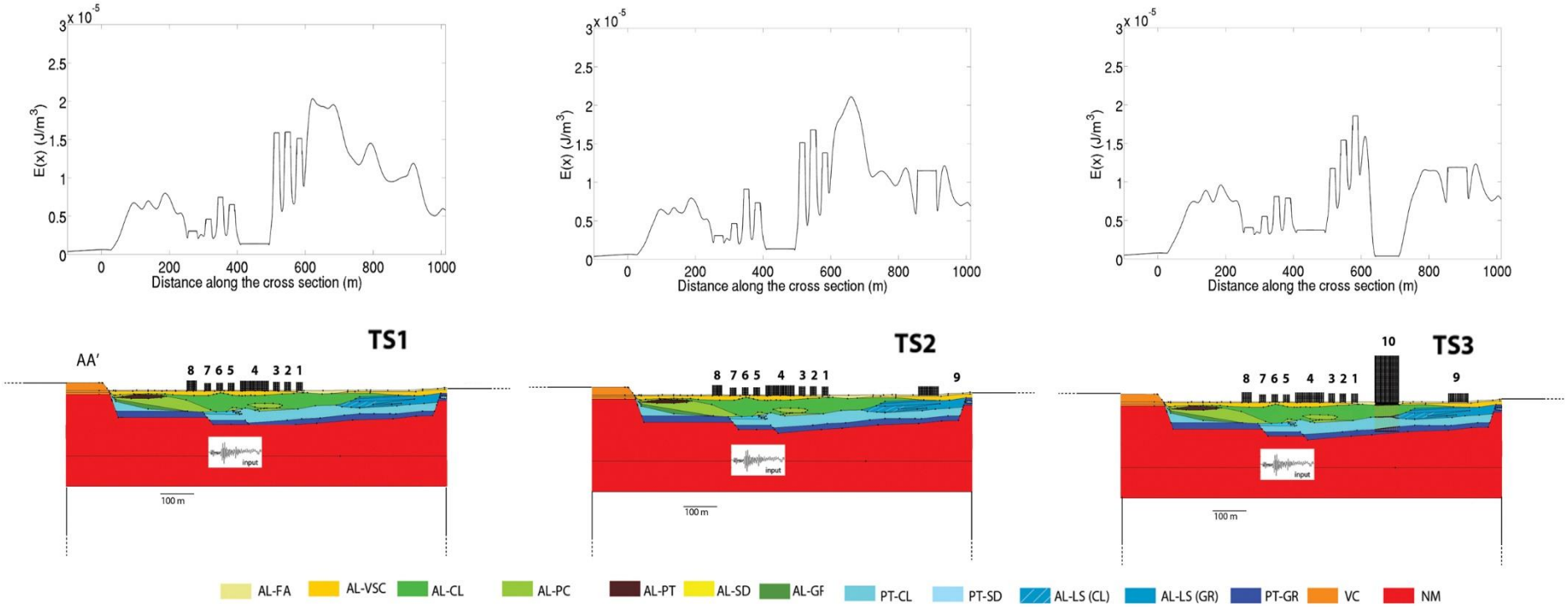

Variation of the kinetic energy E(x) index (top) along the AA' coupled model surface (bottom) forced by EQ-12 earthquake.

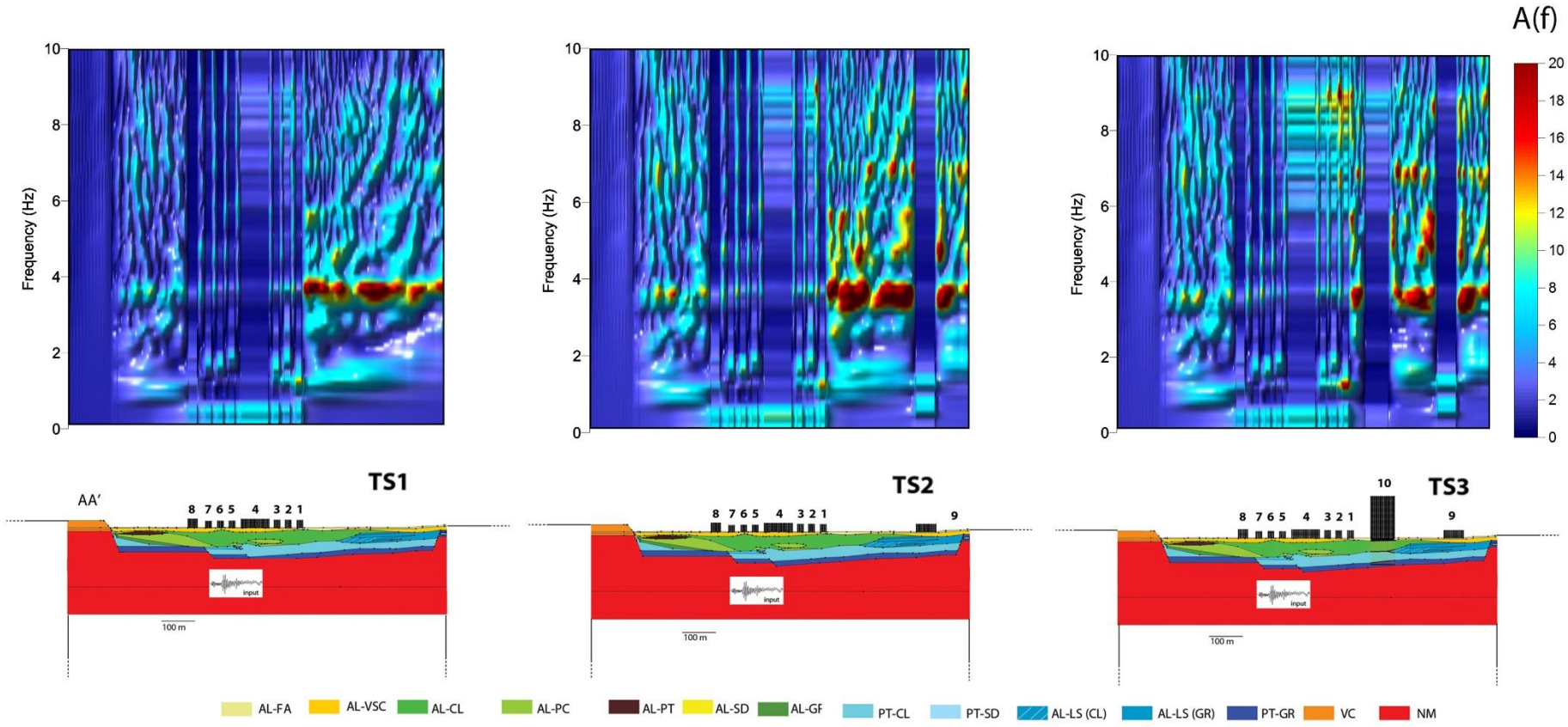

Contour map of the $A(f)_x$ functions distribution (top) along the AA' coupled model surface (bottom) forced by EQ-13 earthquake.

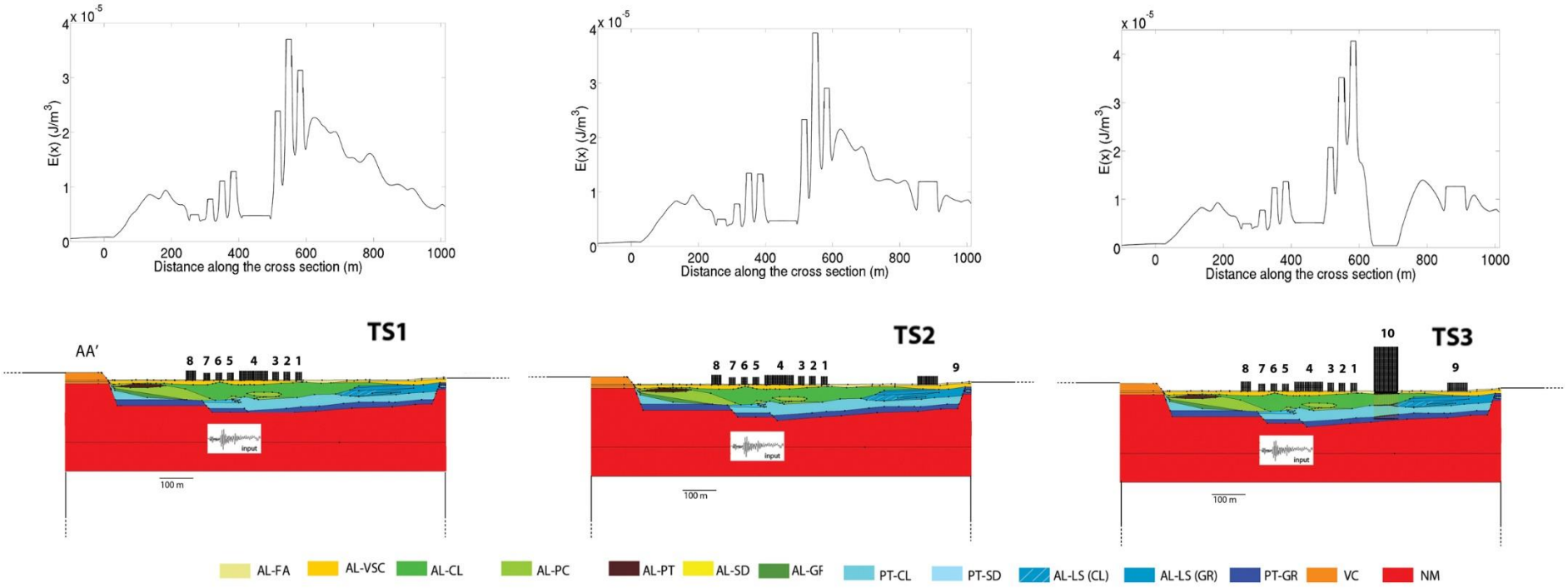

Variation of the kinetic energy E(x) index (top) along the AA’ coupled model surface (bottom) forced by EQ-13 earthquake.

Contour map of the $A(f)_x$ functions distribution (top) along the BB' coupled model surface (bottom) forced by EQ-7 earthquake.

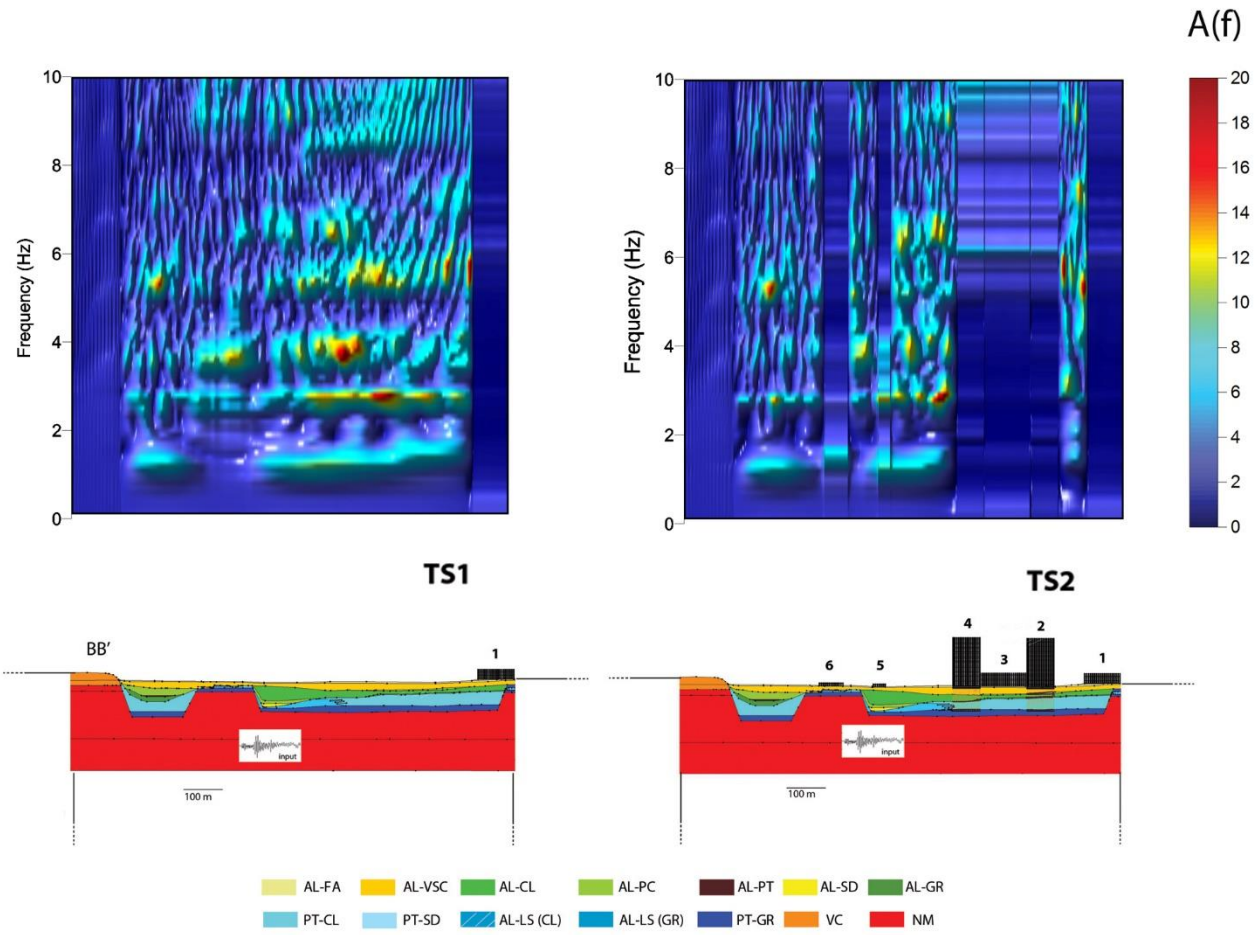

Variation of the kinetic energy E(x) index (top) along the BB’ coupled model surface (bottom) forced by EQ-7 earthquake.

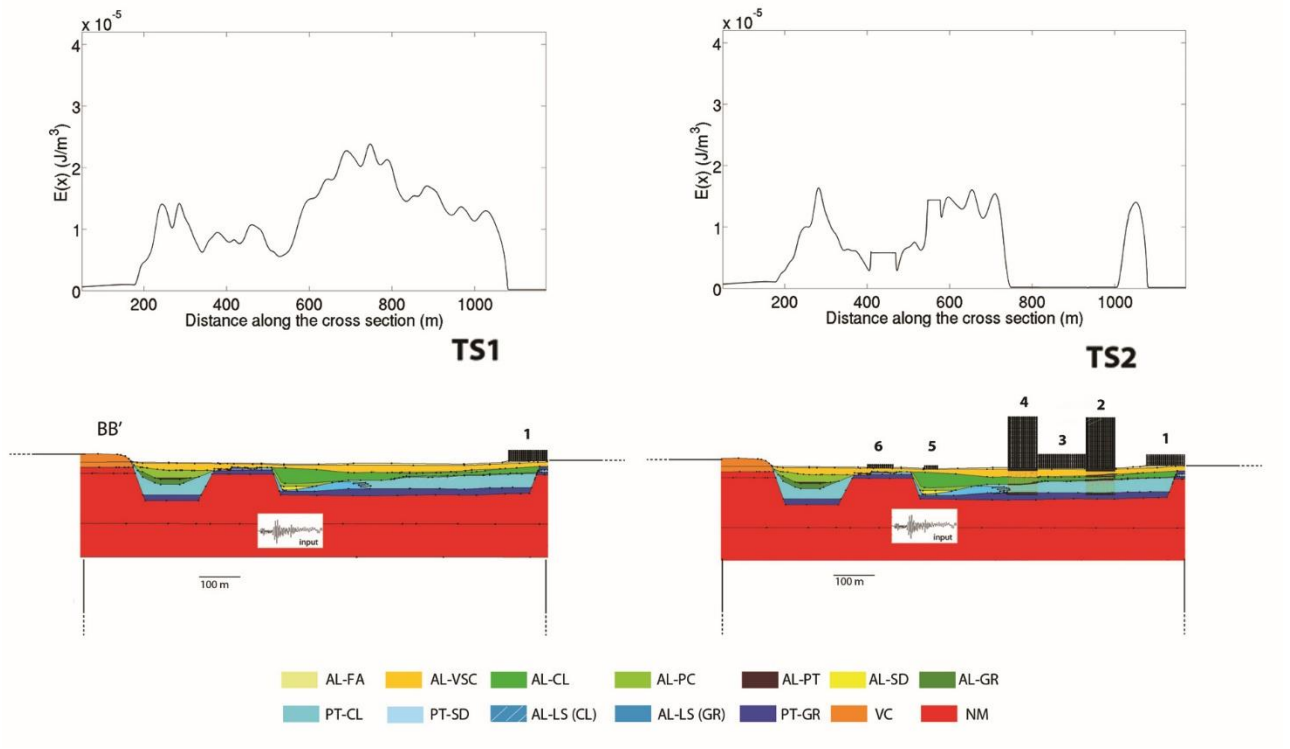

Contour map of the $A(f)_x$ functions distribution (top) along the BB' coupled model surface (bottom) forced by EQ-12 earthquake.

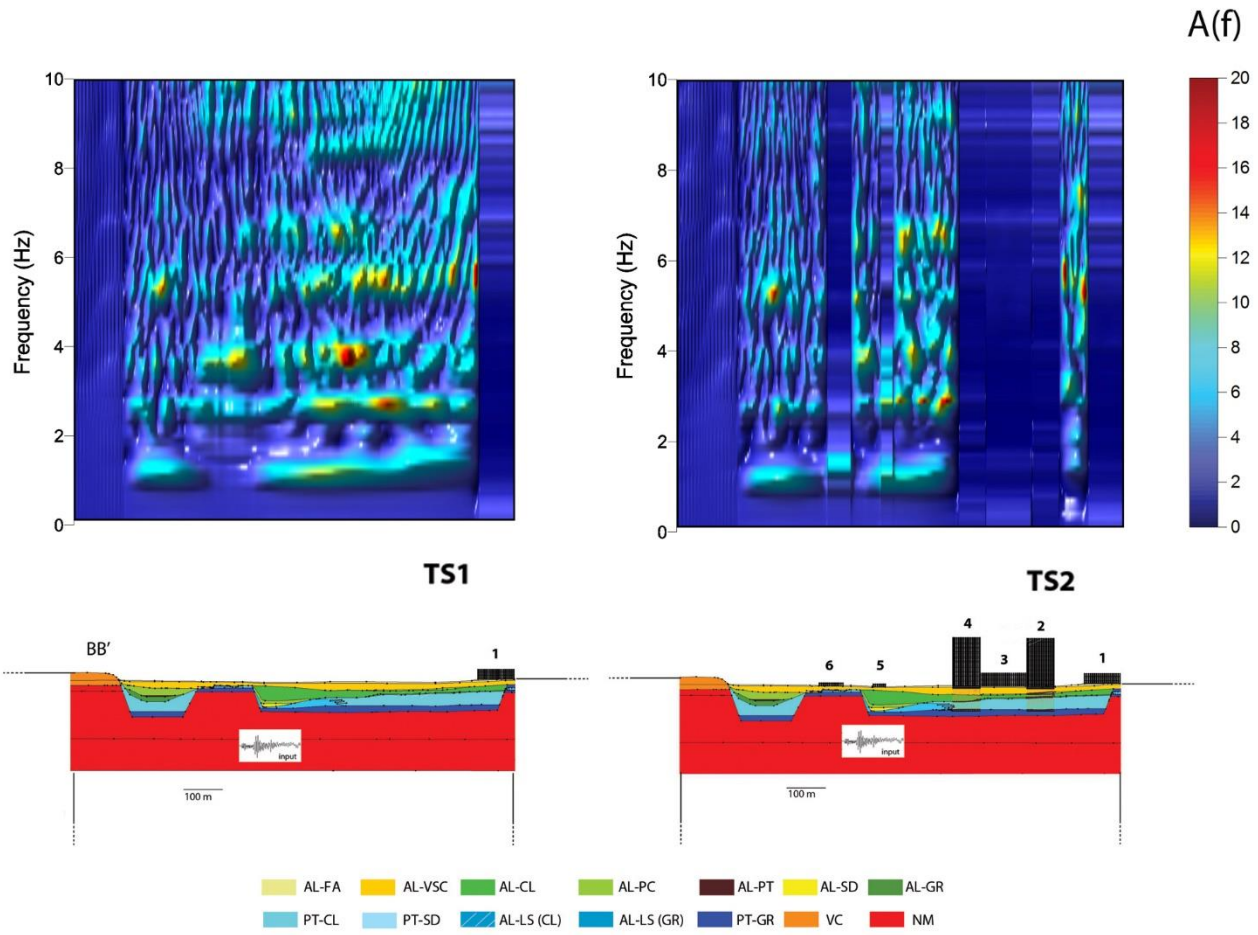

Variation of the kinetic energy E(x) index (top) along the BB’ coupled model surface (bottom) forced by EQ-12 earthquake.

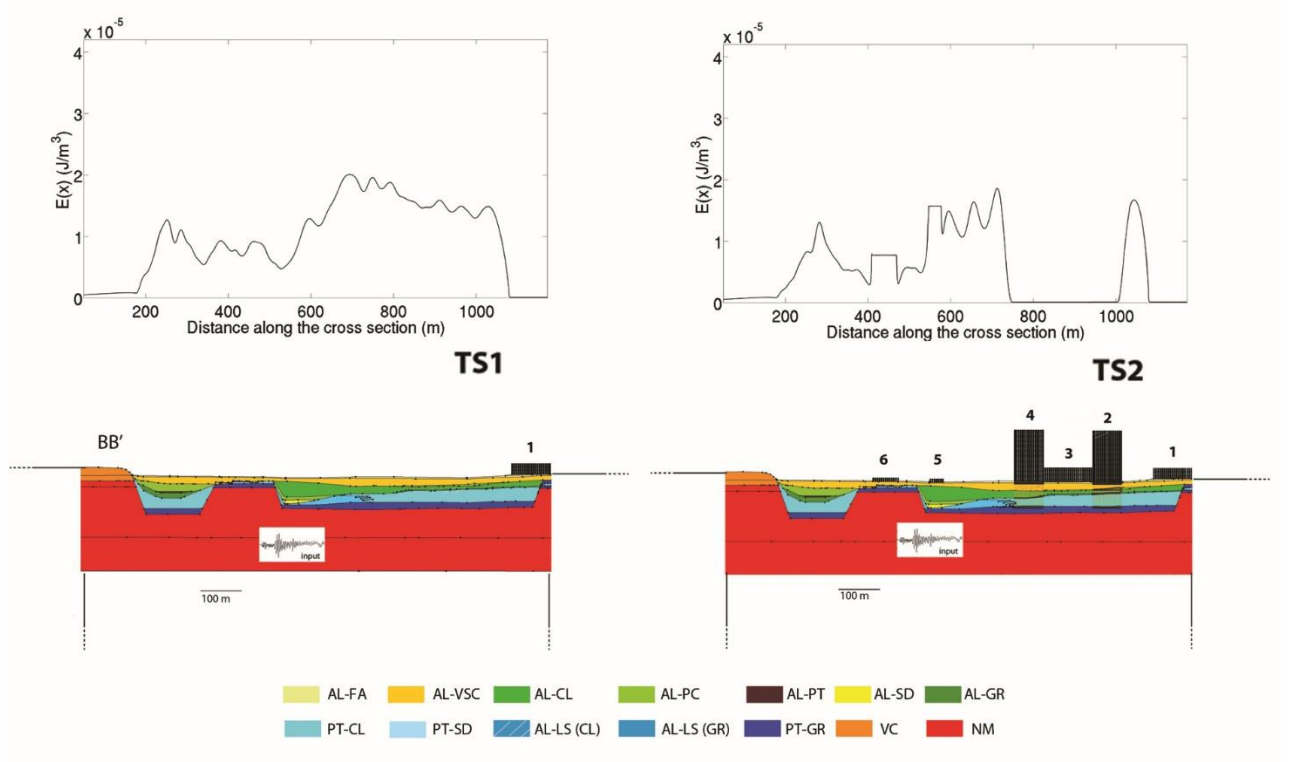

Contour map of the $A(f)_x$ functions distribution (top) along the BB' coupled model surface (bottom) forced by EQ-13 earthquake.

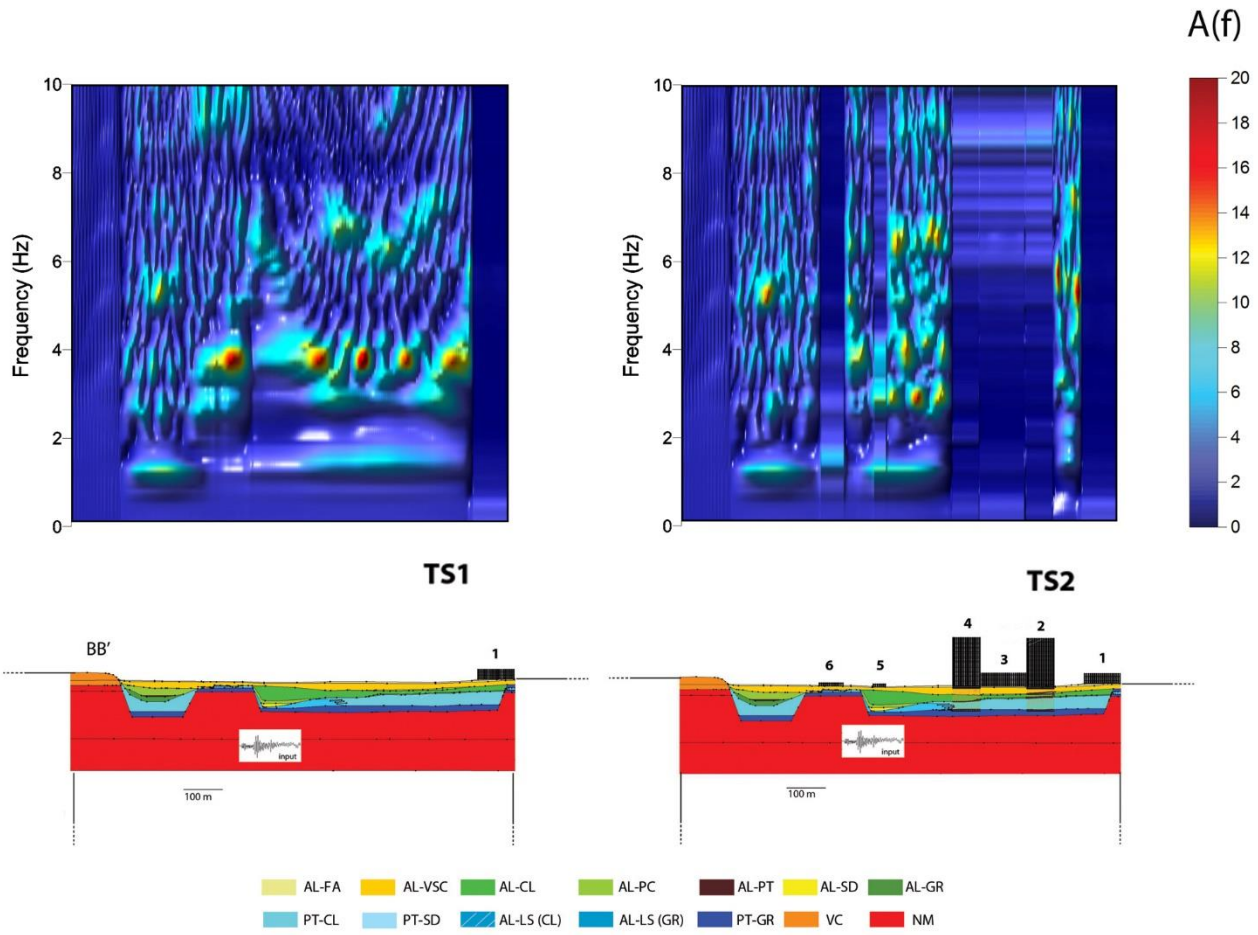

Variation of the kinetic energy E(x) index (top) along the BB’ coupled model surface (bottom) forced by EQ-13 earthquake.

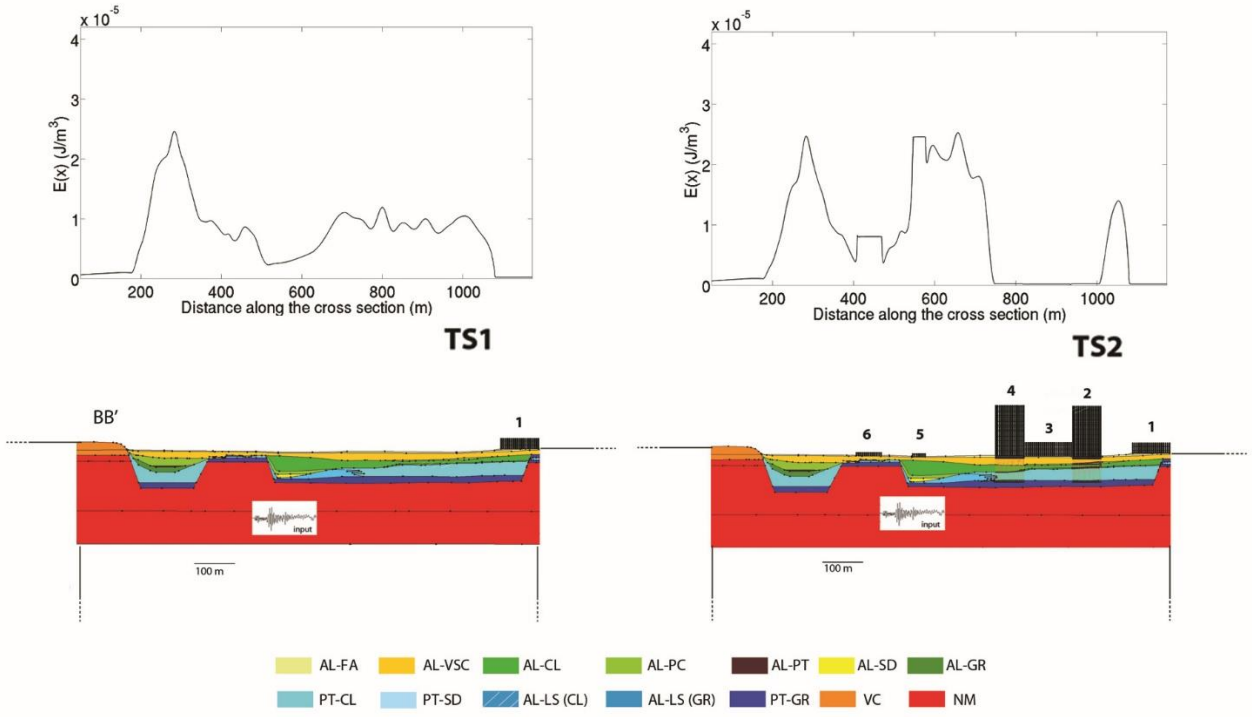

Results of the quantitative analysis of the Site-City Interaction

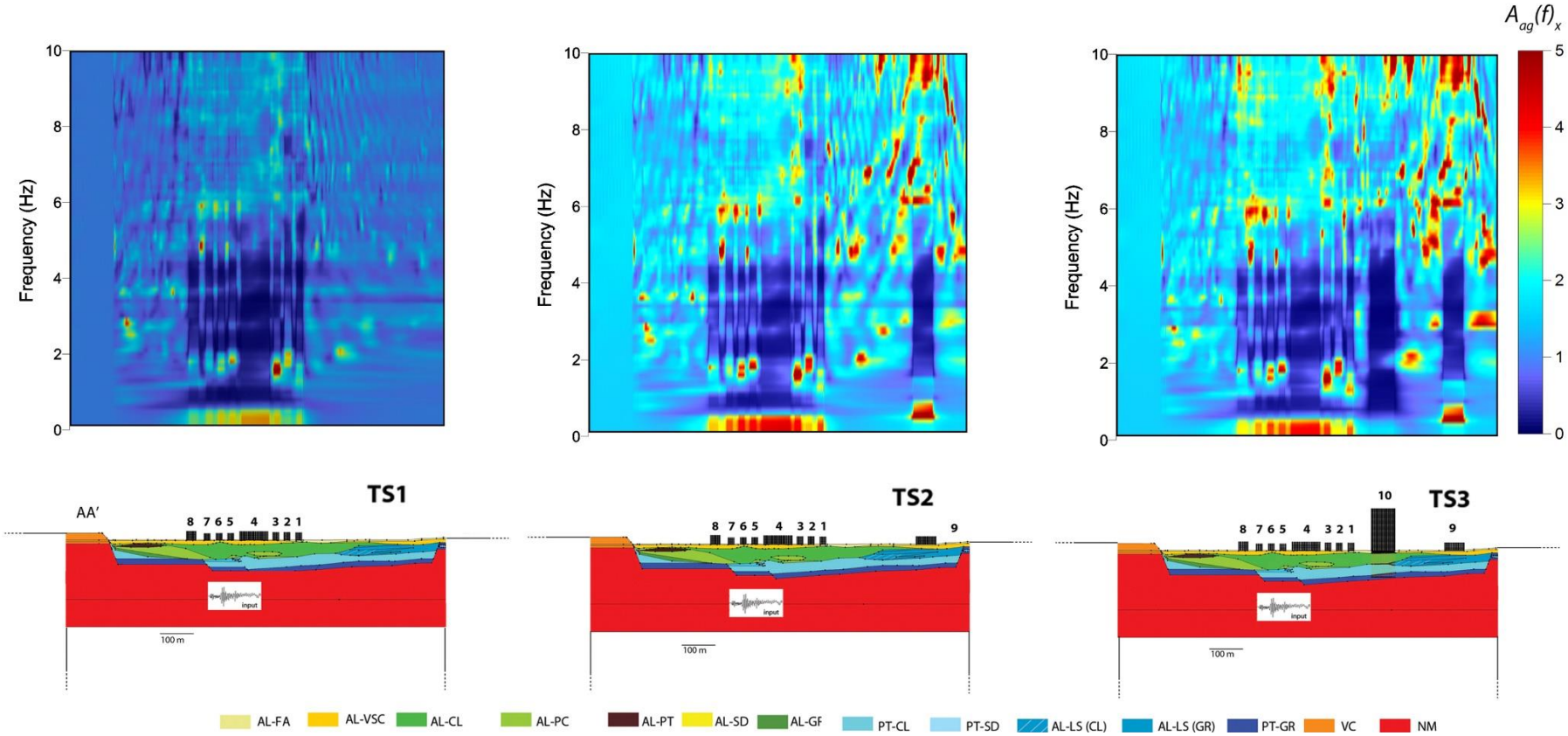

$A_{ag}(f)_x$ distribution (top) along the surface of AA' coupled models forced by EQ-7. From left to right: AA'-TS1/AA', AA'-TS2/AA', AA'-TS3/AA'.

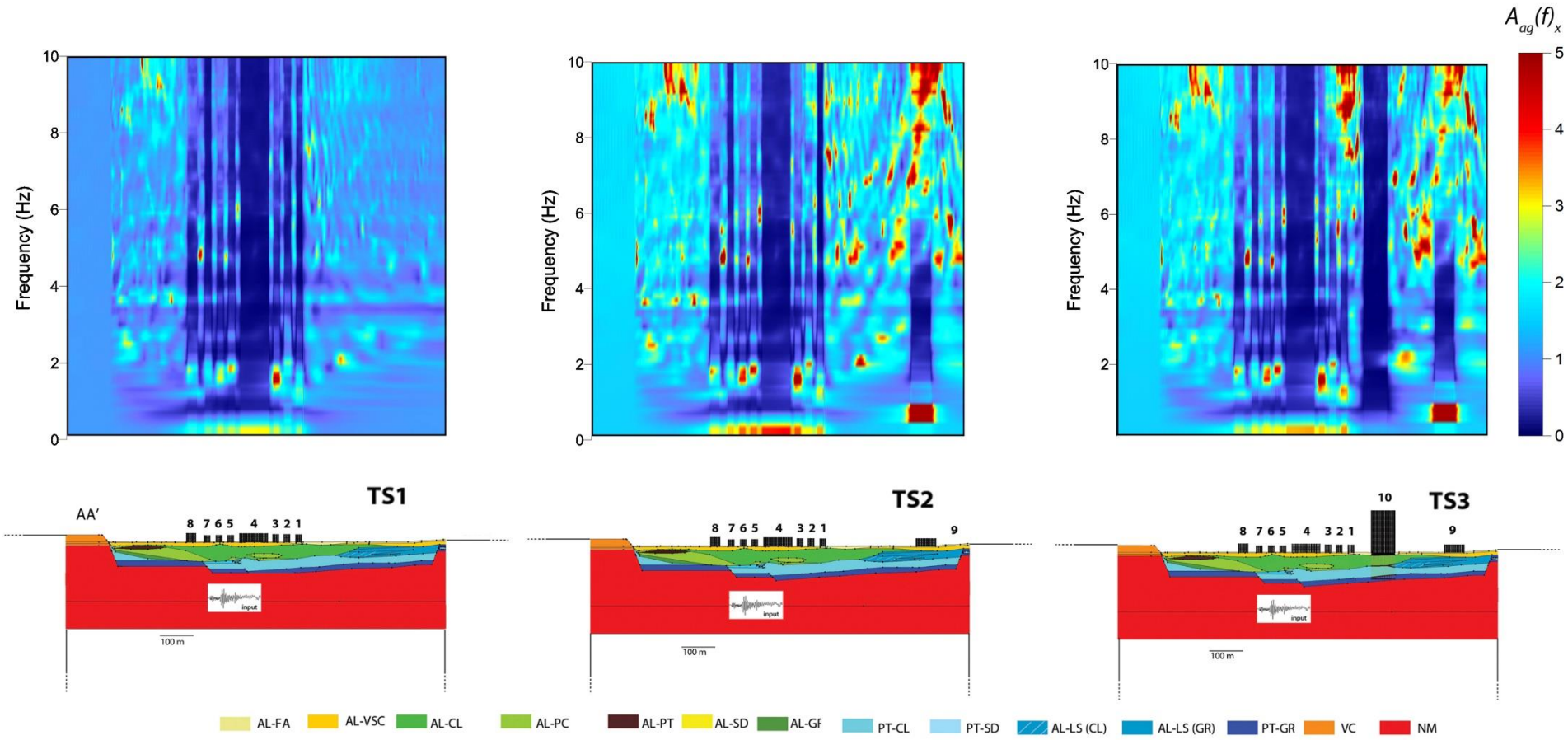

$A_{ag}(f)_x$ distribution (top) along the surface of AA' coupled models forced by EQ-12. From left to right: AA'-TS1/AA', AA'-TS2/AA', AA'-TS3/AA'.

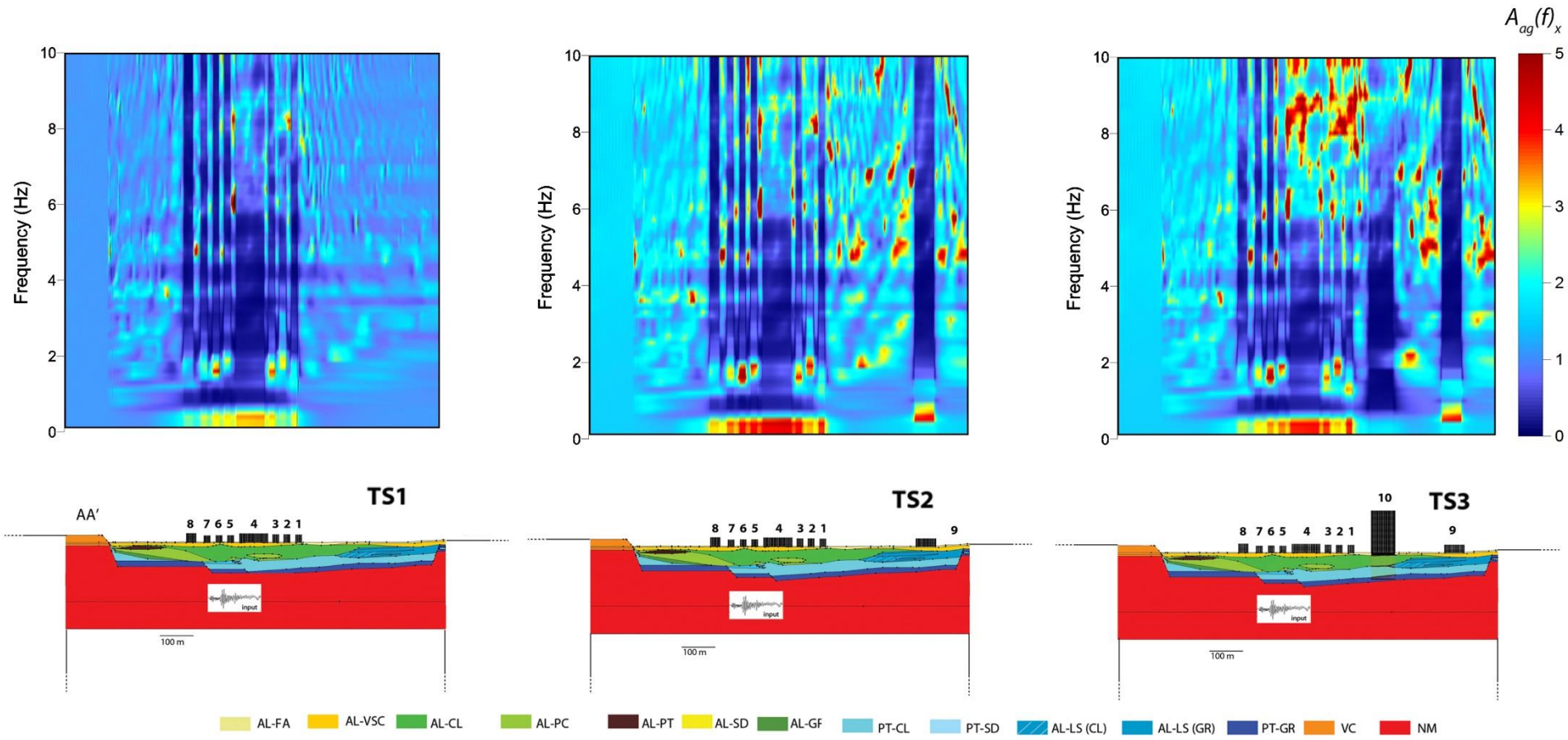

$A_{ag}(f)_x$ distribution (top) along the surface of AA' coupled models forced by EQ-13. From left to right: AA'-TS1/AA', AA'-TS2/AA', AA'-TS3/AA'.

$A_{ag}(f)_x$ distribution (top) along the surface of BB' coupled models forced by EQ-7. From left to right: BB'-TS1/BB', BB'-TS2/BB'.

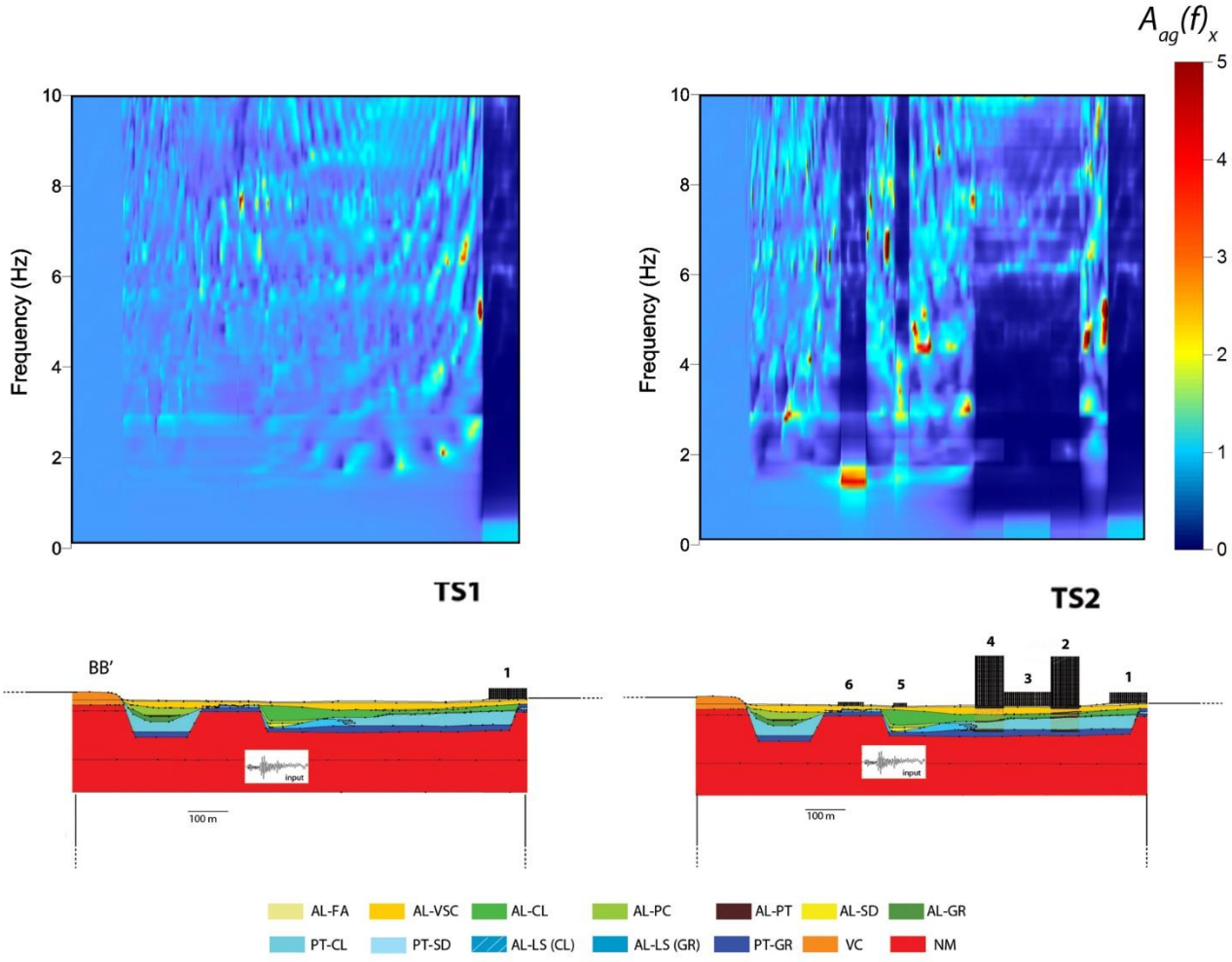

$A_{ag}(f)_x$ distribution (top) along the surface of BB' coupled models forced by EQ-12. From left to right: BB'-TS1/BB', BB'-TS2/BB'.

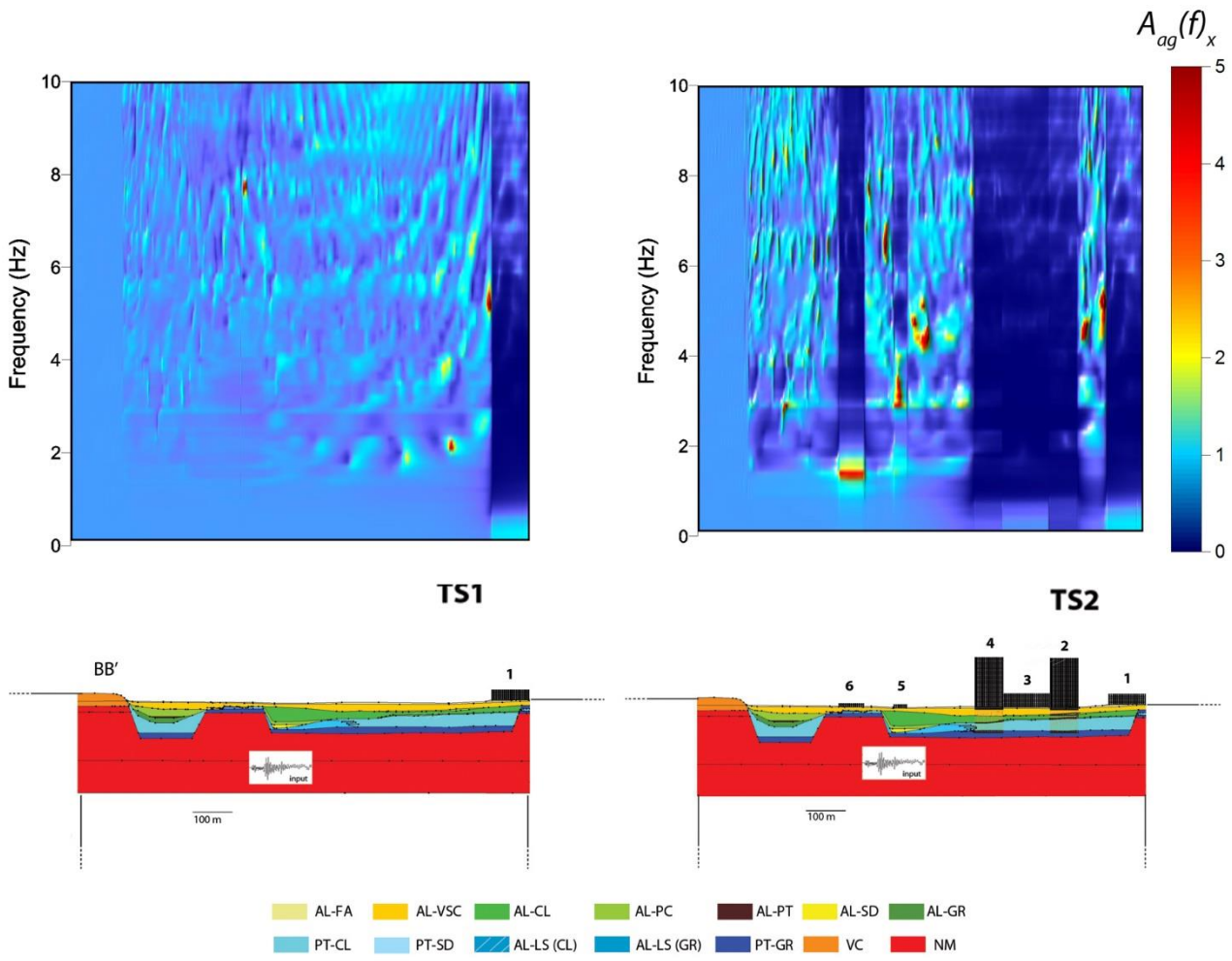

$A_{ag}(f)_x$ distribution (top) along the surface of BB’ coupled models forced by EQ-13. From left to right: BB’-TS1/BB’, BB’-TS2/BB’.

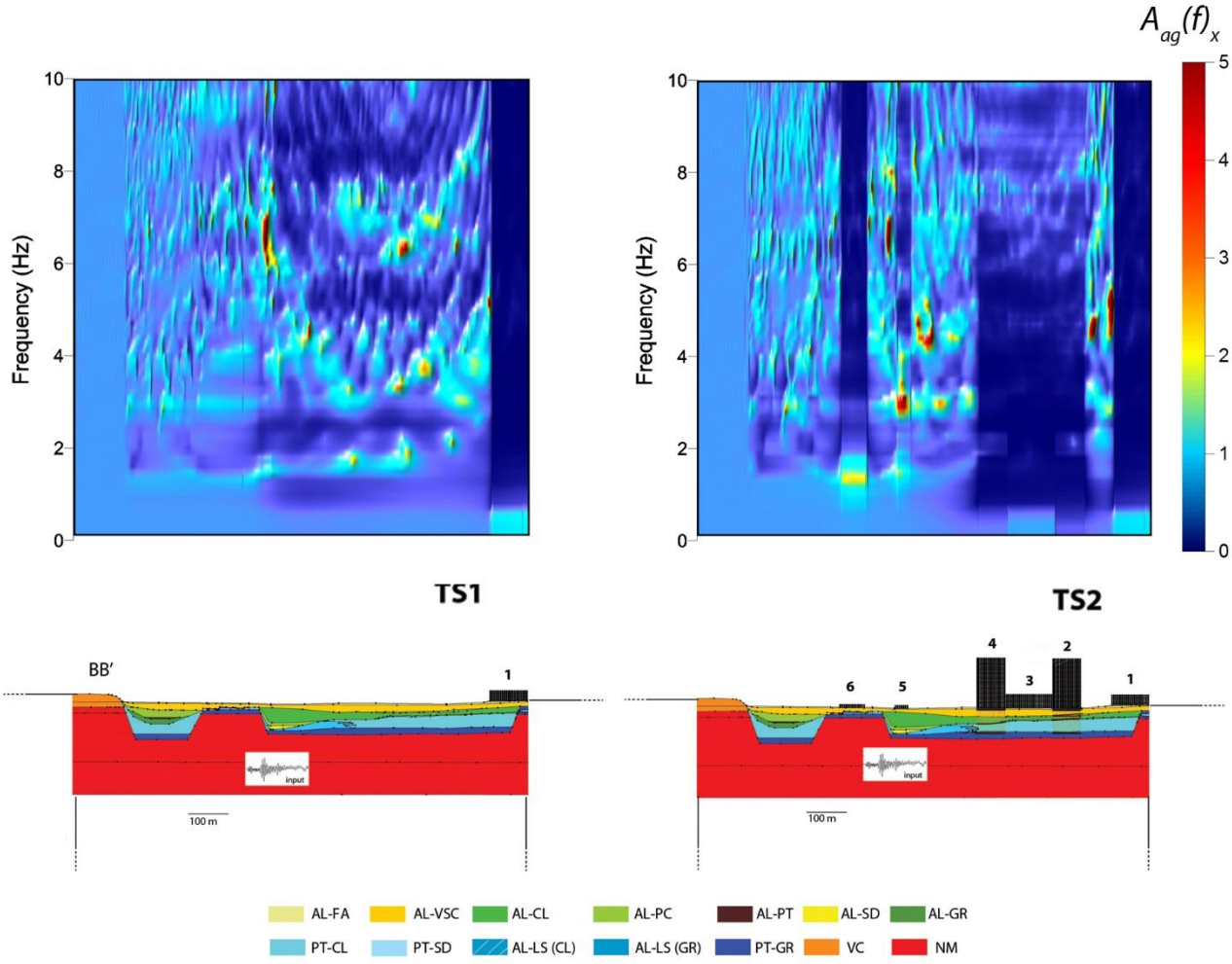

Variation of the ratio between the kinetic energy E(x) index assuming SCI and free field condition along the AA’ model surface forced by EQ-7.

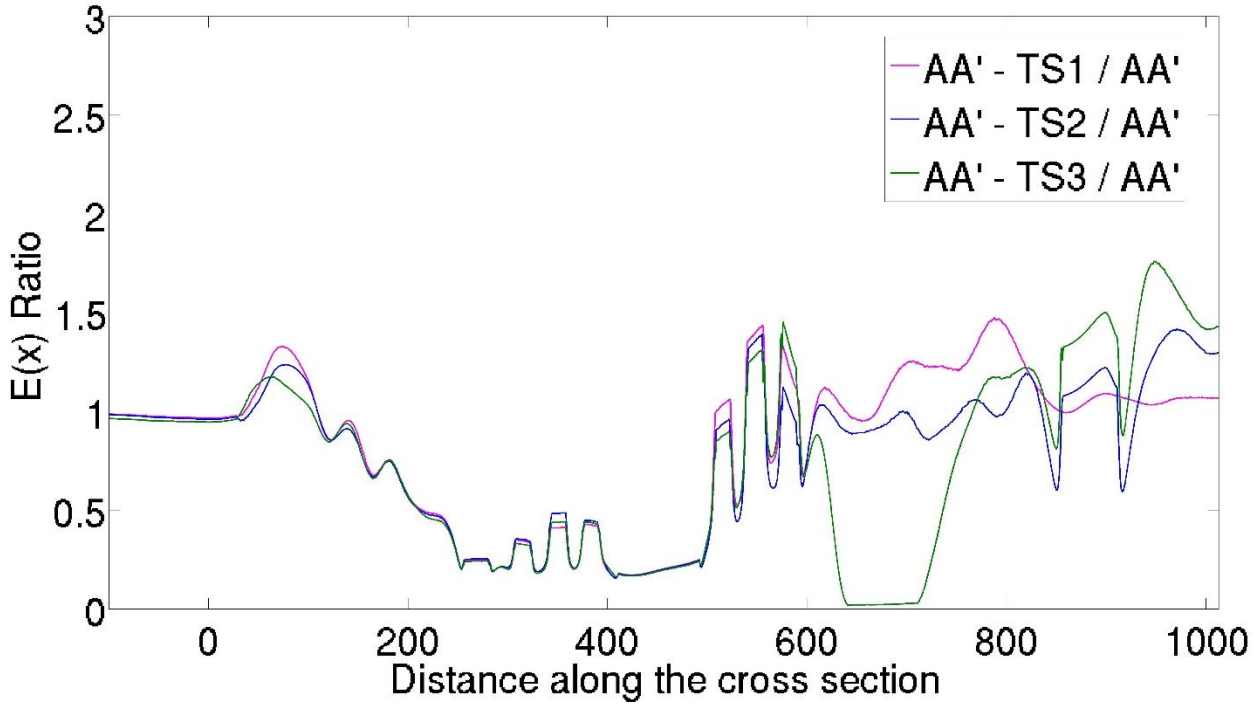

Variation of the ratio between the kinetic energy E(x) index assuming SCI and free field condition along the AA’ model surface forced by EQ-12.

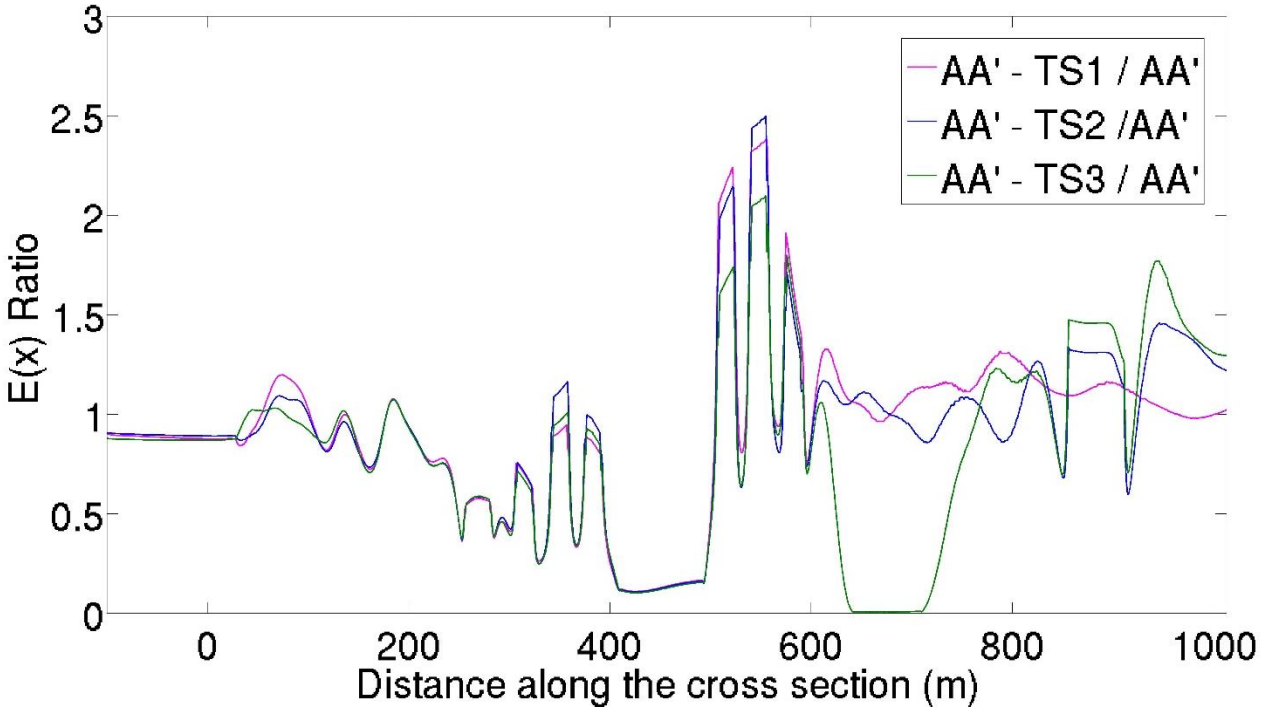

Variation of the ratio between the kinetic energy E(x) index assuming SCI and free field condition along the AA’ model surface forced by EQ-13.

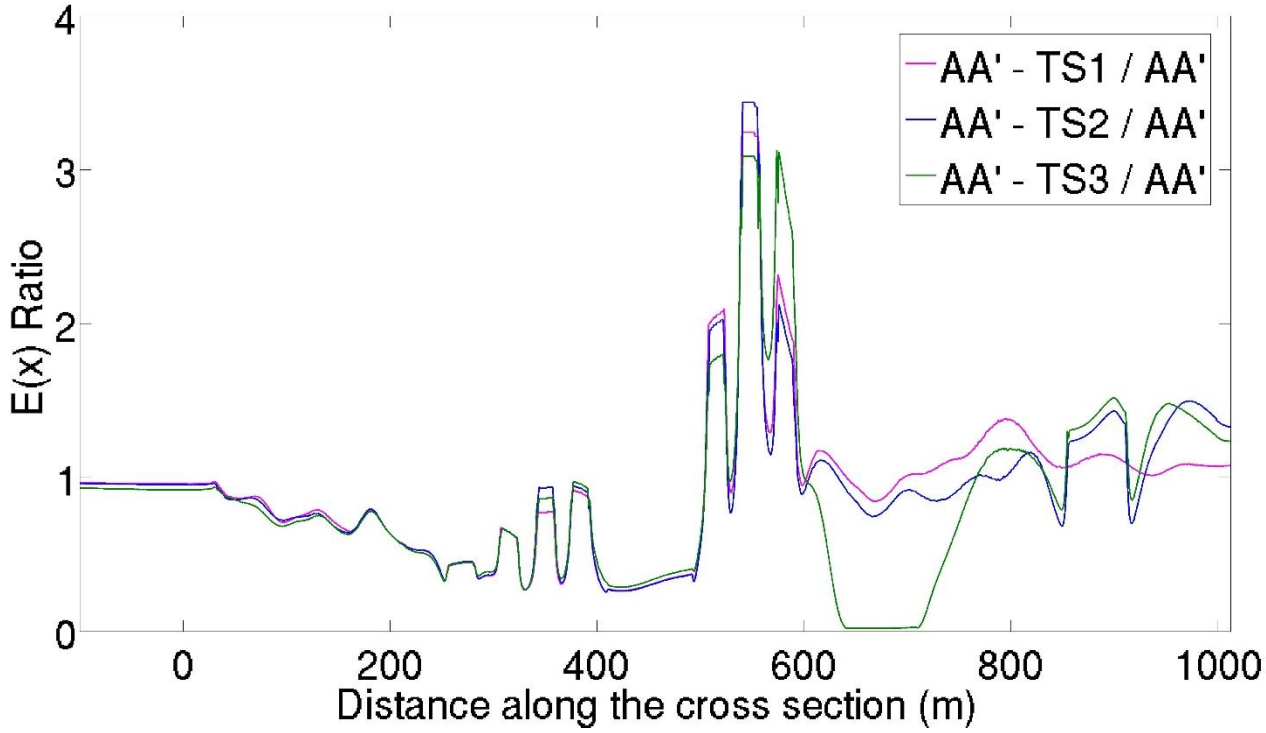

Variation of the ratio between the kinetic energy E(x) index assuming SCI and free field condition along the BB’ model surface forced by EQ-7.

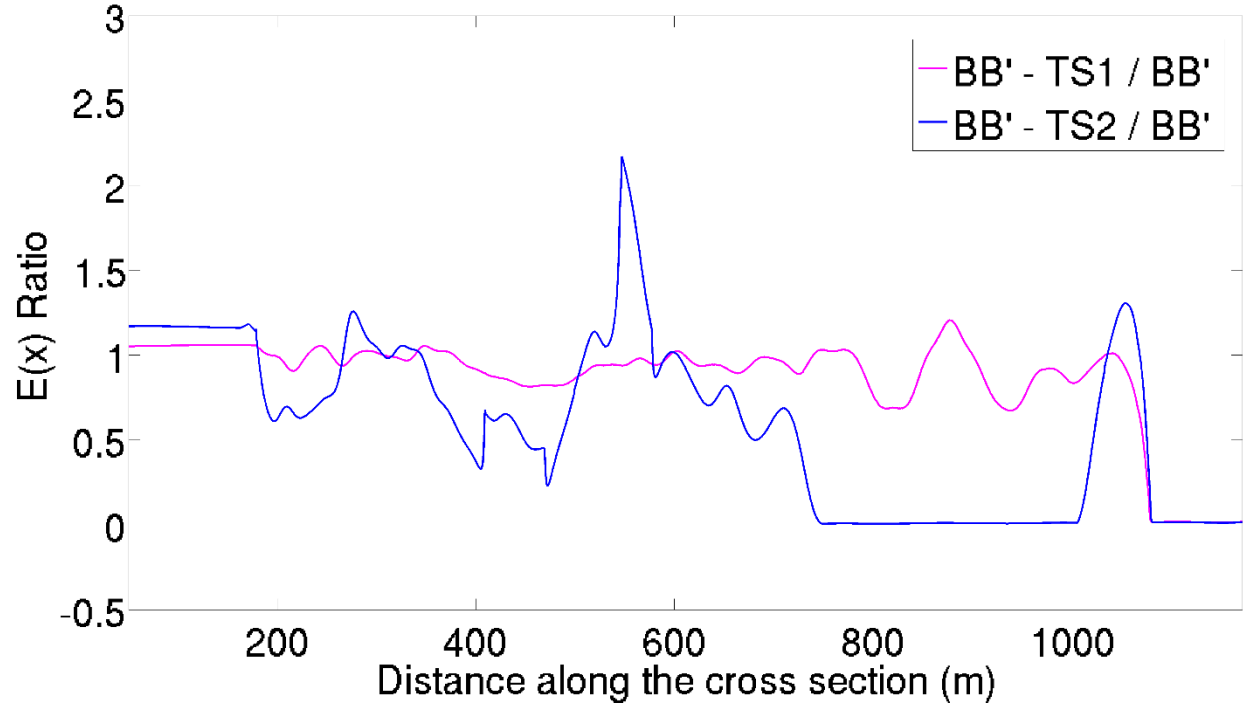

Variation of the ratio between the kinetic energy E(x) index assuming SCI and free field condition along the BB’ model surface forced by EQ-12.

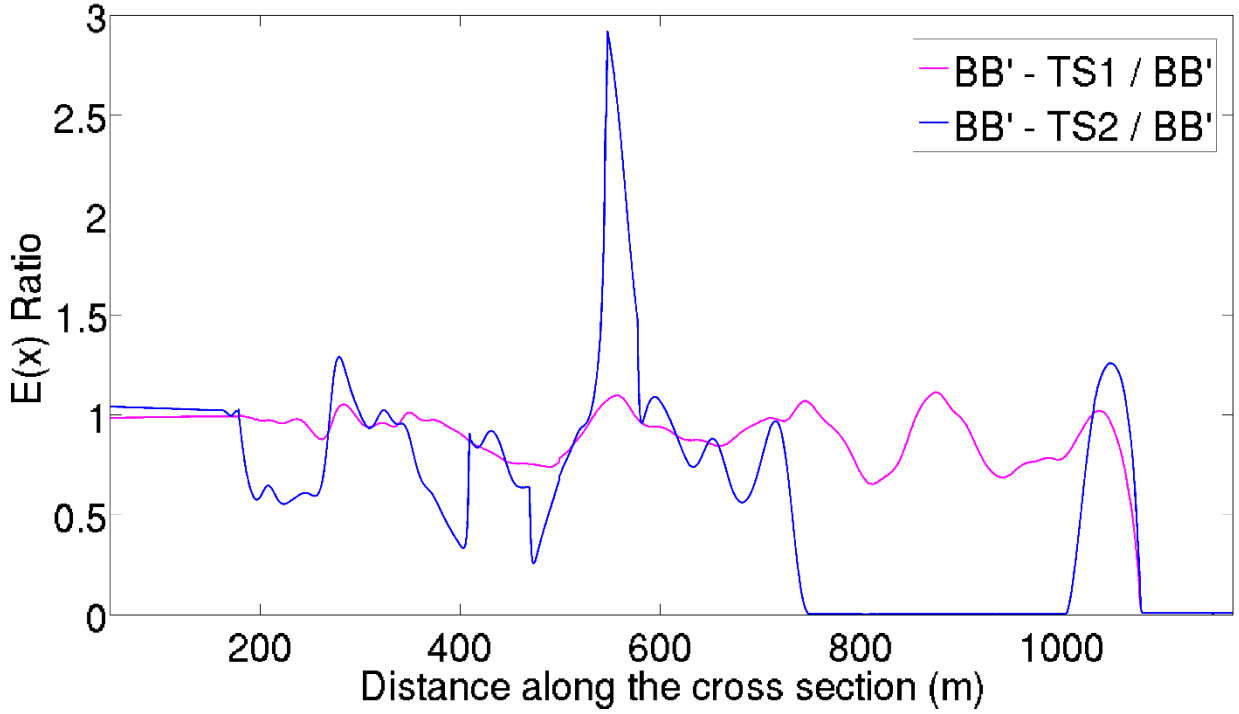

Variation of the ratio between the kinetic energy E(x) index assuming SCI and free field condition along the BB’ model surface forced by EQ-13.